MECHANISMS FOR THE ONSET AND EVOLUTION OF BASALTIC PLINIAN ERUPTIONS INFERRED FROM CASE STUDIES OF ETNA 122 BC AND TARAWERA 1886

A DISSERTATION SUBMITTED TO THE GRADUATE DIVISION OF THE UNIVERSITY OF HAWAI'I IN PARTIAL FULFILLMENT OF THE REQUIREMENTS FOR THE DEGREE OF

DOCTOR OF PHILOSOPHY

IN

GEOLOGY AND GEOPHYSICS

AUGUST 2006

By
Julia E. Sable

Dissertation Committee:

Bruce Houghton, Chairperson
Julia Hammer
Andrew Harris
Don Swanson
Thor Thordarson
Gary Barnes

ACKNOWLEDGEMENTS

Sincere thanks to:

Bruce Houghton, my advisor, for constant patience, encouragement, and good humor, and for teaching me not only about volcanoes, but about successful research practices, diplomatic communication, and the appreciation of fine wine.

Gary Barnes, Julia Hammer, Andy Harris, Don Swanson, and Thor Thordarson, my committee members, for generous encouragement and helpful feedback.

Colin Wilson, Paola Del Carlo, and Mauro Coltelli, my co-authors, for laying the foundation for this dissertation work, and for valuable contributions and kindness.

The National Science Foundation, INGV, and IGNS, for funding this research.

Judy, Steve, and Fleur Collins of Mt Tarawera New Zealand Ltd, for generously granting us access, sampling privileges, and helicopter support for our Tarawera fieldwork.

Costanza Bonadonna, Helge Gonnermann, Takehiro Koyaguchi, Jacopo Taddeucci, and James White, for insightful comments and discussions.

Mike Rosenberg, for indispensable assistance in the field and lab, and for his hat.

Kent Ross, Sarah Sherman, and Sasha Krot, for teaching me to use the microprobe and SEM, and for keeping these instruments running well (sometimes against major odds).

Lucia Gurioli, Chris Gregg, Murray McClintock, Rebecca Carey, Nicole Lautze, and Wendy Stovall, for wisdom, support, camaraderie, coffee, good times, and fun travels.

Chanse Aoki and Ben Sellers, for their bubble-tracing skills and cool personalities.

Nathan Becker, Jim Gharib, Loyc Vanderkluysen, and Margaret Milman, for friendship, generosity, patience, laughter, and tolerance of my eccentricities.

Nancy Adams, for selflessly doing everything first and getting the glitches out for those who follow, and for being a great friend and surfing buddy.

Aisha Morris, Elaine Smid, Jonathan Weiss, and Todd Bianco, for being my family in Hawai'i along with Nancy.

The UHM Counseling and Student Development Center, for doing what they do.

The faculty and students of the Geology and Geophysics and Oceanography departments, for many fun and educational adventures.

My family and friends back home, for believing in me and rescuing me when I needed it.

Thank you very much • *Mahalo nui loa* • *Mille grazie*

ABSTRACT

Basaltic Plinian eruptions are rare, but are increasingly being recognized as an important endmember style of basaltic volcanism. Such high-intensity basaltic eruptions may occur with little warning and affect large populations. This dissertation project characterizes the initiation, progress, and termination of basaltic Plinian eruptions through quantitative studies of the Etna 122 BC and Tarawera 1886 eruptions. The Etna 122 BC eruption had two Plinian phases. The Tarawera 1886 eruption had one climactic phase during which a few vents erupted with Plinian intensity and many other vents hosted weaker explosions. Methods include dispersal measurements, grain size and componentry analysis, measurements of clast densities, descriptions of clast morphologies, and qualitative and quantitative analysis of microtextures, emphasizing bubbles and microlites.

The clasts from both eruptions are microvesicular and have high bubble number densities compared to Hawaiian and Strombolian products, suggesting that the magmas underwent a phase of coupled degassing resulting from rapid decompression. High number densities of microlites in the clasts of both eruptions also agree with the interpretation of rapid degassing. High microlite crystallinities increased the effective viscosity of the magma and encouraged brittle fragmentation.

The Etna 122 BC clasts show remarkable diversity in texture, both between and within samples. Trends toward lower vesicularity and higher crystallinity with time indicate that open system degassing progressively gained importance in both phases. The heterogeneity within samples is attributed to a curved velocity profile that caused melt along the margins to reside longer in the conduit and develop more mature textures.

Accumulation of outgassed, crystalline magma contributed to the decline and end of each Plinian phase.

A wide range of dispersals is observed in the Tarawera 1886 proximal deposits, and many closely spaced vents were active simultaneously with very different intensities and styles. Most dispersals are intermediate between typical Hawaiian-Strombolian and typical Plinian values, suggesting that many particles were released from the margins of the jet portions of the Plinian plumes. All the 1886 magma shared a similar ascent and degassing history, and componentry data suggest that variation in eruptive intensity along the fissure was due to incorporation of variable masses of material from unstable vent walls.

TABLE OF CONTENTS

LIST OF TABLES

LIST OF FIGURES

CHAPTER 1

Introduction

1.1 Project goals

Plinian eruptions are commonly perceived to be confined almost completely to silicic systems. As a result, Plinian eruptions at basaltic volcanoes tend to be neglected in studies of this powerful, sustained style of explosive volcanism. The rationale for this assumption is that, in general, the explosivity of basaltic magma is limited by its relatively low viscosity, higher gas permeability, and lower volatile content in comparison with silicic magma (Vergniolle and Jaupart, 1986). In the last 20 years, however, four basaltic deposits were recognized as having Plinian dispersal (Williams, 1983; Walker et al., 1984; Coltelli et al., 1998). The special conditions that lead to basaltic Plinian events have previously been poorly constrained.

This dissertation project aims to constrain the processes controlling basaltic Plinian volcanism focusing on the eruptions of Etna 122 BC and Tarawera 1886. These are the only two *historical* basaltic eruptions confirmed to have Plinian dispersal characteristics (Carey and Sigurdsson, 1989; Coltelli et al., 1998). Eyewitness accounts are thus available for both and are especially well documented for Tarawera 1886. Because Etna and Tarawera are classified as currently active volcanoes and are surrounded by populated areas, an improved understanding of the mechanisms that produce exceptionally violent explosive activity in these volcanoes can be applied to help their associated communities prepare for the possibility of another Plinian eruption.

Key processes that need to be explained for each eruption are (1) initiation of the intense sustained explosion, (2) evolution and apparent variations in eruptive intensity with time (and with vent location in the case of Tarawera), and (3) cessation of the eruption. This study will explore possible factors that may promote basaltic Plinian volcanism, and how the relative importance of the different processes can be distinguished principally through quantitative microtextural studies of the volcanic products. I also quantify proximal dispersal and sedimentation for the Tarawera 1886 eruption. Methods include field mapping, stratigraphic logging, componentry analyses, bulk density measurements, glass chemistry, and microscopic textural studies through digital image analysis. This last technique is emphasized because it yields valuable quantitative data for size, shape, and distribution of vesicles and crystals, which, in turn, reflect the types, rates, and relative timings of vesiculation and crystallization processes within the magma, as well as the influence of external processes such as interaction between magma and groundwater. My findings for the two volcanoes are compared, but the work for each volcano can also stand independently.

My collaborators on this project are Mauro Coltelli and Paola del Carlo of Istituto Nazionale di Geofisica e Vulcanologia, Catania, for the Etna 122 BC study; Colin Wilson of the Institute of Geological and Nuclear Sciences, New Zealand, and Rebecca Carey of University of Hawai'i for the Tarawera 1886 study; and my advisor Bruce Houghton for all aspects of the project.

1.2 Basaltic explosive volcanism

In terrestrial settings, basaltic volcanoes are typically dominated by effusive and weak explosive behavior (Simkin and Siebert, 1994). Most basaltic explosive activity takes the form of Hawaiian fountains or Strombolian explosions that typically do not send ejecta higher than 500 m and rarely affect areas more than a few kilometers from the vent (e.g., Richter et al., 1970; Chester et al., 1985; Wolfe et al., 1988; Barberi et al., 1993; Simkin and Siebert, 1994; Coltelli et al., 1995).

Highly explosive eruptions, such as subplinian and Plinian types, are far more common in more evolved silicic systems than in basaltic ones (see Table 1 in Carey and Sigurdsson, 1989). Compared to silicic magmas, basaltic magmas have higher eruption temperatures, higher liquidus temperatures, lower viscosities, and lower capacities to hold H_2O and other volatiles in solution. These factors may explain why basaltic magma so rarely produces intense explosions (Sparks et al., 1994). However, several examples of energetic and violent explosive activity have now been documented for basaltic volcanoes, including large phreatomagmatic, subplinian, and Plinian eruptions (e.g. Williams, 1983; Walker et al., 1984; McPhie et al., 1990; Coltelli et al., 1998).

Magma ascent and fragmentation in Hawaiian-Strombolian eruptions

Prior to any eruption, the ascent of magma from the storage zone may be caused or assisted by the buoyancy of gas bubbles (Carrigan et al., 1992). If magma lacks gas bubbles at depth, ascent may be also initiated by accumulated stress around a magma chamber due to injection of a volume of magma from depth (Wilson and Head, 1981).

Factors that affect magma ascent and fragmentation include intrinsic properties of the magma such as pre- and syn-eruptive volatile contents, temperature, crystal content,

melt composition, density, and viscosity (e.g., Pinkerton and Stevenson, 1992; Hess and Dingwell, 1996; Manga et al., 1998; Papale et al., 1998), as well as external influences such as conduit and vent dimensions, confining pressure, and presence of surface or ground water (Wilson et al., 1980; Barberi et al., 1989). All of these factors affect the degassing behavior of the magma, which is the first-order control on ascent (e.g., Vergniolle and Jaupart, 1986; Dobran, 1992; Papale, 1998).

The style and intensity of basaltic explosive behavior are determined by the extent to which the gas and melt are coupled during ascent. The effusive to weakly explosive styles most typical of basaltic volcanism are associated with open system, or decoupled, degassing, where rapid bubble growth and coalescence allow gas bubbles to move relative to the surrounding melt (Cashman and Mangan, 1994). Rising bubbles may intersect the free surface of the magma column, allowing persistent, passive degassing (Allard et al., 1994).

At low rates of magma ascent, bubble coalescence is common and has a cascading effect on bubble size (e.g. Blackburn et al., 1976; Gaonac'h et al. 1996a; Herd and Pinkerton, 1997), permitting the formation of gas slugs that ascend freely through the melt and trigger discrete Strombolian explosions at the free surface (Fig. 1.1; Wilson and Head, 1981; Vergniolle and Jaupart, 1986; Parfitt and Wilson, 1995; Parfitt, 2004). The coalescence may occur dynamically during ascent in the conduit if H_2O is the main volatile involved in vesiculation (Parfitt and Wilson, 1995; Parfitt, 2004), or may occur via sudden collapse of a CO_2-dominated foam accumulated at the top of the magma chamber (Vergniolle and Jaupart, 1986; Jaupart and Vergniolle, 1989; Vergniolle and Brandeis, 1996; Vergniolle et al., 1996; Ripepe and Gordeev, 1999). The foam collapse

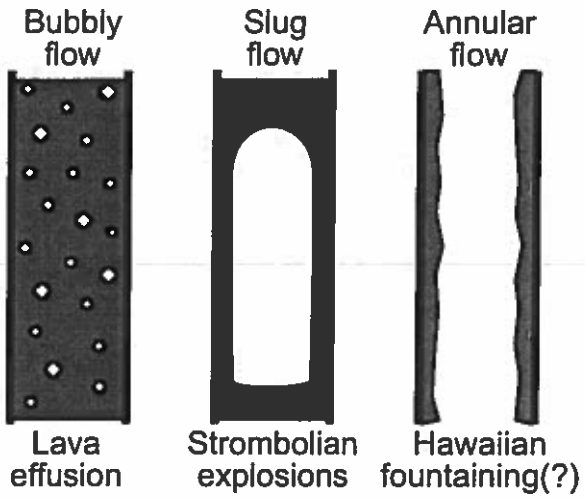

Figure 1.1 Endmember examples of two-phase flow regimes, from Vergniolle and Mangan (2000). For Strombolian explosions, slug flow is a widely accepted mechanism. Whether the annular flow mechanism for Hawaiian fountaining (Jaupart, 2000) is still debated (Parfitt, 2004).

model is supported by geophysical data from Stromboli (Ripepe, 1996; Chouet et al., 1997) and gas emissions at Etna (Allard et al., 2005), but is not supported by data collected at Kilauea (Parfitt and Wilson, 1994; Parfitt, 2004). Some data are consistent with either model (Harris and Neri, 2002; Parfitt, 2004).

Hawaiian fountaining eruptions are associated with a moderately high ascent rate and a relatively low degree of bubble coalescence, leading to partially coupled behavior at shallow levels (Wolfe et al., 1988; Parfitt and Wilson, 1995). These bubbles accelerate upward and drag the melt with them. An alternative model for conduit flow in Hawaiian eruptions suggests that the gas and melt separate to permit annular flow, where the gas streams up the center of the conduit while the melt ascends along the walls (Fig. 1.1; Jaupart, 2000; Seyfried and Freundt, 2000 and references therein).

Hawaiian-Strombolian transport and deposition

Clasts ejected in Strombolian and Hawaiian eruptions are generally modeled to decouple early from the gas phase and follow approximately ballistic trajectories (e.g. Wilson and Head, 1981; Head and Wilson, 1987; Vergniolle and Mangan, 2000). Deposition of clasts is overwhelmingly confined to locally dispersed cinder and spatter cones (Walker, 1973; Head and Wilson, 1989; Riedel et al., 2003), with thinning half-distances of 5-50 m (e.g. Bullard, 1947; Foshag and Gonzales, 1956; Richter et al., 1970; Fedotov et al., 1978; Tokarev, 1983; McClelland et al., 1989; Sumner, 1998; Heliker et al., 2003; Yasui and Koyaguchi, 2004; Calvari and Pinkerton, 2004; Andronico et al., 2005). Small proportions of finer particles rise with the gases and are deposited in more widespread ash blankets, but the blankets generally do not extend beyond 10 km from vent (Walker, 1973). Parfitt and Wilson (1999) model Hawaiian fountains with a modified version of a

Plinian plume model. In their view, the main difference between Hawaiian fountains and Plinian plumes is the contrast in primary grain size distributions of the erupted clasts.

1.3 Plinian volcanism

Strombolian and Hawaiian eruptions are low intensity events that are typically fairly short-lived, lasting seconds to hours (Blackburn et al., 1976; Barberi et al., 1993; Wolfe et al., 1988). They have low degrees of fragmentation and small dispersals (Walker, 1973). In contrast, Plinian eruptions are intense and sustained. They can affect large areas, with potentially catastrophic impact on populations and land use (Cioni et al., 2000). Plinian deposits are assumed to thin exponentially away from vent (Walker, 1973), permitting the use of regular thickness changes with distance to quantify dispersal. According to Walker (1973), for a deposit to be classified as Plinian, the area enclosed by the isopach representing 0.01 of the maximum thickness (T_{max}) must exceed 500 km^2. Pyle (1989) uses two other parameters to define a Plinian deposit: clast half distance (b_c), defined as the radial distance over which the maximum clast diameter decreases by half, and thickness half distance (b_t), the distance over which the thickness of a deposit decreases by half. Pyle's (1989) classification requires that a Plinian deposit have a half distance ratio (b_c/b_t) of 3 or less. Deposits with these dimensions are associated with eruption column heights of at least 20 km as estimated from current models (Cioni et al., 2000).

Magma ascent and fragmentation in Plinian eruptions

Plinian explosive eruptions are driven by the formation and coupled expansion of gas bubbles (e.g. Sparks, 1978; Wilson and Head; 1981). H_2O has a dominant role in eruption dynamics, although exsolution of CO_2 may be important at depth (e.g., Woods and Cardoso, 1997; Allard et al., 2005). Magmas of different compositions have different capacities to hold volatiles in solution (Johnson et al., 1994; Papale, 1999a). The amount of dissolved volatiles greatly influences eruptive style by controlling the volume of gas that can potentially form through exsolution, and affecting the viscosity of the silicate melt (Hess and Dingwell, 1996).

Plinian exit velocities commonly exceed 200 m s^{-1} (Wilson, 1976; Wilson and Head 1981). For magma to accelerate to the necessary velocity to produce a Plinian explosion, models of conduit dynamics require a coupled or "closed system" mode of degassing (Fig. 1.2; Eichelberger, 1986; Papale, 1998 and references therein). Gas bubbles are coupled with the melt and cannot escape; the exsolution and expansion of gas therefore accelerates the mixture upward as bubble overpressure increases (Sparks et al., 1994; Cashman et al., 2000). Fragmentation occurs when the volume fraction of bubbles reaches a threshold (Sparks, 1978), when the bubble overpressure relative to surrounding melt becomes critical (Melnik, 2000), or when the strain rate exceeds the tensile strength of the magma, driving the melt through the brittle-ductile transition (Papale, 1999b). The overpressure and strain-rate criteria are most easily met when the melt is highly viscous and has low volatile diffusivity (Cashman et al., 2000). Under these conditions, it is difficult for volatile species to form clusters large enough to become stable bubble nuclei, and this kinetic hindrance to bubble nucleation leads to the development of H_2O

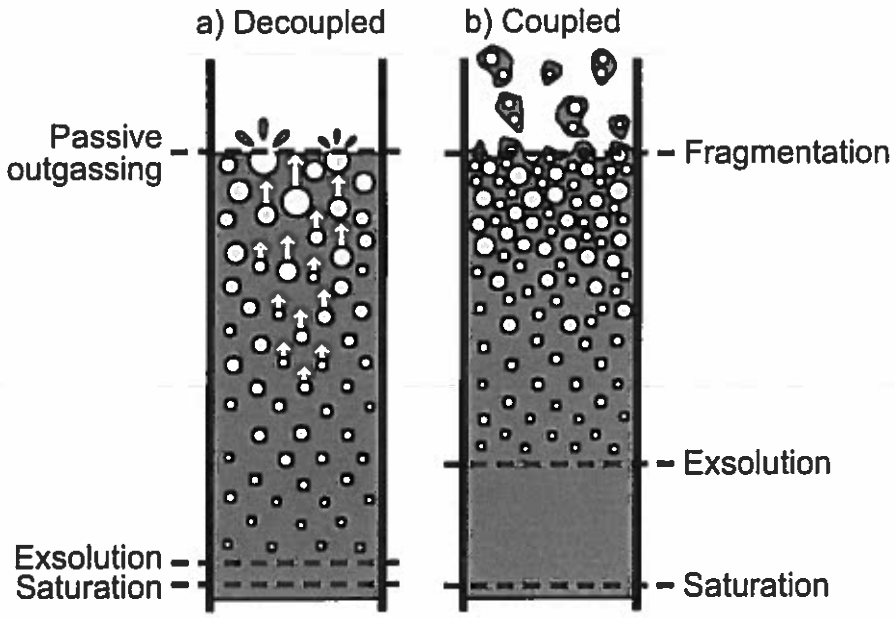

Figure 1.2 Cartoon showing decoupled and coupled degassing. (a) Decoupled degassing is associated with fluid magmas where both dissolved volatile species and exsolved bubbles have high mobility. Bubbles can ascend relative to magma; lengths of arrows show that larger bubbles move faster. (b) In coupled degassing, bubbles cannot move relative to the magma, and overpressure can develop, leading to explosive fragmentation. One mechanism that may promote coupled degassing is delayed exsolution at high supersaturation.

supersaturation (Sparks, 1978; Sparks et al., 1994; Navon and Lyakhovsky, 1998). When the kinetic barriers are finally overcome, high degrees of supersaturation may have been reached and nucleation may be very rapid (Hurwitz and Navon, 1994; Mangan and Sisson, 2000). The resulting runaway vesiculation immediately increases the magma's buoyancy and accelerates ascent toward regions of lower confining pressure. Bubble expansion due to decompression further accelerates the mixture. At the same time, the loss of H_2O through vesiculation increases the melt's yield strength and viscosity, often by several orders of magnitude (e.g. Hess and Dingwell, 1996; Giordano and Dingwell, 2003b). In the shallow conduit, the acceleration is so great that it drives the melt through the glass transition, leading to brittle fragmentation (Papale, 1999).

Plinian plumes: transport and deposition

Upon fragmentation, bubbly magma is transformed into a suspension of clasts supported by expanding gas (Papale, 1998 and references therein). As the suspension approaches the vent, it decompresses to atmospheric pressure (Kaminski and Jaupart, 1997). The gas-clast mixture exits the vent at the speed of sound for the mixture (Woods and Bower, 1995). Typical Plinian exit velocities are 100-400 m s^{-1} (Cioni et al., 2000).

For the first 0.5-4 km of ascent, the erupting mixture travels as a relatively dense, momentum-driven jet (Fig. 1.3; Sparks, 1986; Woods, 1988; Sparks et al., 1997). Models of the jet region of the Plinian plume suggest that turbulent eddies along the jet margins allow air entrainment and sedimentation of coarse particles (Bursik et al., 1992; Ernst et al., 1996), such that the plume expands and becomes buoyant. As a result, the transport mode changes from a momentum-driven jet region to a buoyancy-driven convective region (Fig. 1.3; Sparks, 1986; Woods, 1988). The expansion and buoyancy of the

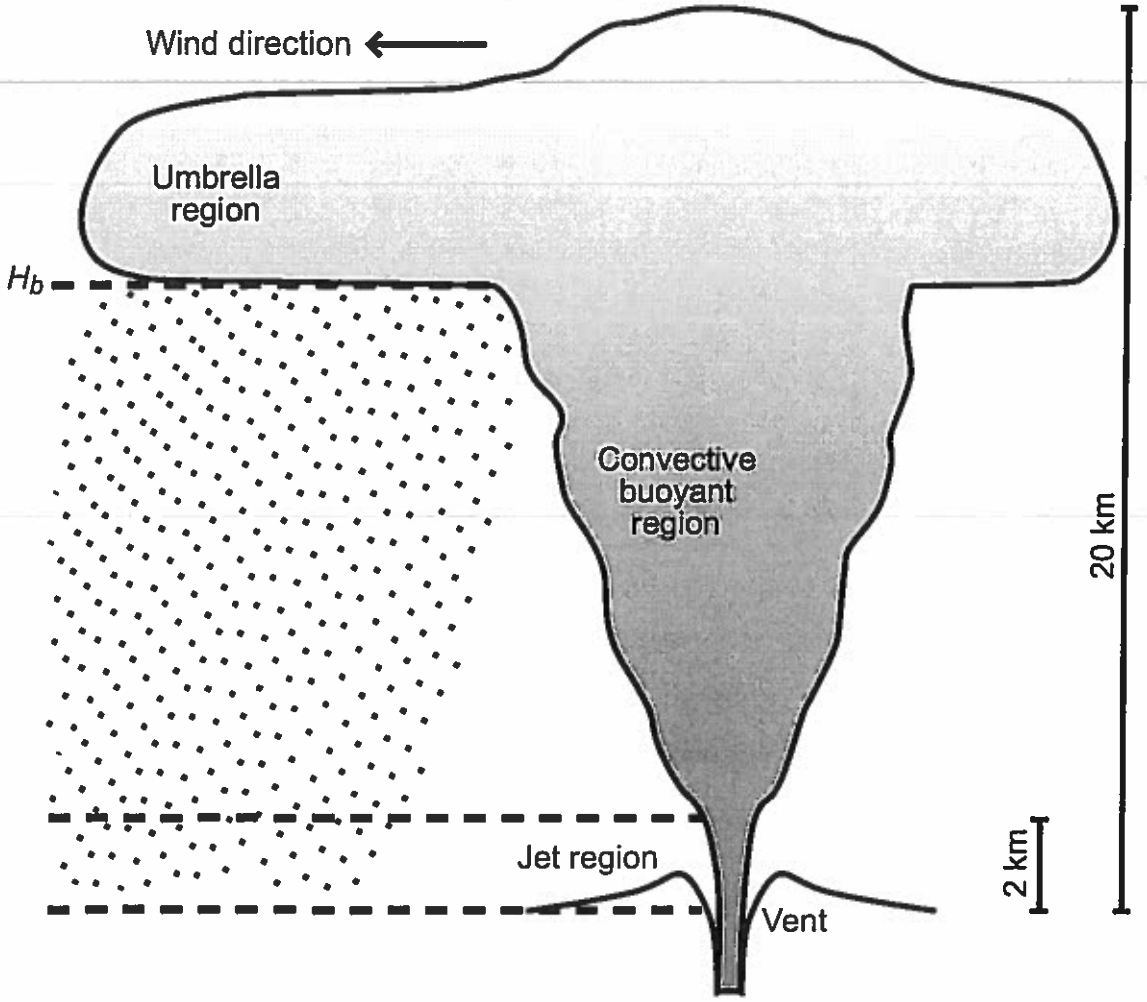

Figure 1.3 Cartoon showing parts of a Plinian plume. The jet region is driven by the upward momentum of the ejected mixture. Entrainment and heating of air allows the mixture to become less dense than the surrounding air so that the plume becomes buoyant. The convective buoyant region extends up to height H_b, at which the mixture reaches neutral buoyancy. From this point the mixture spreads laterally to form the umbrella region. From Sparks (1986).

mixture depend on the efficiency of heat transfer from the hot gas and particles to the entrained air (Sparks et al., 1997). The convective buoyant region of the plume can extend to 5-40 km above the vent depending on exit velocity and temperature of the ascending suspension (Sparks, 1986; Sparks et al., 1997).

The plume rises until it reaches a level of neutral buoyancy in the atmosphere, where it begins to spread laterally, forming the umbrella region of the plume (Fig. 1.3; Sparks et al., 1997). The umbrella region is typically modeled as a gravity current with provisions for advection by wind (Carey and Sparks, 1986; Bursik et al., 1992; Sparks et al., 1992; Koyaguchi, 1994; Bonadonna et al., 1998; Bonadonna and Phillips, 2003). The size, density, and shape of a clast determine its terminal velocity, which, in turn, controls how far it can be carried before it is released (Walker et al., 1971). Clast dispersal is used to calculate column heights for ancient eruptions based on the maximum clast sizes in the deposits (Carey and Sparks, 1986).

1.4 Basaltic Plinian eruptions

Occurrence and significance

Deposits of highly explosive basaltic eruptions are scarce in the geologic record. The main known examples have been recognized only recently, within the last 20 years. They include the scoria fall deposits of the >20 ka Fontana Lapilli and the 6.5 ka San Judas Formation of the Masaya caldera complex in Nicaragua (Williams, 1983), the 122BC eruption of Mount Etna in Sicily (Coltelli et al., 1998), and the 1886 eruption of Tarawera in New Zealand (Walker et al., 1984; Sable et al., 2006b). The intensities of these events are compared to those of other eruptions worldwide on a plot (after Pyle, 1989) of log

deposit thickness vs. square root of area (Fig. 1.4). More intense eruptions produce curves with gentler slopes on this diagram. Height on the y-axis roughly indicates a deposit's relative volume, which depends on both the intensity and duration of an eruption.

The causal mechanisms of highly explosive basaltic eruptions are not well understood. This is a point of concern, because precursors to such eruptions may be misinterpreted or overlooked. In addition, basaltic magma can ascend through a conduit system very rapidly compared with more viscous silicic magma, so that the warning period before a basaltic explosive eruption may be as short as a few hours. Thus a study of basaltic Plinian volcanism has important implications for hazard assessment and mitigation.

Possible mechanisms

The mechanisms proposed to explain explosivity in silicic systems cannot be applied directly or simply to basaltic systems. High magma viscosity is critical to create the coupled degassing behavior that allows magma to accelerate to speeds typical of Plinian eruptions (Sparks et al., 1994; Cashman et al., 2000). The relatively low viscosity and high gas permeability of basaltic magma typically do not promote powerful explosive eruption, because gas escapes fairly continuously (decoupled behavior) and cannot build the necessary pressure to generate a large eruption column (Sparks et al., 1994). Another factor that limits the explosivity of many basaltic eruptions is the magma's low initial volatile content relative to more evolved magma.

A mechanism to suppress or delay open system degassing and promote coupling between gas and melt is necessary to make basaltic Plinian volcanism possible (Houghton

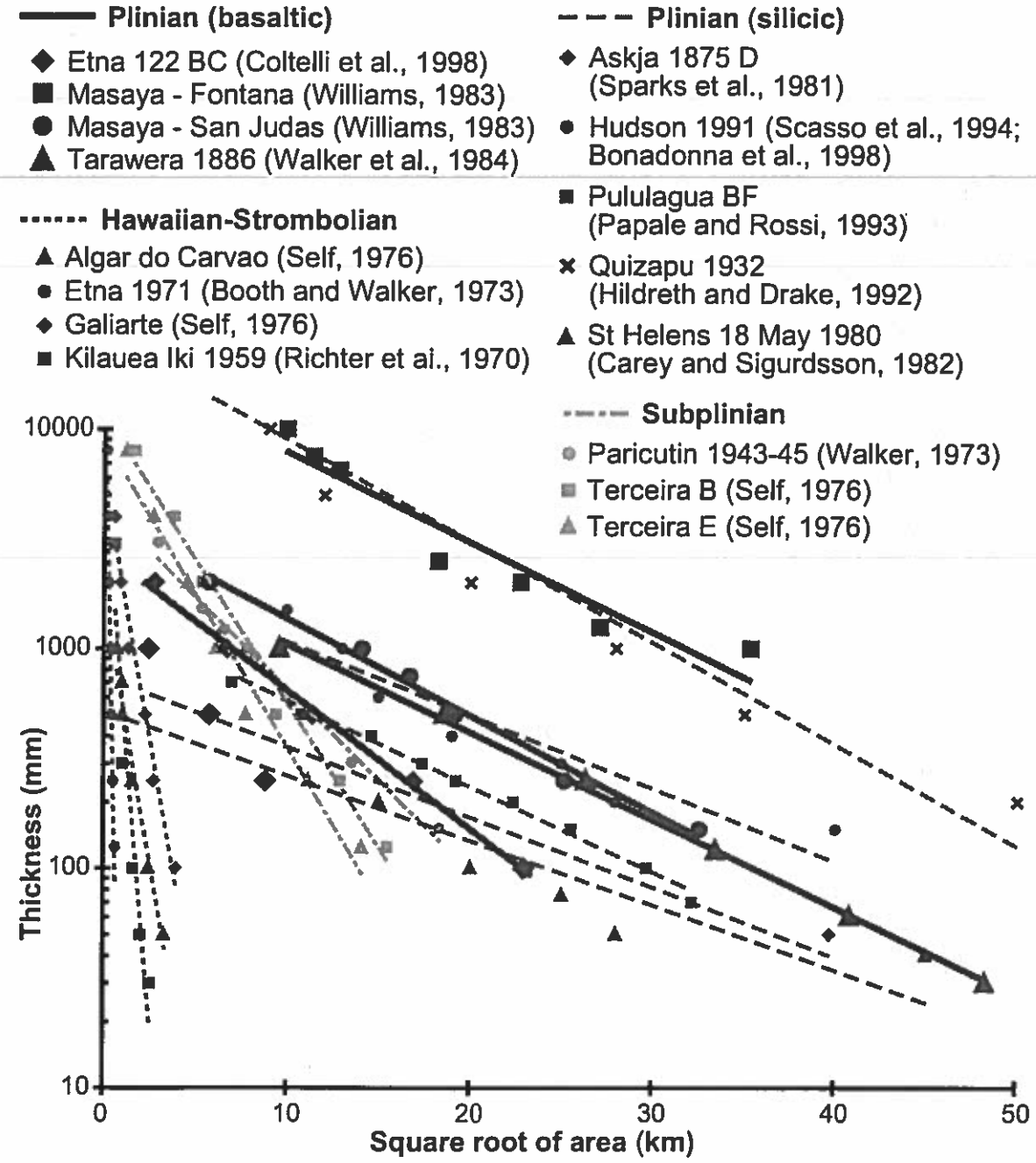

Figure 1.4 On plots of log thickness vs. square root of area, gentler slopes indicate more intense explosive eruptions (Pyle, 1989). The four known basaltic Plinian deposits are compared with selected Hawaiian-Strombolian, subplinian, and silicic Plinian deposits.

et al., 2004a). The basaltic magma must be forced to adopt coupled behavior either by increasing its viscosity or by causing vesiculation to occur within such a short time span that the bubbles do not have time to decouple from the melt. Several possible factors are listed below that may work alone or in combination for different eruptions.

(1) Sudden static decompression of volatile-saturated melt. A sudden depressurization event, such as a large sector collapse, could induce strong disequilibrium followed by rapid bubble nucleation in the shallow conduit (Coltelli et al., 1998). The vesiculation would occur on such a short time scale that the inertial forces inhibiting bubble growth and coalescence would be significant, and bubbles would remain coupled with the melt.

(2) Rapid ascent due to early exsolution of a CO_2-rich volatile phase followed by late homogeneous nucleation of an H_2O-rich phase. The CO_2 vesiculation could cause the melt to ascend so rapidly that H_2O is unable to exsolve at depth due to kinetic barriers (Navon and Lyakhovsky, 1998). Degassing of H_2O would be delayed until the magma reaches a shallow level in the conduit and achieves a very high H_2O supersaturation pressure. The time scale of H_2O vesiculation would be shortened as described in (1).

(3) Shallow interaction between magma and external water. If ascending magma encountered groundwater high in the conduit, the water would vaporize and expand with enough energy to produce a powerful explosion (Barberi et al., 1989; Mastin et al., 2004). Water may also enter the top of the conduit during magma withdrawal or fluctuations in magma column height (Dvorak, 1992). Phreatomagmatic layers are observed above and below the Plinian units of both the Etna 122 BC and Tarawera 1886 basaltic scoria deposits, indicating that external water was present in the rocks forming the walls of the

conduit. Limited amounts of water could have interacted with the magma during the Plinian phases but without leaving obvious signatures on grain size or clast morphology (Houghton and Wilson, 1998).

(4) **Viscosity increase due to microlite crystallization.** Degassing could encourage the formation of microlites by increasing the effective undercooling for anhydrous mineral phases, and the resulting increase in crystallinity can increase magma's viscosity by orders of magnitude (e.g. Klug and Cashman, 1994; Hammer et al., 1999; Spera, 2000; Martel et al., 2001). The high effective viscosity would restrict bubble mobility, allowing gas and melt to stay mechanically coupled (Sparks et al., 1994). Microscopic observations of pyroclasts from the Etna 122 BC and Tarawera 1886 deposits reveal high number densities of microlites. If at least some of the microlites formed early in ascent, the magma's effective viscosity could have been high enough to prevent decoupling of gas and melt during subsequent bubble nucleation and growth.

(5) Early incorporation of wall rock with effects on composition and rheology. Incorporation of wall rock could have several consequences. First, by analogy with entrainment in lava flows, cooling of magma would be enhanced by incorporation, heating, and re-melting of colder material (Crisp and Baloga, 1994). The magma could also lose heat to any groundwater trapped in the wall rock's interstices (Valentine and Groves, 1996). The resulting temperature drop would increase viscosity (Hess and Dingwell, 1996). Second, the magma's effective viscosity would be increased by addition of particles, including crystals that may nucleate due to cooling, as well as wall-rock-derived xenoliths and xenocrysts (Pinkerton and Stevenson, 1992; Lejeune and Richet, 1995; McBirney and Murase, 1984; Spera, 2000). Third, if wall rock were

melted and mixed with the magma, the overall melt composition could change, resulting in a viscosity change (Bottinga and Weill, 1972; Shaw, 1972; Pinkerton and Stevenson, 1992). All three of these factors could promote Plinian behavior by increasing viscosity and preventing decoupling of gas from melt (Sparks et al., 1994).

1.5 Changes in magma during conduit ascent

Records of conduit processes are preserved in the microscopic textural properties of the erupted clasts, such as the numbers, sizes, and shapes of bubbles, microphenocrysts, and microlites (e.g. Cashman, 1990, 1993; Cashman and Mangan, 1994; Gardner et al., 1999; Hammer et al., 2000).

Volatile supersaturation and bubble nucleation

When confining pressure on the melt decreases, the solubility of gases in the melt also decreases (Mysen, 1977; Burnham, 1994; Blank and Brooker, 1994). Solubility of gas also decreases slightly with increasing temperature, but this dependence is weak (Mysen, 1977; Burnham, 1994; Blank and Brooker, 1994).

Water is the most abundant magmatic volatile; both molecular water (H_2O) and OH^- groups are involved in melt vesiculation (Johnson et al., 1994; Bagdassarov et al., 1996). Based on experimental data, Wilson and Head (1981) give approximate solubility relationships for H_2O in rhyolite and basalt. For rhyolite, $n_d = 0.13\ P_b^{0.5}$, where n_d is H_2O solubility in weight percent and P_b is total pressure in bars. For basalt, $n_d = 0.0215\ P_b^{0.7}$ (Wilson and Head, 1981). In comparison, the solubility of CO_2 decreases approximately linearly with decreasing pressure (Sparks et al., 1994, and references therein; Blank and Brooker, 1994). At a given pressure, CO_2 is much less soluble than H_2O. Exsolution of

CO_2 promotes some exsolution of H_2O, even if the melt is not saturated with H_2O at that pressure (Holloway, 1976; Sparks et al., 1994).

After sufficient decompression, the melt may become supersaturated with respect to a given volatile species, such as H_2O. The "supersaturation pressure," $\Delta P = P_{gas} - P_{melt}$, is related to the difference between the actual volatile concentration in the supersaturated melt and the equilibrium concentration within the melt at the given pressure (Sparks et al., 1994; Navon and Lyakhovsky, 1998). The supersaturation pressure changes during magma ascent in response to two competing processes. While the ongoing exsolution of volatiles decreases the degree of supersaturation, the decreasing pressure increases the degree of supersaturation (Toramaru, 1990). The degree of supersaturation thus depends on the decompression rate, but work is still in progress to define an empirical relationship in detail (Hurwitz and Navon, 1994; Gardner et al., 1999; Mangan and Sisson, 2000).

Under conditions of changing pressure, equilibrium degassing occurs if bubbles nucleate and grow at rates sufficient to keep the dissolved gas content equal to its equilibrium value at any given instantaneous pressure (e.g. Gardner et al., 1999). Equilibrium degassing can occur if the rate of decompression is sufficiently slow and the magma viscosity is sufficiently low that diffusion and bubble growth are unrestricted (e.g. Barclay et al., 1995; Mangan and Sisson, 2000). Disequilibrium degassing, in contrast, occurs when the rate of exsolution of volatiles cannot keep up with the rate of decompression, so that supersaturation develops (e.g. Lyakhovsky et al., 1996; Gardner et al., 1999; Mangan and Sisson, 2000; Mangan et al., 2004). A melt can switch between equilibrium and disequilibrium behavior as pressure and volatile content change (Lyakhovksy et al., 1996; Hammer et al., 1998).

The supersaturation at which bubbles start to nucleate depends on melt viscosity, volatile diffusivity, and availability of nucleation sites (Hurwitz and Navon, 1994). The local concentration of H_2O and other volatile molecules fluctuates randomly on a microscopic scale, permitting the formation of small clusters of matching species (Navon and Lyakhovsky, 1998 and references therein). An activation energy is required to assemble the cluster and establish a stable gas-melt interface. When a cluster reaches a critical radius (r_c), the addition of more gas molecules results in a decrease in free energy; further growth is spontaneous and the cluster is considered a stable bubble nucleus (Fig. 1.5; Navon and Lyakhovsky, 1998). The critical radius is smaller at larger ΔP, so that the smallest bubbles are likely to be preserved in clasts that experienced the highest supersaturations (Sparks, 1978).

Classical nucleation theory derives the nucleation rate from the probability that a cluster of H_2O molecules will reach a certain size. The expression for nucleation rate is

$$J = J_0 \exp(-\Delta G/kT)$$

where J is nucleation rate, J_0 is a pre-exponential term related to the distribution of volatile molecules in the melt, ΔG is the change in free energy, k is Boltzmann's constant, and T is temperature (Hirth et al., 1970; Sparks et al., 1994; Navon and Lyakhovsky, 1998 and references therein). The change in free energy depends strongly on the supersaturation pressure (ΔP), and consequently so does the nucleation rate (Navon and Lyakhovsky, 1998). Experimentally measured nucleation rates in rhyolite magma are < 1 $cm^{-3}\ s^{-1}$ (i.e. undetectable) for ΔP = 120 MPa, 10^3-10^5 $cm^{-3}\ s^{-1}$ for ΔP = 130-150 MPa, and 10^6 $cm^{-3}\ s^{-1}$ for ΔP = 160-175 MPa (Mangan and Sisson, 2000). Bubble nucleation rates in basaltic melt have not yet been experimentally measured.

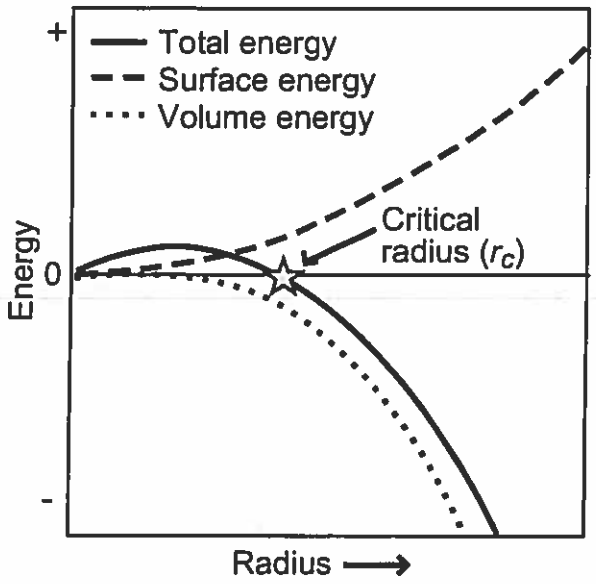

Figure 1.5 Schematic plot showing the relationship between radius and free energy for clusters of atoms. Beyond the critical radius (r_c), the free energy decreases with the addition of more atoms. From Cashman et al. (2000).

Homogeneous nucleation occurs in the absence of nucleation sites such as crystals or anisotropies in the melt (Sparks et al., 1994). Experiments by Gardner et al. (1999) and Mangan and Sisson (2000) suggest that extreme degrees of H_2O supersaturation are needed for homogeneous nucleation. For rhyolitic magma, the supersaturation pressure (ΔP) must be at least 120-150 MPa, equivalent to approximately twice the equilibrium H_2O concentration (Mangan and Sisson, 2000; Mangan et al., 2004). Very high decompression rates (0.25 to 1.0 MPa s^{-1}) are necessary to achieve this supersaturation pressure (Gardner et al., 1999).

Homogeneous nucleation is a sustained rather than an instantaneous process (Mangan and Sisson, 2000; Mangan et al., 2004). The bubble number density depends exponentially on the degree of supersaturation (Mangan et al., 2004). Experimentally obtained bubble number densities attributed to homogeneous nucleation in rhyolitic melt range from 10^6 to 10^9 cm^{-3} (Mangan et al., 2004). This is comparable to the 10^7-10^{10} cm^{-3} range observed in high-silica pumice (Klug and Cashman, 1994; Klug et al., 2002; Polacci et al., 2003; Gurioli et al., 2005). Cited bubble number densities are per volume of bulk rock, rather than per volume of bubble-free melt, unless otherwise specified.

Heterogeneous nucleation, in which bubbles nucleate on existing anisotropies in the melt, requires a lower activation energy and thus starts at a lower supersaturation than homogeneous nucleation (Sparks et al., 1994). In experiments, heterogeneous nucleation is also observed to proceed faster than homogeneous nucleation (Hurwitz and Navon, 1994; Sparks et al., 1994). Biotite, zircon, apatite, and especially Fe-Ti oxide crystals are efficient bubble nucleation sites, but plagioclase crystals are inefficient sites (Hurwitz and Navon, 1994). Experiments suggest that heterogeneous nucleation is an instantaneous

event that leads to equilibrium degassing and produces bubble number densities of about 10^5-10^7 cm^{-3} (Mangan et al., 2004).

The supersaturations at which nucleation starts in experiments are not as high as those predicted by classical theory for homogeneous nucleation (Hurwitz and Navon, 1994; Gardner et al., 1999). A possible explanation is the presence of "cryptic" or unseen nucleation sites in apparently crystal-free melts (e.g. Hurwitz and Navon, 1994; Sparks et al., 1994). The style (homogeneous or heterogeneous) of nucleation at a given decompression rate does not appear to have a strong or systematic effect on the nucleation rate or final bubble number density (Mangan and Sisson, 2000).

Experiments show that it is possible for heterogeneous and homogeneous nucleation to occur in the same melt, though not necessarily at the same time (Mangan et al., 2004). Heterogeneous nucleation on existing crystals is inevitable, but if sufficient ΔP remains after all the heterogeneous nucleation sites have been used, then homogeneous nucleation can occur in the zones between crystals. The two styles of nucleation may even overlap in time (Mangan and Sisson, 2000). Therefore it may be most appropriate to use the terms "homogeneous-dominated" and "heterogeneous-dominated" nucleation to allow for the possibility that the two processes may occur together (Mangan and Sisson, 2000; Mangan et al., 2004).

Bubble growth

Bubble growth occurs by diffusion of volatile molecules into bubbles and expansion of the gas due to decompression (Sparks et al., 1994; Navon and Lyakhovsky, 1998). Both mechanisms are important throughout conduit ascent, but decompressional growth becomes dominant at shallow levels (Sparks, 1978). Bubble growth is limited by

diffusion for fast magma rise but by decompression for slow magma rise (Proussevitch and Sahagian, 1996).

The rate of diffusive bubble growth depends on volatile content, viscosity, diffusivity, and decompression rate (Lensky et al., 2004). At constant temperature and pressure, bubble growth is controlled by the rate of diffusion of volatile molecules toward and through the bubble-melt boundary and by the rate of deformation of the melt to accommodate the expanding bubble (Sparks, 1978; Lyakhovsky et al., 1996; Navon and Lyakhovsky, 1998). The parabolic law for diffusive bubble growth at constant pressure (Scriven, 1959; Sparks, 1978) is

$$R = 2\beta(Dt)^{1/2}$$

where R is the rate of a bubble's increase in cross-sectional area, D is the diffusion coefficient, β is the growth rate constant, and t is time. The original form of the parabolic growth law does not account for effects of surface tension and melt viscosity.

It should be noted that the growth rate constant (β) increases with increasing supersaturation (Sparks, 1978). Thus the relationship between the depth of bubble nucleation and a bubble's final radius is not simple. For example, if supersaturation increases with time, due to cooling or decompression, a bubble that nucleates early at fairly low ΔP will grow slowly. However, a bubble that nucleates later at higher ΔP will grow quickly, and its size will catch up with that of the earlier bubble (Sparks, 1978).

The rate of diffusive bubble growth at constant pressure is at first limited by the viscous melt's ability to flow and deform to accommodate growth. In this early viscous regime, growth is exponential (Lyakhovsky et al., 1996; Navon et al., 1998; Navon and Lyakhovsky, 1998; Lensky et al., 2004). Later, growth is controlled by rate of diffusion

of volatiles into the bubbles (the diffusive regime), and growth follows a square-root law (Lyakhovsky et al., 1996). The transition between these regimes occurs when the gas pressure inside the bubbles approaches the ambient pressure in the melt. Bubble growth may return to a viscosity-controlled regime if magma becomes mostly degassed near the end of ascent and viscosity rises above 10^9 Pa s (Barclay et al., 1995). Pressure buildup in the bubbles may then exceed the tensile strength of the melt and lead to fragmentation (Sparks, 1978; Papale, 1999).

The amount of H_2O or other species available to diffuse into a growing bubble is controlled by the proximity of other bubbles (Proussevitch et al., 1993). Models must account for a concentration gradient that develops in the shell of melt around a growing bubble (e.g. Barclay et al., 1995). The width of the shell of melt that feeds volatiles to each bubble is estimated to be a few tenths of a millimeter thick at a decompression rate of 0.025 MPa s^{-1}, and the shell is thinner at higher decompression rates (Mangan and Sisson, 2000).

Without ongoing decompression, a bubble is predicted to reach its final radius when the concentration of water in its melt shell equals the equilibrium concentration for melt of that composition, temperature, and confining pressure (Navon and Lyakhovsky, 1998). However, bubble growth may be interrupted by exhaustion of dissolved water supply, interaction with neighboring bubbles, or fragmentation (Sparks, 1978).

Bubble growth due to expansion is calculated based on the change of volume of an ideal gas in response to decreasing hydrostatic pressure (Sparks, 1978). Numerical models that combine diffusive and decompressional growth processes indicate that diffusion initially dominates growth and remains dominant for much of magma ascent

(Proussevitch and Sahagian, 1996). Decompression gradually increases in importance with decreasing depth and becomes overwhelmingly dominant at shallow levels (<50 m) in the conduit (Sparks, 1978).

Bubble coalescence

Bubble deformation and coalescence occur when melt is in a fluid or ductile state (e.g. Klug and Cashman, 1996; Burgisser and Gardner, 2005). Dynamic coalescence describes the interaction between bubbles moving through a fluid. While larger bubbles overtake and capture moderately sized ones, the smallest bubbles are displaced and swept into the wake of the larger ones (e.g. Sahagian, 1985; Sahagian et al., 1989; Cashman and Mangan, 1994). The frequency of bubble collisions in dynamic coalescence is determined by the bubbles' number density and range of speeds (Sahagian et al., 1989). This type of coalescence is more likely to occur in magmas where bubbles can move independently of melt, such as in a slowly ascending basaltic magma producing Strombolian explosions (e.g., Wilson and Head, 1981).

Static coalescence occurs when films between adjacent bubbles in a foam thin and rupture (Cashman and Mangan 1994; Cashman et al., 1994). Two time scales control static coalescence: t_{df}, the time for drainage and failure of the film, and t_{rel}, the time for relaxation to a spherical shape (Navon and Lyakhovsky, 1998). Capillary action and gravity favor film thinning, but viscous resistance of the melt counters their effects. The thickness at which a bubble film spontaneously ruptures is observed to be between 0.2 and 1 micron (Klug and Cashman, 1996; Navon and Lyakhovsky, 1998). Static coalescence may occur where foams collect at the roof of the magma chamber or at constrictions in the conduit (e.g. Vergniolle and Jaupart, 1986), or during rapid ascent at

shallow levels in the conduit where coupled degassing leads to high number densities of rapidly growing bubbles (Gaonac'h et al., 2003).

Experiments suggest that bubble coalescence becomes important well before bubbles reach the close packing limit (Westrich and Eichelberger, 1994; Navon and Lyakhovsky, 1998). In more fluid magmas, bubbles are more mobile and films between bubbles thin and rupture faster, so coalescence may occur earlier in ascent (Mangan and Cashman, 1996 and references therein). Bubble coalescence is enhanced by the presence of crystals (Proussevitch et al., 1993; Simakin et al., 1999).

Bubble coalescence can strongly affect the number density of bubbles observed in pyroclasts, which in turn can affect interpretations about bubble nucleation rate, overpressure, and decompression rate. Fortunately, it is possible to tell whether coalescence has modified the initial bubble population in many magmas, because evidence for coalescence is commonly preserved in complex bubble shapes (Heiken, 1987; Orsi et al., 1992; Klug and Cashman, 1994; Cashman and Mangan, 1994). Coalesced bubbles may be unable to relax to spherical shapes because the melt is viscous or because the magma is quenched quickly (Giordano and Dingwell, 2003a).

Outgassing

Evidence for outgassing before and between eruptive episodes has been observed at volcanoes such as Pinatubo (Westrich and Gerlach, 1992), Galeras (Stix et al., 1993), Kilauea (Elias et al., 1998), and several silicic domes and flows (Fink et al., 1992). Gas is released into the atmosphere, and the magma may also lose volatiles to the country rock (Jaupart, 1998; Newman et al., 1988). How the gas escapes passively from the magma is poorly understood. Bubble migration toward the magma free surface and/or

conduit walls is possible in fluid magmas but would be difficult in viscous high-silica magmas. Another process that could provide pathways for bulk gas escape is development of permeability through trains of connected bubbles (Klug and Cashman, 1996; Saar and Manga, 1999). Bubble coalescence and deformation increase permeability (Thomas and Sparks, 1992; Cashman and Mangan, 1994; Burgisser and Gardner, 2005). Measurements indicate that the pores in pumice are almost completely interconnected (Whitham and Sparks, 1986). High permeabilities can be reached even in relatively low-vesicularity clasts (Klug and Cashman, 1996).

Experiments with rhyolitic melt by Burgisser and Gardner (2005) show that at low decompression rates (0.02 MPa s^{-1}) permeability develops at 30-35 MPa, but at higher rates (0.10 MPa s^{-1}) permeability is delayed until the pressure drops to <10 MPa. These results are consistent with the observation that permeability development through coalescence occurs more easily at lower magma ascent rates (Klug and Cashman, 1996). Permeability helps explain why pumice is preserved in explosive eruptions, when the high internal bubble pressures resulting from decompression to atmospheric pressure would be expected to fragment all magma into ash-sized particles (Whitham and Sparks, 1986; Klug and Cashman, 1996).

Microlite nucleation and growth

Classical nucleation theory states that microlite nucleation rate is an exponential function that depends on several variables. There are both kinetic and thermodynamic barriers to the formation of a crystal nucleus (Kirkpatrick, 1981; Hammer, 2004 and references therein). The kinetic barrier is the activation energy required to allow an atom to attach to an existing spherical cluster of atoms. The thermodynamic barriers relate to the

overall free energy change for crystallization per unit volume and the free energy of the crystal-melt interface (Hammer, 2004). Other factors that influence crystal nucleation include the number density of clusters, the number of atoms near the clusters, and the frequency of the atoms' attempts to attach to the clusters (Kirkpatrick, 1981).

Crystal nucleation rate follows a bell-shaped trend with increasing undercooling (Fig. 1.6; Kirkpatrick, 1981). At very low undercooling, the thermodynamic barriers to nucleation cannot be overcome. At very high undercooling, the kinetic barriers become important (Kirkpatrick, 1981). Crystallization in the magma chamber and conduit is typically assumed to be isothermal (e.g. Jaupart, 1996; Papale, 1998 and references therein), so undercooling is not achieved by decreasing the temperature. Instead, an effective undercooling is invoked that arises from the increase in the thermodynamic stabilities of anhydrous phases in response to decompression and dehydration (Lipman and Banks, 1987).

Application of classical nucleation theory requires several assumptions, because the activation energy and surface energy are generally not known. For example, the activation energy of atom attachment and the frequency of attachment attempts are commonly assumed to be coupled with melt viscosity, even though this is not always true (Kirkpatrick, 1981). In addition to the necessary assumptions and approximations, classical nucleation theory is also complicated by the fact that the predicted nucleation rate is extremely sensitive to the expression used for the surface energy (Kirkpatrick, 1981). The result is that predicted nucleation rates often differ from observed rates by several orders of magnitude (Kirkpatrick, 1981; Hammer, 2004).

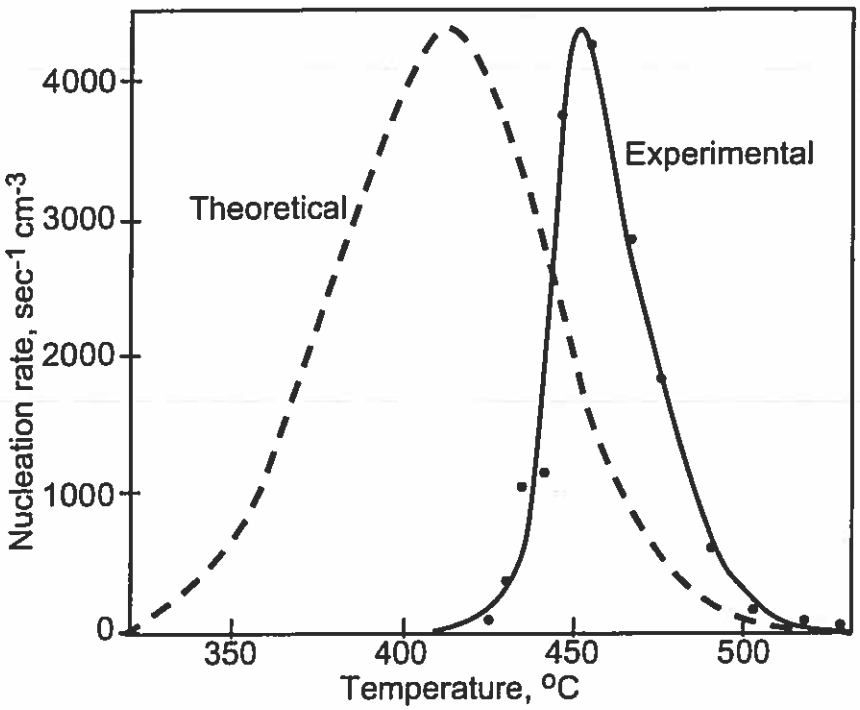

Figure 1.6 Theoretical and experimental relationships between temperature and crystal nucleation rate for lithium disilicate, with theoretical maximum normalized to match experimental peak. Classical theory tends to underestimate the temperature of peak nucleation rate and overestimate the width of the bell-shaped trend. From Kirkpatrick (1981).

An alternative to the classical theory of crystal nucleation is diffuse interface theory (Fig. 1.7; Turnbull, 1964). Instead of invoking a sharp boundary between the liquid and a crystal nucleus, this theory envisions a gradient in thermodynamic properties such as enthalpy and entropy over a zone between the two phases. The position and slope of the gradient across the interfacial zone depend on temperature and composition (Turnbull, 1964). The surface energy also varies across the diffuse interface in a manner that depends on temperature and H_2O content (Hammer, 2004).

The rate of crystal growth is controlled primarily by the efficiency of attachment of atoms at the crystal-melt boundary and the ease of diffusion of species through the melt (Kirkpatrick, 1981). Other processes, such as flow of heat produced during crystallization and convection of the melt, are considered to have relatively insignificant influence (Kirkpatrick, 1981). If growth is interface-controlled, the rate of attachment of atoms is lower than the rate of diffusion of atoms toward the interface. If growth is diffusion-controlled, the atoms are not able to travel toward the crystal as fast as they are able to attach to the crystal (Kirkpatrick, 1981).

The relative rates of diffusion and atom attachment also determine the habit of a crystal (Lofgren, 1974; Kirkpatrick, 1981). Experiments show that growth becomes increasingly diffusion-controlled at greater undercooling, producing a sequence of tabular, acicular, skeletal, dendritic, and spherulitic crystal habits with increasing undercooling (Lofgren, 1974).

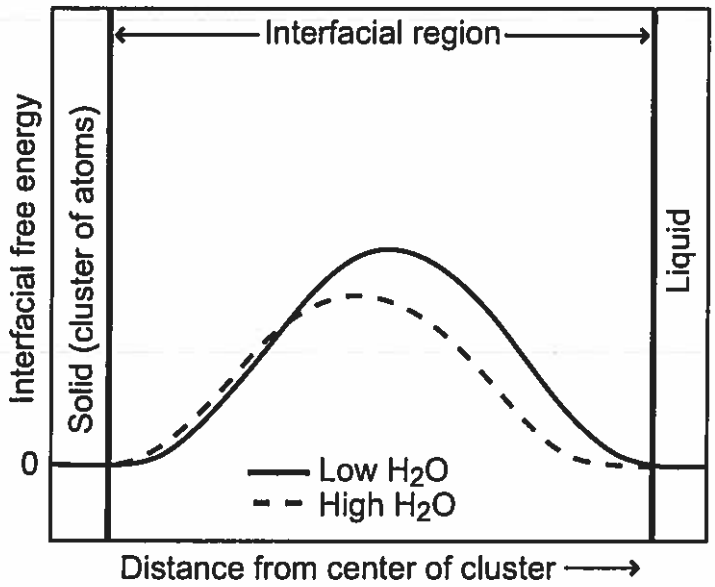

Figure 1.7 Schematic illustration of the interfacial region between a crystal nucleus and the surrounding melt, based on diffuse interface theory. Interfacial free energy varies with distance from the center of the cluster of atoms. Diffuse interface theory may explain phenomena such as the temperature dependence of free energy better than classical nucleation theory. From Hammer (2004).

1.6 Importance of microtextural studies of clasts

The processes described above leave different signatures on the bubble and crystal populations in the magma. Recent experimental studies (e.g. Gardner et al., 1999; Hammer et al., 1999) suggest that processes of volatile exsolution, gas escape, and microlite growth, before and during eruption, are reflected in the microtextures of the eruption products. The amounts, shapes, and sizes of vesicles, phenocrysts, and microlites can be quantified on thin section images from representative clasts. Theoretical and empirical relationships may then be used to constrain the conditions of nucleation and growth of these features (e.g., Marsh, 1988; Sparks et al., 1994). Microtextural analysis techniques have been used successfully to constrain the degassing and crystallization histories for several eruptions (e.g., Mangan et al., 1993; Klug and Cashman, 1994; Mangan and Cashman, 1996; Klug et al., 2002; Gurioli et al., 2005; Adams et al., 2006a, 2006b).

Vesicles

Quantitative parameters for vesicles include number density, size, and shape. Vesicle number densities can be used to estimate the rate and duration of bubble nucleation. This is most effective for silicic magmas because their behavior is well constrained by decompression experiments (Hurwitz and Navon, 1994; Lyakhovsky et al., 1996; Gardner et al., 1999; Mangan and Sisson, 2000; Klug et al., 2002). At present, interpretations for basaltic magmas rely more on theory (Mangan and Cashman, 1996), but a new set of decompression experiments on basalt has been funded for 2006 (B.F. Houghton, pers. comm. 2006).

Ranges of bubble number densities for some well-constrained deposits are listed in Table 1.1. Reticulite, a coarse open-celled foam, has the lowest number bubble number density. Scoria from Kilauea and Stromboli, whose fountaining and Strombolian events represent the most common styles of terrestrial explosive volcanism, have slightly higher values (10^4-10^5 cm^{-3}). Scoria from the Tarawera 1886 and Keanakako'i 1500-1790 eruptions have moderate number densities on the order of 10^6 cm^{-3}. The Etna 122 BC basaltic scoria have some of the highest number densities yet measured in basalt. As a group, the silicic Plinian deposits have bubble number densities of 10^7 to 10^{10} cm^{-3}.

Table 1.1. Ranges of total bubble number density (N_{Vtot}) for some basaltic and silicic eruptions. Number densities are stated per volume of bulk rock, rather than per volume of melt.

Eruption	Range of N_{Vtot}, cm^{-3}			Reference
Kilauea reticulite	1.10×10^2	to	1.78×10^3	Mangan and Cashman (1996)
Kilauea scoria	7.30×10^4	to	1.77×10^5	Mangan and Cashman (1996)
Stromboli	5.39×10^4	to	3.44×10^5	Lautze and Houghton (2005)
Tarawera 1886	1.5×10^6	to	2.4×10^6	This study
Keanakako'i	1.32×10^6	to	5.61×10^6	Mastin et al. (2004)
Etna 122 BC	2.57×10^6	to	6.13×10^7	This study
Campanian Ignimbrite	8.2×10^7	to	1.4×10^8	Polacci et al. (2003)
Vesuvius	8.1×10^7	to	8.8×10^8	Gurioli et al. (2005) and unpublished data
Mount St Helens	8.2×10^8	to	2.0×10^9	Klug and Cashman (1994)
Mazama 7700 BP	7.76×10^7	to	1.00×10^{10}	Klug et al. (2002)

Vesicle size data can be plotted in several ways for comparing bubble populations and extracting quantitative information. A widely used approach is to define a set of bins that encompass certain size ranges, and present the data in frequency distributions (Toramaru, 1990; Mangan et al., 1993; Cashman et al., 1994; Klug and Cashman, 1994; Mangan and Cashman, 1996; Klug et al., 2002; Gurioli et al., 2005; Adams et al., 2006b). Details of the procedure are described in section 1.9.

Frequency distributions may be displayed as histograms showing the volume percent of bubbles of each size range (Cashman and Mangan, 1994; Klug et al., 2002; Gurioli et al., 2005); such plots are simple, intuitive, and useful for first-order comparisons. Frequency distributions that show vesicle number density rather than volume percent vesicles are slightly more complicated, but they offer more information about number and duration of bubble nucleation events, and timing and extent of bubble growth and coalescence (Toramaru, 1990; Cashman and Mangan, 1994; Blower et al., 2001; Blower et al., 2002). The "classical" vesicle size distribution, or VSD (Sarda and Graham, 1990), compares the log of the bubble number density for each size bin ($\ln(n)$) with the bubble diameter (L) on which that bin is centered. Classical theory derived from crystal studies predicts that continuous bubble nucleation and growth will produce an exponential relationship, which appears as a straight line on this plot (Cashman and Marsh, 1988; Marsh, 1998). The line's intercept gives initial bubble number density and the slope is believed to reflect the combined effect of bubble growth rate and duration of vesiculation (e.g. Mangan et al., 1993; Cashman et al., 1994; Blower et al., 2001). However, not all VSDs are exponential (e.g. Simakin et al., 1999; Mangan et al., 2004). Furthermore, some numerical models (Toramaru, 1989; Toramaru, 1995) and

experiments (Lyakhovsky et al., 1996; Gardner et al., 1999; Mangan et al., 2004) suggest that the theory's assumptions that nucleation is homogeneous and ongoing may not be consistent with actual behavior in natural systems. Deviations from an exponential relationship are commonly explained by coalescence (Mangan et al., 1993; Cashman and Mangan, 1994; Gaonac'h et al., 1996a, 1996b; Mangan and Cashman, 1996; Klug et al., 2002; Gaonac'h et al., 2005) or extended nucleation (Blower et al. 2001, 2002). Simakin et al. (1999) suggest that non-exponential trends reflect a combination of extended nucleation and coalescence.

Other plots may also be used to compare bubble populations, such as $\log(N_V{>}L)$ vs. L (Klug et al., 2002). The quantity $N_V{>}L$ refers to the sum of the bubble number densities in all size bins up to a bin defined by a given value of L. The plot shows the nature of the size-frequency relationship much like the VSD, and also allows quick estimation of the total bubble number density. Some workers use radius (Blower et al., 2001, 2002) or area (Gaonac'h et al., 1996b; Blower et al., 2002; Gaonac'h et al., 2005) rather than diameter to make plots of this type. A less common plot is cumulative volume percent vesicles vs. L, which shows at a glance how a bubble population deviates from an "ideal" one that would have a perfectly exponential VSD (Klug et al., 2002).

Shape parameters are indicators of processes such as bubble coalescence and collapse (Gaonac'h et al., 1996b; Saar and Manga, 1999). Complex bubble shapes are abundant in nearly all the samples studied in this project, suggesting that coalescence was important in both of the basaltic magmas considered here.

Crystals

Clasts in silicic Plinian deposits are typically poor in microlites (Fierstein and Hildreth, 1992; Hildreth, 1983; Sutton et al., 2000). However, microlites are abundant in all clasts of both the Etna 122BC and the Tarawera 1886 deposits. Growth of microlites may feed back to influence magma rheology through the compositional effect of increasing SiO_2 in the residual melt and through the physical effects of adding particles in suspension (McBirney and Murase, 1984; Pinkerton and Stevenson, 1992; Lejeune and Richet, 1995; Saar et al., 2001; Llewellin et al., 2002; Mourtada-Bonnefoi and Mader, 2003; Costa, 2005). If the crystals strongly increase the magma's effective viscosity, they may be important for promoting high eruptive intensity.

Qualitative observations of crystals permit general interpretations and comparisons. For example, phase assemblages indicate crystallization conditions (Métrich and Rutherford, 1998; Hammer et al., 1999). Crystal habits indicate growth mechanisms and can be compared to infer relative growth rates (Lofgren et al., 1974). Estimates of crystal number densities allow first-order comparisons of differences in undercooling (Kirkpatrick, 1981). The relative timing and rates of nucleation and growth can be gauged qualitatively (Lofgren, 1980; Kirkpatrick, 1981; Hammer and Rutherford, 2002). Evidence of stress, shear, and flow patterns may be found in bent, broken, or aligned crystals (Hammer et al., 1999).

Quantitative characterizations of crystal sizes, shapes, and number densities have been used to constrain many aspects of volcanism, such as time in the magma storage zone (Mangan, 1990); timing of crystallization, i.e., whether it was pre-eruptive or syn-eruptive (Cashman, 1992; Hammer et al., 2000); relative rates of crystal nucleation and

growth (Cashman, 1988; Cashman and Blundy, 2000); the relationship between undercooling and nucleation/growth rates (Cashman, 1988); and the trigger for crystallization, whether heat loss or devolatilization (Cashman, 1992; Gardner et al., 1998). Nucleation and growth rates may be estimated quantitatively if eruption duration and other parameters are constrained (Cashman and Marsh, 1988; Marsh, 1998). Limitations of time and resources precluded the detailed quantification of crystal size distributions in my project. Thus the microlite data for the Etna 122 BC and Tarawera 1886 clasts are primarily qualitative with some general quantitative estimates.

1.7 The Etna 122 BC study

My study of the Etna 122 BC eruption (Chapter 2) seeks to explain the initiation, progression, and termination of the two Plinian phases of this basaltic eruption through quantitative studies of textural diversity in pyroclasts from many stratigraphic levels in the deposits. I describe the 122 BC eruption in Chapter 2, but here I provide some geologic and tectonic background for the volcano.

Mt. Etna: setting and background

Since the late Jurassic, the tectonic setting of the Mediterranean region has been dominated by the subduction of the African plate beneath the European plate (Fig. 1.8), but has been complicated by interactions among additional smaller plates that are not fully constrained (Moores and Fairbridge, 1998; Cavazza and Wezel, 2003; Carminati and Doglioni, 2004). Etna is not a typical arc volcano; it is ~100 km closer to the trench than the Aeolian arc volcanoes associated with the subduction zone (Fig. 1.8; Doglioni et al., 2001). Etna sits on an accretionary prism directly over the "hinge" of the subducting

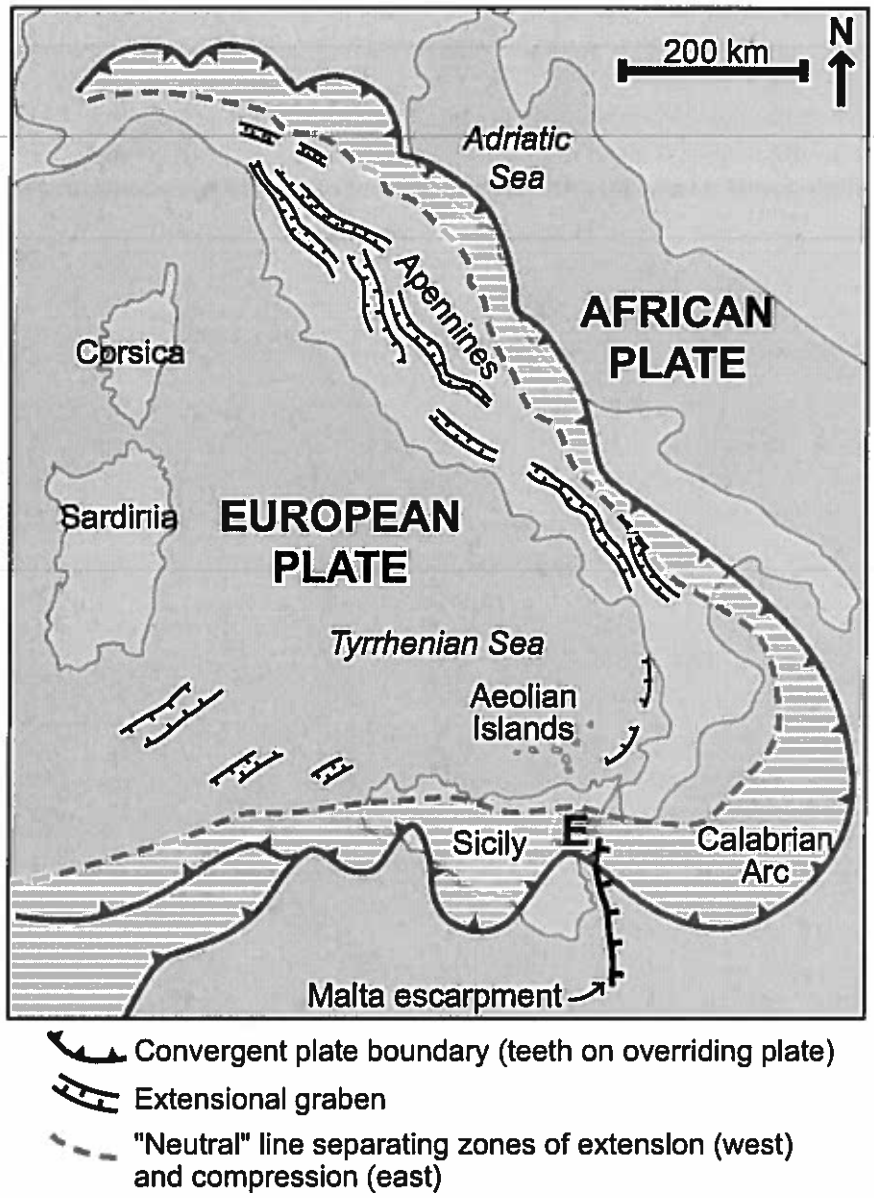

Figure 1.8 Simplifed tectonic map of Italy. Striped zone indicates compressional regime. In contrast, the ridge of the Apennines is in a tensional regime. Etna (labeled E) is adjacent to the Malta escarpment. From Moores and Fairbridge (1998).

African plate. Seismic and tomographic studies show that the subducting slab dips nearly vertically at this location (Moores and Fairbridge, 1998). The magmas of Etna are dominantly tholeiitic to mildly Na-alkaline (e.g., Kamenetsky and Clocchiatti, 1996; Armienti et al., 2002; Métrich et al., 2004), unlike the calc-alkaline composition typical of the Aeolian archipelago and other arc systems (Doglioni et al., 2001).

Several explanations for the origin of Etnean magmatism have been proposed based on the complex arrangement of tectonic features in the region (e.g. Continisio et al., 1997; Lanzafame et al., 1997; McGuire et al., 1997; Tanguy et al., 1997; Doglioni et al., 2001 and references therein). Some models are supported by more numerous and diverse data sets than others. One recent model is well supported by indirect measurements of the angle of the slab, data on the locations and types of earthquakes throughout Sicily, and the unusual Na-alkaline magma composition of most of Etna's lavas (Doglioni et al., 2001). The model focuses on the Malta escarpment at the southern end of the Ionian Sea. The Malta escarpment is the boundary between the relatively elevated Hyblean plateau and the thinner, deeper crust of the Ionian Sea (Fig. 1.9). It is not a plate boundary, but is a region associated with faulting and seismicity. Doglioni et al. (2001) propose that the lithosphere on the eastern side of the escarpment is dipping more steeply than the lithosphere on the western side (Fig. 1.9). This differential rollback of the subducting slab results in extensional and right-lateral forces that are focused at Etna's location. Transtension may cause some decompression that promotes mantle melting and may provide pathways for magma migration.

Etna's rock record is dominated by lava flows and weak explosions (e.g., Chester et al., 1985), but subplinian and Plinian eruptions make up a significant if infrequent

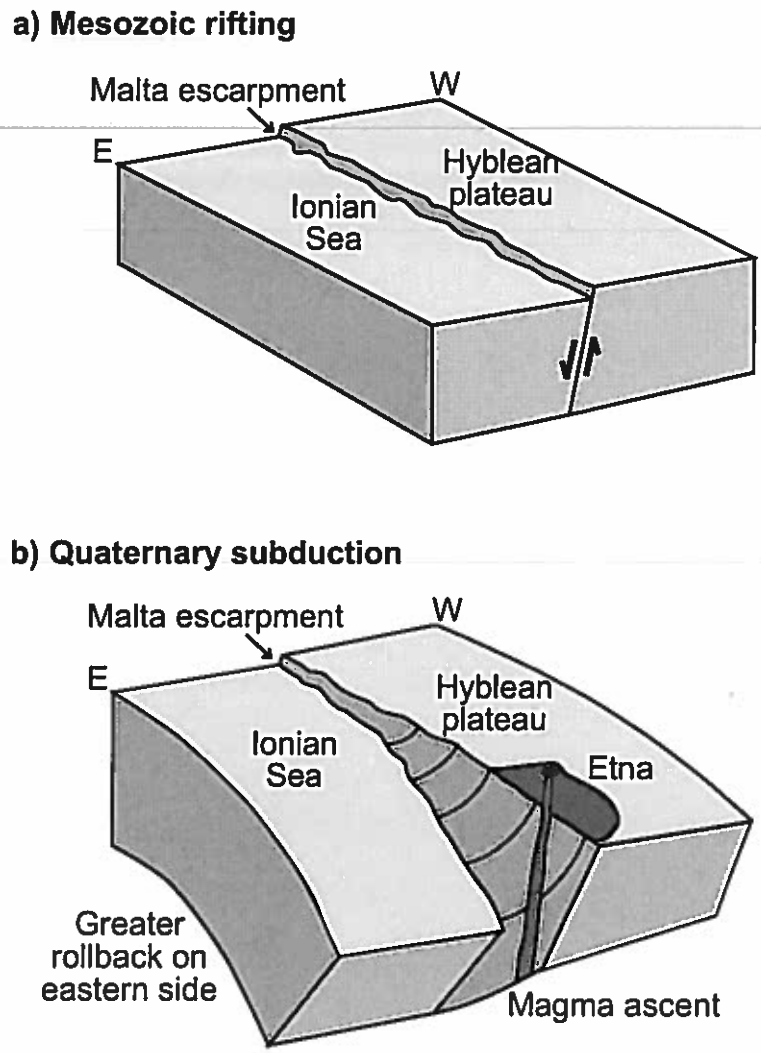

Figure 1.9 Cartoon showing (a) the formation of the Malta escarpment during Mesozoic rifting and (b) differential rollback during Quaternary subduction. The transtension associated with the rollback may result in decompression and melting to produce the magmas of Mount Etna. From Doglioni et al. (2001).

component. For example, Etna's eruptive history since 1500 BC includes eleven eruptions with subplinian phases and one Plinian event (Coltelli et al., 2000). Furthermore, the average rate of lava effusion (Harris et al., 2000) and the frequency of flank eruptions (Calvari et al., 1994) are estimated to be much higher for the period 1950-present than before 1950. Thus Etna's activity appears to be increasing (Clocchiatti et al., 2004).

1.8 The Tarawera 1886 study

My two-part Tarawera study (Chapters 3 and 4) is part of a new research effort that began with a re-interpretation of the proximal stratigraphy by Houghton and Wilson (1998). Houghton et al. (2004a) set forth some preliminary ideas about the mechanisms for the basaltic Plinian volcanism. Carey et al. (2006) present detailed grain size and componentry data for two key proximal sites.

The first part of my study (Chapter 3) addresses issues of transport and deposition during the multiple-vent eruption, with emphasis on the complex overthickened proximal deposits and their relationship to the more widespread Plinian fall. The results will be useful for models that consider proximal transport and deposition in Plinian eruptions. The second part (Chapter 4) aims to constrain the causes for the Plinian intensity of this basaltic eruption through studies of macroscopic and microscopic characteristics of clasts from several localities. The microtextural results are especially useful for comparison with the Etna 122 BC scoria and other basaltic products. The eruption is described in Chapters 3 and 4, while geologic background is provided here.

Mt Tarawera: setting and background

Tarawera volcano is part of New Zealand's Taupo Volcanic Zone (TVZ), a belt of volcanoes extending northeastward from Tongariro volcanic center in the central North Island to White Island off the northeast coast (Fig. 1.10; Cole, 1990). The complex tectonic setting of this region is dominated by the Taupo-Hikurangi arc-trench system, where the Pacific plate subducts beneath the Australian plate (Fig. 1.10; King, 2000). Other boundaries and structural features exist adjacent to and at angles to the Hikurangi trench (Cole, 1990).

The history of Taupo Volcanic Zone is characterized by periods of intense activity interspersed with quieter periods (Wilson et al., 1995a). The zone's first andesitic activity is dated at 2 Ma (Wilson et al., 1984 and references therein), and large rhyolite eruptions began at 1.6 Ma (Houghton et al., 1995; Wilson et al., 1995a). Numerous models have been proposed to explain the intense volcanism (e.g., Stern, 1985; Cole et al., 1995; Hochstein and Regenauer-Lieb, 1989; Cole, 1990; Hochstein et al., 1993), but several of these are problematic (Wilson et al., 1995a), primarily because they overlook the complex spatial and temporal distribution of volcanic deposits within TVZ.

The model best supported by current data suggests that TVZ is an arc that has been active since 2 Ma and has been undergoing rifting since 0.9 Ma or possibly earlier (e.g., Houghton et al., 1995; Wilson et al., 1995a). Crustal extension is concentrated within a ~15 km wide belt within the eastern part of TVZ. An episode of major uplift and erosion between 1 and 0.34 Ma is evident in areas west, south, and east of TVZ and is probably related to the rifting (Wilson et al., 1995a). The current rate of extension varies along the axis of the zone but averages 8 mm per year (Darby and Williams, 1991).

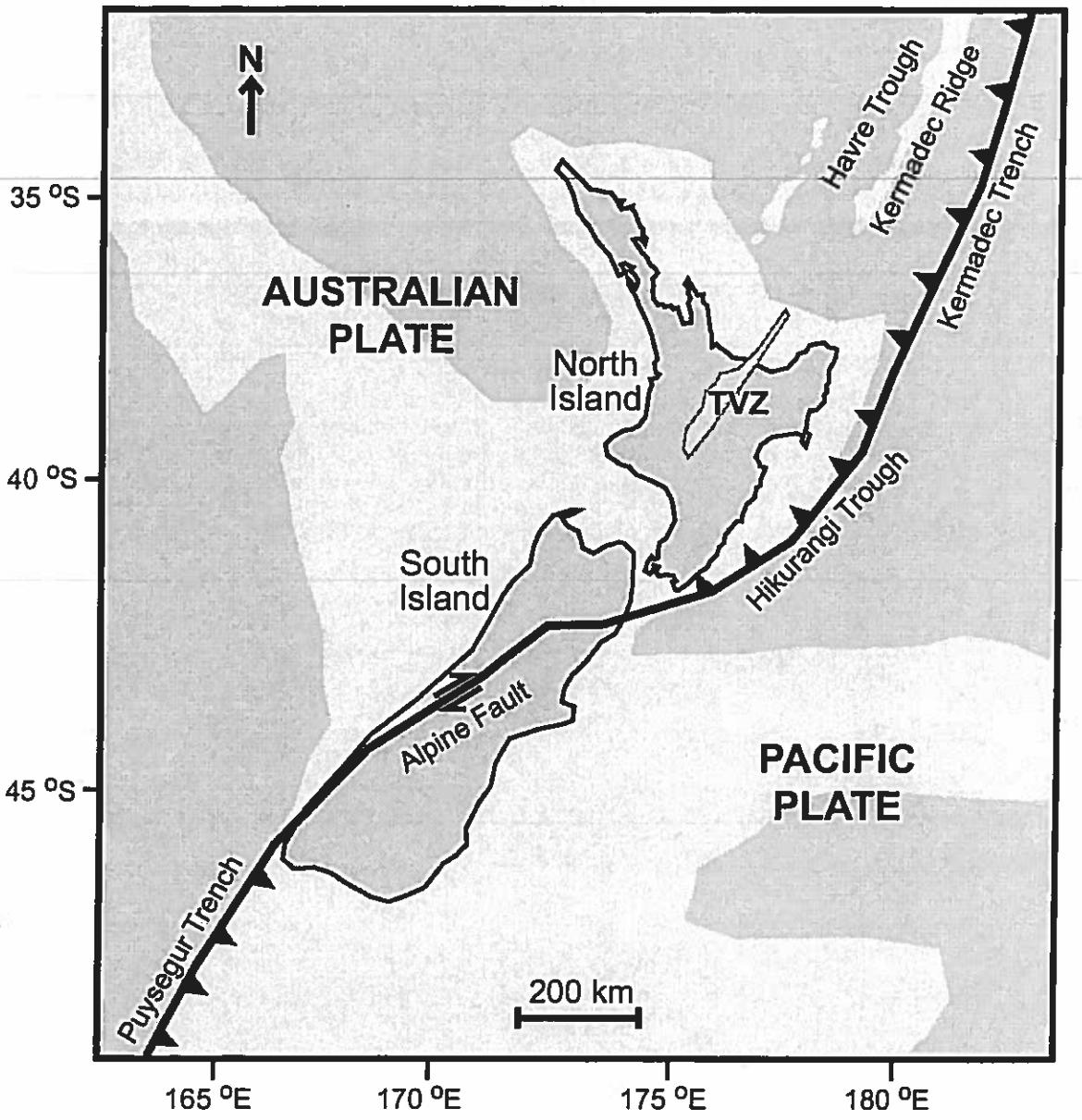

Figure 1.10 Simplified tectonic map of New Zealand. Oblique southwestward subduction of the Pacific plate beneath the Australian plate east of the North Island transitions to a transform boundary (the Alpine Fault) within the South Island. Southwest of the islands, the Australian plate subducts beneath the Pacific plate. Taupo Volcanic Zone is interpreted as a rifted arc. From Wilson et al. (1995a) and Cole (1990).

Taupo Volcanic Zone is segmented, with andesite-dominated volcanism in the northeastern and southwestern segments and large-volume rhyolitic eruptions concentrated in the central segment (e.g., Wilson et al., 1995a). The major eruptive centers in the central segment are listed in Table 1.2 and shown in Fig. 1.11. The most important of these for the current project is the Okataina Volcanic Center, which hosted both the most recent rhyolitic (Kaharoa 1315 AD) and basaltic (Tarawera 1886) eruptions in TVZ (Nairn et al., 2004 and references therein; Walker et al., 1984). The eruptive history of the Okataina Volcanic Center includes a caldera-forming period (280-60 ka) that featured several rhyolitic ignimbrite eruptions, and a caldera-filling period (after 60 ka) in which explosive and effusive silicic deposits accumulated in the calderas (Nairn, 1989; Wilson et al., 1995a).

Table 1.2. Major rhyolitic eruptive centers of central Taupo Volcanic Zone (Houghton et al., 1995; Wilson et al., 1995a). See Fig. 1.11 for locations.

Name	Date
Mangakino	1.6 Ma – 900 ka
Kapenga	710 ka – 64 ka
Whakamaru	340 ka – 320 ka
Maroa	320 ka – 14 ka
Reporoa	~260 ka
Rotorua	300 ka – 50 ka
Taupo	320 ka – 181 AD
Okataina	320 ka – 1886 AD

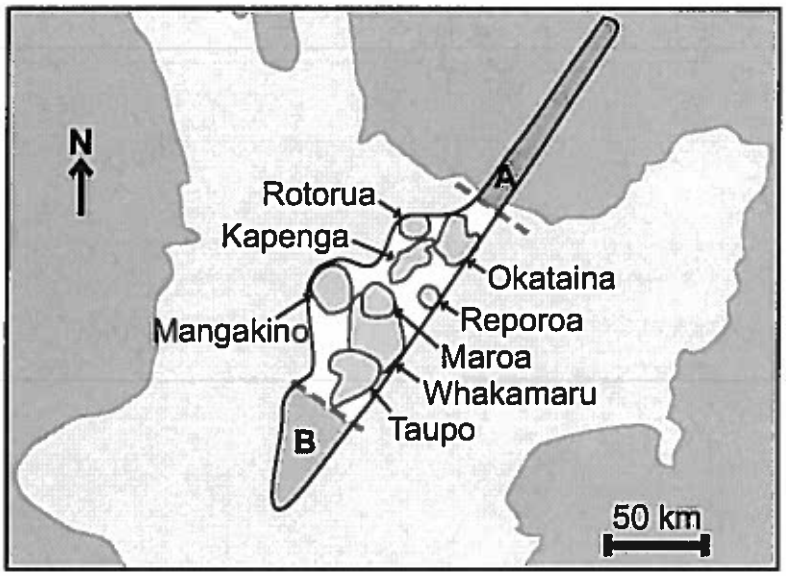

Figure 1.11 Major rhyolitic centers of Taupo Volcanic Zone. The northeastern and southwestern ends of the zone (labeled A and B) are dominated by andesite to dacite. From Wilson et al. (1995a).

The main eruptions of the Tarawera volcanic complex are listed in Table 1.3. The ~1315 AD Kaharoa eruption (Hogg et al., 2003; Nairn et al., 2004) produced a complex of five domes within the Okataina Volcanic Center (Fig. 1.12). The Tarawera 1886 eruption and some subsequent phreatic activity were the most recent events within TVZ. Details of the 1886 eruption are presented in Chapters 3 and 4.

Table 1.3. Eruptions of Tarawera Volcanic Complex. (1) Radiocarbon ages with several hundred years error; Froggatt and Lowe, 1990; Lowe et al., 1999. (2) Tree-ring and radiocarbon dating with +/- 12 years error; Hogg et al., 2003. (3) Historical records; Smith, 1886a, 1886b; Williams, 1887.

Name	Date	Characteristics
Okareka	22500 y BP[1]	Rhyolitic pyroclastics and lavas
Rerewhakaaitu	17700 y BP[1]	Rhyolitic pyroclastics and lavas
Waiohau	13800 y BP[1]	Rhyolitic pyroclastics and lavas
Kaharoa	1315 AD[2]	Rhyolitic pyroclastics and lavas
Tarawera	1886 AD[3]	Basaltic scoria and phreatomagmatic eruptions

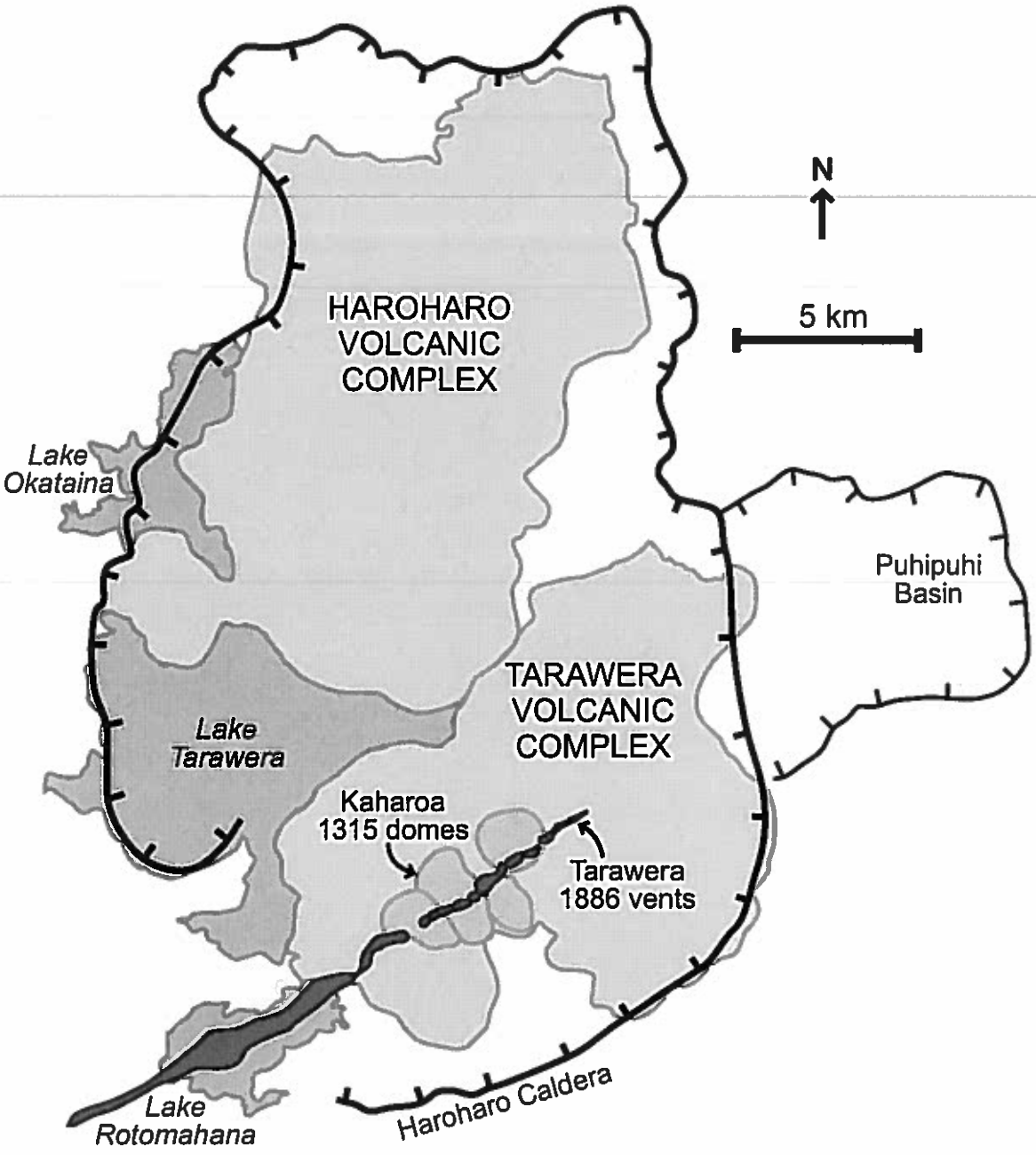

Figure 1.12 Sketch map of Okataina volcanic center. Haroharo and Tarawera volcanic complexes are labeled. The 1886 eruptive fissure cuts through the 1315 AD Kaharoa domes and through Rotomahana basin to the southwest. From Nairn (1989).

1.9 Methods

I use multiple techniques to investigate the roles of a variety of possible mechanisms for basaltic Plinian volcanism.

Mapping and sampling

Fieldwork at each volcano involved mapping, stratigraphic logging, and sampling. For the Etna 122 BC deposit, mapping had been completed by Coltelli et al. (1998) before I started my contribution to the project, so my field efforts focused on sampling two key localities. For the Tarawera 1886 deposit, detailed mapping of the widespread fall was already done (Walker et al., 1984), but I mapped the proximal deposits together with Bruce Houghton, Colin Wilson, Rebecca Carey, and Mike Rosenberg. My field partners and I measured proximal deposit thicknesses in detail at 31 proximal stratigraphic sections and recorded thicknesses of major units at other locations by lowering a tape measure vertically from the top of the fissure wall. I drew the proximal isopachs by assuming symmetric closure around known vent locations. I also drew cross-sections of packages of beds on scaled panoramic photographs of the walls of many of the eruptive craters.

Methods of sample collection differed depending on the goals of the study. For samples intended for grain size and componentry analyses, a stratigraphic level was selected and material was collected from a zone 5-15 cm thick. The complete population of clasts was taken, including all grain sizes and clast types. Samples were collected so that the largest clast did not exceed 5% of the total mass of the sample, producing sample sizes of 500 g to 50 kg. For samples specifically intended for bulk density studies, material was collected from the chosen level over a thickness of 2-3 clast diameters, and

sieved to remove all particles less than 16 mm in diameter. The 100 largest juvenile clasts were then selected to make up the density sample for that stratigraphic level.

Dispersal measurements

For the Tarawera 1886 proximal deposits, I measured linear thickness half-distance ($t_{1/2}$, Houghton et al., 2004) along the crater walls (Fig. 1.13). The $t_{1/2}$ is the horizontal distance over which a bed or package of beds halves in thickness. The measurements were made on cross sectional photographs. The $t_{1/2}$ values may be directly compared with the thickness half-distance (b_t) values of Pyle (1989) if the dispersals of individual 1886 vents are assumed to be radially symmetric. Even without such an assumption, the $t_{1/2}$ values are useful for comparisons within the Tarawera deposits.

Grain size and componentry

Grain size and componentry were measured at 1/2 ϕ intervals by Paola del Carlo for the Etna 122 BC clasts and by Carey (2002) for the Tarawera 1886 clasts. I interpret the grain size data on a simple level, but more detailed discussion for Tarawera 1886 can be found in Carey et al. (2006).

Macroscopic studies of clasts

Macroscopic clast characteristics studied in the lab include surface morphology and bulk density. Clast morphology, including overall shape and fine-scale surface texture, gives information about the rheology of the magma at fragmentation and timing and rate of quenching. Highly fluidal achneliths imply low viscosity of the melt during and following fragmentation. Blocky or ragged to cauliflower-like textures suggest that the magma was viscous when it was torn apart. Planar or curviplanar faces with angular edges suggest brittle fracture and may indicate rapid quenching by air or water (Heiken

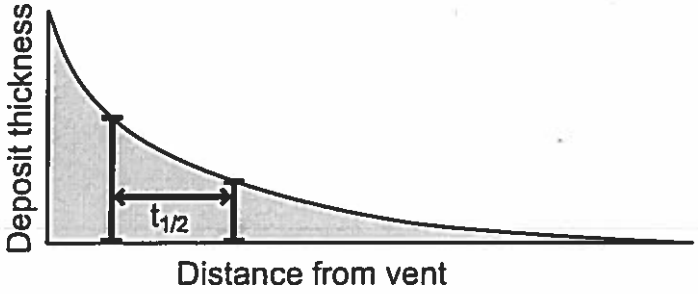

Figure 1.13 Linear thickness half-distance ($t_{1/2}$) is the radial distance over which an exponentially thinning deposit decreases its thickness by half (Houghton et al., 2004b).

and Wohletz, 1985). Clast morphology and surface texture were observed and recorded for the juvenile clasts in selected samples.

The bulk density of each clast was determined by Archimedes' principle, where the clast's weight in air was divided by the difference between its weights in air and in water (Houghton and Wilson, 1989). Each clast was wrapped in a thin, pliable wax sheet of known mass and volume to seal off pores before immersion in water. The percent vesicularities of the clasts were calculated by applying an assumed bubble-free density for the magma (Houghton and Wilson, 1989).

Distributions of bulk clast densities are useful for constraining vesiculation processes (e.g. Sparks and Brazier, 1982; Houghton and Wilson, 1989; Cashman and Mangan, 1994; Klug and Cashman, 1994). Clasts with dramatically different densities and hence vesicularities probably have different ascent histories, even though they may have been collected from the same stratigraphic level. For both the Etna 122 BC and Tarawera 1886 samples, I used density frequency distributions to select representative subsets of clasts for more detailed quantitative textural measurements.

Image acquisition for microtextural studies

A large part of my Etna and Tarawera studies was composed of acquiring, processing, and analyzing images of thin sections. Eight to twelve clasts were selected from each sample to be made into thin sections. Because the results from these small selections of clasts were applied for the entire clast population at the corresponding stratigraphic levels, it was essential to confirm that (1) the 100-clast samples were representative of the entire juvenile clast population at that stratigraphic level, and (2) the 8-12 clasts selected for thin sectioning were truly representative of the sample. To satisfy criterion (1),

Houghton and Wilson (1989) have shown that the 16-32 mm size fraction does serve as a good proxy for the entire clast population down to the grain size that converges with the typical vesicle size. To fulfill criterion (2), two methods were used to ensure selection of the most typical clasts. First, the density histograms were examined, and clasts were selected to represent the peak and extremes of the density distribution for the sample—typically four clasts from the peak and two from each of the tails, with additional clasts in the case of broad or multiple peaks. Second, the selected clasts were compared with the other clasts in their sample to ensure that their macroscopic properties were typical.

For vesicle studies, a set of 15 nested digital images was acquired for each clast. Because vesicle sizes in scoria typically span several orders of magnitude, four magnifications were required to characterize the total vesicle population. The lowest magnification, covering the entire thin section, was captured on a flatbed scanner at a resolution of 1200 dpi, equivalent to a linear scale of 47 pixels per mm. The three higher magnifications were imaged at resolutions of 252, 1000, and 2520 px/mm on a JEOL-5900LV scanning electron microscope (SEM) with a 20 kV accelerating voltage and a 1 nA beam current. All images were output in grayscale in TIFF format.

The images were prepared for analysis in the Adobe Photoshop program. Contrast and sharpness were adjusted if needed, phenocrysts were identified and traced, and incomplete or broken vesicle walls were reconstructed manually. Then the grayscale images were converted to binary black-and-white images and quantified in the Scion Image shareware program. Scion's outputs included the total number of vesicles, the area and perimeter of each vesicle, and percentages of the image area occupied by vesicles, phenocrysts, and clast edges.

Separate sets of SEM images were acquired at very high magnification (25,200 px/mm) for qualitative and quantitative study of microlites. Where possible, I measured number density, volume abundance, characteristic size, and habit for each mineral phase.

Quantitative microtextural analysis of thin section images

To date, most vesicle and crystal data are obtained by measuring features in two-dimensional images of thin sections, then applying a mathematical conversion to these measurements to get three-dimensional estimates of sizes and number densities. The conversion of image-derived data from 2D to 3D presents two main problems of possible sampling bias (as discussed by Mangan et al., 1993). First, the thin section plane has a greater probability of intersecting larger bubbles than smaller ones. Second, most of the possible slices through a bubble give an apparent bubble diameter that is less than the true diameter. Stereological corrections have been developed that account for these biases in converting data from 2D to 3D (Toramaru, 1990; Mangan et al., 1993; Klug and Cashman, 1994; Sahagian and Proussevitch, 1998). The different conversion techniques give similar results (Klug et al., 2002), and all require an assumption that particles are spherical. Unfortunately, most vesicles in the Etna 122 BC and Tarawera 1886 clasts are non-spherical. In the absence of any applicable methods for examining irregular bubble shapes, I have chosen to use the technique of Sahagian and Proussevitch (1998) because the authors present thorough arguments for its validity based on probability theory.

Because natural vesicles are rarely perfectly spherical, vesicle size is best expressed in terms of equivalent diameter or radius (Cashman and Mangan, 1994). I determined equivalent size values by measuring the areas of all the bubbles in a given set of images, arranging the area data into a set of classes or bins, and applying the

probability-based 2D to 3D conversion of Sahagian and Proussevitch (1998) to the whole data set. The spacing of the size bins is geometric, such that bins are related by a mutiplicative factor, in contrast with linear bin spacing, in which the upper limit of one bin is related to that of the bin below it by an added constant (Sahagian and Proussevitch, 1998). Geometric bin spacing is preferable because it simplifies the calculations in the 2D to 3D conversion (Sahagian and Proussevitch, 1998), and because geometric bins are easy to plot on a log scale, which is best for showing the size-frequency relationship (Cashman et al., 1994).

After the size and number density data were converted to three dimensions, they were tabulated and plotted in histograms and frequency distributions such as the vesicle size distribution (VSD; section 1.6). Data were compared among different stratigraphic levels at the same location, among similar levels at different locations, and with data from other pyroclastic deposits worldwide.

1.10 Structure of dissertation

Chapter 2 presents the Etna 122 BC study. Chapters 3 and 4 give the two parts of the Tarawera 1886 study, starting with larger-scale topics such as dispersal and then proceeding into the microtextural study of the pyroclasts. Chapter 5 summarizes the key results and interpretations from both basaltic Plinian eruptions and compares the deposits to each other and to other basaltic and Plinian deposits worldwide.

Chapter 3 has been published in Bulletin of Volcanology (Sable et al., 2006b) and Chapter 2 has completed the review process with Journal of Volcanology and Geothermal Research (Sable et al., 2006a). Chapter 4 is being prepared for submission.

CHAPTER 2

Changing conditions of magma ascent and fragmentation during the Etna 122 BC basaltic Plinian eruption: evidence from clast microtextures

2.1 Abstract

The Etna 122 BC basaltic eruption had two Plinian phases, each preceded and followed by weak phreatic and phreatomagmatic activity. This study infers changing eruption dynamics from density, grain size, and microtextural data from the erupted pyroclasts. The Plinian clasts show no evidence for quenching by external water; instead, all clasts are microvesicular and have high bubble number densities relative to the products of weaker basaltic explosive eruptions, suggesting that the 122 BC magma underwent coupled degassing linked to rapid ascent and decompression. This coupled degassing was probably enhanced by crystallization of abundant microlites, which increased the magma's effective viscosity during conduit ascent.

Detailed measurements of vesicles and microlites show wide variations in number densities, size distributions, and shapes among clasts collected over narrow stratigraphic intervals. For such a diversity of clasts to be expelled together, portions of melt with contrasting ascent and degassing histories must have arrived at the fragmentation surface at essentially the same time. We suggest that a parabolic velocity profile across the conduit ensured that magma near the conduit walls ascended more slowly than magma along the axis, leading to a longer residence time and more advanced degrees of outgassing and crystallization in the marginal magma. In our model, accumulation of this

outgassed, viscous magma along conduit walls reduced the effective radius of the shallow conduit and led to blockages that ended the Plinian phases.

2.2 Introduction

Etna's explosive history

The 122 BC eruption of Etna is one of only four well-documented examples of basaltic Plinian volcanism worldwide (Williams, 1983; Walker et al., 1984; Coltelli et al., 1998). This study uses multiple techniques to understand the mechanisms and conditions that allowed basaltic magma to erupt with such high intensity. Powerful explosive eruptions are significant in the Quaternary record at Etna (Coltelli et al., 2000). Etna's eruptive history since 1500 BC includes eleven eruptions with subplinian phases and one Plinian event (Branca and Del Carlo, 2004). Our work will contribute to efforts to predict and prepare for the hazards associated with future intense explosive eruptions at Etna and other basaltic volcanoes.

Basaltic explosive mechanisms

Like many basaltic volcanoes (Simkin and Siebert, 1994), Etna typically erupts in effusive to weakly explosive styles (Chester et al., 1985; Branca and Del Carlo, 2004; Taddeucci et al., 2005). The ascent of basaltic magma at volcanoes such as Etna, Stromboli, and Kilauea is generally believed to involve decoupled degassing, in which bubbles are able to migrate upward within relatively slowly ascending melt (Blackburn et al., 1976; Wilson and Head, 1981; Vergniolle and Jaupart, 1986; Head and Wilson, 1989; Jaupart and Vergniolle, 1989; Parfitt and Wilson, 1995; Seyfried and Freundt, 2000). In contrast, coupled degassing refers to the situation typical of more silicic melts where

bubbles are immobile relative to the melt (Wilson et al., 1980; Papale et al., 1998). The intensity of basaltic explosive behavior is strongly determined by the extent of decoupling of gas from melt, which is, in turn, a function of the relative rates of ascent of melt and bubbles and the extent of bubble coalescence (e.g., Jaupart, 1998; Papale et al., 1998; Denlinger and Hoblitt, 1999; Parfitt, 2004).

Hawaiian fountaining eruptions are associated with a high magma ascent rate and a relatively low degree of bubble coalescence, leading to partially coupled behavior in the shallow conduit and producing a population of mm to cm scale bubbles (Vergniolle and Jaupart, 1986; Parfitt and Wilson, 1995). Strombolian explosions occur at lower melt ascent rates where gas slugs can form, either due to dynamic coalescence in the conduit (Parfitt and Wilson, 1995) or collapse of a static foam in the magma chamber (Vergniolle and Jaupart, 1986; Vergniolle, 1996). The large ($\geq$1 m) gas slugs decouple from and ascend freely through the melt, triggering discrete explosions at the free surface.

The majority of Etna's eruptions fit the above models, but the Plinian eruption of 122 BC and several subplinian events are not compatible with either model due to their higher intensities and sustained eruption styles. Coupled degassing is required for magma to accelerate to the velocity necessary to produce a Plinian explosion (Jaupart and Allegre, 1991). In such a scenario, bubble nucleation is initially delayed by kinetic barriers (e.g., Lyakhovsky et al., 1996), volatile supersaturation develops in the melt, and finally bubbles nucleate in a runaway fashion accompanied by major acceleration that may drive the melt through the glass transition (Papale, 1999b). Coupled degassing is most readily achieved when the melt is highly viscous, as is common for high-silica melts (Sparks et al., 1994; Cashman et al., 2000).

A mechanism to suppress or delay decoupled degassing behavior and promote physical coupling between gas and melt in basaltic magma seems essential to permit Plinian eruptions of magma of this composition. The basaltic magma may be forced to adopt coupled behavior either by an increase in effective viscosity, or by vesiculation over a time span too short to permit bubbles to decouple fully from the melt. Three mechanisms that may act in isolation or in combination are: (1) very rapid ascent producing a delayed and shallow onset of degassing; (2) instantaneous decompression accompanying unloading due to caldera development or flank instability (Coltelli et al., 1998); and (3) microlite crystallization inducing rheological change.

Previous work

According to Coltelli et al.'s (1998) map of the 122 BC fall deposit (Fig. 2.1), the area within the 10 cm isopach is 530 km^2, confirming that this deposit is Plinian by Walker's (1973) classification. This is consistent with Roman chronicles that describe a large eruption with an ash cloud that hid the sun for days. The inferred vent is near Etna's summit, now buried under the modern summit cone, and the dispersal axis is to the southeast. The total volume of the eruption is 0.4 km^3 DRE (Coltelli et al., 1998). The calculated column height is 24-26 km with an estimated average mass eruption rate of $5.0\text{-}8.5\times10^7$ kg s^{-1} (Carey and Sparks, 1986; Coltelli et al., 1998).

Coltelli et al. (1998) divide the 122 BC deposit into seven units, A-G (Table 2.1). Unit A is a thin layer of well-sorted, coarse black ash of Strombolian dispersal. Units C and E are made up of well-sorted scoria and subordinate wall rock lithic lapilli, and are interpreted as Plinian falls. Units B, D, F, and G are tuffs ranging from bedded to massive in character, attributed to phreatomagmatic and phreatic phases of activity. Thus

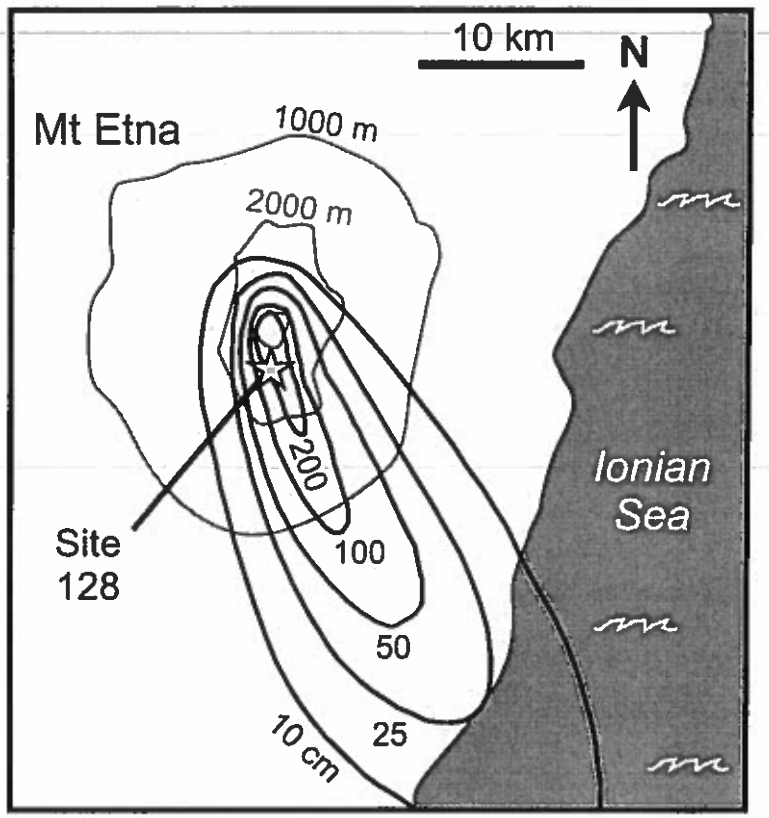

Figure 2.1 Isopach map of the Etna 122 BC Plinian fall from Coltelli et al. (1998). Topographic contours (gray) are in meters, isopachs (black) are in centimeters. Star indicates site 128, the principal sample site.

the 122 BC eruption had two Plinian phases, each preceded and followed by periods of weaker phreatomagmatic activity. Coltelli et al. (1998) also give analyses of bulk chemistry for each Plinian unit.

Table 2.1. Proximal stratigraphy for the 122 BC eruption of Etna. Thicknesses, unit descriptions, and interpretations are summarized from Coltelli et al. (1998). Wall rock contents were measured for this study.

Unit	Max thickness (cm)	Wall rock (wt %)	Description	Interpretation
G	220	<10	Massive fine tuff with large accretionary lapilli	Late phreatic explosions
F	54	<5	Vesiculated coarse and fine brown tuff	Final phreatomagmatic phase with minor surge component
E	51	7-12	Well sorted normal graded lapilli fall	Second Plinian magmatic phase
D	37	< 10	Indurated, bedded and vesiculated, poorly sorted, fine tuff	Phreatomagmatic phase dividing Plinian phases
C	169	10-26	Well sorted lapilli fall	First Plinian magmatic phase
B	17	<10	Yellowish fine lithic-rich poorly sorted, tuff	Weak phreatomagmatic phase
A	11	-	Well sorted coarse juvenile ash	Strombolian initial phase

Coltelli et al. (1998) propose an eruption model in which a sudden decompression event triggered runaway bubble nucleation in the 122 BC melt, allowing the magma to develop rapidly into a microvesicular foam. One possible cause of such a decompression is unloading by a collapse, but there is no evidence for contemporaneous slope failure, and caldera collapse was unlikely at the beginning of the eruption sequence. Instead, the

authors suggest a model in which the rapid injection of >1 km^3 of buoyant magma into the volcanic edifice caused abrupt elastic deformation of the eastern flank.

Del Carlo and Pompilio (2004) report detailed chemical analyses of glass, crystals, and melt inclusions in clasts from Plinian units C and E as well as in other Etna magmas. Electron microprobe analyses show that the composition of matrix glass is hawaiite while melt inclusions are mugearite (i.e., higher in SiO_2 and alkalis). Pre-eruptive volatile contents were measured by transmission IR spectroscopy in melt inclusions within olivine phenocrysts, yielding 1.0-3.1 ± 0.1 wt% H_2O and 200-900 ± 100 ppm CO_2. In the 122 BC clasts, volatile contents vary widely with weak or no dependence on the overall composition of the melt inclusions, whereas in other Etna magmas, variations in volatile content correlate with variations in other incompatible elements. The authors suggest that cooling, crystallization, and differentiation were relatively limited in the 122 BC magma, and the magma probably ascended rapidly with respect to other eruptions at Etna. Using the solubility model of Dixon and Stolper (1995), they estimate that the melt inclusions were trapped at a minimum pressure in the range of 50 to 210 MPa.

Houghton et al. (2004a) interpret some aspects of the eruption's evolution with time based on measurements of grain size and clast densities/vesicularities. The authors suggest that trends toward lower vesicularities late in the first Plinian phase and throughout the second Plinian phase indicate considerable cross-conduit heterogeneity in the magma. In their model, slower-moving magma along the walls of the conduit had more opportunity for outgassing and crystallization, leading to increased viscosity, which further reduced the ascent velocity of this marginal magma. Buildup of slow or stagnant

magma along the margins reduced the effective conduit radius and ultimately caused discharge to wane. The current study adds detail and expands on this conduit model using additional macroscopic data as well as qualitative and quantitative characterization of clast microtextures.

Questions

Three main questions are addressed in this paper. First, what processes caused the basaltic magma to erupt in Plinian fashion? Second, how did the degassing behavior of the 122 BC magma change with time? Third, why did the Plinian plume subside and terminate twice, with phreatomagmatic episodes of significantly weaker intensity intervening? We address these questions via quantitative studies of textural diversity in the pyroclasts from multiple stratigraphic levels in the Plinian units of the deposit.

2.3 Methods

The principal sample site for this study, site 128 (Fig. 2.1), is the most proximal exposure along the dispersal axis of the 122 BC deposits. Eleven pairs of samples were collected from stratigraphic zones 5-10 cm thick. Each pair includes one sample for grain size and one for microtextural studies. Grain size and componentry were measured in the laboratory at 1/2 ϕ intervals. For the microtextural samples consisting of 100 clasts in the 16-32 mm diameter range, clast morphology and surface texture were described and classified. Distributions of clast densities were measured and interpreted following the methods of several other studies (e.g. Sparks and Brazier, 1982; Houghton and Wilson, 1989; Cashman and Mangan, 1994; Klug and Cashman, 1994). The density distribution of each sample was used to select a smaller subset of 4-8 clasts including representative

examples of maximum, minimum, and modal vesicularities. These subsets of clasts were made into polished thin sections for detailed quantitative textural measurements.

Microscopic vesicle textures were quantified in 17 representative clasts selected on the basis of stratigraphic position and clast density. Sets of nested images were acquired at four magnifications. The lowest magnification was captured using an HP flatbed scanner, and the three higher magnifications were imaged on a JEOL-5900LV scanning electron microscope (SEM) with 20 kV accelerating voltage and 1 nA beam current. The resolutions of the digital images from lowest to highest magnification were 47.2, 252, 1000, and 2520 pixels per mm. Images were edited for contrast and clarity in Adobe Photoshop, and bubble areas were measured in Scion Image.

The use of two-dimensional images to represent three-dimensional distributions of vesicles and crystals presents a challenge as discussed by Mangan et al. (1993). Corrections were applied using the stereological technique of Sahagian and Proussevitch (1998). The stereological conversion assumes that vesicles are spherical. This is not the case for the 122 BC samples, but no applicable methods exist for irregular bubble shapes. The bubble sizes indicated in the tables and figures are the diameters and radii of equivalent spheres calculated in the 2D to 3D conversion.

Microlites were also studied qualitatively and quantitatively. Separate sets of SEM images were acquired at high magnification (25,200 pixels per mm) to resolve the microlites. Number density, volume abundance, characteristic size, and habit of each mineral phase were observed and/or measured.

2.4 Results

Eruption dispersal

The deposits of Plinian phases C and E extend beyond 30 km from vent (Fig. 2.1; Coltelli et al., 1998). The dispersal trends of units C and E can be compared using profiles along the dispersal axis (Fig. 2.2) after Pyle (1989). Both units are sheet-forming and have similar $t_{1/2}$ (linear thickness half-distance; Houghton et al., 2004b) values of 10.3 km (unit C) and 10.2 km (unit E), indicating that the two phases were similar in intensity. The smaller volume of tephra in unit E implies a shorter duration for the second Plinian phase.

Grain size, componentry, and clast morphology

Median grain size and componentry data were first presented in Houghton et al. (2004a) with some tentative interpretations. In the current study, sorting data are added and the overall dataset is interpreted in more detail. The median grain size at the principal sample site is consistently relatively coarse (between -2 and -4ϕ) but shows minor fluctuations with time, some abrupt and others gradational (Fig. 2.3). The largest juvenile clasts are found in sample C6, which we infer to represent the peak intensity of the Plinian eruption. Sorting varies throughout the units. The samples with the coarsest median grain size, (C2 and C6), show good ($\sigma\phi \approx 1.0$) sorting, while finer-grained samples are more poorly sorted, such as C7, C4, and E3. The grain size characteristics of the Etna 122 BC samples are identical to those of silicic Plinian falls (Walker, 1980; Walker, 1981) and very different from archetypical phreatoplinian falls (Self and Sparks, 1978; Walker, 1981). Wall rock content generally increases with increasing median grain

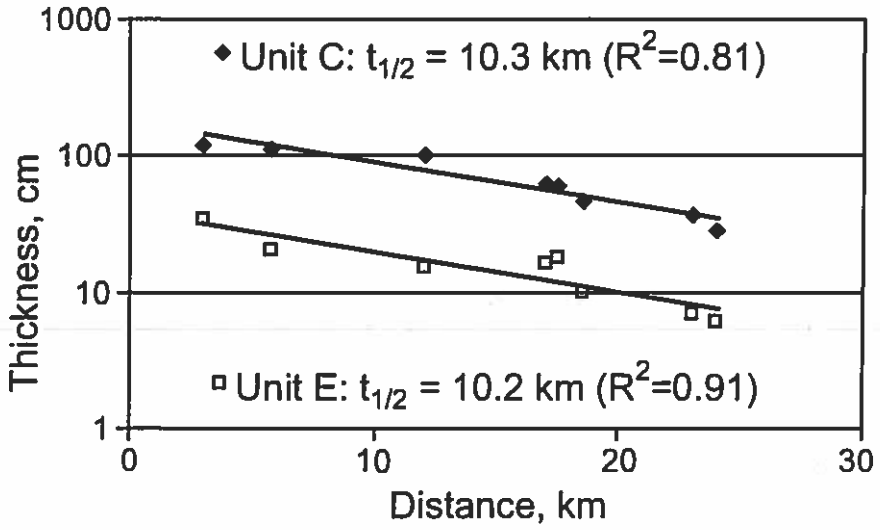

Figure 2.2 Plot of thickness versus linear distance from vent for Plinian units C and E of the Etna 122 BC deposit, with thickness on a logarithmic scale (P. Del Carlo and M. Coltelli, unpublished data). Measurements were taken close to or on the axis of dispersal. The calculated linear thickness half-distances ($t_{1/2}$) values are 10.3 km for unit C and 10.2 km for unit E. Quality of fit is indicated by R^2 values.

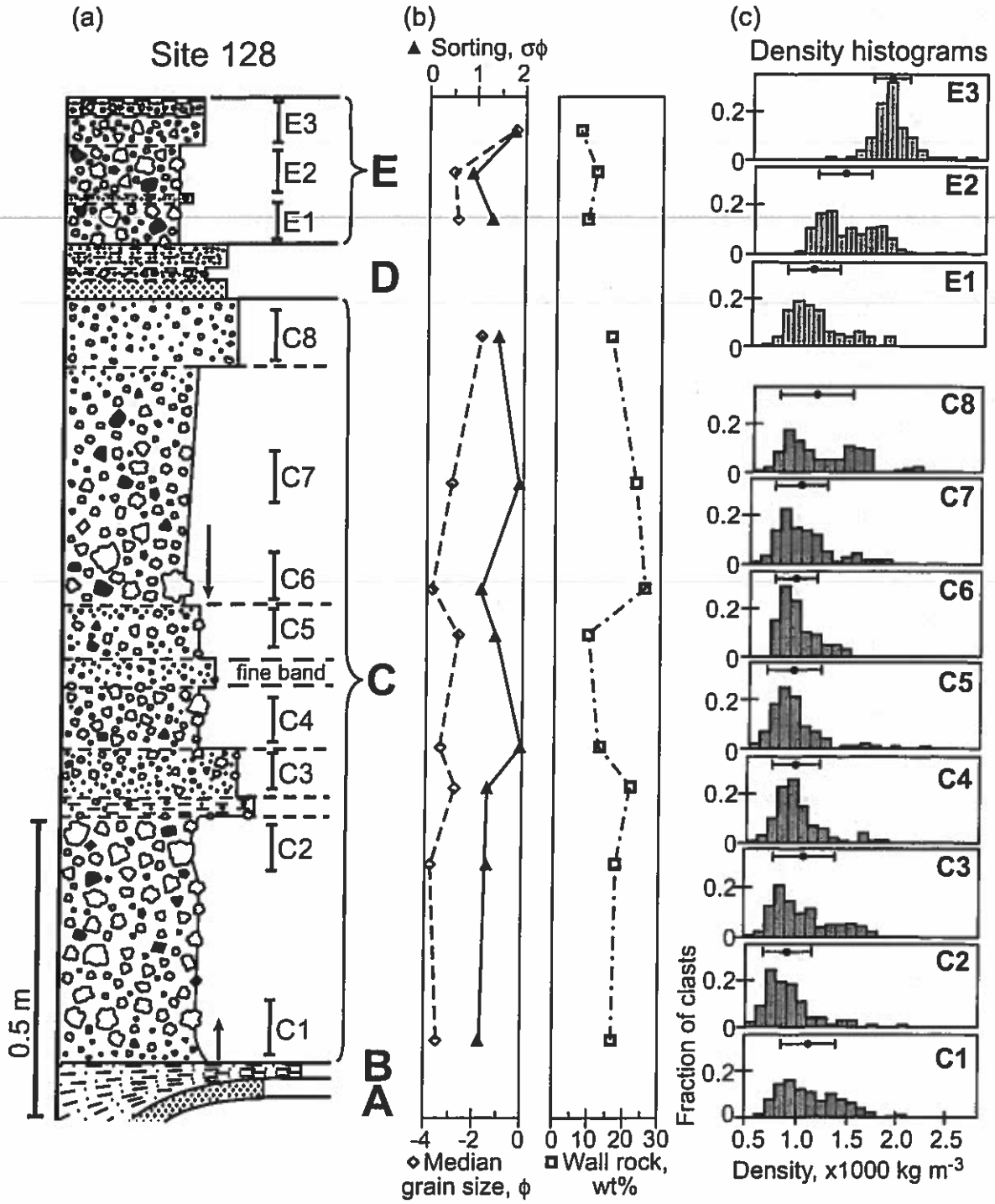

Figure 2.3 (a) Stratigraphic column of proximal site 128 with sample intervals labeled. Vertical arrows indicate graded intervals and point in direction of coarsening. (b) Median grain size, sorting, and wall rock content are plotted for each sample. (c) Histograms of clast density for samples of 100 clasts in the 16-32 mm diameter range. Dots above histograms mark mean densities, and bars extend one standard deviation to each side. All samples have positive skewness (high density tails on the distributions).

size throughout the sequence. At the tops of units C and E, the lithic content decreases along with the grain size (Fig. 2.3).

The 122 BC juvenile clasts do not exhibit quench textures or breadcrust cracks. The clasts are also conspicuously lacking in highly fluid achneliths, Pele's tears, fusiform bombs, and other features associated with Hawaiian and Strombolian basaltic deposits (Richter et al. 1970; Swanson et al., 1979). Instead, samples are typically dominated by blocky, ragged, and cauliflower-like forms. Curviplanar clasts, with flat or concave surfaces bounded by angular edges, are rare in all samples except E3, which contains 25% such clasts.

Clast density and vesicularity

We have revisited and supplemented the density data of Houghton et al. (2004a) as the foundation for selecting clasts for microtextural analysis. Distributions of Etna 122 BC clast densities, and thus clast vesicularities, show that the clast population from the opening of Plinian phase C included a significant proportion of high-density clasts (Fig. 2.3). As the eruption intensity increased, the clast population became more uniform but still had a small proportion of high-density clasts. The proportion of dense clasts then increased until a bimodal density distribution developed near the end of phase C (sample C8), coincident with a decrease in grain size. The secondary peak in the bimodal distribution of C8 matches the dense tails in earlier samples C2 through C7 (1500 to 1700 kg m^{-3}). For unit E, the density distribution broadens early (sample E2) and then forms a single distinct peak (sample E3) of high-density clasts.

Vesicle data

Qualitative observations

The 122 BC clasts have high bubble number densities, with respect to Hawaiian and Strombolian ejecta, and a wide range of bubble textures (Fig. 2.4). All samples are microvesicular, with bubbles sizes ranging from 5 μm to 5 mm in diameter. Very small (<10 μm) bubbles are rare. The most crystalline clasts contain tiny, angular voids between microlites (Fig. 2.4d), but these "diktytaxitic" textures result from contraction during microlite crystallization, not vesiculation (Walker, 1989; Saar and Manga, 1999; J.E. Hammer pers. comm., 2005). Most bubbles are surrounded by melt, but a few bubbles adhere to phenocrysts. In general, bubbles are uniformly dispersed in the 122 BC clasts regardless of size, but some clasts also have irregular zones 0.2-0.5 mm wide that are dominated by intermediate or small vesicles (e.g. Fig. 2.4c).

Complex shapes characterize all bubbles larger than 50 μm as well as most bubbles down to 10 μm diameter. Some bubbles have shapes composed of merged convex rounded forms (e.g. Fig. 2.4a), while others have shapes that are more attenuated with some concave margins (e.g. Fig. 2.4d). No preferred direction of elongation is observed.

Quantitative measurements

As previously described, 3-4 thin sections of mode, minimum, and maximum density clasts were selected from each 100-clast sample for quantitative measurements of vesicle size and number density. The modal clast of a sample is assumed to be representative of the bulk of the magma erupted at a given time, and the low and high density clasts constrain the degree of heterogeneity at that time.

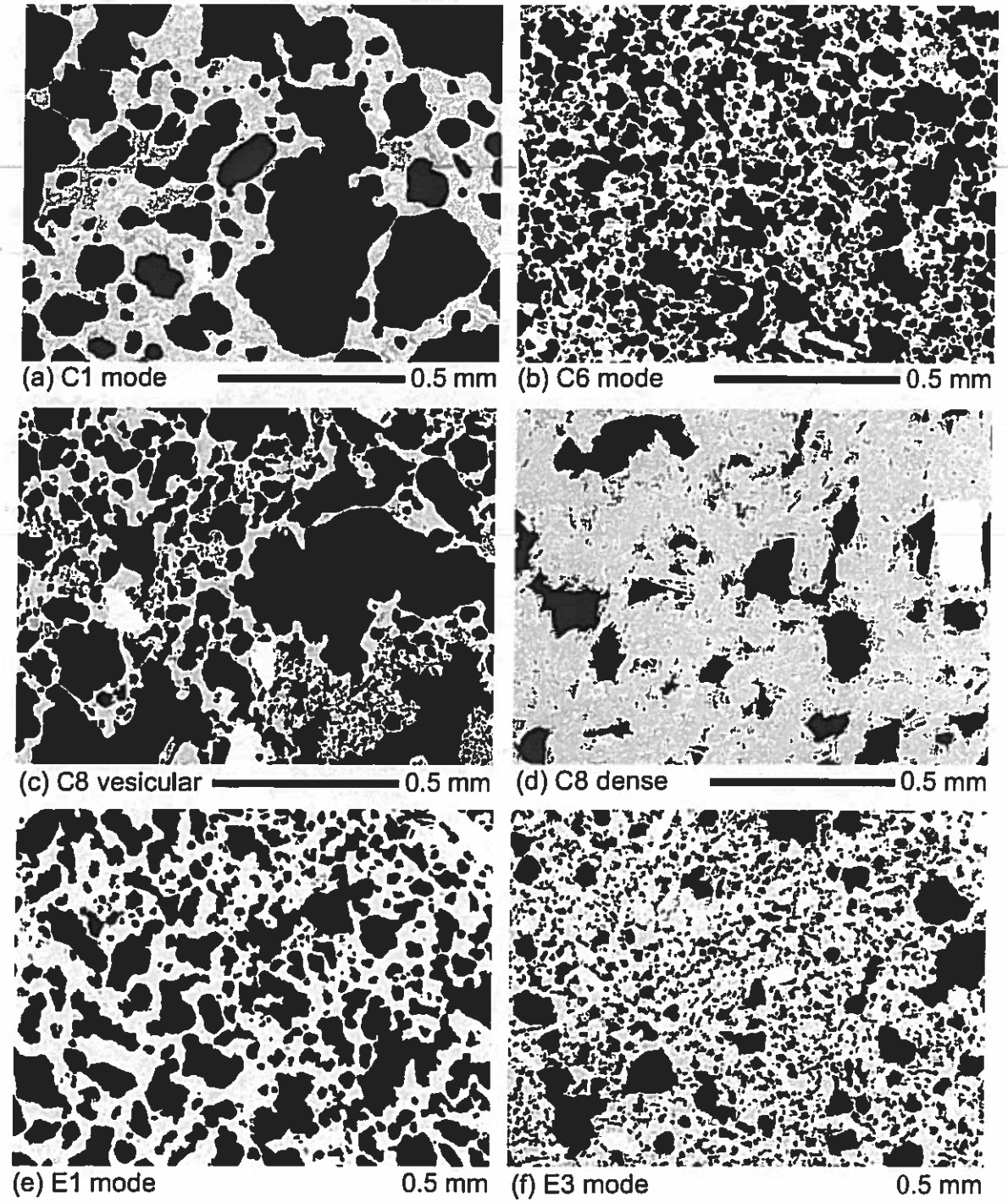

Figure 2.4 Selected SEM images of vesicle textures. Bubbles are black; glass and crystals are pale grey to white.

Total bubble number densities for the Etna 122 BC clasts range from 3×10^6 cm^{-3} to 9×10^7 cm^{-3} (Table 2.2; Fig. 2.5). These values partially overlap those measured in silicic Plinian pumice (6×10^7 to 1×10^{10} cm^{-3}; Klug and Cashman, 1994; Klug et al., 2002; Gurioli et al., 2005). Typical basaltic scoria and reticulite have lower bubble number densities, ranging between 1×10^2 and 4×10^5 cm^{-3} (Mangan and Cashman 1996, Lautze and Houghton, 2005). The only well-characterized basaltic pyroclasts with bubble number densities comparable to those of Etna 122 BC come from a subunit of the Keanakako'i Ash of Kilauea, which, though phreatomagmatic, probably was of subplinian intensity (Mastin et al., 2004).

The range in bubble sizes in the Etna 122 BC clasts covers three orders of magnitude (Fig. 2.5), while the widest size range of typical cone-forming basaltic tephra spans only two and lacks the smallest bubbles (Table 2.2; Mangan and Cashman, 1996; Lautze and Houghton, 2005). In comparison to silicic pumice, the 122 BC clasts have a similar range of bubble sizes but a coarser mode bubble diameter (Table 2.2).

Table 2.2 (next page). Bubble size ranges, typical sizes, and total number densities (N_{Vtot}) for explosive products of a range of compositions. Minimum bubble diameters are estimates that depend on limiting image resolution. Total bubble number densities are per volume of bulk rock, rather than per volume of melt. References: (1) this study, (2) Mastin et al., 2004; (3) Mangan and Cashman, 1996; (4) Lautze and Houghton, 2005; (5) Gurioli et al., 2005; (6) Polacci et al., 2003; (7) Klug and Cashman, 1994; (8) Klug et al., 2002.

Table 2.2. Bubble size ranges, typical sizes, and total number densities (N_{Vtot}) for explosive products of a range of compositions.

Eruption	Sample	Diameter range, cm	Typical diameter, cm	N_{Vtot}, cm^{-3} (bulk rock)
Etna 122 BC[1]	early C mode	0.0007-0.25	0.0501	2.57×10^6
	peak C mode	0.0007-0.25	0.0237	3.42×10^7
	late C mode	0.0007-0.158	0.0199	1.71×10^7
	early E mode	0.0007-0.316	0.0398	8.07×10^6
	mid E mode	0.0007-0.199	0.0100	2.83×10^7
	late E mode	0.0007-0.158	0.0158	6.13×10^7
Keanakako'i[2]	520b			5.61×10^6
	517b			1.32×10^6
	508f			1.48×10^6
	502h			1.71×10^6
	409b			1.44×10^6
Kilauea reticulite[3]	2500R1	0.001-0.2	0.107	1.78×10^3
	45-2	0.001-0.36	0.182	3.75×10^2
	45-3	0.001-0.36	0.184	3.32×10^2
	2500R4-A	0.001-0.46	0.228	1.10×10^2
Kilauea scoria[3]	487T	0.001-0.12	0.009	1.77×10^5
	500S1	0.001-0.12	0.009	1.60×10^5
	OoB	0.001-0.14	0.012	1.10×10^5
	282T	0.001-0.18	0.011	7.30×10^4
	300T2	0.001-0.10	0.010	1.20×10^5
Stromboli[4]	1952-high			5.39×10^4
	1911-low			3.44×10^5
Vesuvius[5]	EU2-mean	0.0008-0.267	0.005	5.6×10^8
	EU3b-mean2	0.0008-0.435	0.005	8.1×10^7
	EU3t-mean2	0.0005-0.413	0.002	8.8×10^8
	EU4-mean2	0.0008-0.248	0.002	5.2×10^8
Campanian Ignimbrite[6]	CI60-70m1	0.0011-0.0016	0.0011	1.4×10^8
	CI60-70t	0.0011-0.0016	0.0016	8.2×10^7
	CI110-120m1	0.0012-0.0013	0.0012	1.3×10^8
	CI110-120t	0.0012-0.0013	0.0013	1.3×10^8
Mount St Helens[7]	Gray	0.0002-0.3	0.002	2.0×10^9
	White	0.0002-0.3	0.005	8.2×10^8
Mazama 7700 BP[8]	PF15	0.0002-0.5	0.002	7.76×10^9
	WT9	0.0002-0.4	0.001	1.00×10^{10}
	CP10	0.0002-0.6	0.005	2.29×10^9
	CP11	0.0002-0.2	0.004	1.29×10^9
	CP14	0.0002-0.8	0.501	7.76×10^7

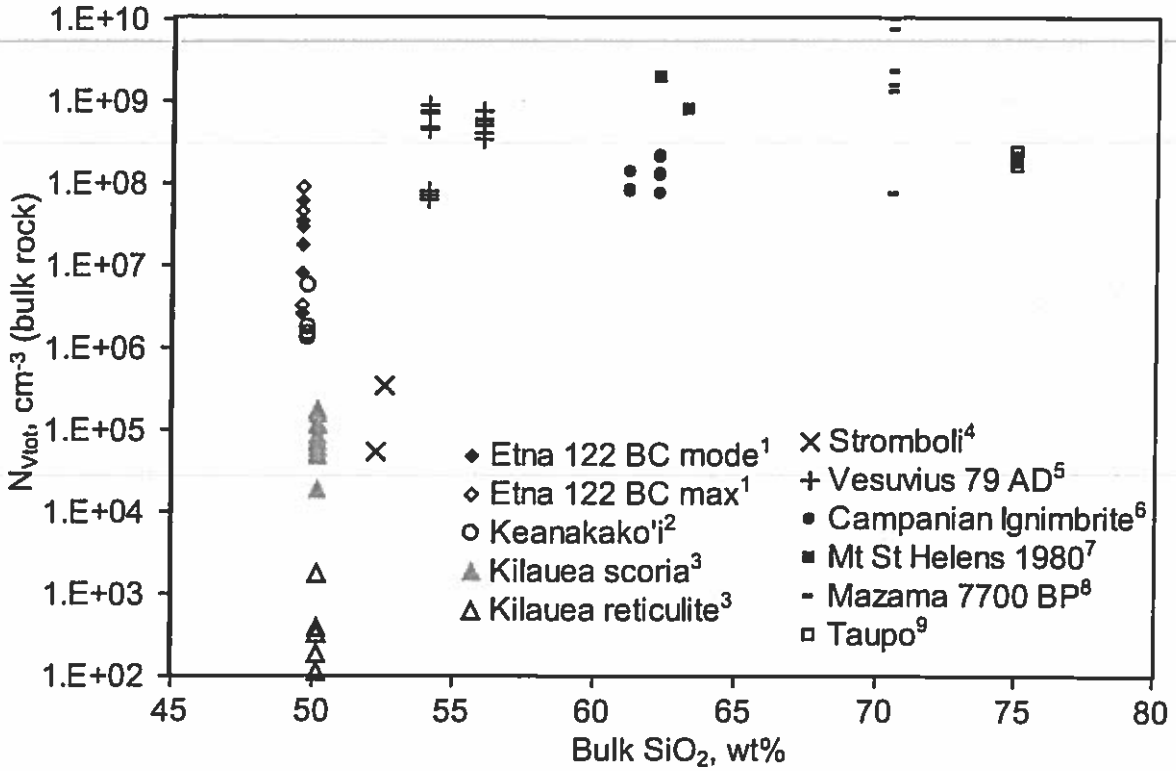

Figure 2.5 Comparison of total bubble number densities (N_{Vtot}) for explosive eruptions with a range of magma compositions indicated by bulk SiO_2 content. Number densities are given per volume of bulk rock, rather than per volume of melt. References: (1) this study, (2) Garcia et al., 2003; Mastin et al., 2004; (3) Garcia et al., 1992; Mangan and Cashman, 1996; (4) Lautze and Houghton, 2005; (5) Civetta et al., 1991; Gurioli et al., 2005; (6) Signorelli et al., 1999; Polacci et al., 2003; (7) Criswell, 1987; Klug and Cashman, 1994; (8) Klug et al., 2002; (9) Froggatt, 1981; B. Houghton, unpublished data.

Distributions of vesicle sizes are shown as histograms of volume fraction vesicles versus vesicle diameter (Fig. 2.6). The modal density clast from sample C1 has a narrower but coarser bubble size peak than the other modal clasts of unit C. The distribution of bubble sizes shifts toward smaller values in samples C2 and C6, but includes significant subpopulations of both coarser and finer vesicles by the end of phase C (sample C8). The modal density clast from the start of phase E (sample E1) has a coarse bubble size peak similar to the start of phase C. Overall vesicularity then decreases (sample E2) until vesicles of all sizes are strongly depleted in sample E3. All minimum density clasts from phases C and E are rich in large vesicles. The maximum density clasts at the start and end of phase C (samples C1 and C8) also have modes of coarse vesicle sizes, but the dense clasts in phase E have smaller bubbles (E1 and E2) or a lower overall volume fraction vesicles (sample E3).

Crystal data

Phenocrysts

Phenocrysts make up 1-10% of the samples by volume (Coltelli et al., 1998), and include plagioclase and minor clinopyroxene, olivine, and iron-titanium oxide. Plagioclase phenocrysts are subhedral and commonly show zoning and some resorption textures. Clinopyroxene phenocrysts are euhedral to rounded. Fe-Ti oxide phenocrysts are equant and subangular. Although phenocrysts provide information about conduit processes for some eruptions (e.g., Rutherford and Hill, 1993), this is not the case for the Etna 122 BC phenocrysts. It is difficult to distinguish features related to conduit ascent from features inherited from the phenocrysts' formation in the magma storage zone. Thus we reserve our detailed study for the microlites, which indicate conduit processes more directly.

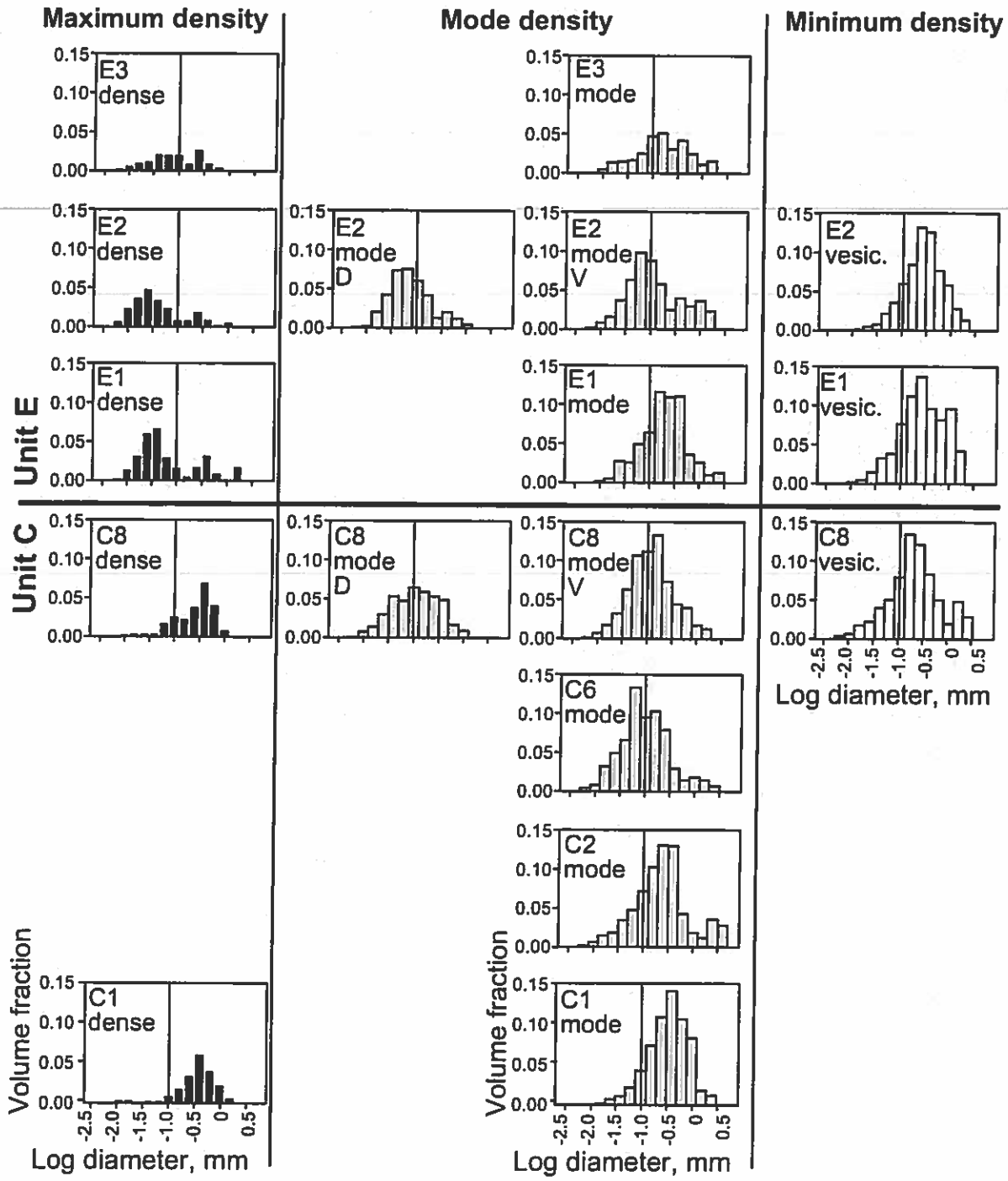

Figure 2.6 Histograms of volume fraction vesicles with vesicle size arranged according to stratigraphic height. For samples with multiple modes, the more vesicular modes (mode V) are in right column, secondary denser modes (mode D) in left. Vertical lines are drawn at 0.1 mm equivalent diameter to assist comparison.

Microlite observations

Clasts in silicic Plinian deposits are typically poor in microlites (Hildreth, 1983; Fierstein and Hildreth, 1992; Sutton, 1995), and Hawaiian-Strombolian ejecta also have very low to moderate microlite contents (e.g. Lautze and Houghton, 2005; Polacci et al., 2006). In contrast, microlites are abundant in samples from all stratigraphic levels of the Etna 122 BC deposits. The groundmass textures of 25 clasts have been characterized qualitatively and quantitatively. Sizes and habits of the microlites are extremely diverse (Fig. 2.7; Table 2.3). We group the textures into three categories (holocrystalline, hypocrystalline, hypohyaline) based on the measured or apparent relative abundance of microlites and glass. We also define three classes based on dominant sizes of clinopyroxene (cpx) and oxide (ox) microlites (Table 2.3). Plagioclase is not used in the size classification because it can vary greatly in size and habit within a single clast.

A weak inverse correlation between vesicularity and microlite crystallinity is observed for both phases C and E. The high density clasts are mostly holocrystalline with euhedral tabular and prismatic microlites. The lowest microlite number densities are associated with the coarsest microlites, which occur in the dense clasts from the close of Plinian phase C. Clusters and patches of extremely fine (<0.3 μm) clinopyroxene and oxide grains are irregularly distributed between the coarser microlites.

Most of the modal and minimum density clasts are hypocrystalline. Clasts from unit C typically contain fine-grained microlite populations, with thin needles of plagioclase and blades of clinopyroxene occurring alone or in radiating fans and bundles (Fig. 2.7a, b). Microlites in clasts from phase E have more euhedral habits (Fig. 2.7e, f). Fe-Ti oxide has an equant subhedral to euhedral habit in nearly all clasts, but size and

Table 2.3. Summary of microlite textures observed in thin sections of representative 16-32 mm clasts. Density classes: vesicular = lowest density clast of a sample; modeV = the more vesicular of two modes; modeD = the denser of two modes; dense1 = highest density clast of a sample; dense2 = second densest clast of a sample. Apparent grain size categories: fine = cpx <2.5 (up to 11) μm, ox <0.7 (up to 3.0) μm; medium = cpx 2.0-3.0 (up to 12) μm, ox 0.8-1.4 (up to 4.0) μm; coarse = cpx 3.0-8.0 (up to 20) μm, ox 1.5-2.2 (up to 6.0) μm. All clasts have some microlites outside these ranges, but classes are based on the most dominant sizes.

Sample	Clast	Density category	Vol% vesicles	Apparent crystallinity	Apparent grain size	Microlites, # mm^{-2}	Vol% in groundmass				Typical size, μm			Textural features present				
							glass	plag	cpx	ox	plag	cpx	ox	skeletal	radiate	dendrite	needle	incip
C1	20	vesicular	70	hypohyaline	medium	1.8E+05	45	30	21	4	12	1.6	0.72		X		X	
C6	33	vesicular	73	hypohyaline	medium	9.9E+04	57	23	20	1	14	3	1.2		X		X	
C8	72	vesicular	71	hypocrystalline	medium	1.5E+05	28	36	35	0.2	12	0.8	0.6	X	X	X	X	
E1	14	vesicular	74	hypocrystalline	fine	3.0E+05	22	47	28	3	10	1.8	0.6	X	X	X	X	
E2	68	vesicular	65	hypocrystalline	fine-med						13	2.6	0.72	X	X	X	X	X
C1	18	mode	63	hypocrystalline	medium	2.0E+05	33	35	28	3	9	2.2	0.8				X	
C2	35	mode	70	hypocrystalline	fine	2.8E+05	11	48	39	2	8	1.4	0.6		X	X	X	X
C6	23	mode	67	hypocrystalline	fine-med	2.8E+05	22	38	39	0.4	8	2.8	0.8			X		
C8	44	modeV	67	hypocrystalline	fine	3.1E+05	14	54	31	1	12	2	0.6		X	X	X	X
C8	35	modeD	41	holocrystalline	fine						20.8	8	0.24			X		X
E1	2	mode	61	hypocrystalline	fine	3.1E+02	30	37	29	4	8	2.6	0.8				X	
E2	22	modeV	53	hypocrystalline	fine	5.2E+05	10	54	34	2	3.6	2.2	0.72		X		X	X
E2	40	modeD	37	hypocrystalline	fine-med						10	3	1	X			X	X
E3	21	mode	30	hypocrystalline	medium	2.2E+05	17	49	31	3	12	2.2	1.2		X		X	
C1	29	dense	22	holocrystalline	medium	4.8E+05	0	42	55	3	10	2.4	0.8		X	X		X
C2	59	dense1	47	hypocrystalline	fine						16	1.2	0.6		X		X	
C2	20	dense2	42	hypocrystalline	fine	2.9E+05	23	40	36	1	7.2	1.2	0.6		X	X	X	X
C6	4	dense1	48	hypocrystalline	fine	2.9E+05	12	45	43	0.2	8	2	0.6		X	X	X	
C6	31	dense2	48	hypocrystalline	medium						3	0.36	0.36				X	X
C8	81	dense1	26	holocrystalline	coarse	1.1E+02	0	69	22	8	>48	2	1.6					
C8	21	dense2	24	hypocrystalline	coarse	1.4E+02	31	41	23	5	>50	8	2.2	X				
E1	31	dense	32	holocrystalline	fine	2.8E+05	0	67	29	4	10	3.2	0.6	X				X
E2	45	dense	25	holocrystalline	fine						8	2	0.8	X				X
E3	11	dense1	16	holocrystalline	medium						14	3.2	1.6	X				
E3	27	dense2	3	hypocrystalline	fine	7.0E+05	9	51	38	2	4	2	0.4		X			X

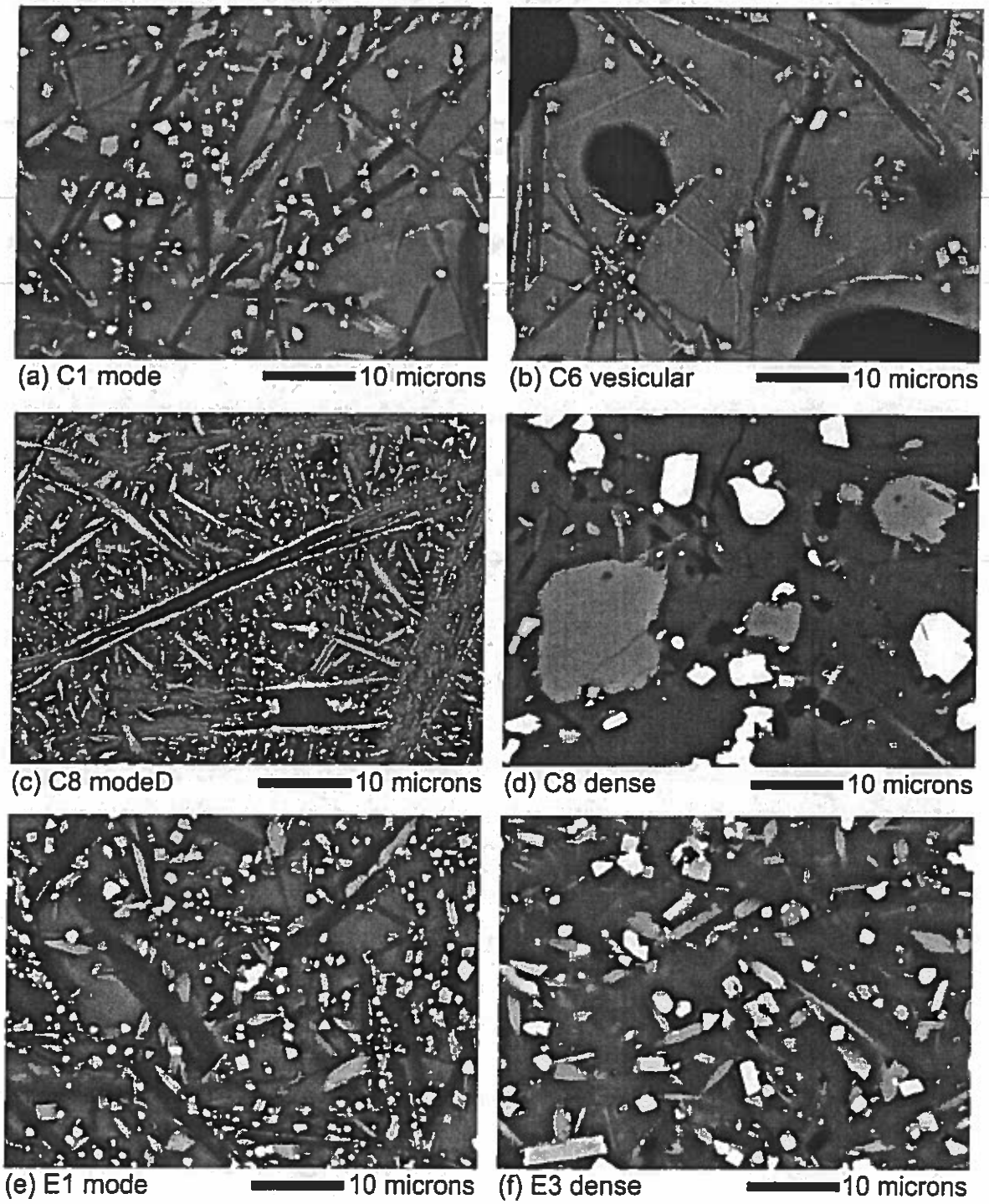

Figure 2.7 Selected SEM images showing microlite textures.

number density vary slightly. Most of the modal clasts also contain pockets of very fine-grained crystals similar to those described for the high density clasts (Fig. 2.7e). At high magnification, the glassy matrix appears mottled and seems to be a collection of tiny crystallites with poorly resolved boundaries.

2.5 Interpretations

Interpretations of macroscopic data

Changes in median grain size with stratigraphic height are a useful proxy for changes in eruptive intensity with time (Fisher and Schmincke, 1984), assuming constant wind velocity and in the absence of significant shifts in clast density (Fig. 2.3). The grain size data suggest that during phase C, the eruption built rapidly to a relatively powerful intensity (represented by sample C2), then entered a period of fluctuating and somewhat weaker intensity depositing alternating beds of coarser and finer lapilli (samples C3, C4 , C5). This was followed by a second period of more vigorous sustained eruption centered around sample C6, which represents the maximum eruptive intensity. Intensity decreased sharply at the close of phase C (sample C8). Phase E built quickly to its peak intensity, represented by the relatively coarse and well sorted samples E1 and E2. This intensity was maintained, apart from a minor waning interval, until nearly the end of the phase when it declined rapidly (sample E3).

Variations in lithic wall rock content of pyroclastic fall deposits suggest possible variations in the intensity of the eruption and/or the degree of involvement of external water (Fisher and Schmincke, 1984). For the 122 BC Plinian phases, increases in lithic content do not necessarily indicate increases in external water involvement, because they

are not accompanied by decreases in median diameter or increases in fine ash content, which would be expected from onset of interaction with water. Instead, median grain size increases with increasing lithic content (Fig. 2.3). We infer that the Plinian phases were essentially dry, and that more wall rock was incorporated during periods of higher eruption intensity due to enhanced scouring of the sides of the conduit. Similarly, the concurrent decreases in grain size and lithic content at the close of each Plinian phase indicate declining eruptive vigor and reduced capacity to incorporate and transport large clasts (e.g., samples C6 to C8 and E2 to E3).

The lack of quench textures and other features typical of phreatomagmatic clasts (Heiken and Wohletz, 1985) further supports the interpretation that the 122 BC Plinian phases were dry. The lack of highly fluidal clast morphologies suggests that at the time of fragmentation, the 122 BC magma was probably more viscous than magmas in typical low-intensity basaltic eruptions. The observed blocky to ragged clast morphologies are interpreted to result from tearing apart of viscous yet fluidal magma. The shift in dominant clast morphology from viscous/fluidal to brittle at the end of phase E is a vivid indication that significant changes in melt rheology accompanied the close of sustained explosive eruption.

Changes in clast density/vesicularity distributions are broad indicators of changes in the extent and style of degassing in the conduit (e.g., Houghton et al., 2000; Gurioli et al., 2005; Adams et al., 2006b). For example, the sharp high vesicularity peak of the density histogram for sample C6 suggests that, at the intensity maximum, the entire width of the conduit was occupied by relatively uniform, actively vesiculating magma. The shift toward high density in upper unit E indicates substantial gas loss from the erupting

magma. Our results support Houghton et al.'s (2004a) inference that the tails or secondary modes of dense clasts on all the density histograms imply physical heterogeneity in the magma that approached the fragmentation surface at a given time. This heterogeneity was most pronounced at the ends of phases C and E, but was also significant at the start of C (Fig. 2.3). We caution that interpretations based on clast vesicularity alone are partly speculative. Detailed microtextural studies are used to evaluate and enhance these interpretations to provide a more complete picture of the vesiculation processes.

Interpretations of vesicle size and shape data

The modal and minimum density clasts of samples C1 through E2, as well as the maximum density clasts of samples C1 through C6, are dominated by convex and rounded polylobate bubble shapes (Fig. 2.4a, b). The complex shapes of bubbles in the 122 BC clasts are best explained by bubble coalescence (Gaonac'h et al., 1996a; Gaonac'h et al., 2005). The maximum density clasts of samples C8, E1, and E2, and both the modal and maximum density clasts of sample E3, are dominated by smaller bubbles with more angular and wrinkled contours (Fig. 2.4d, e, f). This suggests that, starting in late phase C, bubble coalescence was followed by some process of bubble collapse or shrinkage in parts of the magma.

Large and moderately sized bubbles have the most complex shapes in the 122 BC clasts, but even the smallest bubbles are not perfectly spherical, although they might be expected to have shorter and simpler growth histories and thus simpler shapes. This pattern appears in clasts from every stratigraphic level and suggests that coalescence became important very early in the magma's ascent. Coalescence may occur more easily

and reach a more advanced stage in basaltic magmas than in more silicic magmas due to the lower viscosity of basaltic melt (Herd and Pinkerton, 1997). The evidence for extensive coalescence implies that the maximum bubble number densities were even higher than the already high values indicated by our measurements. Possible reasons that the coalesced bubbles failed to relax to spherical shapes include a short time scale due to rapid ascent of the 122 BC magma, and relatively high effective viscosity of the magma (Herd and Pinkerton, 1997). In contrast to the patterns in the Etna 122 BC clasts, the larger (cm-sized) bubbles in Strombolian scoria have complex shapes and are commonly connected in chains indicating substantial coalescence, but the smaller (mm-sized) bubbles are spherical (Lautze and Houghton, 2005; B.F. Houghton, unpublished data).

Bubble number densities in the modal density clasts vary by less than an order of magnitude (Table 2.2), suggesting that most of the melt experienced similar nucleation conditions. Differences in bubble size, shape, and spacing become more pronounced in samples from higher stratigraphic levels, especially in the densest clasts. We suggest below that these variations were produced by late stage processes in the upper conduit after a common early ascent history.

The bubbles in the Etna 122 BC clasts range down to much smaller sizes than in other basaltic ejecta (e.g., Mangan and Cashman, 1996; Simakin et al., 1999; Lautze and Houghton, 2005), suggesting that the interval of bubble nucleation may have extended until close to fragmentation (Blower et al., 2002). Alternatively, the influences of growth and coalescence of bubbles may have been increasingly restricted due to increasing viscosity and crystallinity of the ascending magma. Careful observations of clasts in thin section show that the largest bubbles are not concentrated at the centers of clasts, but are

distributed uniformly throughout the clasts. We infer that post-fragmentation expansion was not an important factor in the development of the largest bubbles in clasts of the size studied (16-32 mm diameter).

The unusually high bubble number densities and small bubble sizes in the Etna 122 BC clasts suggest that the bubble nucleation rate was probably much faster than the rates in Hawaiian or Strombolian eruptions. Such rapid bubble nucleation occurs at high supersaturation pressures, which equate to high rates of decompression (Sparks, 1978; Navon and Lyakhovsky, 1998; Mangan and Sisson, 2000; Mangan et al., 2004). Rapid decompression and ascent have been proposed for the 122 BC magma by Coltelli et al. (1998) and Del Carlo and Pompilio (2004). Our microtextural data confirm that a high ascent rate was an important factor in causing the 122 BC eruption to reach Plinian intensity.

Vesicle or bubble size distributions (VSDs or BSDs) may be plotted and analyzed in several ways to show the mathematical relationship between bubble number density and size, and the best-fit trends give information about conduit processes (Toramaru, 1989; Toramaru, 1990; Mangan et al., 1993; Cashman and Mangan, 1994; Klug and Cashman, 1994; Gaonac'h et al., 1996a,b; Mangan and Cashman, 1996; Simakin et al., 1999; Blower et al., 2001, 2002; Klug et al., 2002; Polacci et al., 2003; Gaonac'h et al., 2005; Gurioli et al., 2005; Toramaru, 2006). Some researchers interpret exponential trends in VSDs based on a steady-state population density function (e.g., Mangan et al., 1993; Cashman and Mangan, 1994; Klug and Cashman, 1994; Mangan and Cashman, 1996). Other workers report power law VSDs, but there is no consensus on the best formulation of the power law (e.g., Gaonac'h et al., 1996a,b; Simakin et al., 1999;

Blower et al., 2001; Blower et al., 2002; Klug et al., 2002). We follow Blower et al. (2001, 2002) in using the form $N_V{>}R = AR^{-d}$, where R is bubble radius (in mm), $N_V{>}R$ is the cumulative number density of bubbles (in mm^{-3}) with radii larger than R, A is a constant of proportionality, and *d* is the power law exponent.

For the 122 BC vesicle data, power laws with exponents ranging from $d = 2.7$ to 2.9 give better fits than exponential trends (Fig. 2.8). Two contrasting models have been proposed to explain power law VSDs (Blower et al., 2001; Blower et al., 2002; Gaonac'h et al., 1996a,b), but they cannot be distinguished based on *d* alone. Both models are probably simplified, and the physical meaning of power law exponents for natural bubble populations is still not clear. In light of these ambiguities, we report our power law fits for the purpose of comparison with data from other eruptions, but we do not emphasize the significance of the VSDs in our subsequent interpretations.

The drastic (30-50%) drop in vesicularity and the decrease in modal bubble size through phase E indicate a significant role for outgassing, i.e., loss of the gas phase. In Strombolian eruptions, outgassing is accomplished when large coalesced bubbles rise through relatively stationary melt, intersect the free surface, and burst to release their gas (Vergniolle and Mangan, 2000). However, the high microcrystallinities observed in the Etna 122 BC clasts suggests that this magma was too viscous for gas bubbles to move easily relative to the melt in the shallow conduit.

We suggest instead that the angular, pinched shapes of the bubbles in the high density samples of phases C and E are consistent with processes of permeability development followed by bubble collapse. Experiments on vesicular basalt and hydrated rhyolite show that bubble coalescence creates interconnected pathways through which

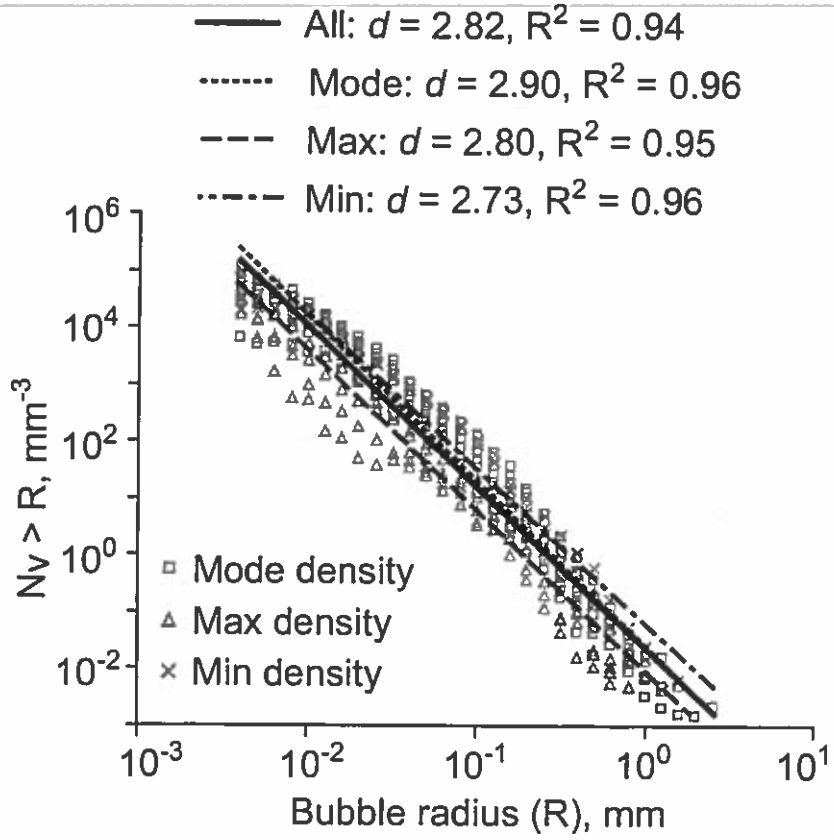

Figure 2.8 Plot of cumulative volumetric bubble number density (N_V>R) against equivalent bubble radius (R) in bilogarithmic coordinates. Power law trends fit the data better than exponential or other trends. Values of exponents (*d*) are indicated.

gas can escape, causing shrinkage and distortion of bubbles (Saar and Manga, 1999; Burgisser and Gardner, 2005). Microfractures and tiny void spaces between microlites may also bridge areas between bubbles to promote permeability (Walker, 1989; Saar, 1998). Such connections among bubbles may be obscured after gas loss as bridging pore spaces can collapse (Saar, 1998). Permeability can affect some parts of the magma while adjacent parts remain impermeable (Klug and Cashman, 1996). We do not attribute the bubble collapse to gravity or shearing because the collapsed bubbles do not align in any preferred orientation.

Interpretations of microlite textures

Vesicle and microlite data are summarized and matched with stratigraphic height in Fig. 2.9. For our interpretations of the 122 BC microlite textures, we follow current models for Plinian eruptions in assuming that rapid ascent precludes significant undercooling through heat loss in the conduit (e.g., Jaupart, 1996; Papale, 1998). The effective undercooling that triggers microlite formation arises instead from an increase in the thermodynamic stabilities of anhydrous mineral phases in response to decompression and dehydration (Lipman and Banks, 1987; Geschwind and Rutherford, 1995).

We also assume that the sampled lapilli were quenched in the plume and no further crystallization occurred after clasts left the vent. Experiments and models relating to the cooling of pyroclasts in plumes (Tait et al., 1998; Hort and Gardner, 2000) show that the timescale of quenching depends on the size of the clast. The glass transition temperature for Etna basalt, calculated as the temperature at which the melt's viscosity reaches 10^{11} Pa s, is 982 K (Giordano and Dingwell, 2003a). In 2-3 cm lapilli, the clast diameter that we used for microtextural studies, the rims take 10 seconds to cool from an

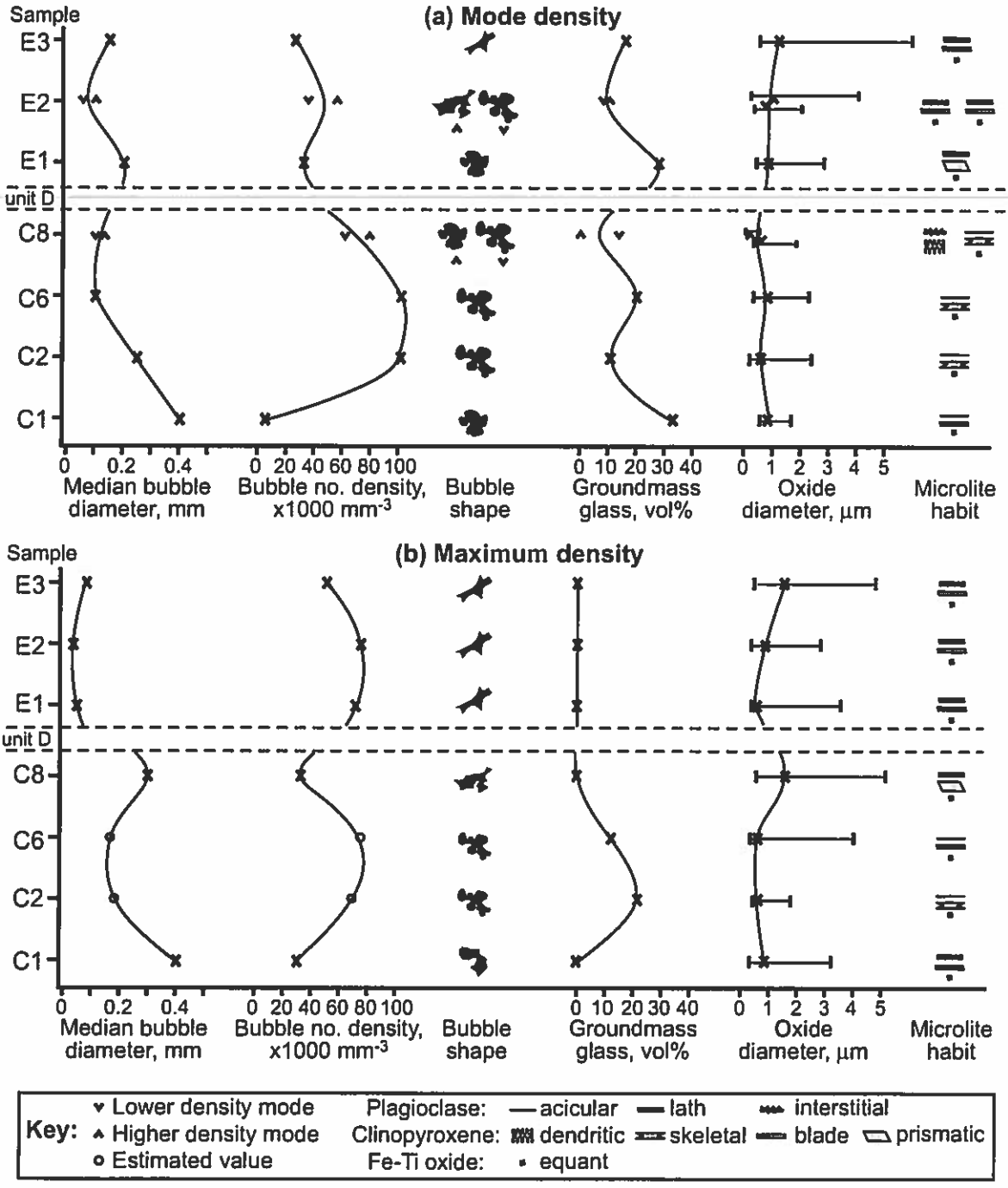

Figure 2.9 Summary diagram of bubble and crystal data for (a) modal and (b) maximum density clasts of units C and E. Only the most dominant bubble shapes and crystal habits are indicated; every clast has a range. For size of Fe-Ti oxide microlites, X marks typical size and bars indicate range. Open circles indicate estimated values that were not quantified as rigorously as the rest.

eruption temperature of 1100 K to the glass transition temperature, and the centers reach this temperature within 150 s (Hort and Gardner, 2000). This time interval is too brief for significant post-fragmentation crystallization to occur in clasts of this size.

Microlite nucleation rates cannot be estimated quantitatively with the available data. Crystal number density is not a foolproof indicator of nucleation rate for two reasons. Firstly, estimation of a rate requires a constraint on the time interval. The great textural heterogeneity in the Etna 122 BC magma near the point of fragmentation suggests different ascent histories for different parts of the magma. We cannot assume that the time available for crystallization was the same for all the magma, and thus we cannot assume that differences in crystal number density directly reflect differences in nucleation rate. For example, the relatively low number density of microlites in the mode and minimum density clasts of most of phase C (Table 2.3; Fig. 2.7a, b) could suggest a low nucleation rate, but they more likely reflect short residence time in the conduit. Secondly, the observed groundmass textures reflect the conditions for only the final stage of ascent before fragmentation. Other conditions may have prevailed earlier in the magma's history, but evidence of those earlier conditions may become obscured or overprinted by changes in the upper conduit. Experiments on analog materials show that the crystal texture of a rock can transform dramatically if the magma is held at a temperature near the solidus for some time (Means and Park, 1994). The time scale for such crystal ripening is days for a high-silica melt (Hammer and Rutherford, 2002) and probably much shorter for basaltic melts with lower viscosity and higher component diffusivity (Zhang and Stolper, 1991; Zhang and Behrens, 2000).

The patches of very small microlites common in the highly crystalline clasts probably represent a second stage of crystal nucleation at a high level in the conduit. The crystallites that impart a mottled look to the glassy matrix of more crystalline clasts are also interpreted as late-nucleating crystals that had a limited growth time. Taddeucci et al. (2005) observe evidence for a second microlite nucleation in clasts from Strombolian-style eruptions of Etna, and suggest that it was triggered by cooling during a long (hours to days) residence time in the conduit. The time scale for the 122 BC Plinian eruption was much shorter, so we suggest that if a second microlite nucleation did occur, it was triggered instead by exsolution of the last H_2O from the melt, possibly accompanying pressure drop due to the downward propagation of the fragmentation wave (Cashman et al., 2000).

If interpreted cautiously, crystal size may give some information about rates and timescales of crystal growth. Fe-Ti oxide microlites are likely to give the most reliable constraints because their growth rate is relatively insensitive to H_2O content. Assuming constant temperature throughout most of the magma's ascent, the main factor governing size of Fe-Ti oxide crystals is the time interval available for growth. The modal clasts from unit C share a relatively consistent range of crystal size (Fig. 2.9a). The size range is wider in the maximum-density clasts of phase C (Fig. 2.9b). In phase E, all clasts are dominated by relatively coarse (e.g. cpx up to 20 μm) microlites, and the textural contrast between modal and maximum density clasts is diminished. We infer that by the end of the second Plinian phase, all the remaining melt had resided in the conduit for a considerable time. A weakness of these interpretations is that they assume constant crystal growth rate, which is unlikely to apply to all the magma.

Crystal habit depends on the relative rates of processes such as diffusion of chemical components, diffusion of heat, and attachment of atoms to crystal surfaces (Kirkpatrick, 1981). Diffusion-controlled growth, associated with large degrees of undercooling and strong disequilibrium, produces spherulitic and dendritic crystal habits (Lofgren, 1974). Microlite habits characteristic of disequilibrium occur in the minimum and modal density clasts of all samples of Plinian phase C (Fig. 2.7a, b, c; Fig. 2.9a). Similar textures to these were observed in basalt crystallization experiments at undercoolings of 30-70°C (Lofgren, 1974). Modal clasts with high number densities of small crystals (Fig. 2.7e) are inferred to have experienced high nucleation rates and low to moderate growth rates, indicating high undercooling. The clast from the secondary density mode of sample C8 (Fig. 2.7c) has microlites with textures suggesting very fast growth, but nucleation rate is poorly constrained because the number density of the complex dendritic crystals cannot be determined reliably. Minimum density clasts with low number densities of acicular and skeletal crystals (Fig. 2.7b) are interpreted to have had high growth rates and either low nucleation rates (in which case the undercooling was moderately low) or very short residence times (associated with fast ascent and high undercooling).

Of the maximum density clasts, only samples C2 and C6 have microlites with disequilibrium habits, including acicular plagioclase and skeletal and elongate clinopyroxene (Fig. 2.9b). The rest of the maximum density clasts are dominated by more prismatic or tabular microlites that do not indicate such rapid diffusion-controlled growth. We infer that dense clasts with lower numbers of coarse subhedral crystals (Fig. 2.7d) experienced fairly high growth rates but low nucleation rates, indicating the lowest

degrees of undercooling over a prolonged interval. The maximum density clast of sample C8 has exceptionally large microlites with equant and euhedral habits, indicating slow growth in relatively steady conditions for at least the last portion of that magma parcel's history (Kirkpatrick, 1981).

Combined interpretations

Rapid ascent

The high bubble number densities indicate rapid bubble nucleation at high H_2O supersaturation. The small bubble sizes suggest that bubbles had limited opportunity to grow. The high number densities of microlites in most clasts of unit C suggest a dominance of crystal nucleation over growth, consistent with large degrees of undercooling. Disequilibrium microlite habits in many samples also suggest large undercooling. Due to the short time scale of ascent in the Plinian eruption, this undercooling is most likely induced by rapid devolatilization, rather than by conductive heat loss.

All of these interpretations indicate that the 122 BC magma was subjected to rapid decompression associated with rapid ascent. Coltelli et al. (1998) suggest that flank deformation induced sudden decompression, leading to a surge of bubble nucleation that propelled rapid ascent. Our microtextural data do not specifically support or disprove this hypothesis, and it is one viable cause of the high rate of bubble nucleation. Another possible cause arises from recent work on the primitive magmas of Etna's 2001 and 2002-03 flank eruptions, which are chemically similar to the 122 BC magma (Métrich et al., 2004). When melt inclusion analyses for several elements are combined and compared with models, the results suggest that the initial dissolved CO_2 is at least 1.5

wt%, much higher than previously thought (Papale et al., 2006; Spilliaert et al., 2006). Much of this CO_2 is lost through early open system degassing at depths of >9 km (Spilliaert et al., 2006). By analogy, we suggest that early formation of CO_2 bubbles could have accelerated the 122 BC magma upward by increasing the magma's volume and buoyancy. Sufficiently fast ascent could have led to supersaturation in H_2O. In this model, dehydration accompanying the CO_2 loss could have induced early microlite crystallization, increasing the H_2O concentration in the melt and further encouraging H_2O supersaturation. The presence of the microlites would also have increased the magma's effective viscosity, so that when H_2O exsolution occurred, the gas and melt would remain coupled.

Conduit residence time

Our microtextural results are consistent with Houghton et al.'s (2004a) preliminary interpretation, based on clast density distributions, that conduit residence time was a critical factor in creating a wide range of bubble and microlite textures in the 122 BC magma. Our detailed vesicle and microlite characterizations allow us to describe the effects of contrasting residence times throughout the eruption.

The modal density clast from sample C1 has an atypically low vesicularity for unit C and a low number density of coarse, widely spaced bubbles (Fig. 2.4a; Fig. 2.9a) that resemble textures in typical Strombolian scoria (e.g., Lautze and Houghton, 2005). We suggest that the melt ejected in the earliest stage of phase C had been in the conduit since the end of Strombolian phase A, and thus had time to develop relatively mature vesicle textures.

The high bubble number densities, small bubble sizes, and skeletal microlite habits that dominate samples C2 and C6 (Fig. 2.4b) support an interpretation of shorter conduit residence time and rapid bubble nucleation due to high rates of ascent and decompression. Microlite crystallinity generally increases through unit C, and the microlites in the modal clasts maintain a relatively constant average size with acicular and skeletal habits indicating rapid growth. Dense clasts from samples in the middle of unit C have relatively small, widely spaced bubbles with complex polylobate shapes. These characteristics could develop through an extended period of coalescence and gas loss. Sample C8, from the closing stage of phase C, features a sharp reduction in bubble number density and very complex bubble shapes in both modal density clasts and the high density clast, indicating advanced coalescence and outgassing (Fig. 2.4d; Fig. 2.9a). The groundmass textures of the dense clasts progressively diverge from those of the equivalent modal clasts through the sequence of samples C2-C8, suggesting an increasing contrast in residence time between the portions of melt represented by the two subsets of clasts.

Between samples C8 (end of phase C) and E1 (start of phase E), bubble size and spacing increase while number density and complexity of shape decrease (Fig. 2.4c versus Fig. 2.4e). This combination of changes is consistent with an interval of stable near-equilibrium conditions in the magma that allowed some bubble growth, substantial coalescence, and possibly some relaxation of shape. Also, microlites become larger and less skeletal between samples C8 and E1 (Fig. 2.7c versus Fig. 2.7e), suggesting a trend toward equilibrium crystal growth. We infer that at the end of the first Plinian phase, the

magma slowed until it was effectively stationary in the shallow conduit for minutes to hours during the weak phreatomagmatic phase D.

Groundmass textures appear generally similar throughout unit E, in contrast with the wide range of textures in unit C. We attribute this to the stagnation that affected all the magma in the conduit during phase D. The contrasts in groundmass texture that had developed during mid to late phase C became subdued as the phase E magma was homogenized during a period of near-equilibrium crystallization under uniform conditions. Bubbles appear more shrunken and pinched in later samples (Fig. 2.4f), suggesting increasing importance of bubble collapse with longer residence time.

Houghton et al. (2004a) suggest that the highest degrees of outgassing and crystallization occurred in an annulus of slow-moving magma along the margins of the conduit. This idea is compatible with well-known models of pipe flow. The nature of pipe flow depends on the Reynolds number, defined as $\mathrm{Re} = \rho VD/\mu$ where ρ is density of the fluid, V is mean velocity, D is pipe diameter, and μ is viscosity (Munson et al., 1990). For $\mathrm{Re} < 2100$, pipe flow is typically laminar and Poiseuille flow theory predicts a parabolic velocity profile with the maximum speed along the pipe's central axis. For $\mathrm{Re} > 4000$, pipe flow is turbulent, and the velocity profile is described by an empirical power-law relationship within certain limits (Munson et al., 1990). Intermediate Re numbers are associated with a transition between laminar and turbulent flow.

Assuming steady flow of a fluid with Newtonian rheology through a smooth cylindrical conduit, we estimate the maximum Re for the Etna 122 BC magma at two points: just after bubble nucleation but before significant bubble growth, and just before fragmentation (Table 2.4). Our maximum Re at depth exceeds 4000, indicating turbulent

flow. Higher in the conduit, the magma's effective viscosity increases with increasing microlite content (Pinkerton and Stevenson, 1992; Lejeune and Richet, 1995), and the Reynolds number drops below 200. In addition to the effect of microlites, the bubbles probably also increase the effective viscosity because they show no evidence of strain (Llewellin et al., 2002). Therefore the viscosities in Table 2.4 are minimum estimates, and we suggest that laminar flow is likely for most of conduit ascent. However, we recognize that we use simplifying assumptions and uncertain parameters, and that pipe flow commonly departs from ideal conditions (Kerswell, 2005), so the flow may approach the turbulent transition. Turbulent flow adds complications including a radial component to velocity that may lead to mixing and enhanced bubble interactions (H. Gonnermann pers. comm., 2006).

Laminar and turbulent time-averaged velocity profiles are shown in Fig. 2.10a. Both types of flow have slower-moving zones along the margins, with the important consequence that melt near the margins would have an extended conduit residence time, with the potential to develop more mature vesicle and microlite textures. Parcels of magma that travel through conduits with such velocity profiles yet fragment at the same moment must have traveled along different flow lines with different ascent rates, and experienced different degassing and crystallization histories (Fig. 2.10b). For example, melt that follows path 1 in Fig. 2.10 would be subjected to a shorter rise time and higher decompression rate and would produce more vesicular clasts, while melt that travels along the slower path 3 would experience a closer approximation to equilibrium degassing and crystallization and would produce clasts with more mature populations of crystals and bubbles. As the magma parcels rise to shallower depths, the differences in

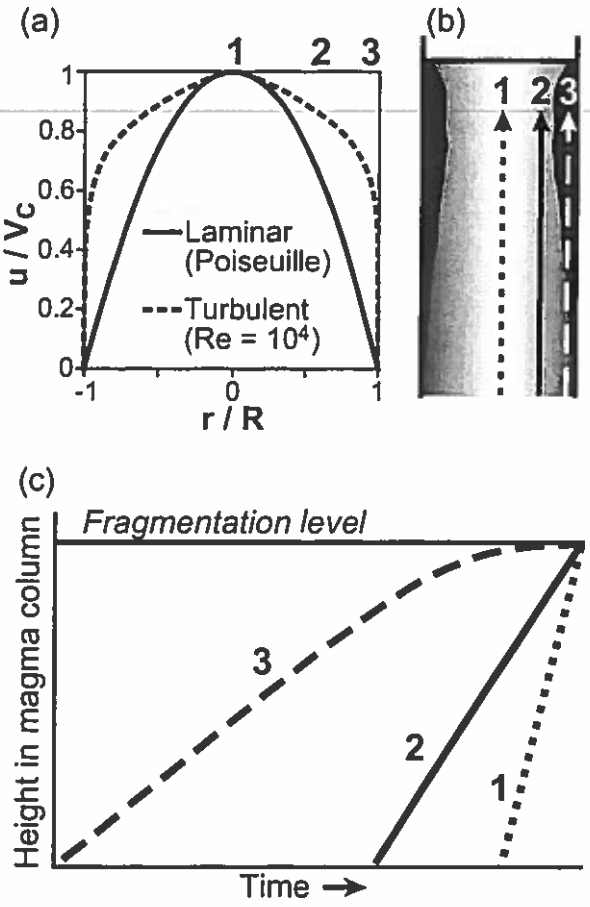

Figure 2.10 (a) Calculated and empirical velocity profiles for laminar and turbulent flow of a steadily flowing Newtonian fluid in a pipe, after Munson et al. (1990). (b) Cartoon of the upper conduit with faster moving magma in lighter gray and stagnant magma in black. (c) Schematic plot of height with time. Bold numbers 1, 2, 3 in each part of the figure indicate magma parcels following three idealized paths assuming laminar flow. Parcel 1 rises rapidly along the center and experiences the highest decompression rate. Parcel 2 rises more slowly and thus must have entered the conduit at an earlier time in order to be erupted simultaneously with 1. Parcel 3, having entered the conduit much earlier, rises relatively slowly and stagnates in the upper conduit, where it undergoes near-equilibrium degassing and crystallization before being ejected along with 1 and 2.

velocity and residence time between the axial (path 1) and marginal (path 3) zones increase, and textural contrasts also become more acute with time.

Table 2.4. Parameters relevant to the Etna 122 BC magma used in estimation of the maximum Reynolds number ($Re_{max} = \rho_{max} V_{max} D_{max} / \mu_{min}$) at two points in conduit ascent: just after bubble nucleation and just before fragmentation.

Early in ascent (just after bubble nucleation): $Re_{max} = 4860$		
Variable	Estimate	Justification
Density (ρ_{max})	2430 kg m^{-3}	Calculated for melt density of 2700 kg m^{-3} and 10% vesicularity
Velocity (V_{max})	1 m s^{-1}	Typical ascent rate (Rutherford and Gardner, 2000)
Conduit diameter (D_{max})	20 m	Common width of basaltic dikes
Viscosity (μ_{min})	10 Pa s	Hot crystal-free basaltic melt (Giordano and Dingwell, 2003a)
Late in ascent (just before fragmentation): $Re_{max} = 170$		
Variable	Estimate	Justification
Density (ρ_{max})	850 kg m^{-3}	Modal clast density at intensity maximum (sample C6)
Velocity (V_{max})	100 m s^{-1}	Maximum estimate (Papale et al., 1998)
Conduit diameter (D_{max})	20 m	Common width of basaltic dikes
Viscosity (μ_{min})	10^4 Pa s	Minimum viscosity of basaltic melt with 60% microlites (Pinkerton and Stevenson, 1992)

Narrative model for the Etna 122 BC eruption

The first activity in the 122 BC eruption (phase A) was Strombolian, not Plinian (Coltelli et al., 1998). Some of the magma involved in the Strombolian explosions remained in the conduit when the activity switched to weak phreatomagmatic explosions (phase B). The residual slow-rising magma was the first material to be ejected in Plinian phase C. The evidence for intensity fluctuations during early phase C suggests that coupling between the gas and melt phases may have been difficult to maintain (Fig. 2.11a). Eruption intensity stabilized at a maximum in the middle of phase C (Fig. 2.11b).

Assuming laminar flow, a parabolic velocity profile across the conduit caused a divergence in behavior between axial and marginal melt. Magma along the central axis maintained at least partially coupled degassing behavior and ascended too rapidly for much crystallization to occur, while material along the conduit walls moved slowly enough to permit significant crystallization, permeability development, and outgassing. As phase C continued, the contrasts between marginal and axial zones of the conduit became more pronounced, and the proportion of highly outgassed magma increased (Fig. 2.11c). The fragmentation surface was still dominated by the more gas-rich, less crystalline magma near the conduit axis, but a lesser and variable proportion of the fragmentation surface also intersected the more outgassed, crystalline melt along the margins.

As proposed by Houghton et al. (2004), stagnation and accumulation of magma along the conduit margins led to a reduction in the effective radius of the conduit in an extension of the model proposed by Wilson et al. (1995b) for Hawaiian explosions. The eruption intensity waned as the ongoing explosion was forced to remove increasingly

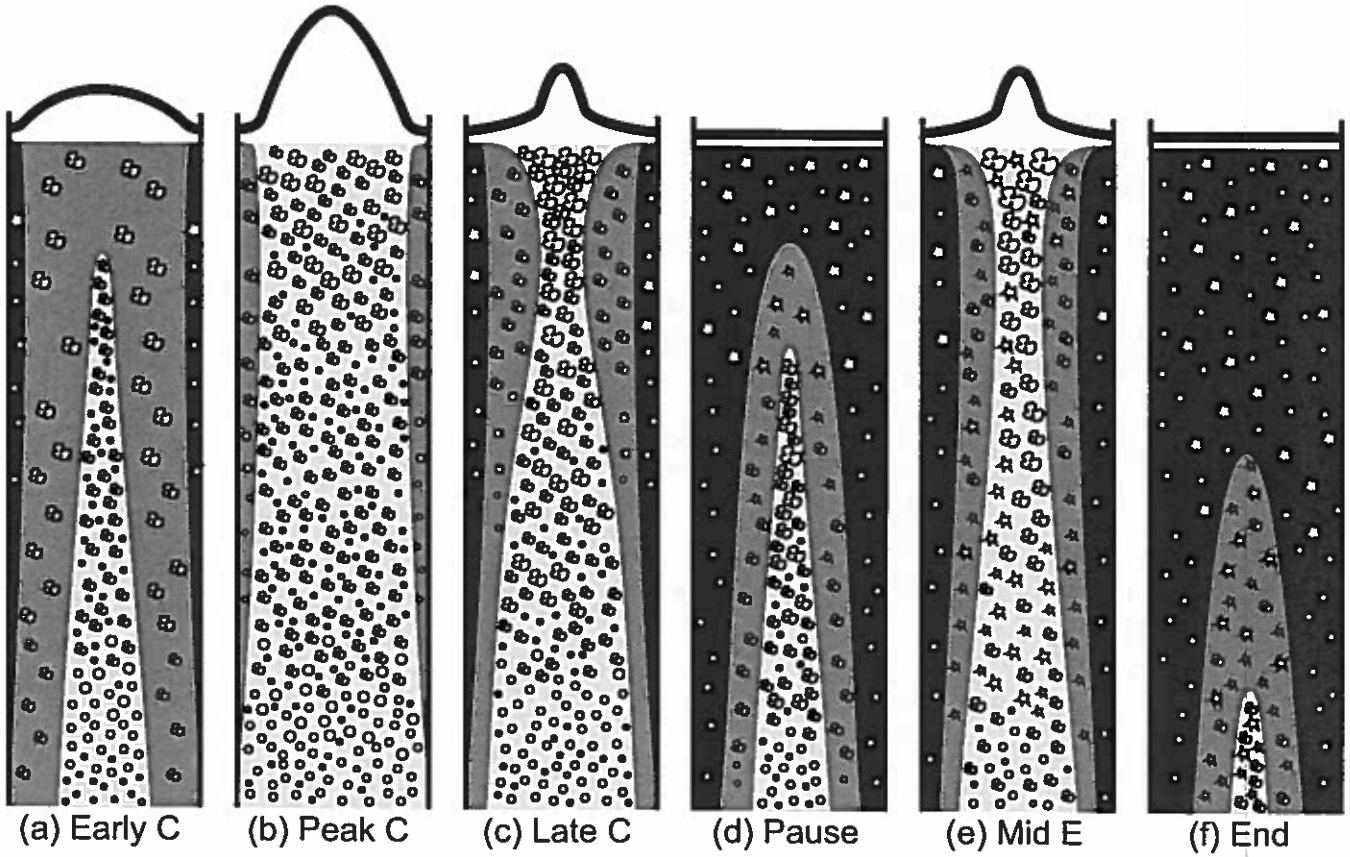

Figure 2.11 Cartoons depicting the conduit at different stages of the 122 BC eruption. Curved lines along top schematically represent laminar velocity profiles near the fragmentation surface. Lighter gray is less dense, more gas-rich magma; black is stagnant, degassed magma. Bubble shapes are drawn to represent extent of coalescence and collapse. (a) Early in phase C, slow-moving magma from the previous Strombolian phase was cleared out. (b) At the peak of C, almost the full width of the conduit was occupied by fast-moving, rapidly vesiculating magma. (c) Accumulation of stagnant material late in phase C led to (d) a pause in Plinian eruption (phase D). (e) Fast-moving magma reached the fragmentation surface again in phase E, but (f) the conduit quickly became blocked again, leading to the termination of the eruption.

large quantities of this obstructing material. Plinian phase C ended when the buildup of dense crystalline material reduced the conduit radius to the point that rapid ascent could not be sustained (Fig. 2.11d).

During the pause and the shallow phreatomagmatic explosions of phase D, the melt left in the conduit underwent additional bubble coalescence and collapse and microlite crystallization. This holding period reduced some of the textural differences that had developed across the conduit during phase C. Removal of the blockage was achieved by passive fragmentation with the aid of external water and/or by mingling with adjacent faster-moving material.

Plinian eruption resumed with the start of phase E, but because melt and gas were already decoupled to some extent in most of the magma, the processes of crystallization, outgassing, and stagnation took effect more rapidly and became more fully developed than in phase C (Fig. 2.11e). Finally, nearly all the magma was extensively outgassed, and the full width of the shallow conduit became blocked (Fig. 2.11f). This prompted a second switch to wet explosions (phases F and G), which were not followed by renewed Plinian eruption.

2.6 Conclusions

Data on pre-eruptive volatile content (Del Carlo and Pompilio, 2004) along with our microtextural evidence show that basaltic Plinian volcanism at Mt Etna in 122 BC was enabled by coupled degassing associated with high contents of CO_2 and H_2O and high rates of magma ascent, decompression, and bubble nucleation. Two possible causes for the rapid decompression that triggered Plinian activity are (1) a large and abrupt flank deformation causing unloading and an instantaneous conduit-wide decompression, or (2) an early nucleation of CO_2-dominated bubbles causing rapid ascent. In either case, the early fast decompression caused a high H_2O supersaturation in the melt and triggered very rapid nucleation of H_2O-dominated bubbles, leading to further acceleration of the magma. Early microlite crystallization probably increased the magma's effective viscosity and allowed coupled degassing to dominate in the most intense stages of the eruption. The next stage of this study will quantify ascent conditions through experiments in which samples of 122 BC melt are subjected to near-instantaneous, steady, and multi-stage decompressions.

The remarkable heterogeneity in bubble and groundmass textures found in a given stratigraphic interval shows that different processes became dominant in different portions of the magma following a shared initial history. We link this to a parabolic velocity profile across the conduit associated with approximately laminar flow. While bubbles continued to nucleate and grow in the rapidly ascending melt along the conduit axis, the slower melt along the conduit margins began to shift toward decoupled behavior, in which gas escaped upward and toward conduit walls through permeable networks of interconnected pore spaces. The marginal magma became increasingly

outgassed and crystalline until it stagnated along the walls of the upper conduit. Accumulation of this sluggish magma reduced the conduit diameter and caused the decline of each Plinian phase.

Acknowledgements

This research was supported by NSF grants EAR01-25719 and EAR-5-37459. The draft manuscript was improved greatly with the help of constructive reviews by Gary Barnes, Helge Gonnermann, Julia Hammer, Andy Harris, Don Swanson, and Jacopo Taddeucci. The field program was generously funded by the Istituto Nazionale di Geofisica e Vulcanologia.

CHAPTER 3

Complex proximal sedimentation from Plinian plumes: the example of Tarawera 1886

3.1 Abstract

The 1886 eruption of Tarawera, New Zealand, was unusual for a Plinian eruption because it involved entirely basaltic magma, occurred from a 17-km-long fissure, and produced extremely overthickened proximal deposits with a complex geometry. This study focuses on an 8-km-long segment cutting across Mount Tarawera where over 50 point-source vents were active during the 5.5 hour eruption. A detailed characterization of the proximal deposits is developed and used to interpret the range of styles and intensities of the vents, including changes with time. We identify the four vents that contributed most heavily to the Plinian plume and evaluate the extent to which current volcanic plume models are compatible with the depositional patterns at Tarawera.

Three proximal units are mapped that have phreatomagmatic, magmatic, and phreatomagmatic characteristics, respectively. Within the magmatic proximal unit, beds of like character are grouped into packages and delineated on scaled cross sections. Package dispersal is quantified by measuring the linear thickness half-distance ($t_{1/2}$) in the planes of the fissure walls. Most packages have localized dispersals (low $t_{1/2}$), indicating that Strombolian-style activity dominated most vents. The more widely dispersed packages (high $t_{1/2}$) reflect contributions from additional transport regimes that were more vigorous but still contributed considerable material to the proximal region.

We conclude that the geometry of the observed proximal deposits requires three modes of fall transport: (1) fallout from the upper portions of the Plinian plume produced principally by vents in four craters; (2) sedimentation from the margins of the lower portions of the Plinian plume including the jets and possibly the lower convective regions; and (3) ejection by weak Strombolian-style explosions from vents that did not contribute significant volumes of particles to the high plume. We suggest that the curvature of the velocity profile across the jet region of the plume (1-4 km height) was important, and that the lower velocity at the margins allowed proximal deposition of a large volume of material with a wide grain-size range.

3.2 Introduction

The 1886 eruption of Tarawera volcano in the Taupo Volcanic Zone was New Zealand's largest and most destructive historical eruption (Walker et al., 1984). This event was unusual in several ways. First, although the eruption involved exclusively basaltic magma, its main phase included intense sustained activity that is rarely associated with basalt, resulting in a >10,000 km^2 Plinian fall deposit (Thomas, 1888; Walker et al., 1984). Second, the eruptive source was a 17-km-long fissure (Fig. 3.1) formed by >50 vents in thirteen major craters across Mt Tarawera itself as well as an uncertain number of vents to the southwest at Rotomahana (Nairn, 1979; Nairn and Cole, 1981; Houghton et al., 2004a). Third, in addition to the Plinian sheet of scoria fall, the eruption produced strongly over-thickened proximal deposits on Mt Tarawera that form a series of half-cones on both sides of the fissure, visible in excellent exposures at sites extremely close (90-300 m) to vent (Houghton and Wilson, 1998). The geometry of the 1886 proximal

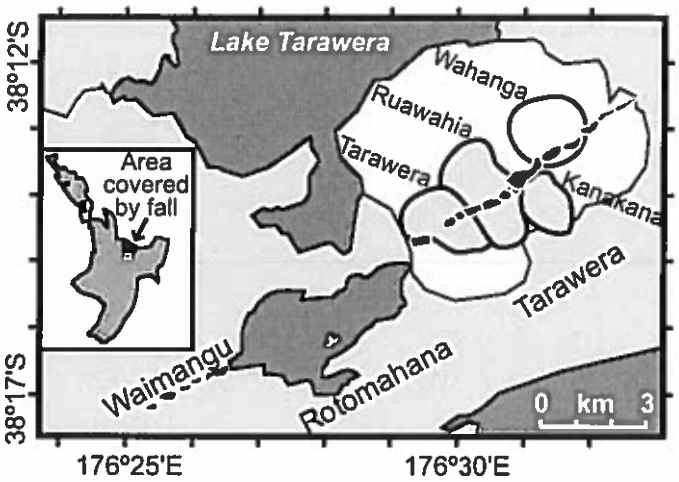

Figure 3.1 Location map with pre-1886 rhyolitic dome complex of Mt Tarawera outlined. The four main Kaharoa domes are labeled and the surrounding pre-Kaharoa lavas are a paler shade. Inset map shows the on-land distribution of the 1886 scoria fall in black, with white rectangle marking area of Tarawera map.

deposits is extremely complex and has consequent implications for the diversity of transport and deposition processes not only for the Tarawera eruption itself but also for Plinian plumes in general. Tarawera 1886 provides a valuable opportunity to study links between fall deposition close to vent and deposition in the far field.

Sedimentation from Plinian plumes

Well-established models divide Plinian plumes into three regions: momentum-driven jet, convective buoyant plume, and umbrella cloud (Sparks et al., 1997 and references therein). Deposition from the umbrella cloud is well-constrained; gravity current and advection/diffusion models provide good fits with field observations of medial-distal deposits (e.g., Carey and Sparks, 1986; Bursik et al., 1992; Sparks et al., 1992; Koyaguchi, 1994; Bonadonna et al., 1998; Bonadonna and Phillips, 2003). Less is understood about sedimentation from the jet and lower convective plume, and few have attempted to model it (Sparks et al., 1997). Bursik et al. (1992) and Ernst et al. (1996) proposed models of sedimentation from turbulent eddies at the margins of the jet and convective plume regions of the column, but the models predict that all particles smaller than a certain threshold (depending on column height) are re-entrained, resulting in near-vent deposits that are both limited in volume and coarse in grain size. We seek a model or combination of models that can account for additional complexities that we observe in the Tarawera 1886 deposits.

The Tarawera 1886 eruption: chronology and previous studies

The sequence of events in the eruption is detailed in eyewitness accounts (summarized in Keam, 1988). Key aspects are described here to provide a context for our study. On June 10, 1886, at 12:30 a.m., earthquakes were felt over a wide area, and this seismicity

intensified until eruption began about one hour later. Shortly after 2:00 a.m., ash columns were observed above two pre-existing lava domes on Mt Tarawera, identified by eyewitnesses as Wahanga and Ruawahia domes (Fig. 3.1; Williams, 1887). Activity spread both northeast and southwest to form an 8-km-long chain of 13 elongate craters separated by septae where the dikes did not break the surface (Nairn and Cole, 1981; Walker et al., 1984). Sustained eruption produced a curtain of fountains and a plume described as more than 10 km high (Keam, 1988). At 2:30 a.m. a second plume rose from a vent farther to the southwest, widely assumed to be due to initial explosions at Rotomahana (Fig. 3.1), a field of hot springs and fumaroles underlain by the same geothermal system that feeds the modern Waimangu field (e.g., Nairn, 1979). At 3:20 a.m. a severe earthquake occurred, probably marking the time when the active geothermal system at Rotomahana began to be disrupted violently by interaction between magma and superheated water (Houghton and Wilson, 1998). Activity then continued along the entire 17-km length of the eruption fissure until 6:00 a.m. (Williams, 1887). In contrast with eruptions at Mt Tarawera, the explosions at Rotomahana generated both a high liquid-water-rich plume and turbulent pyroclastic density currents composed of blocks, ash, and steam, which destroyed four villages (Nairn, 1979). Accumulation of fine damp ash on rooftops caused building collapses that accounted for most of the 108 known deaths (Keam, 1988).

Investigation of the events began immediately after the eruption and yielded a series of published reports (Smith, 1886a, 1886b; Hutton, 1887; Williams, 1887; Thomas, 1888). These workers recognized and mapped the widespread products of the eruption and documented the basic features that distinguish the deposits of the northeastern

portion of the fissure (Mt Tarawera) from those of the southwestern portion (Rotomahana-Waimangu). Thomas's (1888) map of the 1886 deposits is one of the first isopach maps ever published.

The modern phase of investigations at Tarawera began with detailed mapping by Cole (1970). Nairn (1979) studied the southwestern deposits, focusing on the dynamics of the pyroclastic density current phases. Nairn and Cole (1981) determined that the northeastern portion of the rift is divided into a series of right-stepping en echelon segments, each containing several source vents. Walker et al. (1984) produced the most comprehensive study to date, re-mapping the distal eruption products, subdividing the proximal stratigraphy into 5 units, and proposing that the widespread scoria fall was deposited in a late stage of exceptionally vigorous activity. Keam (1988) compiled and re-evaluated all relevant historical accounts to build a more accurate record of the chronology and social effects of the eruption.

This paper is part of a larger study that focuses on the northeastern part of the 1886 fissure because it hosted the Plinian activity (Walker et al., 1984). The first two publications of this study (Houghton and Wilson, 1998; Houghton et al., 2004a) re-interpreted the stratigraphy of and proposed a revised nomenclature for the proximal units, which we adopt in this paper (Table 3.1). The new unit 1 is the same as that of Walker et al. (1984), the new unit 2/3 is their units 2 and 3 combined, and the new unit 4/5 is their units 4 and 5 combined. Houghton and Wilson (1998) correlated the widespread fall deposits with all of proximal unit 2/3 and proposed that intense activity was sustained for most of the eruption's duration, rather than being restricted to a late

stage as in Walker et al.'s (1984) model. The third paper in the current study presents new grain size and componentry data for the three proximal units (Carey et al., 2006).

Table 3.1. General characteristics of the northeastern 1886 Tarawera deposits and comparison with the widespread fall deposits observed at medial-distal localities. Juvenile clasts were divided into five categories: fluidal, ragged, blocky, breadcrusted, and angular, and ranked in order of abundance for each unit. Grain size and sorting data are from Carey et al. (2006).

Unit	Juvenile clast morphology	Juvenile clast vesicularity	Wall rock content	Median grain size ϕ	Sorting $\sigma\phi$	Interpretation
Medial-distal	Ragged, blocky	Moderate-high	Moderate	-3.3 to +2.3		Plinian fall
Proximal I	Ragged, breadcrusted	Moderate-high	Moderate	-4.2 to -1.4	2.2 to 3.4	Initial phreato-magmatic
Proximal 2/3	Fluidal, ragged, blocky	Moderate-high	Low-moderate	-6.1 to -1.8	1.6 to 3.2	Main phase including Plinian
Proximal 4/5	Blocky, angular	Low	High	-3.4 to -1.1	1.2 to 2.1	Late-stage phreatomagmatic

Distribution and characteristics of the 1886 deposits

The southwestern portion (Rotomahana-Waimangu) of the 1886 eruptive fissure (Fig. 3.1) was the source for the fine-ash-rich deposits with common accretionary lapilli collectively called the Rotomahana Mud (Nairn, 1979). The southwestern deposits include localized pyroclastic density current deposits and a widespread fine-ash fall with a northerly dispersal that forms a significant component within the upper levels of the otherwise scoria-dominated 1886 fall deposits.

The northeastern portion of the fissure, which cuts the preexisting rhyolitic dome complex of Mt Tarawera (Fig. 3.1), differs from the southwestern portion in the nature of its activity and resulting deposits (Walker et al., 1984; Houghton and Wilson, 1998). The northeastern vents produced both sheet-forming and cone-building deposits of basaltic scoriaceous lapilli (Walker et al., 1984). The widespread scoria sheet covers an area of 6000 km^2 within the 2.5 cm isopach, and an estimated total area of 10,000 km^2, with a dispersal axis toward the northeast (Thomas, 1888; Walker et al., 1984). The large extent and low rate of thinning (b_t = 4.3 km after Pyle, 1989) qualify the deposit as Plinian, with an estimated column height of ~28 km (Walker et al., 1984). Median grain size of the widespread scoria fall decreases systematically with increasing distance, changing from -3.3 ϕ (1 cm) at 1 km to 2.3 ϕ (0.2 mm) at 40 km from vent; however, these values include up to 15% of the fine-grained Rotomahana Mud (Walker et al., 1984).

The cone-forming proximal deposits surround the 7-km-long Mt Tarawera portion of the rift and are confined to an area within 400 m of it. Complete sequences are well exposed along sub-vertical walls on both sides of the fissure. The proximal deposits are dominated by scoriaceous, phenocryst-poor, moderately to highly vesicular juvenile basalt (Walker et al., 1984). The minor wall rock component comprises fragments of rhyolitic lava and pyroclasts derived from shallow portions of the pre-existing dome complex. A distinctive feature in nearly all the basaltic pyroclasts is the presence of mm-sized rhyolite inclusions in abundances ranging from 1.1 to 3.6 wt % (Carey, 2002).

Table 3.1 summarizes characteristics of the proximal units. Unit 1 was produced during the relatively brief phreatomagmatic initial stage of the eruption and is rich in vesicular basalt clasts and rhyolitic wall rock fragments, the former occasionally with

denser outer rims indicative of rapid quenching (Houghton and Wilson, 1998). Unit 2/3, correlated with the widespread Plinian fall (Houghton and Wilson, 1998), is a moderately bedded red-black scoria fall deposit with alternating welded and non-welded subunits that thicken and thin along the fissure walls. At the top of the succession, unit 4/5 consists of rhyolitic wall-rock particles ranging from ash to blocks and subordinate dense juvenile basalt clasts, together with sparse Rotomahana Mud material. This unit is inferred to represent the closing phreatomagmatic to phreatic phase of the eruption (Walker et al., 1984; Houghton and Wilson, 1998). Grain size data for each proximal unit are shown in Table 3.1.

Questions and objectives

A number of key issues about the 1886 eruption remain unresolved, particularly about the dynamics of explosions along the northeastern, or Mt Tarawera, portion of the eruption fissure. The questions addressed in this paper include: (1) What was the range of styles and intensities present at different vents and different times? (2) Which of the >50 vents along the fissure contributed to the Plinian umbrella cloud(s)? (3) What plume model(s) can predict the variety of dispersals observed at Tarawera? Answers are sought through a detailed quantitative study of proximal deposit geometry. The results are compared with data from other deposits in order to infer a combination of transport mechanisms that best explains the observed range of styles and dispersals. This information ultimately will permit more realistic modeling of Plinian transport and deposition in the proximal environment.

3.3 Methods

Measurements of proximal deposit thicknesses come from 31 detailed stratigraphic sections as well as spot measurements at several locations obtained by lowering a tape measure vertically from the top of the fissure wall. The data were marked on color panoramas made from mosaics of ground-based photographs of the rift walls. The scaled photographs could then be used to interpolate thicknesses at points between measurement locations. Lateral distances were measured on the map or estimated from the scaled photographs. Isopachs were then drawn and closed using an assumption of symmetry around known vent locations. Some walls in craters A, B, C, G, and L were too inaccessible to be photographed or measured, so the data presented here are not continuous for the entire Mt Tarawera fissure.

Study of proximal packages

In a complex setting with multiple vents, isopach maps alone are insufficient to indicate the intensity of eruptions from the individual vents. To constrain the behavior of individual vents, we divide and describe the proximal deposits on a detailed scale. Our quantitative studies focus on unit 2/3 because it formed during the Plinian phase of the eruption (Houghton and Wilson, 1998).

The excellent exposures on the walls of the eruption fissure allow individual components of unit 2/3 to be delineated in the planes of the fissure walls (Fig. 3.3). For convenience of description, we define *packages* as groups of beds within a unit that share common characteristics of dispersal, grain size, componentry, and degree of welding. Packages were identified and mapped onto scaled photographic panoramas to create fifteen cross-sectional diagrams, eight of which are shown in Fig. 3.3. Each package is

labeled with the letter of the inferred crater of origin and a number. Packages on the southeastern walls are distinguished by a prime mark after the letter. Numbers are not meant to represent stratigraphic order or relative age and packages with the same number on opposite sides of a crater are not correlated. For example, H5 and H'5, on the northwest and southeast sides of crater H, respectively (Fig. 3.3f, g), were not necessarily deposited at the same time, nor were they necessarily derived from the same vent within crater H.

A useful parameter for describing and comparing deposit dispersals is the thickness half-distance (b_t; Pyle, 1989), the radial distance over which a deposit's thickness changes by a factor of two. Although thickness half-distance is typically calculated from isopach areas to reduce distortion due to asymmetric dispersal, the limited exposure perpendicular to the Tarawera 1886 fissure precludes estimation of isopach areas for individual packages. Instead, we measure *linear* thickness half-distance ($t_{1/2}$; Houghton et al., 2004b) in the planes of the crater walls. The $t_{1/2}$ values may be directly compared with b_t values (Pyle, 1989) from other deposits if it is assumed that the 1886 packages are radially symmetric. Even if the packages are not perfectly symmetric due to wind or varying ejection angles, the $t_{1/2}$ values are still useful for comparisons among Tarawera packages.

3.4 Results

Thickness trends of proximal units

First, bulk properties of the proximal deposits are described for the whole Mt Tarawera fissure. Fig. 3.2 shows isopach diagrams for the entire proximal deposit and for units 1, 2/3, and 4/5 individually. The total proximal deposit (Fig. 3.2a) is at least 10 and more typically >20 m thick almost everywhere along the fissure's edges, but thins rapidly away from the rift, decreasing to <10 m within 600 m of most of the inferred vent locations. Total thicknesses on the fissure walls range from 15 to 70 m and vary on an extremely local scale, such that thicknesses may change from 20 to 60 m within single crater segments over distances of tens to hundreds of meters (e.g., craters D, F, L; Fig. 3.2a). These variations are largely controlled by the thickness of unit 2/3, which makes up 90-95% of the total 1886 deposit at most sites. Thicknesses of individual units vary independently. For example, unit 1 is thickest at locations in craters D, J, and the northeastern corner of F (Fig. 3.2b), while the thickness maxima for unit 2/3 are in craters D, F, K, and L (Fig. 3.2c). Thickness patterns are asymmetric across the fissure for all proximal units.

The thickness of unit 1 (Fig. 3.2b) ranges from 0.5 m to 8 m along the fissure's edge, but at most locations its thickness is <2 m. Unit 1 is especially thick at locations in craters D, E, F, J, and K. In particular, at the northeastern edge of crater F, unit 1 thickens from 1 m to 9 m over a lateral distance of only 200 m. At this location, the contact between units 1 and 2/3 is clearly diachronous, suggesting that the influence of external water persisted longer at some sites than at others.

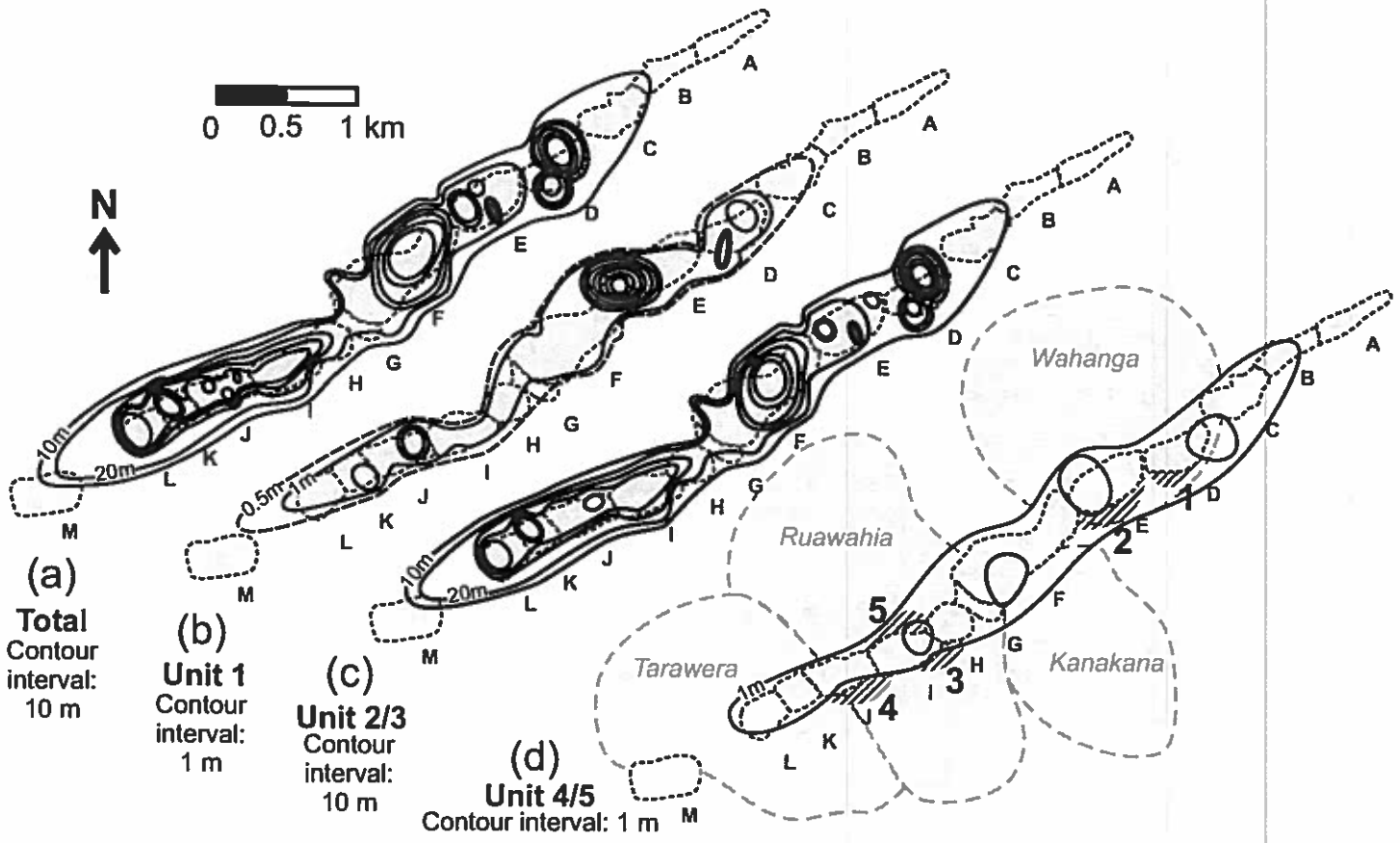

Figure 3.2 Proximal isopach maps for (a) total deposit, (b) unit 1, (c) unit 2/3, and (d) unit 4/5. Pale yellow indicates 1886 craters (fine dotted outlines). Contour intervals are indicated for each map. Craters are labeled with letters A-M. In (d), Kaharoa domes are marked with dashed outlines, and block aprons are shaded and numbered 1-5.

Unit 2/3 (Fig. 3.2c) ranges from <10 to 62 m thick along the fissure. The depositional pattern of unit 2/3 is more complex than those for units 1 or 4/5, with sharp changes in thickness observed between craters and even within some of the larger craters. For example, extremely localized accumulation characterizes the deposits in the northeastern end of crater D, where unit 2/3 thickens from 20 to 65 m over a lateral distance of 100 m. The other extreme is seen in craters H-J, where the thickness of unit 2/3 is uniformly 40-50 m over a distance of 700-800 m along the rift. The dramatic variations in total thickness of the 1886 products are largely controlled by the thickness of unit 2/3, the most voluminous proximal unit.

Unit 4/5 (Fig. 3.2d) is 1-2 m thick along most of the fissure, with minor anomalies in craters D, E, F, and I. The unit also includes several aprons of discrete 0.3-1.0 m diameter lithic blocks that extend ≤1 km outward from some craters (labeled 1-5 on Fig. 3.2d). The variably thick unit 4/5 is interpreted as the product of numerous relatively weak phreatomagmatic explosions during late-stage withdrawal of magma from the fissure.

Observations of proximal packages

No fine ash partings or erosional breaks are observed in the unit 2/3 deposits. Visible bedding within packages is formed by abrupt shifts in grain size and wall rock content or by contrasting welding states. Bedding planes dip mostly outward at moderate to steep angles. The deposits commonly mantle the pre-1886 topography, but in some places thicken to fill valleys (e.g., D1 and H7 in Fig. 3.3b, f). The upper and lower boundaries of packages are distinct over most of the length of each crater, but the lateral terminations of packages are not. Horizontally adjacent packages merge end-to-end with no clear

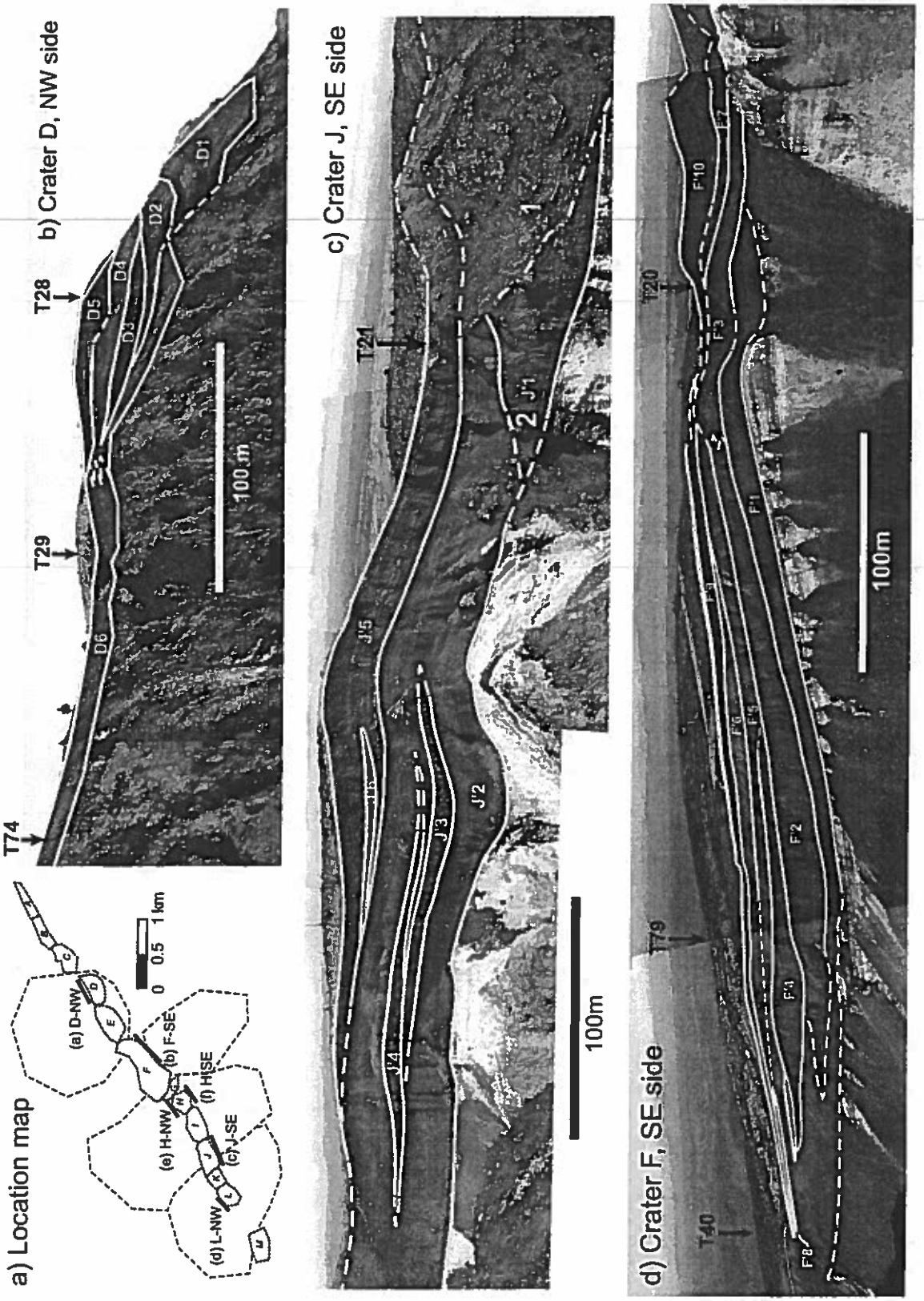

Figure 3.3 Sketches of package geometry for representative 1886 craters at Mt Tarawera. (a) Locations of lines of section; (b) northwest wall of crater D; (c) southeast wall of crater J; (d) southeast wall of crater F; continued on next page.

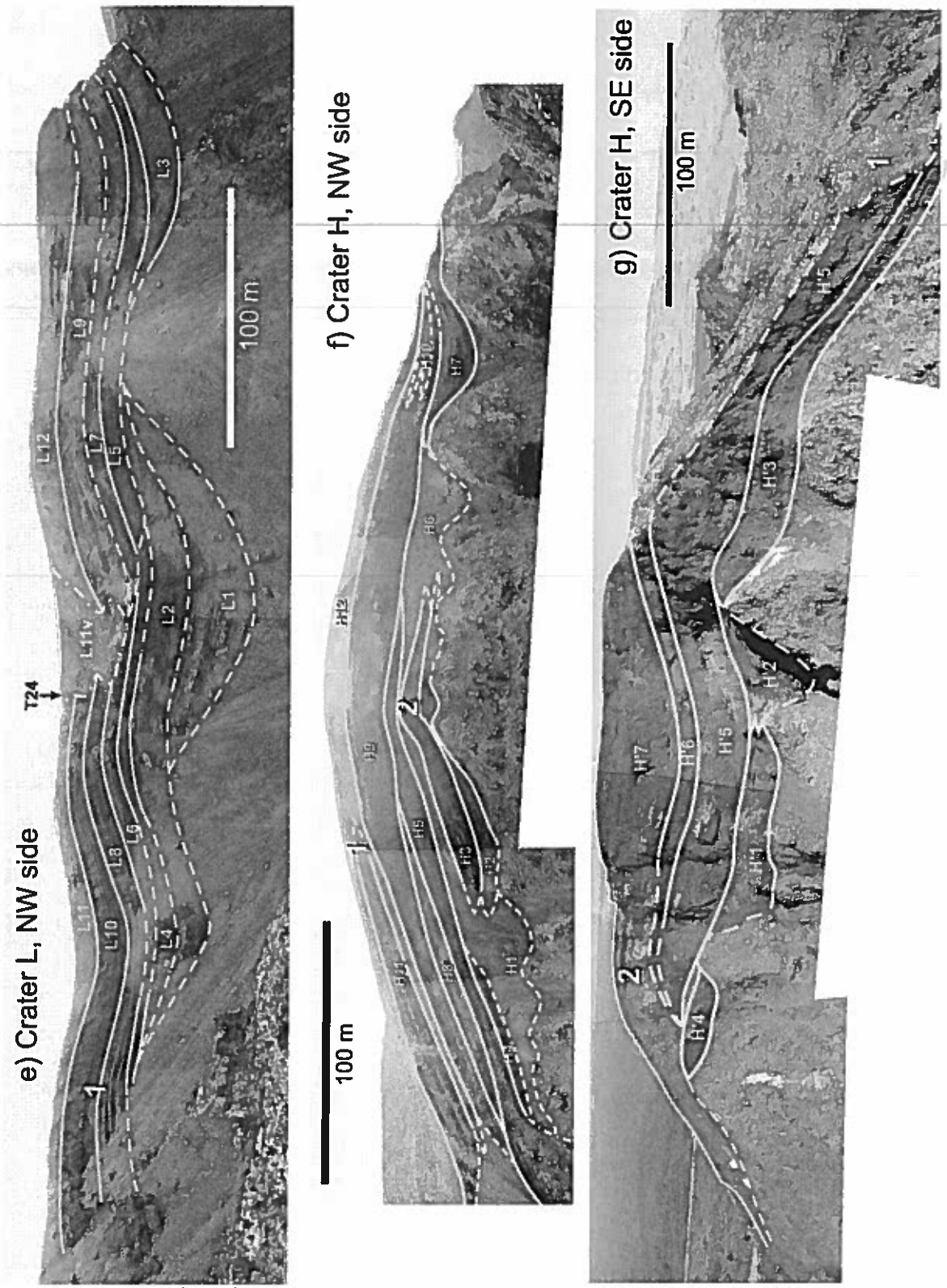

Figure 3.3 continued: (e) northwest wall of crater L; (f) northwest wall of crater H; (g) southeast wall of crater H. Locations of detailed stratigraphic sections are named and marked with arrows. Numbers refer to sites mentioned in the text. Thickness half-distance values for sections T28 and T79 are listed in Table 2.

boundary, indicating that neighboring vents erupted simultaneously with overlapping dispersals.

The majority of packages are confined within single craters, suggesting that most of the ejecta fell within tens to hundreds of meters of their parent vent(s). Package continuity is rarely maintained over the septae between craters. Exceptions are a few packages near crater ends that contain major proportions of material ejected from vents in adjacent craters (e.g., packages F'10 and L3 in Fig. 3.3d, e). Where deposits are uniform and non-welded, the crater walls have clean near-vertical faces with the best cross-sectional views. On the inter-crater septae, slopes are gentler and less regular. Tack-welded veneers of juvenile material commonly adhere to these surfaces, forming one or more irregular slope-parallel layers (e.g., points marked 1 on Fig.3.3c, g).

Package dispersals range from very localized, occupying only a narrow portion of a crater (e.g., package D1 in Fig. 3.3b), to widespread, spanning the full length of a crater and beyond (package J'2 in Fig. 3.3c). The more widespread packages are commonly higher in the stratigraphy (e.g., Fig. 3.3b, e, f, g). Exceptions to this rule occur in craters F and J (Fig. 3.3c, d), where even the basal unit 2/3 packages have large dispersals. Lateral color changes within packages are uncommon, but where they do occur (e.g., point 2 on Fig. 3.3g) they are gradational over tens of meters. The distinctness of bedding varies both horizontally (e.g., point 1 on Fig. 3.3f) and vertically (point 1 on Fig. 3.3e) along crater walls. Welded packages show lateral variations in their degree of welding, ranging from abrupt (e.g., point 2 on Fig. 3.3c) to gradational (point 2 on Fig. 3.3f). Welding is more common in locally dispersed packages (e.g., D5 in Fig. 3.3b), but strong welding does occur in a few very widespread packages (J'5 in Fig. 3.3c).

All craters show remarkable contrast between their northwestern and southeastern walls in characteristics such as dominant dispersal, grain size, color, and welding state. For example, in crater F, while the southeastern wall (Fig. 3.3d) is composed mostly of red nonwelded scoria with very wide dispersal, the northwestern wall is dominated by localized packages with dark color and strong welding. The asymmetry prevents packages from being traced or correlated across the fissure.

Dispersal variations are shown quantitatively in a plot of linear thickness half-distance measurements for 153 packages along the fissure (Fig. 3.4). A wide range of $t_{1/2}$ values is common in most craters. Nearly every crater contains one or more packages with $t_{1/2} \leq 20$ m (Fig. 3.4), similar to the equivalent $t_{1/2}$ values of recent Strombolian and Hawaiian cones (e.g., Richter et al., 1970; Heliker et al., 2003). Most craters also have more widespread packages, including a few packages with half-distances exceeding 150 m (Fig. 3.4). In some craters two or three separate packages are observed at equivalent stratigraphic heights (e.g., packages F'2 and F'3 on Fig. 3.3d), each with a distinct $t_{1/2}$ value.

Dispersal extremes: observations at selected sections

Several craters are dominated by packages with a narrow range of dispersals. Localized packages dominate craters D and E, and widespread packages dominate craters F, H, J, and L. We expand on our general description with more detailed observations at sites that typify these dispersal extremes.

A representative section for the localized extreme is T28 on the northwestern wall of crater D (Fig. 3.3b), where all packages are localized, with $t_{1/2}$ between 20 and 35 m (Table 3.2). Many beds within the packages show various degrees of agglutination,

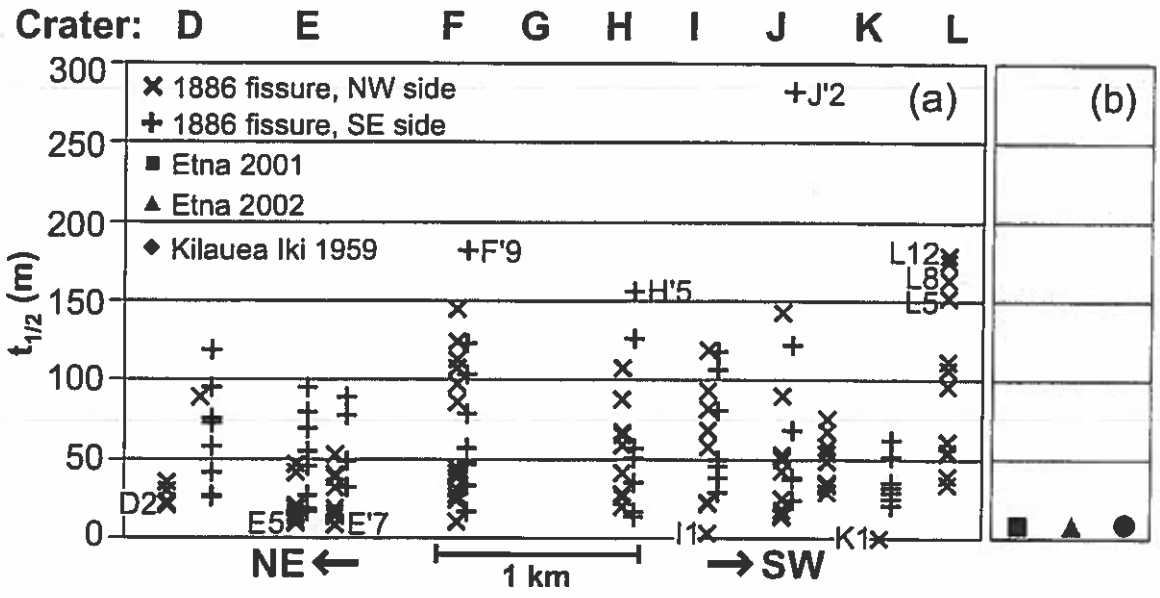

Figure 3.4 (a) Summary of linear thickness half-distance ($t_{1/2}$) values for individual packages within the 1886 proximal deposits, with different symbols for the two sides of the fissure. Crater names along the top are spaced according to the positions of their deepest portions along the fissure. Packages with extreme $t_{1/2}$ values are labeled. (b) Half-distances of three historical cones formed by Hawaiian and Strombolian explosions are shown for comparison.

ranging from weak tack welding to moderately strong welding where clasts adhere firmly to each other but still have distinct boundaries. Clasts of glassy, coarsely re-vesiculated rhyolite are commonly found encased in basalt. Basalt clasts generally have a red oxidized color. The grain size is coarse, and sorting is moderate to poor due to the abundance of ash-sized wall-rock particles; quantitative grain size analyses are presented in Carey et al. (2006). Basalt clast morphologies are typically ragged, slaggy, and knobbly. The wall-rock lithic content is typically 5-15% and rarely up to 40%, ranging in size from ash to 20-30 cm blocks and rare 1 m blocks.

Table 3.2. Thickness half-distance measurements for packages at stratigraphic sections T28 and T79. Sections were selected because they represent the dispersal extremes for the proximal deposits.

Crater D, NW side		Crater F, SE side	
Package	$t_{1/2}$, m	Package	$t_{1/2}$, m
		F'9	123
D5	23	F'6	126
D4	22	F'5	181
D3	30	F'4	33
D2	20	F'2	103
D1	35	F'1	182

A characteristic example of the opposite extreme is section T79 in crater F (Fig. 3.3d), where four of the six packages have $t_{1/2}$ > 100 m (Table 3.2). Packages are typically non-welded and massive to weakly bedded. The grain size ranges from coarse ash to 10-20 cm bombs, but is dominated by fine to coarse lapilli. Wall-rock lithic content is 5-20% in the form of ash and scattered blocks. Juvenile clasts are commonly red to brown, with ragged, knobbly or blocky morphologies. Some dense cauliflower bombs are present, along with a minor proportion of slaggy clasts.

3.5 Interpretations

Accumulation rates of the 1886 deposits

Time-averaged accumulation rates during the Plinian portion of the 1886 eruption can be estimated by dividing unit 2/3 thickness values at the crater rims by an assumed duration of 5 hours (Keam, 1988; Houghton and Wilson, 1998). The minimum thickness is 7.4 m and the maximum is 65.5 m (Fig. 3.2c), giving time-averaged accumulation rates ranging from 1.5 to 13 meters per hour.

Accumulation rates over shorter timescales can be interpreted qualitatively in greater detail from the degree of welding in the deposits (Sparks and Wright, 1979). The rates varied among vents and fluctuated with time. There does not appear to be a simple relationship between accumulation rate and intensity; packages with similar degrees of welding may have $t_{1/2}$ anywhere between 5 m (e.g., package H7 in Fig. 3.3f) and 100 m (L10 in Fig. 3.3e).

The accumulation rates for several non-welded packages are above the suggested minimum rates for welding (e.g., 2-12 m/h; Sparks and Wright, 1979). To explain the

absence of agglutination, we consider factors that might have reduced the temperature of the ejecta before landing. The non-welded packages may contain an abundance of clasts sedimented from upper levels of the plume whose longer transport times allowed greater cooling. Greater release heights are expected to result in wider dispersals (e.g., Sparks, 1986; Sparks et al., 1997), so this idea is most compatible with the packages with large $t_{1/2}$ values. However, many non-welded packages are observed to have $t_{1/2}$ values of less than 50 m. Two alternative cooling influences could be (1) a higher content of originally cold particles of rhyolitic wall rock, or (2) some minor degree of magma-water interaction, similar to that proposed for the Tarawera Plinian phase by Walker et al. (1984) and Houghton and Wilson (1998).

Temporal and spatial variations in eruptive behavior

The wide range in thickness half-distance values signifies a wide range of eruptive intensities in each crater. Low-intensity vents were common in all craters, but this did not preclude the presence of higher-intensity vents in close proximity. In some craters, packages with very different characteristics are laterally juxtaposed at identical stratigraphic levels. This indicates that vents less than 100 m apart were active simultaneously with contrasting eruptive styles and intensities.

The minimum time-averaged discharge rate for the 1886 eruption is 1×10^5 m^3/s (3.9×10^4 m^3/s DRE), calculated by dividing the estimated total volume (2×10^9 m^3; Walker et al., 1984) by the duration (5 hours; Walker et al., 1984; Keam, 1988). In detail, the proximal packages indicate significant variations with location and time in each of the 13 craters. The range of inferred discharge rates in single craters commonly spans at least an order of magnitude. For example, crater F (Fig. 3.3d) shows a high

average intensity but also contains packages consistent with much less vigorous vents that may have been active only briefly. The converse is also observed, where a crater dominated by weak activity also bears evidence of an interval of intense eruption (e.g., crater E).

The temporal variations in eruptive intensity at each vent can be interpreted qualitatively, but not enough variables are constrained for more precise characterization. The changes with time in two craters at opposite dispersal extremes are illustrated schematically (Fig. 3.5). Vent locations are inferred to be in the deepest parts of craters and opposite the thickness maxima of the packages produced by the vents. Relative eruption intensities are interpreted from package thickness half-distances; accumulation rates are inferred from observed degrees of welding; timings are interpreted from positions in the stratigraphy; and durations are estimated from package thickness, adjusted for differences in accumulation rate.

At the earliest stage of the eruptive phase that produced proximal unit 2/3, two vents were active in crater D, one at the crater's northeast end and one slightly southwest of the crater's center (Fig. 3.5a). Activity at the northeastern vent was quite weak, but the accumulation rate fluctuated greatly and at times was high enough to promote agglutination of clasts. The southwestern vent erupted with greater intensity and lower, less variable accumulation rate, so its deposit (package D6) is more widespread, less welded, and more uniform. Activity at the northeastern vent waned and then ceased midway through the main phase, but the southwestern vent was active nearly to the end of the phase. At approximately the same time that the vent at the far northeastern end of crater D expired, another vent became active just northeast of the crater's center (Fig.

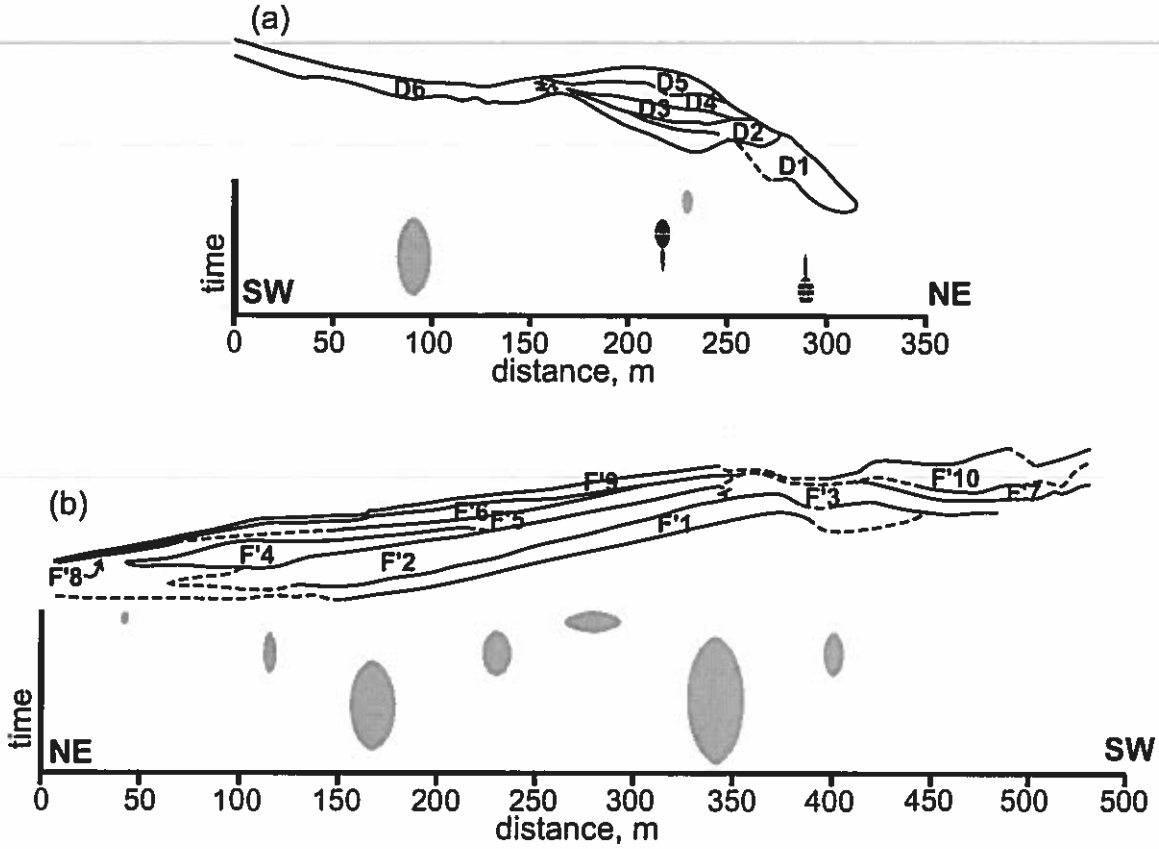

Figure 3.5 Diagrams showing changes in vent position and behavior with time for (a) northwest wall of crater D and (b) southeast wall of crater F. Width of symbol signifies intensity. Shade indicates accumulation rate (black is high, lighter gray is low). Distances in meters; time axis is not quantitatively constrained. Note that there is no one-on-one correspondence between number of vents and number of packages. Source of package F'10 is believed to be located in the NE end of crater G, and is thus not shown in this diagram.

3.5a). This central vent's maximum intensity was comparable to that of the far northeastern vent. After a brief period of consistently weak activity, the vent shifted about ten meters to the northeast and resumed activity at a slightly weaker level, then finally stopped. We infer this shift based on the observation that the upper packages on the northwestern side of crater D are offset toward the northeast. The shift may have involved the death of one vent and the birth of a new one nearby. Alternatively, the offset packages may all originate from the same vent but may have been affected by a change in ejection angle.

In crater F (Fig. 3.5b), vents erupted with relatively high intensity from the beginning of the phase that produced proximal unit 2/3. Material was first ejected from a vent slightly southwest of the center of this elongate crater. This vent had a high intensity and was long-lived, producing package F'1 and contributing to packages F'2, F'3, F'5, and F'9. Shortly after the first vent became active, a second one started about 150 m northeast of it (Fig. 3.5b). It was also intense and long-lived. Later on in this eruptive phase, a few weaker vents began to contribute some localized material, starting at roughly the same time that activity at the more intense vents was waning. The relative timing of the initiation of the weaker vents and the termination of the more intense vents is uncertain, so it is unclear whether the shifts in activity are causally related. The main phase in crater F closed with a final burst of relatively intense activity from a vent near the crater's center.

Some of the divisions between packages in proximal unit 2/3 resemble bedding planes; this raises the question of whether the Plinian eruption was discontinuous, with locally dispersed packages accumulating during pauses in activity at the more intense

vents. Walker (1980) showed that pauses or periods of reduced intensity in an eruption can be marked by fine-grained beds, bedding planes, or ash partings, if the interval of decreased activity is longer than the transport time for lapilli and bombs. In the Novarupta 1912 Plinian deposits, Houghton et al. (2004b) observed bedding planes within but not beyond 10 km from vent. They calculated the maximum time for 5 cm pumices to travel that far, and concluded that the eruption never paused longer than 15 minutes.

We apply the same chain of reasoning to the Tarawera 1886 deposits. Ash partings are absent and lapilli with ≥2 cm diameter are present in every level of the deposits within 12 km from vent. The average density of Tarawera juvenile clasts is ~1000 kg m^{-3} (Carey et al., 2006). The time to rise to the top of a 28 km plume is ~250 s (Walker et al., 1984; Hort and Gardner, 2000). The time for particles to travel 12 km laterally within the umbrella cloud is estimated to be 200 s, based on umbrella cloud models (Sparks, 1986; Bonadonna and Phillips, 2003) and observed propagation speed of the Mt St Helens ash plume front (Sarna-Wojcicki et al., 1981). The fall time from the umbrella cloud is 750 s (Wilson, 1972). This sums to a total travel time of 20 minutes for a 2 cm lapillus. We conclude that during the main (unit 2/3) phase of the eruption, the Plinian plume never stopped for longer than ~20 minutes, although individual vents may have started and stopped activity at different times within that duration.

The cessation of intense activity cannot be precisely correlated among craters due to local variations in accumulation rate. Magma withdrawal accompanying the transition to the weaker final phreatomagmatic (unit 4/5) phase was associated with vent wall collapse. The outward dip of beds along most of the fissure is a result of late-stage

faulting and slumping during and after the deposition of phreatomagmatic unit 4/5, such that nearly all the inward-dipping inner-wall beds are gone. In some areas, collapse was relatively gradual and progressive, resulting in angle-of-rest slopes. At other locations, the walls remained stable throughout the main phase, but when the magma retreated, large segments of the walls failed, leaving near-vertical surfaces. The slope-parallel tack-welded veneers of juvenile material covering several slopes were probably generated in the closing stage of the eruption. Ejecta from weak explosions adhered best to the scarp surfaces with the gentlest slopes.

Asymmetry across the fissure

The asymmetry in deposit characteristics across the fissure may be partially explained by the influence of wind on the plume. For the first half of the eruption, the wind blew toward the north, across the fissure. We envision that, at this time, the peak of downwind accumulation of material from the upper convective region of the Plinian plumes was displaced outward, beyond the very proximal area. In contrast, clasts released from lower heights, such as ejecta from weaker vents, were less affected by wind and concentrated immediately downwind from source in a manner described for the Pu'u 'O'o and Kilauea Iki eruptions (Richter et al., 1970; Heliker et al., 2003). In craters that hosted intense activity starting early in the eruption, this combination of wind effects would result in packages of more limited apparent dispersal on the downwind (northwestern) side of the fissure. Observations in craters F, H, and J are consistent with this idea (Figs. 3, 4). Another source of the cross-fissure asymmetry, considered in the discussion, is uneven sedimentation associated with heterogeneities in the jet portion of the plume.

Locations of Plinian vents

Our detailed study of package dispersals has illuminated patterns of eruptive intensity in several craters. Most craters are dominated by low-intensity vents. Sporadic high-intensity activity occurred in several parts of the fissure, but truly sustained intense activity was restricted to only a few locations. Four craters are dominated by widespread packages: F, H, J, and L (Fig. 3.3c, d, e, f). Vents within these craters are the most likely locations for the high-intensity sources that fed the Plinian umbrella cloud.

The four intense sources did not necessarily start and stop at the same time. Widespread packages typically occur in the middle to upper levels of the unit 2/3 stratigraphy, suggesting that eruption intensity increased with time over most of the fissure. However, craters F and J have widespread packages at the base of unit 2/3, and we interpret that high-intensity vents in these craters began erupting very early in the eruption and maintained their high intensities through the full duration of the main (unit 2/3) phase. Thus it seems that the early high column was mostly fed from vents in craters F and J.

Comparison with cone-forming deposits

To develop an appropriate model for the dynamics of the 1886 eruption, we examine current plume models and consider our package dispersals and accumulation rates in a global context. Table 3.3 presents published heights, durations, and accumulation rates for some historical cone-forming eruptions that lacked Plinian phases. The eruptions include Strombolian (e.g., Pacaya 1981; McClelland et al., 1989), Hawaiian (e.g., Kilauea Iki 1959; Richter et al., 1970), "violent Strombolian" (e.g., Paricutin; Cashman et al., 2004), and subplinian (e.g., Asama 1783; Yasui and Koyaguchi, 2004) examples.

Average accumulation rates were calculated from cone height and total eruption duration, and maximum accumulation rates for shorter intervals were recorded by observers during some of the eruptions. The average accumulation rates for most of these eruptions are an order of magnitude lower than the 9-13 m/h calculated for the selected Tarawera 1886 sites. Even the maximum accumulation rates of the other examples are typically only 1-3 m/h. The relatively high rate of 6 m/h for Oshima 1986 was associated with unusually vigorous Hawaiian-style fountaining (Sumner, 1998).

We have calculated approximate linear thickness half-distances from the dimensions of the cones in Table 3.3. Each cone's $t_{1/2}$ represents an average dispersal over the whole cone-forming eruption (individual beds cannot be identified). The $t_{1/2}$ values for the Hawaiian-Strombolian cones range between 6 and 30 m. Of the 154 Tarawera packages that were measured, 45 have $t_{1/2}$ values in this range, including the five at section T28 (Table 3.2). This confirms that some packages are dominated by clasts from weak explosions analogous to the historical cone-building eruptions. The maximum heights reached by these clasts could have ranged between 250 and 700 m, by comparison with measurements of historical lava fountaining eruptions (Table 3.4). However, many Tarawera packages have significantly wider dispersals: 50% of packages have $t_{1/2}$ values over 50 m, and 18% have $t_{1/2} > 100$ m, with a maximum of 283 m (crater J; Fig. 3.3c, Fig. 4).

Table 3.3. Parameters for several cone-forming eruptions. The Tarawera $t_{1/2}$ data are averages over the packages at each of two stratigraphic sections. Average accumulation rates are calculated from cone height and time in eruption (quiescent intervals are not included). Maximum accumulation rates measured over shorter time intervals are indicated where available. Most of the deposits are listed by Riedel et al. (2003). References: 1) this paper; 2) Yasui and Koyaguchi (2004); 3) Calvari and Pinkerton (2004); 4) Andronico et al. (2005); 5) Sumner (1998); 6) Richter et al. (1970); 7) Heliker et al. (2003); 8) SEAN (1988); 9) McClelland et al. (1989); 10) Bullard (1947), Foshag and Gonzales (1956); 11) Fedotov et al. (1978), Tokarev (1983); 12) Fedotov et al. (1978).

Eruption	$t_{1/2}$	Final cone height, m	Time in eruption, hours	Average acm. rate	Max. acm. rate
Tarawera 1886 (T28)[1]	26 m	65 m	5 h	13 m/h	
Tarawera 1886 (T79)[1]	171 m	46 m	5 h	9 m/h	
Asama 1783[2]	35 m	70 m	1440 h	0.05 m/h	3.3 m/h
Etna 2001[3]	8.2 m	62 m	288 h	0.2 m/h	
Etna 2002[4]	8.0 m	150 m	816 h	0.2 m/h	
Oshima 1986[5]	33 m	40 m	7 h	6 m/h	
Kilauea Iki 1959[6]	9.7 m	50 m	864 h	0.06 m/h	
Kilauea (Pu'u 'O'o) 1983-86[7]	34 m	255 m	1128 h	0.2 m/h	2.0 m/h
Lonquimay (Navidad) 1988[8]	17 m	210 m	240 h	0.9 m/h	2.1 m/h
Pacaya 1981[9]	23 m	148 m	672 h	0.2 m/h	3.0 m/h
Paricutin 1943-44[10]	14 m	324 m	1800 h	0.2 m/h	3.0 m/h
Tolbachik (cone I)1975 [11]	21 m	330 m	528 h	0.6 m/h	4.7 m/h
Tolbachik (cone II) 1975[12]	12 m	270 m	720 h	0.4 m/h	2.1 m/h
Tolbachik (cone III) 1975[12]	6.1 m	140 m	240 h	0.6 m/h	2.3 m/h
Veniaminof 1983[9]	29 m	150 m	168 h	0.9 m/h	

Table 3.4. Average and maximum fountain heights for four Hawaiian eruptions and one subplinian eruption (Oshima) that featured Hawaiian-style fountaining. References: 1) INGV (2001); 2) INGV (2002); 3) Richter et al. (1970); 4) Heliker et al. (2003); 5) Sumner (1998).

Eruption	Average fountain height	Max height
Etna 2001[1]	250 m	250 m
Etna 2002[2]	270 m	500 m
Kilauea Iki 1959[3]	230 m	670 m
Pu'u 'O'o 1983-86[4]	270 m	470 m
Oshima 1986[5]	500 m	1600 m

To determine the exact style of activity at Tarawera's weakest vents, we revisit section T28, because the site is overwhelmingly dominated by localized packages (average $t_{1/2}$ = 26 m; Table 3.2). The clasts in the T28 packages are red, oxidized, ragged, and blocky. Clasts do not have highly fluidal shapes or glassy rinds as would be expected in products of Hawaiian fountains (Heiken and Wohletz, 1985). Lithic content at T28 ranges averages 17% (Carey et al., 2006), much higher than typical for Hawaiian lava fountains (e.g., less than 1% for Kilauea Iki 1959; B. Houghton, unpublished data). The deposits are bedded, suggesting intermittent explosions. We thus conclude that the style of the weak vents was Strombolian.

Comparison with Plinian deposits

Suitable comparisons between the Tarawera 1886 deposit and other Plinian deposits are limited, because very few Plinian deposits exist with exposures so close to vent. One Plinian deposit where proximal products are preserved is from the andesite-dacite eruption of Novarupta 1912 (Fierstein and Hildreth, 1992; Fierstein et al., 1997; Houghton et al., 2004b). The very proximal (<1 km from vent) ejecta ring at Novarupta grew within a ~24-hour interval (Fierstein et al., 1997). The ejecta ring's thickness ranges up to 250 m, giving average accumulation rates up to 10 m/h. This value fits within the range of accumulation rates calculated for Tarawera, suggesting that the plumes in these two eruptions may have behaved similarly. The model that we will propose includes some features from that of Fierstein et al. (1997), adapted to a basaltic system for Tarawera 1886.

The dispersals of the Tarawera 1886 deposit and other Plinian deposits are compared on a plot of log thickness vs. square root of area (Fig. 3.6; Pyle, 1989). The extent of the Tarawera 1886 deposit appears limited compared to the other Plinian deposits only because much of the 1886 fall landed in the ocean (Walker et al., 1984). The 1886 proximal and medial-distal deposits have thickness half-distances (b_t calculated from isopach areas after Pyle, 1989) of 0.05 km and 4.3 km, respectively, showing that the proximal deposits have a much greater rate of thinning. The best-fit exponential curves intersect at 0.53 km on the square root of area axis (Fig. 3.6), equivalent to a distance of 300 m from vent. This is approximately consistent with field observations of a change from steeper to gentler slopes 300-400 m out from the edges of the Mt Tarawera rift.

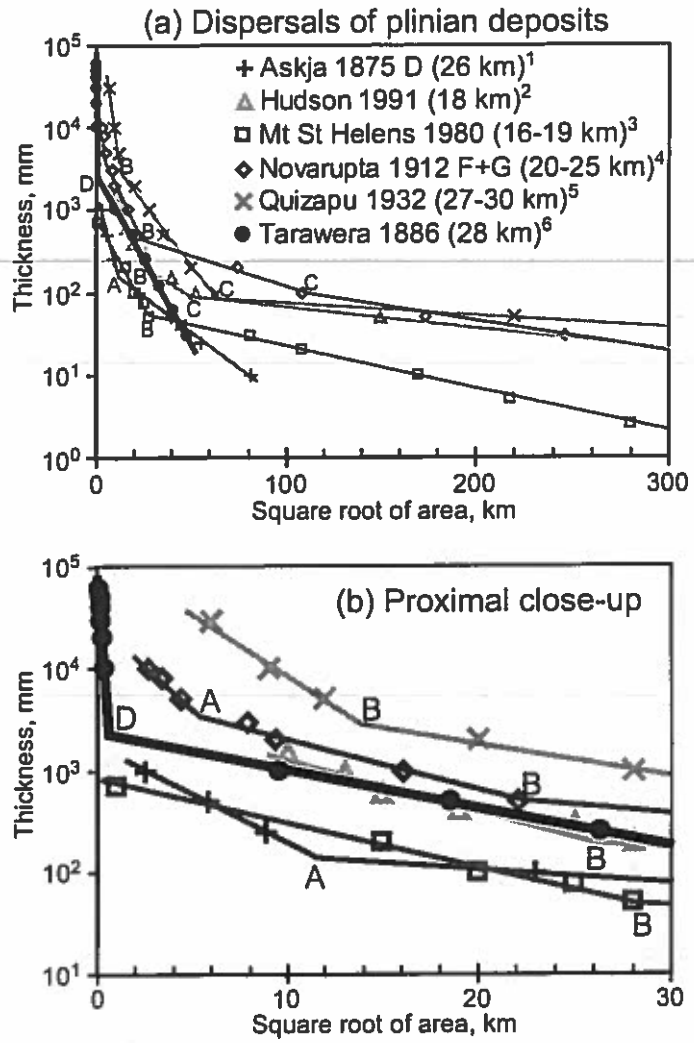

Figure 3.6 Plots of ln thickness vs. square root of area (after Pyle 1989) comparing Tarawera 1886 with other Plinian deposits. Breaks in slope are lettered according to their interpreted sedimentation regimes (after Bonadonna et al. 1998), as follows. A: transition from plume margin to large Reynolds number umbrella cloud sedimentation. B: transition from large to intermediate/mixed Reynolds number sedimentation from the umbrella cloud. C: transition from intermediate/mixed to small Reynolds number sedimentation from the umbrella cloud. Point D, at an equivalent radius of 300 m, is much closer to vent than the points labeled A. (a) Large-scale view for context, with observed or calculated column heights in parentheses. (b) Close-up highlights the contrasting positions of the breaks in slope. References: 1) Sparks et al. (1981); 2) Scasso et al. (1994), Bonadonna et al. (1998); 3) Carey and Sigurdsson (1982), Carey and Sparks (1986); 4) Fierstein and Hildreth (1992); 5) Hildreth and Drake (1992); 6) Walker et al. (1984), this paper.

Many Plinian deposits have two or more exponential thinning trends that appear as line segments with different slopes on the log thickness-area$^{1/2}$ plot (Pyle, 1989; Fierstein and Hildreth, 1992; Hildreth and Drake, 1992; Sparks et al., 1992). Bonadonna et al. (1998) proposed a model to explain the multiple segments. The innermost and steepest segment signifies fallout from the margins of the convective region of the plume (Ernst et al., 1996). The junction between this segment and the next represents the corner, where the sedimentation mechanism changes from shedding from the plume margins to vertical fallout from the umbrella cloud, with possible advection by wind (e.g., Sparks et al., 1997; Bonadonna and Phillips, 2003). More distal line segments represent other umbrella cloud regimes where sedimentation is dominated by different particle Reynolds numbers (Bonadonna et al. 1998). Not all segments are observed for all deposits due to differences in preservation and methods of data collection.

The most proximal line segments of the Novarupta units F and G and Askja unit D deposits probably indicate column margin sedimentation (Bursik et al., 1992; Ernst et al., 1996), because the breaks in slope (labeled A on Fig. 3.6) fall within the estimated distances to the plume corners based on the columns' respective heights (Bonadonna et al., 1998). However, the innermost segments for the Quizapu, Hudson, and Mount St Helens deposits are too far from vent to be related to the plume margins, and instead probably represent the large Reynolds number regime of sedimentation from the umbrella cloud (Bonadonna et al., 1998). The most proximal part of the Tarawera 1886 deposit is unique among these deposits: the line segment is much steeper, and the break in slope is positioned much closer to vent, than in the other trends on Fig. 3.6. This is interpreted to

be due to sedimentation from much lower heights than postulated for any of the other eruption plumes.

3.6 Discussion

In preparation for developing a sedimentation model for Tarawera 1886, we summarize the important aspects of the proximal deposits that must be considered. (1) The majority of the proximal packages have $t_{1/2}$ values greater than typical values for Hawaiian-Strombolian deposits (Fig. 3.4). (2) Proximal thicknesses of up to 70 m (Fig. 3.2) indicate near-vent accumulation rates that greatly exceed those recorded for Hawaiian and Strombolian explosions. (3) The overall proximal deposit has, however, an extremely rapid rate of thinning and is confined to within 400 m of vent, compared to 3 km or more for deposits inferred to have sedimented from the margins of the convective portions of other Plinian plumes (Fig. 3.6). (4) The proximal deposits contain a considerable proportion of fine particles.

Plume models

A simple plume sedimentation model assumes that all non-ballistic particles are swept up to the full height of the plume and are released from the base of the umbrella cloud (Sparks et al., 1997). Sedimentation starts at the eruption column's "corner," the point where the ascending convective plume reaches neutral buoyancy and the gas/clast suspension begins to spread laterally. Only ballistic particles are deposited within the zone between vent and corner, typically 1-10 km from vent (Sparks et al., 1997 and references therein; Bonadonna and Phillips, 2003). A simple model thus does not

account for the overthickened and yet relatively fine-grained proximal deposits observed at Tarawera.

Recent plume models (Bursik et al., 1992; Ernst et al., 1996) add a second transport regime consisting of the turbulent margins of the convective region of the plume. Particles may be released or re-entrained by eddies depending on grain size and height within the column. To make the equations workable, these models generally average the velocity across the plume, effectively assuming a "top hat" or uniform velocity profile. The turbulent eddies are added along the boundary between the ascending plume and the still atmosphere. For a 25 km plume, pumices < 1 m are totally re-entrained at heights up to 5 km within the plume, and pumices < 1 cm are totally re-entrained to the full height of the plume (Ernst et al., 1996). This implies that no particles smaller than 1 cm can accumulate inside the position of the plume corner, estimated to be ~6 km from vent for the 25 km column example (Bonadonna and Phillips, 2003). No particles <1 m can accumulate within about 2 km of vent (Sparks, 1986). In these models, re-entrainment becomes especially important for smaller particles and more intense plumes, resulting in reduced accumulation rate within a few hundred meters of vent (Bursik et al., 1992, Ernst et al., 1996). These models' predictions are not consistent with the overthickened and yet relatively fine-grained proximal deposits observed at Tarawera.

Riedel et al. (2003) adapted these models for eruptions with coarse grain size distributions and low eruption velocities, such as Hawaiian-style fountains. Their "jet fallout" version of the model and an alternative model of ballistic transport with drag provided equally good fits to data for rapidly accumulated cone-forming deposits. The

authors suggested that proximal overthickening in Plinian deposits could form by fallout of coarse particles from the margins of the jet region of the column. Our proximal deposits are, however, too fine-grained (Table 3.1) to fit such a model of jet margin sedimentation. Another problem is that no single model can explain the very large range of dispersals at Tarawera.

Significance of Tarawera's intermediate thickness half-distances

The $t_{1/2}$ values of deposits from typical Plinian umbrella clouds range from ~4 km to >100 km (calculated from b_t based on isopachs; Pyle, 1989). At the other extreme, most Hawaiian-Strombolian deposits have $t_{1/2} \leq 20$ m (e.g., Richter et al., 1970; Calvari and Pinkerton, 2004; Andronico et al. 2005). Most of the values for Tarawera 1886 fall between these two characteristic ranges (Fig. 3.4).

One possible cause for the intermediate $t_{1/2}$ values is mixing of material from the top of the convective region of one or more of the 1886 plumes ($t_{1/2} \approx 4$ km) with material from nearby Strombolian explosions ($t_{1/2} \approx 20$ m). We tested this idea by modeling the apparent $t_{1/2}$ value arrived at by adding a widespread layer with a maximum thickness (T_0) value of 3 m and a $t_{1/2}$ value of 4 km to a wedge with a T_0 of 84 m and a $t_{1/2}$ value of 28 m (the thickness and average $t_{1/2}$ for unit 2/3 at section T28). The $t_{1/2}$ value of the combination is 31 m. For the $t_{1/2}$ to increase above 100 m, the widespread fall component would need to be much thicker, with $T_0 = 80$ m. Thus the intermediate (100-280 m) $t_{1/2}$ values are not adequately explained by mixing of clasts from the umbrella cloud with products of low-intensity vents.

We infer that the Tarawera 1886 proximal segment must reflect sedimentation from levels lower than the typical release heights in the other Plinian plumes, yet higher

than the typical maximum heights attained by lava fountains and Strombolian explosions. A large amount of material with a wide grain size range accumulated very close to vent at a rapid rate, up to an order of magnitude higher than accumulation rates recorded for typical Hawaiian-Strombolian eruptions (Table 3.3). We suggest that the Tarawera 1886 eruption featured substantial sedimentation from the margins of low portions of the column, including the lower convective region and especially the momentum-driven jet region that makes up the basal 1-4 km (Sparks, 1986). This requires that the jet margin regime be a very important contributor of clasts of all grain sizes, in contrast to what is depicted in current jet-margin sedimentation models (e.g., Ernst et al., 1996; Riedel et al., 2003).

Model and implications

Our proximal sedimentation model for the Tarawera 1886 eruption is heavily based on a recent model for the Novarupta 1912 eruption (Houghton et al., 2004b). The Novarupta deposits include beds with $t_{1/2}$ values of between 20 m and 400 m located within 3 km of vent, defining a cone of fall ejecta (the "ejecta ring") and surrounding sector-confined wedges of fall lapilli (Fierstein et al., 1997; Houghton et al., 2004b). Fall units 1 and 2 at Novarupta (Houghton et al., 2004b) are the only deposits we know of worldwide with complex proximal structure and $t_{1/2}$ values comparable to those at Tarawera. The data of Fierstein et al. (1997) and Houghton et al. (2004b) show that the sedimentation that built Novarupta's ejecta ring was both episodic and confined to narrow sectors. To achieve a sufficiently high rate of deposition to account for the full proximal deposit thickness, they suggested that the jet had a Gaussian velocity profile, allowing more material to be released from the slower-moving margins. They also suggested that the non-systematic

variation in sedimentation of the 1912 deposits was due to unsteadiness and heterogeneity in the pulses of material entering the jet region of the 1912 plumes.

We propose that deposition in the proximal environment during the Tarawera 1886 eruption included three elements (Fig. 3.7): (1) clasts released from near the full height of the Plinian plumes, i.e. upper margins of the convective region (Sparks et al., 1997); (2) particles shed from the margins of the jet and possibly lower convective regions of the plumes; and (3) ejecta from Strombolian vents that did not contribute significantly to the Plinian plumes. The eruption featured at least two (craters F and J), and probably up to four (craters H and L) principal sources for the Plinian columns, along with Strombolian-style explosions from dozens of other vents along the fissure. At least one of the high-intensity vents and many of the weaker vents were active at any given time during the phase that produced proximal unit 2/3. The idea of multiple vents feeding a single shared umbrella cloud (Walker et al., 1984) is consistent with some eyewitness accounts that describe between three and seven discrete columns (Keam, 1988).

To explain the contribution of the jet portions of the Plinian plumes, we require a modified model for transport dynamics that includes a more realistic velocity profile in the jet, permitting substantial sedimentation from the jet margins. Classical fluid dynamical theory predicts that the magma in the upper conduit ascends more slowly along the margins (e.g., Holman, 1992; Dobran, 2001). We suggest that the jet perpetuates a curved velocity profile inherited from the mixture ascending in the upper conduit. We also suggest that jet margin sedimentation is highly variable due to asymmetries and fluctuations in particle concentration in the mixture entering the jet.

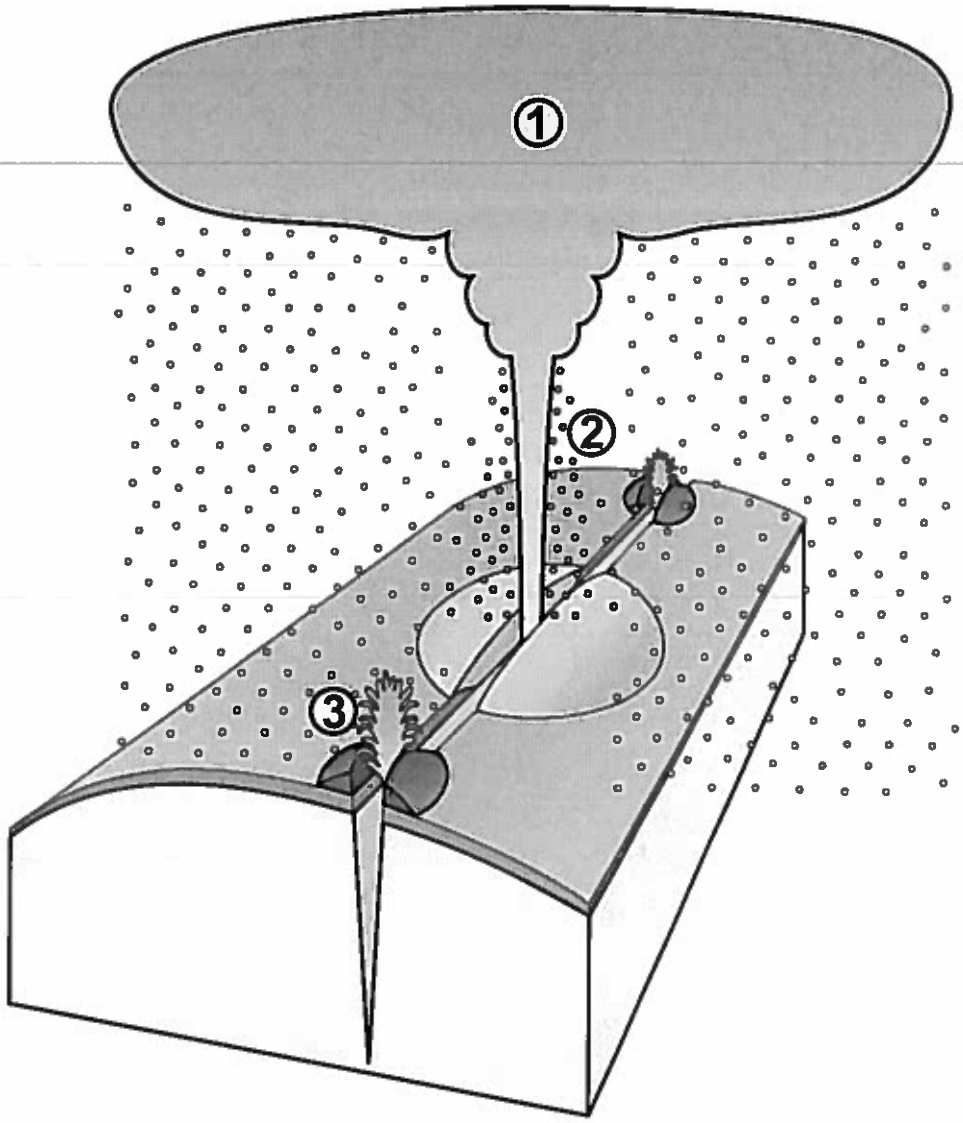

Figure 3.7 Cartoon with schematic depictions of three transport regimes. (1) Upper plume: particles are carried to the full height of the plume, travel laterally due to wind or buoyancy controlled spreading, and are showered predictably over both proximal and distal areas. (2) Margins of jet (and lower convective plume): the relatively low velocity, unsteady motion and high particle concentration along the margins allow particles of all sizes to escape and land in the proximal area. (3) Low-intensity Strombolian explosions.

Although the multiple-vent configuration at Tarawera is rare, our conceptual model for complex proximal sedimentation may apply to many Plinian eruptions. In particular, it may be common for a Plinian column to release particles both from near its full height and from the margins of the jet and lower convective plume. Descriptions of two recent subplinian eruptions (Asama 1783 and Oshima 1986) suggest that they were also characterized by sedimentation from both the high plume and from lower elevations on the margin of the plume, implying that such mingling may be more common than previously thought (e.g., Sumner, 1998; Yasui and Koyaguchi, 2004). Unfortunately, the data from these subplinian eruptions lack sufficient detail for quantitative comparison with the 1886 proximal deposits.

We suggest that sedimentation models sacrifice accuracy by assigning a uniform average velocity across the jet, and that the Gaussian velocity profile across the jet needs to be emphasized (e.g., Carey and Sparks, 1986; Sparks et al., 1997). Lower velocities along the jet margins allow near-vent deposition of a larger volume of material with a significant proportion of fine particles. While models tend to assume steady-state conditions to facilitate calculations, our data indicate that the jet regions of Plinian plumes are likely to be highly variable and heterogeneous.

3.7 Conclusions

The unusually high quality of preservation and exposure close to the Tarawera 1886 vents has facilitated a detailed study of proximal deposition of a Plinian eruption. The 1886 Tarawera proximal deposits have a complex geometry reflecting deposition from several regions within Plinian plumes, together with coeval Strombolian style eruption from other vents. We observe a wide range in the thicknesses and geometry of proximal deposit packages, reflecting strongly varying intensities for the vents along the fissure. The $t_{1/2}$ values of most packages are intermediate between typical basaltic (Hawaiian-Strombolian) and typical Plinian dispersals, suggesting that every package is a mixture of a widely dispersed component that fell from the upper margins of the Plinian plume and a locally dispersed component that is a combination of (a) ejecta from weakly explosive vents that did not contribute to the high plume and (b) particles from the margins of the jet and lower convective plume. Though the Strombolian vents may not have contributed much material to the high plume, the air heated above them could have contributed substantially to the buoyancy of the high plume and enhanced its vigor (e.g., Houghton et al., 2004b and references therein).

The vents that contributed most to the high plume were localized, not spread evenly along the fissure. Of the thirteen major craters, four (F, H, J, L) are dominated by the most widespread packages and are inferred to have contained Plinian vents, whereas other craters contributed virtually nothing to the high plume (e.g., D, E), based on their lack of widespread packages. One important conclusion is that a significant volume of particles with a wide grain size range was released from the transport regime associated with the slower-moving margins of the momentum-driven jet (lowermost 1-4 km) and the

lower convective regions of the plume. The particle concentration in the jet was probably variable and asymmetric, contributing to the heterogeneity in the proximal deposits.

The proximal deposits of Tarawera 1886 are unusual, but they may not be unique. Overthickened proximal deposits are probably produced in most Plinian eruptions but rarely preserved. Caldera collapse, pyroclastic density currents, secondary remobilization processes, and lava dome growth may remove or obscure the proximal deposits of Plinian eruptions at other volcanoes.

Acknowledgements

This research was supported by NSF grant EAR01-25719. We thank Michael Rosenberg of IGNS, Wairakei, for invaluable assistance in the field and lab. CJNW thanks the UK NERC and the New Zealand Foundation for Research, Science & Technology for financial support. The manuscript benefited greatly from the constructive comments of Costanza Bonadonna, Takehiro Koyaguchi, Steve Self, and James White. We also thank Gary Barnes, Julia Hammer, Andrew Harris, and Don Swanson for thorough and helpful comments on the draft manuscript.

CHAPTER 4

Eruption mechanisms during the climax of the Tarawera 1886 basaltic Plinian eruption inferred from microtextural characteristics of the deposits

4.1 Abstract

During the climactic Plinian phase of the 1886 basaltic eruption of Tarawera, New Zealand, vents along the 17 km eruptive fissure erupted explosively with a wide range of intensities. The 8 km long segment of the fissure cutting across Mt Tarawera contains approximately 50 vents and includes the sources of both the weakest and most intense activity of the 5-hour eruption. We seek to explain (1) what allowed the intensity to reach Plinian values rarely achieved by basaltic magma, and (2) what caused adjacent vents to erupt with very different dispersals and intensities despite identical magma composition.

All juvenile clasts from this eruption have relatively vesicle high number densities ($\sim 10^6$ cm^{-3}) and exceptionally high microlite crystallinities (60-90% of the groundmass), unlike typical products of weaker Hawaiian and Strombolian basaltic explosions. Microtextural evidence suggests that microlite crystallization increased the effective viscosity of the 1886 magma such that it could ascend and fragment in a manner analogous to that postulated for silicic Plinian eruptions by Papale et al. (1998). The main differences among different locations along the Mt Tarawera fissure segment are in the content and grain size of the wall rock lithic component of the deposits. We infer that the 1886 magma had a common history at depth, but that local variations in vent wall

geometry and stability affected the conditions in the shallow conduit and led to the diversity of eruptive styles along the fissure.

4.2 Introduction

The climactic phase of the 1886 basaltic eruption of Tarawera, New Zealand, shows evidence for multiple vents along a fissure erupting simultaneously with diverse intensities and styles, ranging from weak cone-forming explosions to Plinian columns (Sable et al., 2006). Although all the erupted basaltic magma had the same bulk chemistry (A. Freundt, pers. comm. 2006), closely spaced vents showed extreme differences in style and dispersal. This study interprets qualitative and quantitative data for clast densities and microtextures to develop an explanation for the diversity of behavior exhibited during this 5-hour eruption.

The basaltic Plinian problem

Basaltic volcanism is generally restricted to lava effusion and weak explosions ranging from Strombolian to Hawaiian in style and intensity (Walker, 1973). However, there is increasing recognition that a wider range of explosive behavior is possible in basaltic systems (e.g. Parfitt, 2004). Violent phreatomagmatic, subplinian, and Plinian examples of basaltic volcanism have now been confirmed based on historical and prehistoric deposits of widespread dispersal (e.g. Williams, 1983; Walker et al., 1984; Koyama and Hayakawa, 1996; Coltelli et al., 1998; Belousov and Belousova, 2002).

The intensity, style, and duration of explosive eruptions are influenced by processes operating in both the magma storage zone(s) and the volcanic conduit. In the magma chamber, crystal fractionation affects the melt composition, and volatile

exsolution builds overpressure that may drive early magma ascent (Wilson and Head, 1981). In the conduit, vesiculation, crystallization, and interaction with wall rock and/or groundwater may change the rheology and flow behavior of the ascending magma, determining the style and intensity of the resulting eruptions (Barberi et al., 1989; Pinkerton and Stevenson, 1992; Hess and Dingwell, 1996; Koyaguchi and Woods, 1996; Manga et al., 1998; Papale et al., 1998).

The most intense silicic explosive eruptions reach mass flow rates of 10^5 to 10^{10} kg s^{-1} due to strong upward acceleration immediately preceding and following fragmentation (Wilson et al., 1978; Wilson and Walker, 1987). Shortly before fragmentation, disequilibrium vesiculation promotes this acceleration by increasing the magma's buoyancy and bulk volume (Papale et al., 1998). During and after fragmentation, the expansion of the hot erupting gas when subjected to atmospheric pressure creates further acceleration (Woods, 1988).

Acceleration in the conduit is achieved most efficiently through coupled or closed system degassing, in which there is little or no relative motion between bubbles and melt (Mangan et al., 1993; Cashman and Mangan, 1994). In silicic systems, coupled degassing behavior is commonly associated with delayed and disequilibrium bubble nucleation, which produces pumice with large vesicle number density and small mean vesicle diameter (Mangan and Sisson, 2000; Klug et al., 2002). In contrast, Hawaiian and Strombolian eruptions do not produce such microvesicular clast textures (Walker and Croasdale, 1972; Mangan and Cashman, 1996). Most models of basaltic magma ascent and fragmentation are based on Hawaiian and Strombolian styles and thus predict little or no coupling between bubbles and basaltic melt (e.g., Wilson and Head, 1981; Vergniolle

and Jaupart, 1986; Parfitt and Wilson, 1995). However, based on evidence from gas emissions and melt and fluid inclusions, some recent studies infer that many basaltic systems feature both coupled and decoupled types of degassing, with each type in a different depth regime (Famin et al., 2006; Spilliaert et al., 2006b).

Basaltic magma must undergo a sustained period of coupled degassing behavior in order to reach the high exit velocities and mass flow rates necessary for Plinian explosion. Here we use textural evidence to characterize the conduit behavior that produced the 1886 basaltic Plinian eruption of Tarawera volcano, New Zealand.

The Tarawera 1886 eruption

Precursors to the 1886 eruption of Tarawera included increased activity at hot springs and geysers in the region during the preceding months and seiche-like waves 0.3 m high on Lake Tarawera on June 1 (Smith, 1886a, 1886b; Thomas, 1888). No other precursors were observed until earthquakes began to be felt at 00:30 on June 10, one hour before the eruption began (Smith, 1886a).

Explosions began at 01:30, and over the next hour an 8-km-long fissure opened across the Mt Tarawera dome complex (Fig. 4.1), with a line of elongate craters producing lava fountains and feeding an eruption column over 10 km high (Keam, 1988). At 02:30, the fissure extended to the southwest and more explosions began at Waimangu, producing a second plume. A severe earthquake at 03:20 was accompanied by the start of eruption at Rotomahana, the site of an active geothermal system (Keam, 1988). Interaction between the magma and hydrothermally altered and weakened country rock produced a high ash-and-steam-rich column centered on Rotomahana and Waimangu (Nairn, 1979). This plume distributed "Rotomahana Mud," composed of wet fine ash and

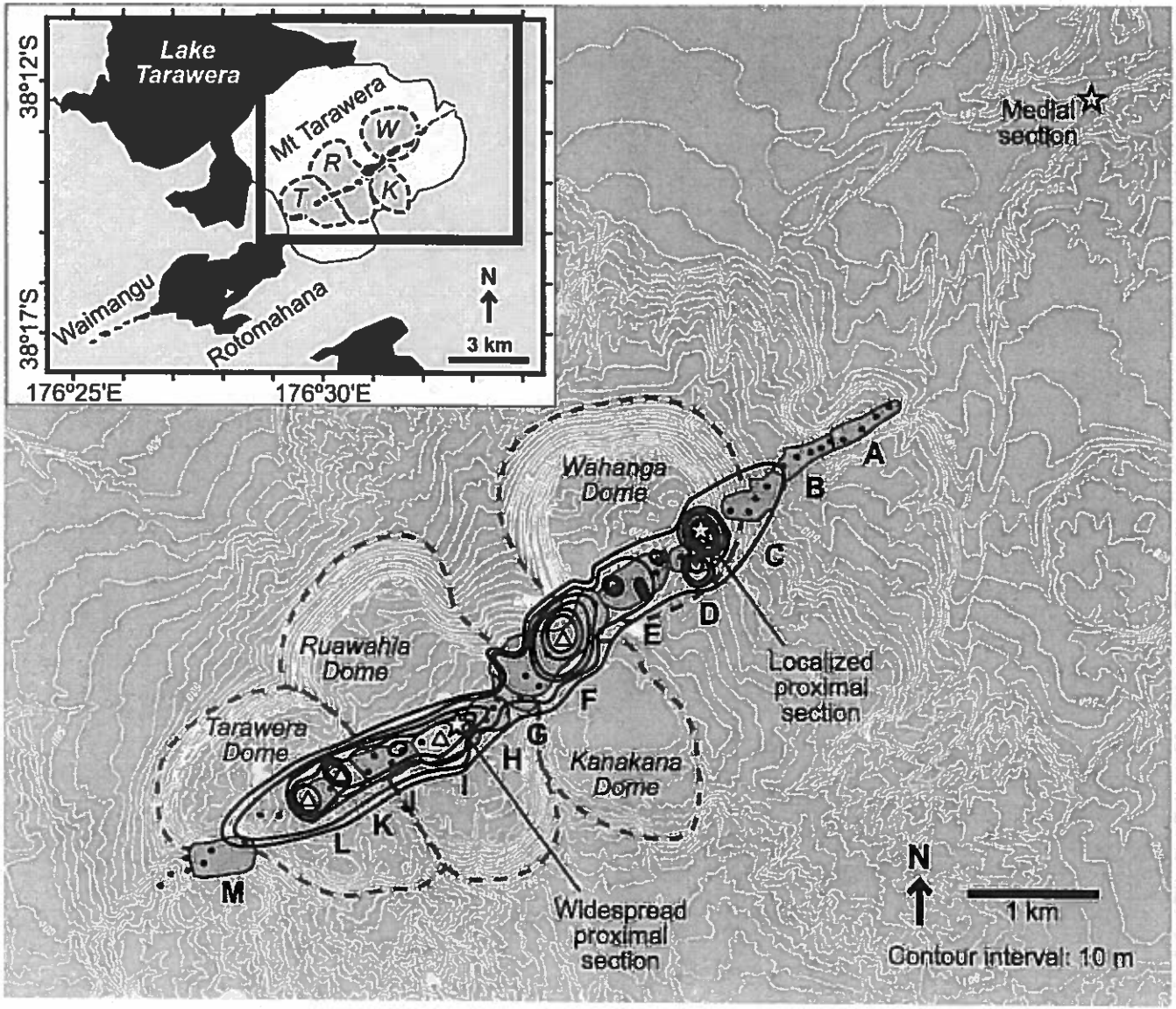

Figure 4.1
Topographic map of the Mt Tarawera area (enclosed in rectangle on inset map) with isopachs showing thickness of unit 2/3 of the 1886 proximal deposits (10 m contour interval). Main rhyolitic domes of the Mt Tarawera dome complex are marked with dashed outlines and labeled in italics (abbreviated W, R, K, T on inset map). Capital letters label the thirteen craters along the 8 km long Mt Tarawera fissure segment. Triangles mark locations of the four likely sources of Plinian plumes (from Sable et al., 2006). Stars mark the three key sections studied here: widespread proximal, localized proximal, and medial.

accretionary lapilli, over a 10,000 km^2 area (Cole, 1970). The Rotomahana vents also generated pyroclastic density currents that destroyed three villages (Nairn, 1979). At the same time the northeastern or Mt Tarawera segment of the fissure produced an intense Plinian phase that marks the climax of the 1886 eruption. At this point the total eruption fissure was 17 km long, and eyewitnesses described three to seven distinct eruption columns (Keam, 1988). The Plinian umbrella cloud reached a height of at least 28 km (Walker et al., 1984; Carey and Sparks, 1986). The wind blew initially from the south but shifted southwest at about 04:00, distributing basaltic scoria over 1200 km^2 of land as well as a large area of ocean (Fig. 4.2). Explosions continued until 06:00, and occasional weak phreatic eruptions persisted for months afterward, mostly at Rotomahana (Nairn, 1979).

The 1886 deposits from Mt Tarawera

The focus of this study is the 8 km portion of the fissure on Mt Tarawera, where the Plinian plumes originated (Fig. 4.1). Although the 1886 eruption was basaltic, Mt Tarawera is mainly composed of rhyolitic tephra and lavas (Cole, 1970). The most recent rhyolitic products are interbedded tephras and lavas emplaced during the 1315 AD Kaharoa eruption (Nairn et al., 2004), which form the shallow basement for the 1886 fissure. The wall rock of the 1886 dikes thus includes massive rhyolitic dome lava as well as compacted pumice and ash deposits.

Medial-distal deposits

Walker et al. (1984) produced the most detailed map to date of the medial-distal 1886 deposits (Fig. 4.2) and demonstrated that the widespread Plinian basaltic scoria originated only from the northeastern, or Mount Tarawera, portion of the fissure. From maximum

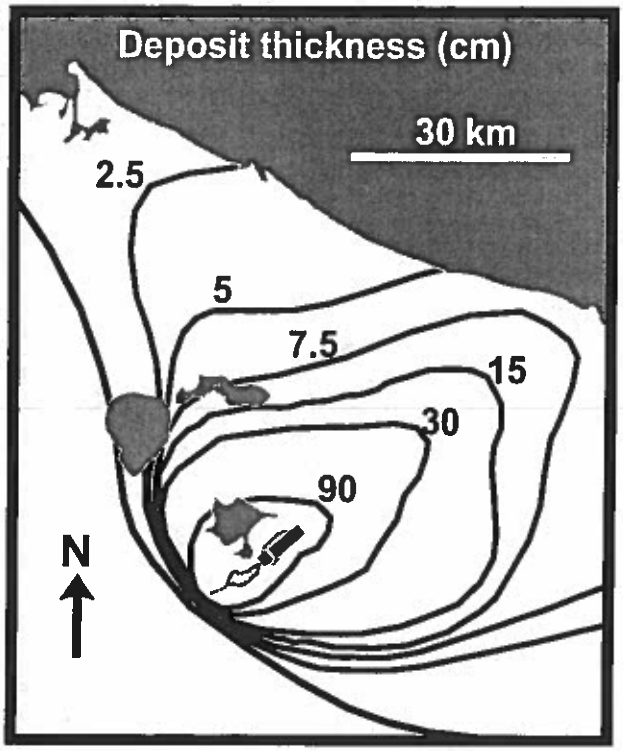

Figure 4.2 Isopach map of widespread scoria fall from the Tarawera 1886 eruption, after Walker et al. (1984).

clast data, Walker et al. (1984) estimated an erupted bulk volume of 2 km^3 and a column height of 28 km using the model of Wilson et al. (1978). Carey and Sparks (1986) calculated a 34 km high column using a similar model that additionally accounts for a crosswind.

The widespread scoria fall from the climactic phase of the eruption has generally homogeneous grain size characteristics (Walker et al., 1984). Clast sizes range from ash to lapilli; 64 cm lapilli are present within 10 km of vent, and rare 8 cm lapilli are found within 35 km of vent (C. Wilson and B. Houghton, unpublished data). Rotomahana Mud becomes abundant (10-15 wt%) midway through the section and forms accretionary lapilli and coatings on some scoria clasts (Walker et al., 1984; Houghton and Wilson, 1998). We observe ragged to knobby juvenile clast morphologies in the medial-distal deposits.

Proximal deposits

Overthickened proximal deposits form a 400-m-wide halo around the edges of the Mt Tarawera portion of the fissure (Fig. 4.1), with the geometry of a series of half-cones centered on numerous point sources along the fissure (Walker et al., 1984; Sable et al., 2006b; Carey et al., 2006). The deposits are well exposed in the steep crater walls on either side of the fissure, within 100-200 m of the vent. Unlike the medial-distal deposits, these proximal deposits show large variations in thickness, grain size, and other characteristics on distance scales of hundreds of meters (Sable et al., 2006b). The current stratigraphy divides the proximal deposits into three units named, from oldest to youngest, 1, 2/3, and 4/5 (Carey et al., 2006; Sable et al., 2006b). The paired numbers in

the names of the upper two units refer to the amalgamation of two pairs of units in the stratigraphy originally proposed by Walker et al. (1984).

Unit 1 is dark in color, poorly sorted, and relatively lithic-rich, and is inferred to have been produced by weak phreatomagmatic explosions (Walker et al., 1984).

Unit 2/3 dominates the volume of the proximal deposits and is red-brown to black, moderately sorted, and generally lithic-poor. Its thickness varies between <10 m and 60 m along the fissure, and bedding is not laterally continuous between adjacent craters. Instead, groups of beds form subunits or "packages" with lens-like geometries that are observed to overlap and intermingle in the fissure wall exposures (Sable et al., 2006b). The packages form a complex geometry that reflects the simultaneous eruption of the 50 or so vents distributed along the Mt Tarawera fissure. Different vents erupted with contrasting styles, and the products of different vents can be distinguished based on dispersal, welding, and bedding characteristics (Sable et al., 2006b). Unit 2/3 is correlated with the medial-distal Plinian scoria fall (Houghton and Wilson, 1998), but Sable et al. (2006b) add that not all the clasts in this unit were carried to the full height of the Plinian columns; a proportion of clasts was released from lower heights within the columns or was ejected by weaker explosions.

Unit 4/5 is rich in dense juvenile clasts and rhyolitic wall rock fragments ranging from ash to 3 m blocks. It is interpreted as a phreatomagmatic closing phase (Walker et al., 1984; Houghton and Wilson, 1998).

Summary of previous work

The earliest studies of the 1886 deposit include descriptions of the deposits from the northeastern (Mt Tarawera) and southwestern (Rotomahana) portions of the fissure (Smith, 1886a, 1886b; Hutton, 1887; Williams, 1887), and an isopach map (Thomas, 1888). Cole's (1970) petrologic study helped distinguish the 1886 basalt from other basic products of Mt Tarawera complex. Nairn (1979) characterized the phreatomagmatic fall and surge deposits from Rotomahana and Waimangu and confirmed that some juvenile basalt did erupt from the southwestern vents. Nairn and Cole (1981) mapped dikes and determined that the fissure was divided into a right-stepping series of segments, each feeding several vents. Walker et al. (1984) expanded and improved upon the previous work to produce a new isopach map and a detailed stratigraphy that showed the link between the proximal and widespread fall deposits from the Mt Tarawera vents.

A revival of research on this eruption has begun with Houghton and Wilson (1998), who modify Walker et al.'s (1984) stratigraphy and discuss the possible extent and timing of magma-water interaction during the Plinian and phreatomagmatic phases of the eruption. Houghton et al. (2004a) present preliminary data for grain size, clast density, and lithic content, and propose a model for the transitions between the stages of the 1886 eruption. Based on a decrease in clast vesicularity at the top of proximal unit 2/3, the authors suggest that the magma shifted from coupled to decoupled degassing behavior near the end of the phase that included the Plinian activity. Gas loss and microlite crystallization caused the magma to become viscous and sluggish and to accumulate along the walls of the upper conduit, leading to a decrease in eruption rate (Houghton et al., 2004a). Sable et al. (2006b) conduct detailed studies of the geometry

and dispersal of the proximal Mount Tarawera deposits and show that the Plinian activity was concentrated at four source vents, while weaker explosions occurred at many other vents. The transport was complex and included significant sedimentation from the margins of the jet and lower convective portions of the Plinian plumes.

Carey et al. (2006) analyze grain size, componentry, clast bulk vesicularity, and clast morphology for the proximal deposits at Mount Tarawera, and their data are important to the interpretations in this study. They find that median grain size and sorting are consistent with Sable et al.'s (2006b) interpretation that eruptive intensity varied both along the fissure and with time. Carey et al. (2006) also show that the grain size distributions are affected by the pre-existing grain size of the lava and tephra in the country rock; for example, lithic blocks from unstable vent walls add an especially coarse component at some locations. Changes in the proportions of shallow- and deep-derived lithic particles in the proximal deposits suggest that the fragmentation surface was deeper and magma flux probably lower in the phreatomagmatic phases (units 1 and 4/5) than in the main phase (unit 2/3), allowing more groundwater to enter the conduit at those times (Carey et al., 2006).

4.3 Rationale and approach

Questions

The previous work answered some questions but generated many more, and the mechanisms that allowed the basalt to erupt in Plinian style have not yet been resolved. It further remains to be explained how vents spaced as little as 50 m apart could simultaneously erupt with extreme contrasts in intensity and style. This study centers on three questions: (1) How did the Tarawera 1886 magma achieve Plinian intensity? (2) Why did some of the 1886 magma fail to achieve Plinian intensity? (3) What caused the Plinian activity to cease? We address these questions through a detailed study of deposit and clast characteristics at several scales.

Sample sites and methods

To discern the differences in conditions between the intensely and weakly erupting vents along the Mt Tarawera fissure, we study deposits both near and far from the vents.

Sable et al. (2006b) delineate packages of beds within the proximal deposits. Each package represents an accumulation of a mixture of locally dispersed scoria from nearby weakly erupting vents and more widespread products from vents with intense activity. Some sites are dominated by extremes of dispersal, with minimal mixing from adjacent vents; these sites provide the purest examples of the end-member eruptive styles. Two examples of dispersal extremes are a localized proximal section in crater D and a widespread proximal section in crater I (Fig. 4.1). In the context of the proximal deposits, the term "widespread" describes a package with $t_{1/2}$ greater than ~80 m, compared with the localized proximal packages that have $t_{1/2} < 50$ m (Sable et al.,

2006b). None of the proximal packages is truly widespread in the sense of Plinian sheet-forming fall deposits that can be traced for many kilometers.

The localized proximal section is near the northeastern end of the Mt Tarawera fissure, far from the proposed sources of the Plinian plumes (Sable et al., 2006b). The clasts from this section are interpreted as products of weak explosions that never reached heights greater than 500 m. The widespread proximal section is adjacent to one of the likely Plinian vents. The majority of its clasts were released from the margins of the jet at heights of approximately 1-4 km, according to the model of Sable et al. (2006b). These two proximal sections also form the focus of the grain size study of Carey et al. (2006).

A medial section located ~5 km from the northeastern end of the fissure (Fig. 4.1) was also sampled for studies of grain size, componentry, and clast microtextures. This particular section was chosen because of its excellent preservation. The medial section provides an important basis for comparison because clasts could have reached this site only if they rose to the full height of the Plinian plume and traveled in the umbrella region (Sparks, 1986; Bonadonna and Phillips, 2003). Thus although clasts from the proximal sections may originate from several contrasting vents, clasts from the medial section represent magma that unequivocally erupted with Plinian intensity.

We collected 24 samples from the widespread proximal section and 21 from the localized proximal section for grain size and componentry studies. For density measurements and microtextural study, additional samples were collected consisting of 100 juvenile clasts in the 16-32 mm size range. The density/microtextural sample set includes 72 samples from the widespread section, 44 from the localized proximal section,

and 11 from the medial section. All samples were taken from narrow vertical intervals no more than 2-3 clast diameters (5-10 cm) thick.

Several methods were used to determine commonalities and differences in dominant clast texture among the sections. Macroscopic methods included measurements of grain size, componentry, clast densities, and the content of visible xenoliths. The detailed grain size and componentry data are presented in Carey et al. (2006). Each clast's density was determined by comparing its weights in air and in water following the methods used by Houghton and Wilson (1989), Gurioli et al. (2005), and Adams et al. (2006a, 2006b). Approximate vesicularities were calculated assuming an average density of 2700 kg m^{-3} for the vesicle-free rock.

Microscopic studies involved observation and quantification of bubbles, crystals, xenoliths, and xenocrysts. Frequency distributions of clast densities were considered in the selection of typical maximum, minimum, and modal density clasts from several samples for microtextural study. Polished thin sections of the selected clasts were imaged at several magnifications, the lowest being 47.2 px/mm on a flatbed scanner. Backscatter images were acquired with a JEOL-5900LV SEM at three magnifications: 1000 px/mm and 5040 px/mm for measuring bubbles, and 25,200 px/mm for microlites. Bubble sizes and number densities were analyzed using the Scion Image program, and three-dimensional size distributions were calculated using the method of Sahagian and Proussevitch (1998). Proportions of microlite phases were measured by point counting on high-magnification backscatter images. Xenoliths and xenocrysts were identified under an optical microscope and their abundances quantified with Scion Image.

4.4 Results

Macroscopic studies

Bulk density measurements

The histograms in Fig. 4.3 show bulk density distributions for ten samples from each section. Samples are restricted to the portion of the deposit that was emplaced during Plinian activity. Most samples have histograms with strongly defined modal peaks (1σ = 200 kg m^{-3}). The distributions with the sharpest modal peaks occur in the middle portion of the widespread proximal section. Some samples from the medial section have broader distributions with more weakly defined modes indicating greater variation (1σ = 300 kg m^{-3}). Tails of dense clasts are evident in nearly all distributions, and the samples from the medial site contain the highest proportions of dense clasts.

The lowest density modes are in the middle to upper stratigraphic levels of the localized proximal section. The highest density modes for both proximal sites are found at the base of unit 2/3 (Fig. 4.3), just above phreatomagmatic unit 1, which is dominated by denser, quenched juvenile clasts and abundant lithics. Apart from the denser basal sample at each proximal section, the density distributions show only minor fluctuations, and no systematic change with position in the stratigraphy.

Typical density ranges are 500-2000 kg m^{-3} for the localized proximal samples, 800-2000 kg m^{-3} for the widespread proximal section, and 800-2200 kg m^{-3} for the medial section. The density modes for the medial and widespread proximal samples are similar, averaging 1190 kg m^{-3} and 1170 kg m^{-3}, respectively. In contrast, the modes for the localized proximal section are lower, averaging 1010 kg m^{-3}. Samples from the localized proximal section generally have the greatest proportion of clasts with densities

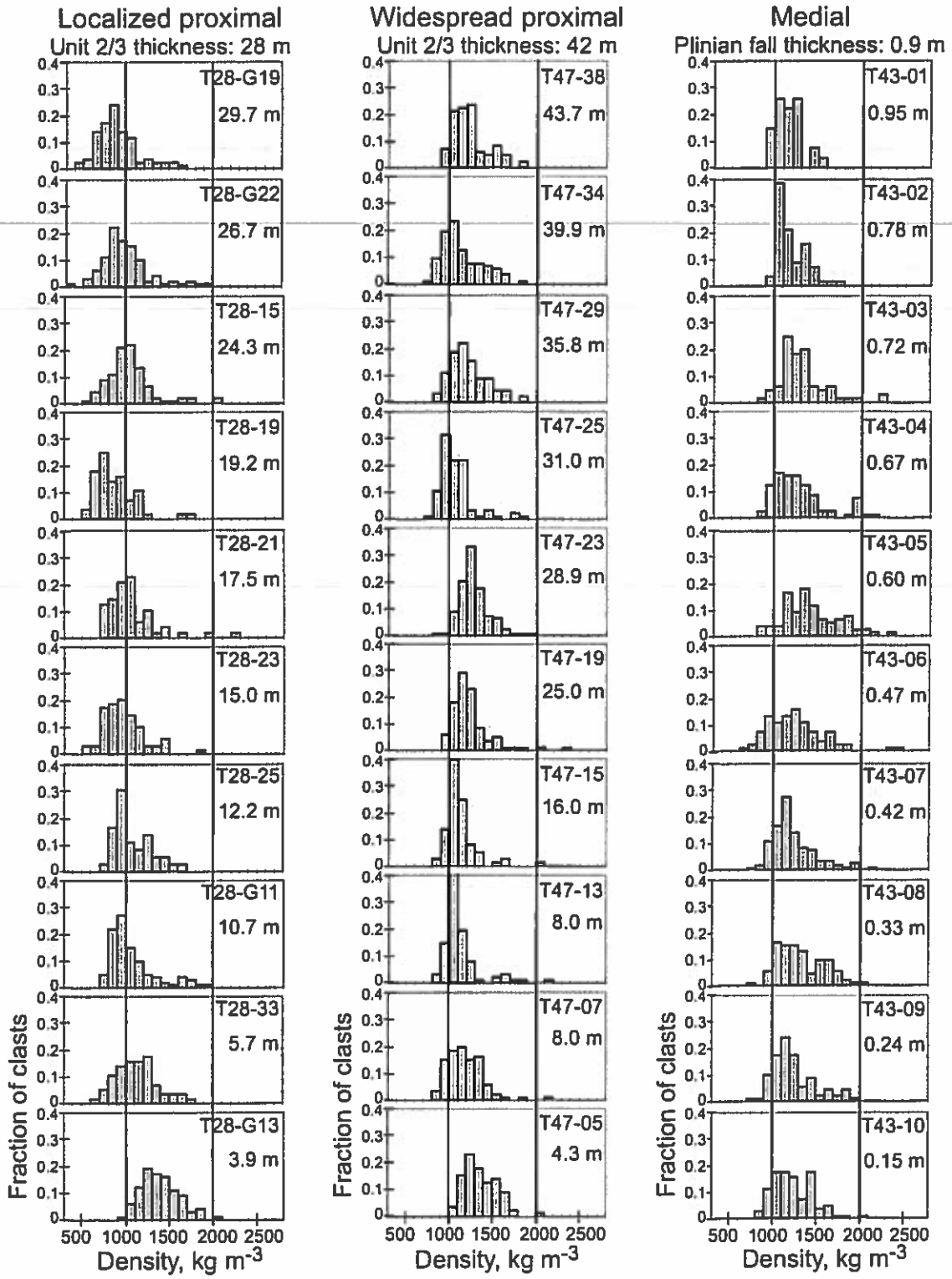

Figure 4.3 Histograms of bulk clast density for samples from the three sections in stratigraphic order with youngest at top. Sample number and height above base of section are indicated in corner of each plot; note that the medial section is much thinner than the two proximal sections. Vertical lines are drawn through 1000 and 2000 kg m^{-3} to facilitate comparison.

less than 1000 kg m^{-3}; those from the medial section have the greatest proportion of clasts with densities above 1000 kg m^{-3}; and those from the widespread proximal section appear transitional between the other two sections (Fig. 4.3).

Contrasts in grain size and componentry

Carey et al. (2006) supply detailed grain size analyses and show the relative abundances of juvenile basalt clasts and rhyolite wall rock lithics for the two proximal sections. The deposit at the localized proximal section is slightly coarser and notably poorer sorted than that at the widespread proximal section (Table 4.1).

Wall rock lithic content is variable for both sections (Carey et al., 2006). Unit 4/5 has the highest wall rock content throughout the Mt Tarawera fissure. In unit 2/3, loose wall rock fragments are most abundant at the localized proximal section, averaging 18 wt% (Fig. 4.4a). At the widespread proximal section, lithic content is typically 8 wt% or less except in some samples in the uppermost levels where unit 2/3 transitions into unit 4/5 (Fig. 4.4a).

Table 4.1. Average values and standard deviations for median diameter, Inman sorting coefficient, and loose lithic content for the two proximal sections (Carey et al., 2006). Unit 4/5 is not preserved at the localized proximal section.

Section	Unit	Median diameter, ϕ	Inman coeff., $\sigma\phi$	Lithics, wt%
Localized proximal	1	-2.5 ± 1.3	1.4 ± 0.2	12 ± 5
	2/3	**-4.1 ± 1.0**	**2.7 ± 0.4**	**18 ± 11**
Widespread proximal	1	-2.8 ± 0.5	1.5 ± 0.1	6 ± 4
	2/3	**-3.9 ± 0.6**	**2.0 ± 0.4**	**2 ± 2**
	4/5	-2.6 ± 0.8	2.8 ± 0.6	35 ± 28

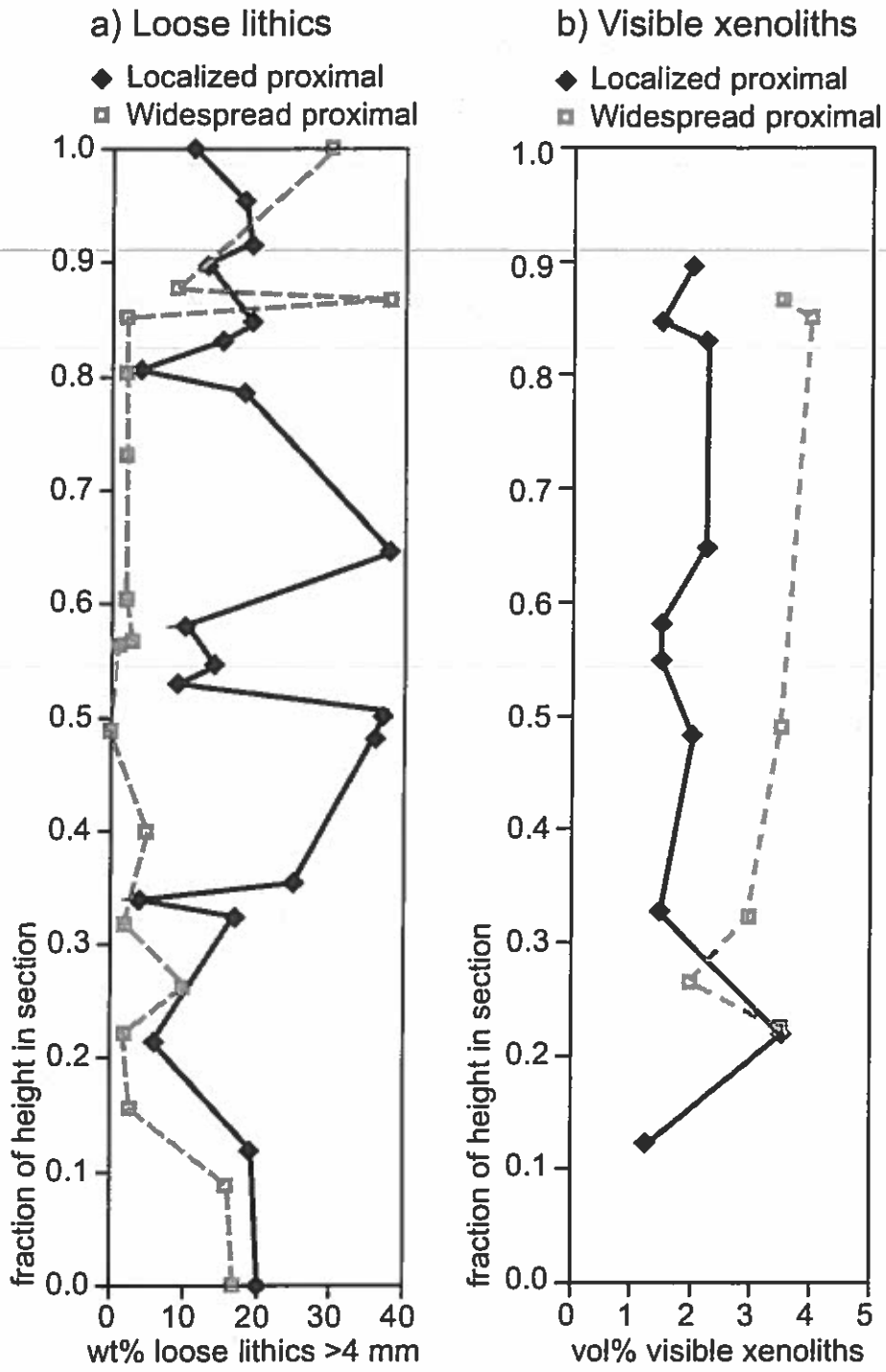

Figure 4.4 Variation in contents of a) loose wall rock lithic fragments and b) visible xenoliths for unit 2/3 of the two proximal sections. Widespread proximal section is marked with open squares and dashed lines. Localized proximal section is marked with filled diamonds and solid lines. The localized proximal section has more loose lithics, but the widespread proximal section has a greater content of xenoliths embedded in the basaltic clasts.

Visible xenoliths

The abundance of rhyolite xenoliths embedded in proximal juvenile clasts was quantified by mapping cut surfaces of basaltic bombs (Carey, 2002). For both proximal sections, the xenolith content shows minimal variation except near the base of unit 2/3 (Fig. 4.4b). The localized proximal deposit contains ≤2.5 vol% xenoliths over most of the section, while the widespread proximal deposit typically has ≥3 vol% xenoliths (Fig. 4.4b). The greater xenolith content in the widespread proximal section is the reverse of the pattern observed for the content of loose lithic particles (Fig. 4.4a; Table 4.1).

Microtextural studies

The 1886 pyroclasts contain complex assemblages of bubbles, microlites, glass, xenocrysts, and xenoliths, all of which supply information about the processes leading up to and accompanying explosive fragmentation.

Bubbles

Most clasts share similar bubble size and shape characteristics (Fig. 4.5). Nearly all bubbles have complex polylobate shapes; spherical shapes are rare, even for very small (<50 μm) bubbles. Chains of connected bubbles are observed in some places (e.g. Fig. 4.5c). The areas of groundmass between bubbles are on the order of 1-2 bubble diameters (typically 5-50 μm). In contrast, bubbles in silicic pumice are commonly separated by glass films only 1-5 μm thick (Klug and Cashman, 1996; Klug et al., 2002; Adams et al., 2006a). Bubbles span the same range of sizes in all the Tarawera clasts, with a main population of bubbles between 0.02 to 3 mm in diameter. Bubble number densities are consistently of the order of 10^6 cm^{-3}. Each clast has a population of tiny (<0.01 mm diameter) void spaces that appears detached from the main bubble population.

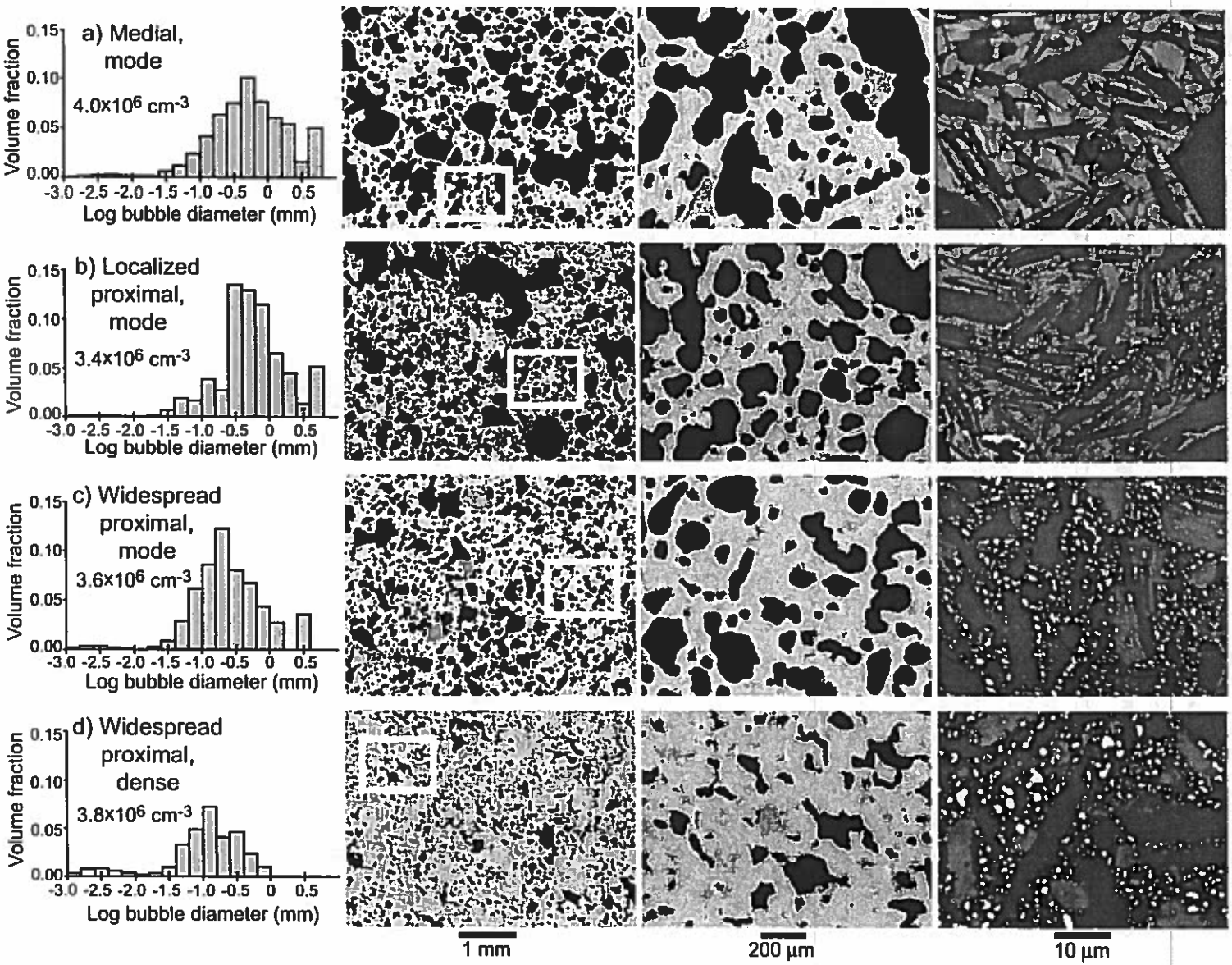

Figure 4.5 SEM images and vesicle volume histograms. a) Modal density clast from the medial section. b) Modal clast from the localized proximal section. c) Modal clast from the widespread proximal section. d) Dense clast from the widespread proximal section. Modal density clasts represent the bulk of the magma in the conduit. Dense clasts show signs of outgassing.

These very small, irregularly shaped cavities are unlikely to be related to bubble nucleation. They are instead interpreted as diktytaxitic voids, formed when the magma contracts during crystallization (Walker, 1989; Saar and Manga, 1999). Our reported estimates for bubble number density do not include these smallest bubbles.

Microlites

The groundmass of all the Tarawera 1886 clasts is remarkably crystalline, with 85-99 vol% of microlites. All of the clasts probably contain some glass in pockets between microlites, but the glassy areas are generally much too small to be analyzed reliably with an electron microprobe. Phenocrysts are extremely rare, making up less than 0.5 vol% of the clasts. In comparison, scoria from eruptions of Stromboli in 2002 contain almost no microlites and have abundant phenocrysts (Lautze and Houghton, 2005).

Groundmass characteristics common to all the clasts include high crystal number densities, random orientation of crystals, and the presence of pockets and clusters of very small rounded crystals. Approximate microlite number densities range from 10^{12} to 10^{13} cm^{-3}. Average volume proportions of the microlite phases are 57% plagioclase, 40% clinopyroxene, 2% olivine, and <1% Fe-Ti oxide. The phase proportions vary slightly among clasts, even though bulk compositions are very consistent (A. Freundt, pers. comm. 2006). For example, the widespread proximal clasts have a higher proportion of Fe-Ti oxides, while this phase is very rare in clasts from the medial section.

We commonly observe a texture of relatively large (up to 200 μm long) plagioclase laths with angular or swallowtail ends randomly oriented in a matrix of finer crystals. Typical crystal sizes and shapes are: 5-20 μm long plagioclase needles, 20-200 μm long plagioclase laths, 10-30 μm long elongate clinopyroxene prisms, 5-15 μm equant

pyroxene grains, and 0.5-3 μm equant Fe-Ti oxide and olivine grains. Slight deviations from these dominant crystal habits are related to location. For example, dendritic microlite habits are observed only in some clasts from the medial site, and clinopyroxene microlites are larger, on average, in clasts from the medial site. These variations are not correlated with clast vesicularity or stratigraphic position.

Microscopic xenoliths and xenocrysts

The clasts contain 0.1-3.5 vol% xenoliths and xenocrysts that are visible with an optical microscope. The most common types of xenoliths are fragments of devitrified rhyolite, pieces of fresh rhyolitic glass containing small round bubbles, and clumps of rhyolitic ash. Xenocrysts include plagioclase and rare quartz and amphibole crystals with shapes ranging from elongate to equant euhedral forms, and angular to rounded fragments. Furrowed and eroded edges are common but not ubiquitous among the xenocrysts. Several plagioclase crystals are zoned, and the innermost zones contain indentations and holes attributed to resorption. Details of the xenoliths cannot be distinguished visually because the original features of the rhyolite have been overprinted by changes from contact with the basaltic melt.

The sizes and numbers of microscopic xenoliths were measured in representative clasts from the three sites (Fig. 4.6). The largest numbers of microscopic wall rock inclusions are found in the clasts from the widespread proximal section, consistent with the trend in the visible xenoliths (Fig. 4.4b). In contrast, all the clasts from the localized proximal section have ≤1.5 vol% of microscopic xenoliths, with the exception of one apparent outlier. The microscopic xenolith contents of the medial section range up to large values, but the numbers of xenoliths are small, indicating that the xenoliths are

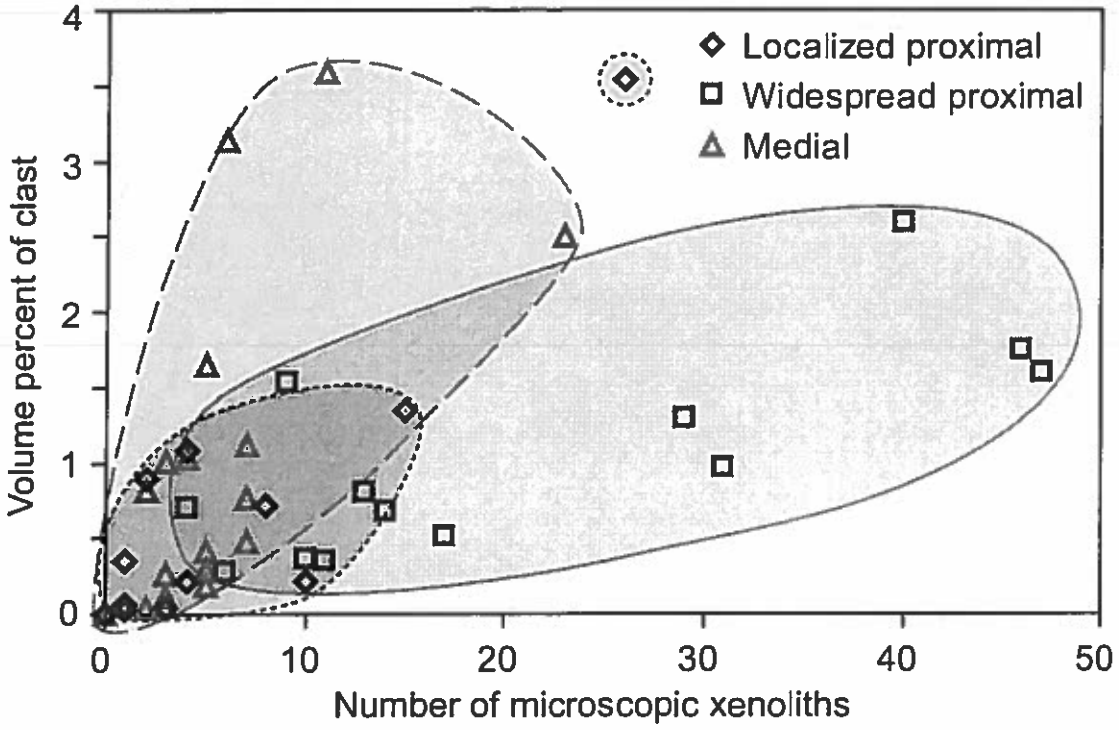

Figure 4.6 Number of microscopic xenoliths versus xenolith volume fraction for clasts from each of the three sections. The widespread proximal section (green field with solid outline) has the highest number of xenoliths and the smallest average xenolith size.

typically larger in size than at the other sections. The widespread proximal section shows the opposite relationship between number and size of xenoliths, indicating that these xenoliths have the smallest average size.

4.5 Interpretations

We organize the interpretations around the three questions asked in section 4.3.

How did the Tarawera 1886 magma achieve Plinian intensity?

The rarity of basaltic Plinian eruptions implies that they require an unusual set of conditions before and during fragmentation. Therefore the 1886 melt must have undergone some event not typical to basaltic systems that caused prolonged closed system vesiculation, leading to the acceleration necessary for Plinian eruption (Wilson et al., 1980; Woods, 1988; Papale et al., 1998). In this section we explore factors that may have contributed to this behavior.

Rate of decompression

Tarawera's bubble number densities span a limited range (1.5-2.5×10^6 cm^{-3}; Fig. 4.7), and all the clasts have similar ranges of bubble sizes, bubble shapes, and groundmass crystallinities. This relative homogeneity indicates that all the 1886 magma shared a common early ascent history. The high number densities of microlites and bubbles in the 1886 clasts support an interpretation that this shared early history was characterized by high rates of ascent and decompression.

The microlite crystallinities of the 1886 clasts are unusually high for basaltic products (e.g., Andronico et al., 2005; Lautze and Houghton, 2005). Such high crystallinities can develop during cooling (Cashman and Marsh, 1988; Cashman et al.,

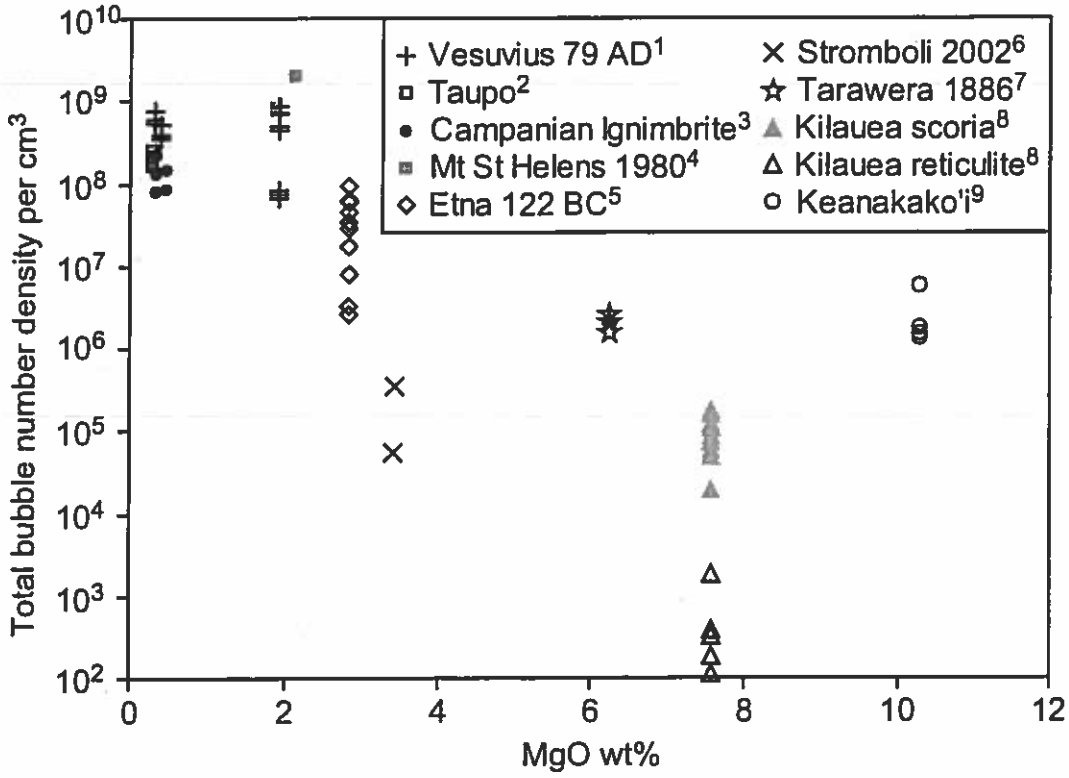

Figure 4.7 Comparison of bubble number densities for explosive eruptions with a range of magma compositions indicated by bulk MgO content. References: (1) Civetta et al., 1991; Gurioli et al., 2005; (2) Froggatt, 1981; B. Houghton, unpublished data; (3) Signorelli et al., 1999; Polacci et al., 2003; (4) Criswell, 1987; Klug and Cashman, 1994; (5) Sable et al., in review; (6) Lautze and Houghton, 2005; (7) this study; (8) Garcia et al., 1992; Mangan and Cashman, 1996; (9) Garcia et al., 2003; Mastin et al., 2004.

1999) or devolatilization (Cashman and Blundy, 2000; Hammer and Rutherford, 2002). We follow previous workers in assuming that the magma did not cool significantly during ascent and that microlites crystallized in response to H_2O exsolution as pressure decreased (Geschwind and Rutherford, 1995; Hammer et al., 1999; Cashman and Blundy, 2000; Hammer and Rutherford, 2002; Couch et al., 2003). The high number densities of microlites ($\geq 10^{12}$ cm^{-3}) in all the 1886 clasts are consistent with high crystal nucleation rates (Kirkpatrick, 1981; Marsh, 1988), which have been experimentally linked to rapid decompression to a relatively low final pressure (Hammer and Rutherford, 2002).

The bubble number densities for the Tarawera 1886 clasts are of the order of 10^6 cm^{-3}, 1-2 orders of magnitude higher than those observed in Strombolian and Hawaiian scoria and 1-3 orders of magnitude lower than those encountered in silicic explosive eruptions (Fig. 4.7). The Tarawera bubble number densities do, however, overlap with the lower end of the range for the Etna 122 BC Plinian eruption (Sable et al., 2006b) and are equal to the values for a pumice-rich phase of the Keanakako'i tephra, which has subplinian dispersal (Mastin et al., 2004). Experimental data are not available for bubble nucleation in basalts, but experiments with silicic magmas show that the rate of bubble nucleation scales with the decompression rate (Mangan and Sisson, 2000; Mangan et al., 2004). We thus suggest that relatively high rates of ascent and decompression led to a rate of bubble nucleation that was higher than the rates in most Strombolian and Hawaiian eruptions but lower than the rate in the Etna 122 BC basaltic Plinian eruption (Sable et al., 2006b).

Decompression could be associated with magma ascent or could result from unloading followed by the downward propagation of a decompression wave (Martel et

al., 2000; Koyaguchi and Mitani, 2005; Namiki and Manga, 2005; Toramaru, 2006). No evidence for a catastrophic unloading event is observed on Mt Tarawera, so we attribute the inferred rapid decompression to rapid magma ascent in the shallow conduit.

Volatile budget

We investigate the amounts and types of volatiles that may have been available to drive the rapid ascent of the 1886 magma. Melt inclusions are not available in the Tarawera clasts due to the scarcity of cognate phenocrysts, but the H_2O content of the 1886 magma is roughly constrained by the whole rock compositions adjusted for the presence of xenocrysts, phenocryst assemblage (plagioclase + clinopyroxene + olivine), and clinopyroxene compositions (A. Freundt, pers. comm. 2006). Clinopyroxene geobarometry (Nimis, 1999) yields a range of P_{total} values from <100 to >700 MPa, with a high frequency of values from 100 to 300 MPa for the 1100 ± 20°C temperature suggested by pyroxene-melt geothermometry (Nielsen and Drake, 1979). To estimate the H_2O content, whole rock normative compositions are projected through plagioclase onto the Fe-free quartz-olivine-clinopyroxene ternary phase diagram contoured for various combinations of P_{total} and P_{H2O} (Grove and Kinzler, 1986). The normative compositions plot along the experimentally determined plagioclase-clinopyroxene-olivine cotectic at P_{total}=100-300 MPa and P_{H2O}=100-170 MPa, indicating an initial dissolved water content of 3-5 wt% (Moore et al., 1995). The overlap between the ranges of P_{total} and P_{H2O} indicates that the melt may have been H_2O-saturated ($P_{H2O}=P_{total}$) or moderately undersaturated ($P_{H2O}<P_{total}$) during phenocryst crystallization. Scatter in the P_{total} constraint provided by clinopyroxene thermobarometry and the scarcity of experimental data for basalts at elevated P_{H2O} contribute to uncertainty in the H_2O concentration

estimate. Although ≥3 wt% H2O is considered high for basaltic melt (e.g., Métrich et al., 1993; Anderson and Brown, 1993; Dixon and Clague, 2001), olivine-hosted melt inclusions in clasts from the Etna 122 BC eruption (Del Carlo and Pompilio, 2004) and the 2002-03 flank eruption of Etna (Spilliaert et al., 2006a) contain up to 3.5 wt% H_2O.

The high initial H_2O content was certainly important in powering the eruption, but its influence was most likely limited to the relatively shallow conduit, because H_2O typically cannot exsolve at depths of several kilometers (Wallace and Anderson, 2000). We consider the additional possibility that a high CO_2 content could have played a critical role by driving some vesiculation early in ascent. Recent work from Etna and Kilauea suggests that very high initial CO_2 contents (of the order of 1-3 wt%) may be common, especially for subduction zone related volcanoes (Papale et al., 2006; Spilliaert et al., 2006a). By analogy, we suggest that the Tarawera magma could have contained at least 1 wt% CO_2. For Etna and Kilauea, much of the initial CO_2 is lost through open system degassing processes during residence in shallow magma reservoirs (Gerlach and Taylor, 1990). However there is no seismic evidence for a shallow crustal magma chamber beneath Mt Tarawera (Bibby et al., 1995), and petrologic data indicate that the basaltic magma may have risen directly through ~15 km thick crust (Graham et al., 1995). We speculate that the exsolution of significant CO_2 at depth could have given an early start to the upward acceleration of the magma.

Effective viscosity of magma

Several observations suggest that the Tarawera 1886 magma had a considerably higher bulk viscosity than typical basaltic magmas. Clast morphologies from the Plinian phase are ragged to blocky and lack the fluidal morphologies produced in Hawaiian and Strombolian eruptions. In addition, the complex shapes of bubbles, which contrast with the spherical forms of Strombolian bubbles (Lautze and Houghton, 2005), indicate that the magma was too viscous for bubbles to relax to spherical shapes in the time available between coalescence and fragmentation. Several factors influence the effective viscosity of magma, including temperature (McBirney and Murase, 1984; James et al., 2004); chemical composition of the melt, particularly SiO_2 and H_2O contents (Shaw, 1972; Giordano and Dingwell, 2003b); number and size of bubbles (Manga et al., 1998; Llewellin et al., 2002); number, size, and shape of crystals and other suspended particles (Pinkerton and Stevenson, 1992; Lejeune and Richet, 1995); and shear rate (Smith, 1997; Sonder et al., 2006). We consider each of these factors below.

The 1886 magma is a high-alumina basalt with 51 ± 0.3 wt% SiO_2, 6.2 ± 0.1 wt% MgO, and ~3 wt% initial H_2O (A. Freundt, pers. comm. 2006). As previously described, the temperature of the 1886 magma is estimated at 1100°C. The Shaw (1972) empirical model gives calculated viscosities of 20 Pa s for melt with 3 wt% H_2O or 200 Pa s for anhydrous melt at 1100°C. The experimentally calibrated model of Giordano and Dingwell (2003b) agrees that the loss of 3 wt% H_2O produces an order of magnitude increase in the melt viscosity.

We consider the chemical and physical effects of microlites on the rheology of the 1886 magma. Mass balance calculations show that as microlite crystallinity increases

from 0 to 90 wt% with the phase proportions observed in the Tarawera clasts, the SiO_2 content of the residual melt increases from 51 wt% to 56 wt% (basalt to basaltic andesite). The elevated SiO_2 causes an increase in the anhydrous melt viscosity from 200 to 700 Pa s (Shaw, 1972). H_2O also may become concentrated in the melt as anhydrous mineral phases crystallize, but this cannot be quantified at present because the relative rates of crystallization and H_2O loss due to degassing are not constrained. Dissolved H_2O is very effective at reducing viscosity (Dingwell et al., 1996), and even a small increase in H_2O concentration in the melt would probably more than cancel out the effect of the increase in SiO_2 (Giordano and Dingwell, 2003b). We conclude that changes in melt chemistry accompanying microlite crystallization probably change the melt viscosity only slightly, if at all.

Although the microlites have only a modest chemical effect on the melt viscosity, they have a large physical effect on the effective viscosity of the bulk magma. Several workers have measured or modeled the rheological effects of solid particles in suspension (Roscoe, 1952; Sherman, 1968; McBirney and Murase, 1984; Pinkerton and Stevenson, 1992; Saar et al., 2001), but only a few have considered crystallinities over ~50 vol% because effective viscosities cease to be predictable with the onset of interaction among crystals (Van der Molen and Paterson, 1979; Lejeune and Richet, 1995; Costa, 2005). In experiments with synthetic crystal suspensions, Lejeune and Richet (1995) observed that viscosity initially increased slowly and exhibited a Newtonian variation with shear rate as crystallinity increased from 0 to 40 vol%. Between 40% and 60% crystallinity, the viscosity soared by as much as 8 orders of magnitude and became strongly non-Newtonian. At still higher crystal contents, the viscosity resumed a slow increase with

crystallinity, and acted like a Bingham fluid with a yield strength. Lejeune and Richet (1995) suggested that a crystallinity of 40 vol% marks the onset of crystal interaction and accompanies a transition from an approximately Newtonian regime dominated by the liquid phase to a non-Newtonian regime dominated by a framework of closely packed particles. Van der Molen and Paterson (1979) observed a similar rheological transition at 60-70% crystallinity in suspensions of rhyolitic composition. The 85-99% groundmass crystallinities of the Tarawera clasts fall completely into the non-Newtonian rheological regime of Lejeune and Richet (1995). We thus envision a magmatic suspension with a high yield strength and a viscosity of at least 10^7 Pa s that depends strongly on shear rate (Lejeune and Richet, 1995; Costa, 2005; Sonder et al., 2006).

Microlites are not the only solid particles in the Tarawera magma. Juvenile clasts also contain 1-3 vol% foreign inclusions comprising xenoliths and xenocrysts derived from rhyolite country rock. The xenoliths are evidence for early incorporation of wall rock at depth in the conduit (Carey, 2002). This small abundance of foreign particles increases the effective viscosity by far less than an order of magnitude (Sherman, 1968; Lejeune and Richet, 1995), so the physical effect of the inclusions is dwarfed by the massive effect of the microlites. However, the xenoliths and xenocrysts were cold when they were entrained, causing the melt to decrease in temperature and thus increase in viscosity (McBirney and Murase, 1984). Heating and vaporization of groundwater in the pores of the pumiceous xenoliths also would have cooled the magma and further increased the effective viscosity.

We estimate the mass of groundwater that might accompany the wall rock inclusions in the magma, assuming that the wall rock particles come from nonwelded

rhyolite pumice deposits saturated with groundwater. Wet and dry measurements of typical Kaharoa pumice lapilli indicate that they can hold 12 wt% water. The typical porosity for coarse granular deposits is ~30% (Pettijohn, 1957), so 1 vol% water may be added for every 2 vol% wall rock inclusions found in the basalt. In 100 kg of basaltic melt, we thus estimate that 2.5 kg of rhyolite and 0.7 kg of groundwater may be incorporated.

To calculate the maximum temperature drop that the basalt would experience during interaction with the rhyolite and groundwater, we add up the enthalpy changes as shown in the equation

$$\Delta H_{total} = M_{H2O}\int_{298K}^{373K} C_{pH2O(l)}dT + M_{H2O}\Delta H_{vap(H2O)} + M_{H2O}\int_{373K}^{1273K} C_{pH2O(v)}dT$$

$$+ M_{rhy}\int_{298K}^{1173K} C_{prhy(s)}dT + M_{rhy}\Delta H_{fus(rhy)} + M_{rhy}\int_{1173K}^{1273K} C_{prhy(l)}dT$$

where ΔH_{total} is the total enthalpy change, T is temperature, M is mass, C_p is heat capacity, and ΔH_{fus} and ΔH_{vap} are the heats of fusion and vaporization of the indicated phases (s, l, and v denote solid, liquid, and vapor, respectively). Published heat capacities (C_p) and heats of fusion (ΔH_{fus}) for basaltic and rhyolitic solids and liquids are obtained from Neuville et al. (1992) and Spera (2000). After the total enthalpy change is calculated, the temperature change of the basalt is determined using $\Delta T = \Delta H_{total} / C_{pbas(l)}$. The enthalpy change associated with heating cold rhyolite, melting it, and heating the melt to ~1000°C would cause the basaltic melt to cool from 1100°C to 1065°C. Heating and vaporizing the groundwater and heating the steam to ~1000°C would cool the basaltic melt by another 35°C, yielding a final temperature of 1030°C. The viscosity model of Giordano and Dingwell (2003b) predicts that such a temperature drop would

cause a 50-1000 Pa s increase in melt viscosity, depending on conditions such as shear rate and the H_2O content of the melt at the time of wall rock interaction.

The contents of both visible and microscopic xenoliths (Fig. 4.4b; Fig. 4.6) are greater in clasts from the widespread proximal section (average 3.5 vol%) than in clasts from the localized proximal section (average 1.5 vol%). The contrasts between the sections elicit the question of whether early wall rock interaction could have been a critical factor in determining the intensity of the eruption. However, our calculations indicate that the difference between the wall rock contents is too small to produce a significant difference in effective magma viscosity or temperature.

Role of external water

Several workers have considered the nature and amount of external water involved in the 1886 eruption (e.g., Cole, 1970; Nairn, 1979; Walker et al., 1984; Houghton and Wilson, 1998). In contrast to Walker et al.'s (1984) proposal that hot geothermal fluids from the Rotomahana area (Fig. 4.1) were responsible for the high intensity of the 1886 eruption, Houghton and Wilson (1998) show that the conditions immediately around Rotomahana were distinct from those on the Mt Tarawera portion of the fissure where the Plinian activity was centered. Houghton and Wilson (1998) argue that the phreatomagmatic explosions that generated proximal units 1 and 4/5 involved not hot geothermal fluids, but cold groundwater. Based on grain size and componentry studies, Carey et al. (2006) propose that the phreatomagmatic phases occurred when the magma column was lowest and groundwater had the greatest access to the conduit. The juvenile clasts from these phreatomagmatic units are dense with glassy outer rinds and breadcrust textures.

The extent of magma/water interaction remains to be established for the climactic phase of the eruption represented by proximal unit 2/3 and the medial-distal fall deposits. The clasts from this phase are ragged and lack quenched rinds or surface cracks. The clasts' dry appearance does not completely rule out external water, however; Houghton and Wilson (1998) note that a small amount of external water may contribute to the explosivity of an eruption without leaving a strong signature on clast morphology.

We use the volume of incorporated wall rock as an indicator for the minimum amount of groundwater that may have interacted with the ascending magma during the climactic phase. In this example we imagine that the magma interacts with the groundwater at a depth of ~100 m (2 MPa pressure); all the water is vaporized and heated to 1030°C, the final temperature of our previous calculations; and the vapor expands to the appropriate volume for that pressure. The volume of 100 kg of basaltic melt is 0.034 m^3, assuming a melt density of 2900 kg m^{-3} (Murase and McBirney, 1973). The volume of 0.7 kg of groundwater is 0.0007 m^3. Assuming ideal gas behavior, 0.7 kg of water vapor at 2 MPa and 1030°C has a volume of 0.02 m^3, or roughly 3000% of its volume as a liquid. This expansion would increase the bulk volume of the magma by 60%. This value is likely to be an extreme overestimate, because mixing is expected to be far from complete in natural systems (Wohletz, 1986). In addition, the calculated water-magma ratio of 0.007 is below the threshold for thermal detonation (Wohletz, 1986), meaning that the magma would not break up along the interface with the water, and the surface area for interaction would remain small. We conclude that external water was not significant in determining the high intensity of the 1886 eruption.

Nature of fragmentation

The lack of fluidal clast morphologies in the Tarawera 1886 deposits suggests that all the magma fragmented while in a brittle state. The high microlite crystallinity may have forced this brittle fragmentation; crystal-rich magmas have been shown to fragment in brittle fashion after less depressurization than crystal-poor magmas (Martel et al., 2001; Taddeucci et al., 2006).

Fragmentation may occur (1) when the magma reaches a threshold vesicularity of ~75% (Sparks, 1978; Wilson et al., 1980); (2) when overpressure within bubbles becomes great enough to exceed the tensile strength of the magma (Zhang, 1999; Melnik, 2000; Spieler et al., 2004; Namiki and Manga, 2005); or (3) when the strain rate is so high that deformation can no longer be accommodated by ductile flow and the melt crosses the glass transition (Papale, 1999b). Criterion (1) is unlikely for the 1886 magma because clast vesicularities span a wide range that extends far below the 75% threshold of Sparks (1978). Criteria (2) and (3) are both good candidates to describe the brittle fragmentation of the 1886 magma, and could even apply jointly (Koyaguchi and Mitani, 2005).

Aspects of the nature and degree of fragmentation may be interpreted from grain size and ejecta characteristics (Walker and Croasdale, 1972; Walker, 1973). Plinian deposits typically have median clast diameters (Md) of 10-50 mm at distances of 1-2 km from vent (Walker, 1981). The Md of the Tarawera 1886 Plinian fall deposit within 2 km of the eruptive fissure is –3.3 ϕ (10 mm; Walker et al., 1984). Several samples from both the localized and widespread proximal sections have Md close to this value (Fig. 4.8; Carey et al., 2006).

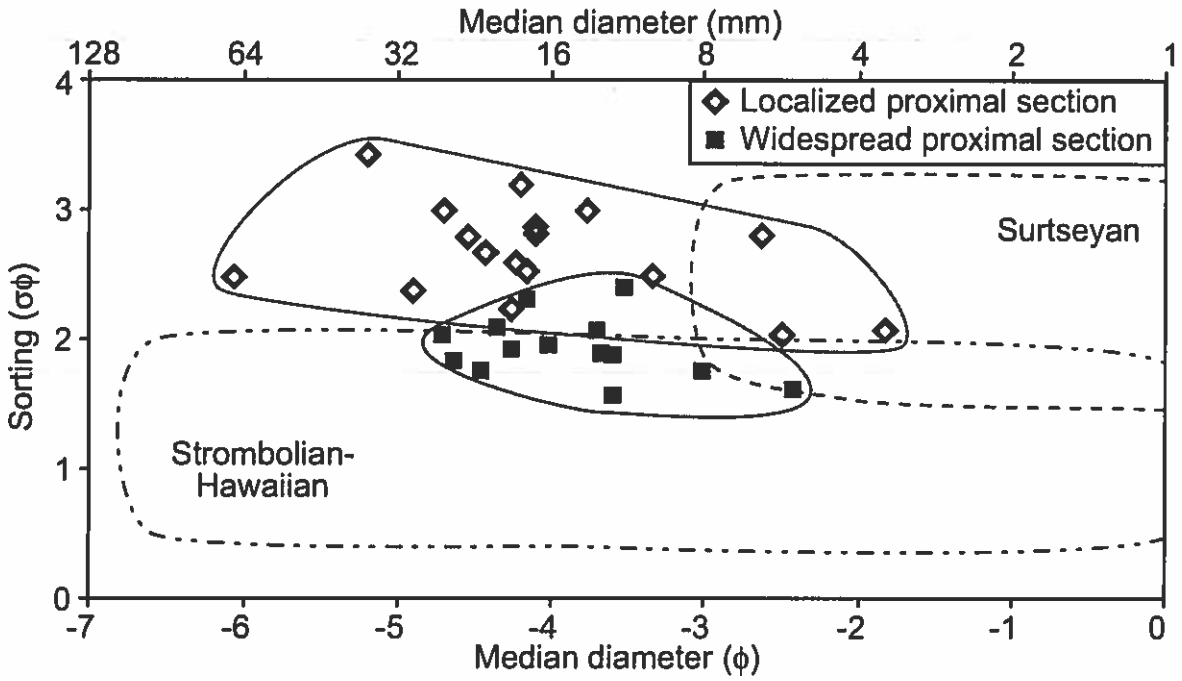

Fig. 4.8 Plot of median diameter vs. sorting for the two proximal sections from Carey et al. (2006). Typical regions for Surtseyan and Strombolian-Hawaiian deposit types are indicated after Walker and Croasdale (1972).

Both sections, but especially the localized proximal section, have poorer sorting than is generally associated with Strombolian and Hawaiian eruptions (Walker and Croasdale, 1972). One reason for the poor sorting in the localized proximal deposits is the presence of large lithic blocks that are probably derived from collapses of unstable vent walls (Fig. 4.9; Carey et al., 2006). The sorting improves when this coarse lithic component is removed, but the localized proximal deposits still contain a significant proportion of ash in contrast with the typical grain size distributions of Strombolian-Hawaiian deposits (Walker and Croasdale, 1972). Sable et al. (2006b) cite this richness in fines as evidence that many clasts in the localized proximal packages were not ejected in Strombolian-style explosions, but were carried to limited heights within the jet regions of Plinian plumes.

As shown previously, the Tarawera clasts show remarkable textural uniformity across the three sections studied, even though these sections have contrasting dispersal characteristics and are spaced kilometers apart. This is powerful evidence that all the Tarawera magma shared a common history over much of ascent. Based on the similarity in grain size characteristics between the localized and widespread proximal sections, we now expand this interpretation to suggest that this shared history extended all the way until fragmentation. Further, both the microtextural and grain size data are consistent with conduit processes associated with Plinian rather than Strombolian eruptions. We conclude that most of the ascent and fragmentation history prepared the magma to erupt with Plinian intensity, but that some mechanism(s) during or after fragmentation prevented the fulfillment of this Plinian potential at several locations.

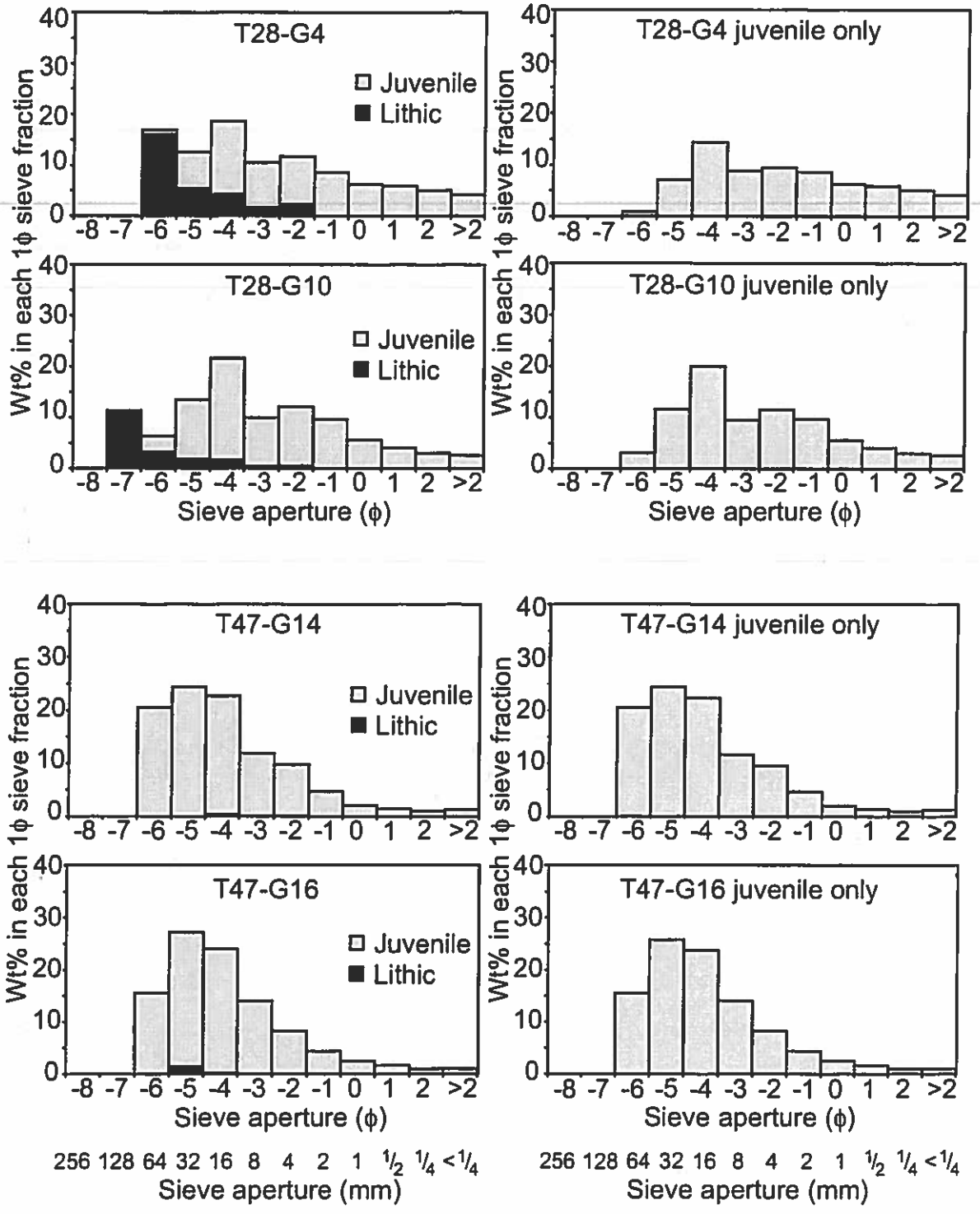

Figure 4.9 Grain size histograms for samples from the localized proximal section and the widespread proximal section, from Carey et al. (2006). The proximal localized section is richer in fines. Right column shows that removal of the coarse lithic component from the localized proximal section's distributions improves the sorting.

Why did some of the 1886 magma fail to achieve Plinian intensity?

Most of the 1886 ejecta were carried in high columns and distributed over a wide area, yet only a few vents erupted with Plinian intensity. In the proximal region, locally dispersed packages of beds are more numerous than widespread packages; thus the majority of the vents along the Mt Tarawera fissure erupted with weaker styles (Sable et al., 2006b). To determine what allowed a single body of basaltic magma to erupt with a diversity of styles, two basic questions must be answered.

(1) Where did the changes happen that led to the diversity? We have established that the 1886 magma had a common history up to the point of fragmentation, so the contrasting characteristics at different vents must have developed at very shallow levels during fragmentation or expulsion from the vent.

(2) What was the nature of the changes that produced the diversity? The similarities in microtextures among sections indicate that the changes did not originate within the magma through vesiculation and crystallization processes; rather, the changes were imposed by variability in external factors such as vent geometry, vent wall stability, and/or groundwater interaction. We explore one such scenario below.

Comparison of ascent histories for locally and widely dispersed clasts

Sable et al. (2006b) described the weak activity on Mt Tarawera as "Strombolian-style" based on the dispersals of the localized packages and the ragged morphology of the clasts. However, the Tarawera 1886 clasts differ from true Strombolian ejecta in several ways. The 1886 deposits lack fluidal and fusiform morphologies that are observed in Strombolian deposits (Walker and Croasdale, 1972; Lautze and Houghton, 2005). In comparison to the microtextures of Strombolian scoria, the Tarawera 1886 clasts have

smaller, more numerous bubbles that are much more irregular in shape, and a far more crystalline groundmass (Fig. 4.10; Lautze and Houghton, 2005). All the 1886 clasts, including those from the most locally dispersed packages, strongly resemble basaltic Plinian and subplinian clasts from eruptions such as Etna 122 BC (Sable et al., 2006b) and Keanakako'i 1500-1790 (Mastin et al., 2004). We therefore suggest that the weaker explosions along the fissure were not "Strombolian-style" (Sable et al., 2006b), but were effectively failed Plinian eruptions.

Variations in vent wall stability

We favor a model in which all the magma was able to vesiculate rapidly, crystallize extensively, and accelerate dramatically before fragmentation, but the erupting jets were affected by differences in vent wall stability and geometry. Carey et al. (2006) show that the abundance of loose wall rock particles in the Tarawera deposit is a poor indicator of explosivity or degree of involvement of external water but a good indicator of wall rock stability in the shallow conduit and vent. Lithic content averages 2 wt% over most of the widespread proximal section, but 18 wt% at the localized proximal section. Most of the lithic particles are derived from shallow depth, and some are partially coated with basalt (Carey et al., 2006).

We propose that the vents that produced the localized proximal deposits had unstable walls that underwent a series of minor collapses during the 1886 eruption. Each collapse sent cold wall rock particles into the vent, where they perturbed the thermal, rheological, and dynamic properties of the ascending gas-pyroclast mixture. The temperature of the erupting jet decreased while its bulk density increased from the addition of the dense lithics. Erosion by vent wall collapse also may have led to a flared

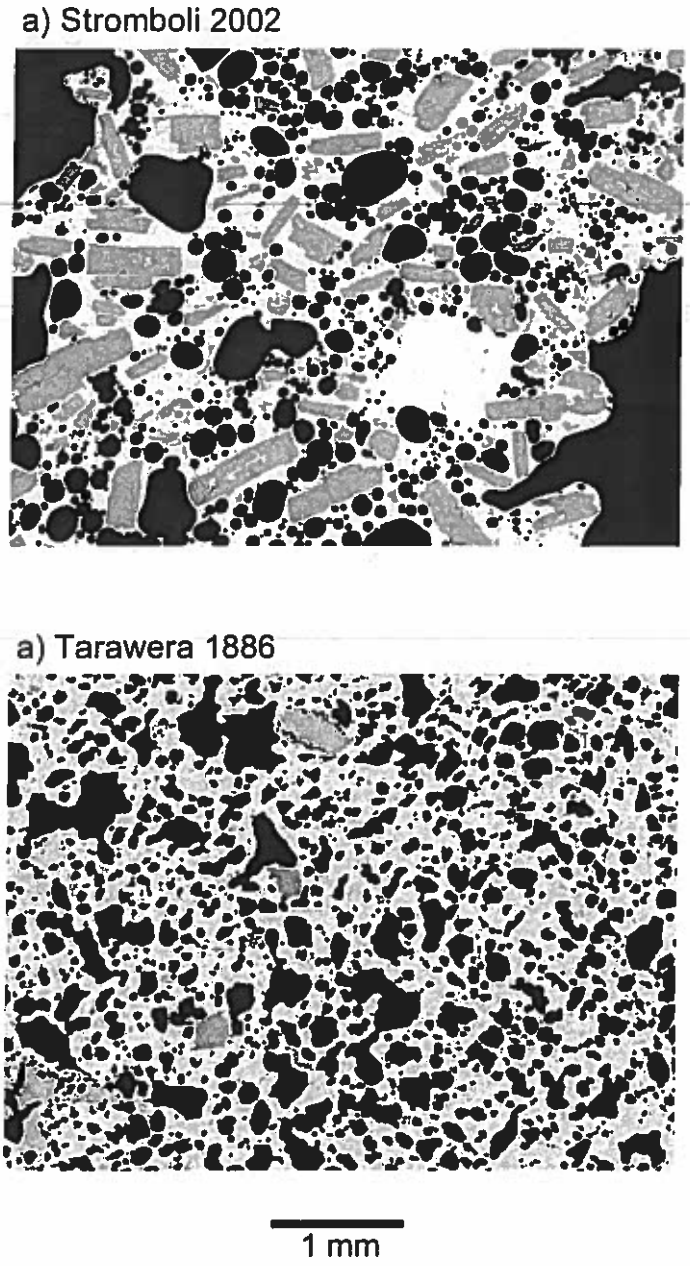

Figure 4.10 Backscatter images of clasts from a) an eruption of Stromboli in 2002 and b) the widespread proximal section of the Tarawera 1886 deposit. The clast from Stromboli has nearly spherical bubbles and many phenocrysts, while the clast from Tarawera has irregular bubble shapes, almost no phenocrysts, and some xenoliths.

vent geometry in some locations, which could have affected the mass eruption rate and the exit velocity of the erupting gas-pyroclast mixture (Wilson et al., 1980; Woods and Bower, 1995). The geometries of the vents during the climactic phase are poorly constrained because late-stage collapses destroyed or obscured previous structures (Nairn and Cole, 1981; Walker et al., 1984). In summary, we suggest that the wall rock interfered with the development of a stable buoyant plume and made sustained eruption impossible at many locations along the fissure.

What caused the Plinian activity to cease?

Bubble coalescence and outgassing

Bubble coalescence is recorded in the complex shapes of vesicles in all the clasts (Fig. 4.5; Klug and Cashman, 1994; Herd and Pinkerton, 1997). Because the patterns of bubble shapes do not vary discernibly among different vent locations and eruptive styles, we suggest that coalescence was an important process in the early shared history of all the 1886 magma. The densest clasts have comparatively small, widely spaced bubbles (Fig. 4.5d), which we interpret as the results of shrinkage due to gas loss after significant growth and coalescence. If the bubbles had been quenched in an early stage of growth, they would be nearly spherical (e.g., Hurwitz and Navon, 1994; Sparks et al., 1994).

Every clast also contains a few large bubbles that plot outside the main size distribution (Fig. 4.5). The bubbles may have expanded to large sizes during transport after fragmentation, but if that were the case, we would expect the large bubbles to be located near the center of each clast. Instead, many of the large bubbles are located close to the edges of the clasts. We infer that the large bubbles are the products of advanced coalescence.

More information about bubble coalescence may be learned from a plot of $\log(N_V{>}R)$ vs. $\log(R)$, where R is bubble radius and $N_V{>}R$ is the cumulative number density of bubbles with radii larger than R (Fig. 4.11; Blower et al., 2001, 2002). Data plotted in this way have been observed to follow power laws or exponential relationships (e.g. Mangan et al., 1993; Cashman et al., 1994; Klug and Cashman, 1994; Mangan and Cashman, 1996; Gaonac'h et al., 1996a,b; Simakin et al., 1999; Blower et al., 2001; Polacci et al., 2003). Power law trends with the form $N_V{>}R = AR^{-d}$, where A is a constant of proportionality and d is the power law exponent, are observed in several natural and experimental examples (Gaonac'h et al., 1996a,b; Simakin et al., 1999; Blower et al., 2001). Gaonac'h et al. (1996a) predict that "pure" cascading coalescence produces a power law with $d = 4.0$, while Blower et al. (2002) predict that continuous bubble nucleation yields lower d values that increase with the length of the interval up to a limit of $d = 2.45$ (Fig. 4.11).

The vesicle populations of the Tarawera modal density clasts are best fit by power laws with $d \approx 3.2$, a value directly between those predicted by the models of Blower et al. (2002) and Gaonac'h et al. (1996a). This result is equivocal on its own, but two other lines of evidence are useful. First, the dense clast from the widespread proximal section follows a power law with $d = 3.8$, close to Gaonac'h et al.'s (1996a) prediction for the cascading coalescence mechanism. This is consistent with our interpretation based on bubble shapes that this dense clast has undergone advanced coalescence.

Second, the minimum bubble diameter in the Tarawera 1886 clasts (0.01 mm) is larger than the bubble size minima for many Plinian deposits (e.g., 0.002 mm for Etna 122 BC and 0.001 mm for Mazama and Mt St Helens; Klug and Cashman, 1994; Klug et

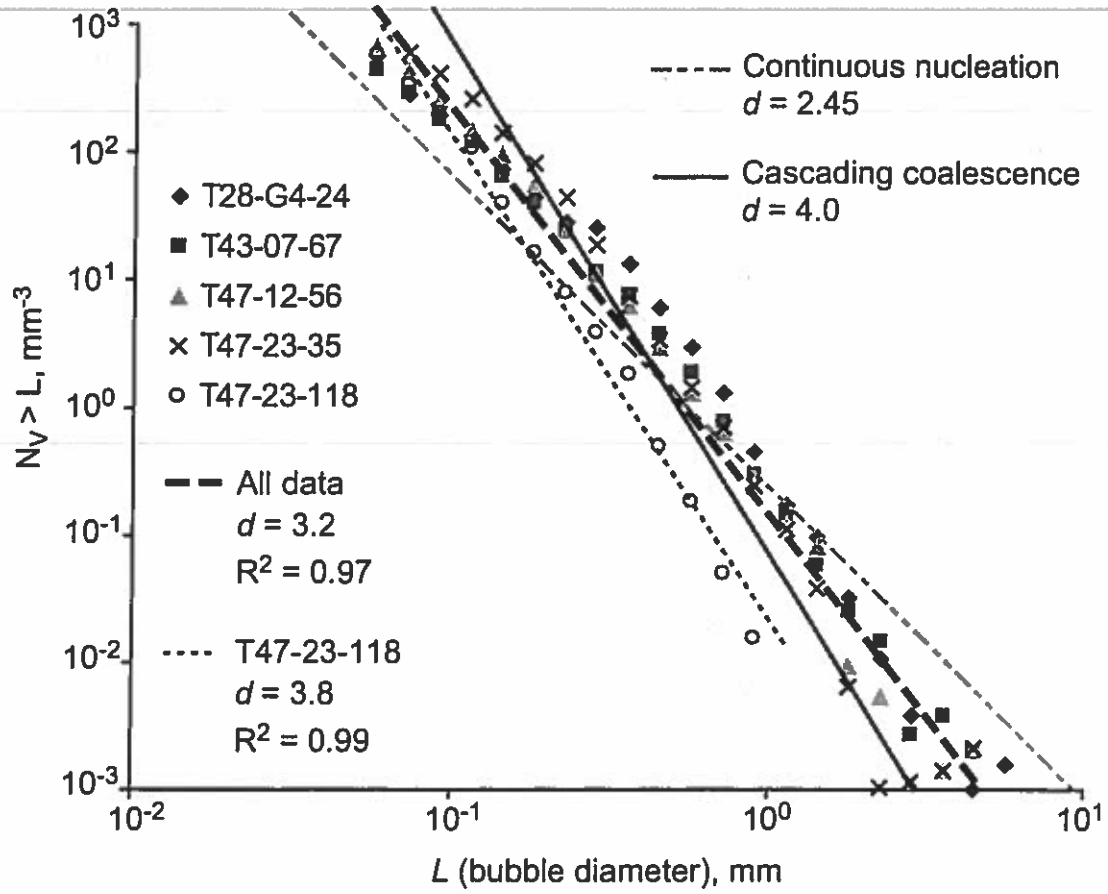

Fig. 4.11 Cumulative frequency distributions of vesicle size. $N_V>L$ refers to the number density of bubbles greater than a given diameter (L). Power laws of the form $N_V>L = AL^{-d}$ fit the data better than exponential or other trends. The d values are shown for the full data set and for the outlying data of sample T47-23-118. Power laws predicted by models of continuous nucleation (Blower et al., 2002) and cascading coalescence (Gaonac'h et al., 1996a) are shown for comparison.

al., 2002; Sable et al., 2006a). We infer that the interval of depth and/or time over which bubbles nucleated in the 1886 magma was shorter than the nucleation intervals in many silicic magmas (Blower et al., 2002). We caution that this interpretation relies on the simplifying assumption that bubbles follow similar growth trends with time regardless of when or where they nucleate.

When considered in combination, the shape, size, and number density data favor the interpretation that coalescence was more important than continuous nucleation in the development of the vesicle populations in the Tarawera 1886 clasts. Bubble coalescence is common in basalts; for example, the gas slugs in Strombolian explosions are produced by the coalescence of many bubbles (Wilson and Head, 1981; Jaupart and Vergniolle, 1989; Herd and Pinkerton, 1997; Parfitt, 2004). Coalescence to this extreme degree leads to decoupling of gas from melt and outgassing by means of upward bubble migration (Blackburn et al., 1976; Parfitt and Wilson, 1995). Low magma viscosity is necessary for this type of outgassing (Wilson and Head, 1981; Parfitt and Wilson, 1995).

We suggest that the high viscosity of the Tarawera 1886 magma would have prevented the production or escape of large, mobile bubbles such as gas slugs. Outgassing could have occurred by an alternative mechanism in which gas travels upward and toward conduit walls through networks of connected bubbles or microfractures (Jaupart, 1998; Gonnermann and Manga, 2003). In highly vesicular clasts, trains of coalesced bubbles (Fig. 4.5a,c) suggest an early stage of permeability development in the 1886 magma (Klug and Cashman, 1996; Gaonac'h et al., 2003; Burgisser and Gardner, 2005). Gas loss through permeable networks may be more common than previously thought, because evidence of these networks is not always

preserved in the clasts. Recent studies show that partially coalesced bubbles may be linked by narrow apertures that serve as pathways for gas, then collapse when gas pressure drops (Gardner et al., 1996; Saar and Manga, 1999). Bubbles may also be connected by microscopic cracks that form by brittle fracture if shear rate is high or stress is locally concentrated (Spieler et al., 2004), then heal or anneal before fragmentation (Tuffen et al., 2003; James et al., 2004; Taddeucci et al., 2004).

Outgassing through permeable networks is probable in the Tarawera eruption, but it only affected a small portion of the magma during the climactic phase. At the transition between proximal units 2/3 and 4/5, a major increase in the proportion of dense juvenile clasts (Carey et al., 2006) suggests a rapid shift toward advanced outgassing. Loss of gas probably led to an increase in magma viscosity and a decrease in eruption rate as suggested by Houghton et al. (2004a).

A conceptual model for the Tarawera 1886 eruption

In our model (Fig. 4.12), the sequence of processes in the 1886 eruption began with the saturation of a continuous body of basaltic melt with CO_2 at a depth close to the base of the crust (~15 km). When CO_2 exsolved, a small proportion of H_2O and other volatiles also diffused into the bubbles (Holloway and Blank, 1994). The mixed gas phase was then lost by bubble migration upward or toward conduit walls. We propose this early vesiculation because open system loss of a CO_2-rich gas phase is now being proposed widely for several basaltic volcanoes (e.g., Papale et al., 2006; Spilliaert et al., 2006a). We envision two important consequences of this early phase of open system degassing. Initially, the gas bubbles increased the magma's bulk volume and buoyancy, resulting in some upward acceleration. The acceleration was limited at this point, however, because

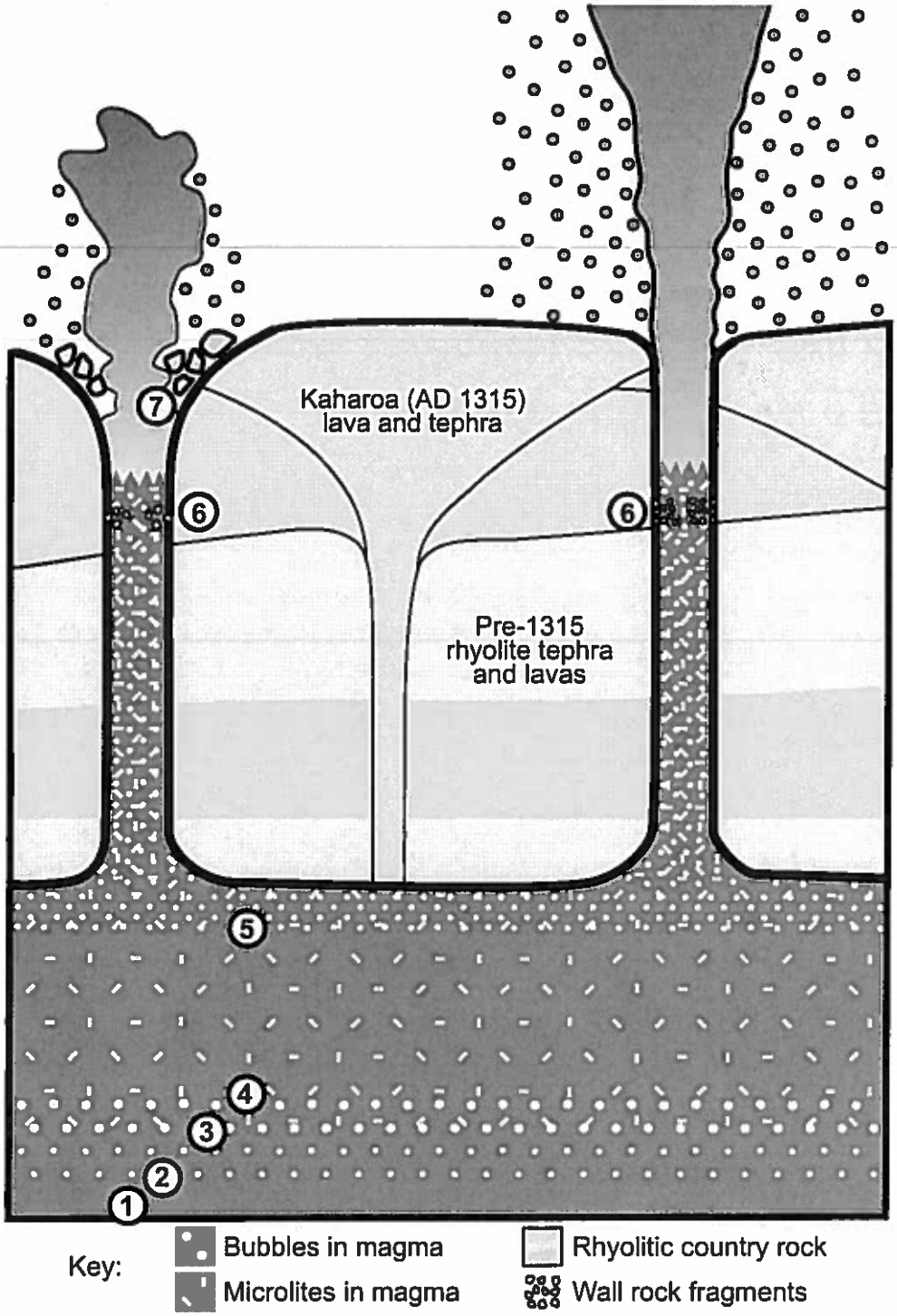

Figure 4.12 Cartoon of processes during the climactic phase of the 1886 eruption. (1) Saturation with CO_2-rich volatile phase. (2) Nucleation of CO_2-rich bubbles. (3) Nucleation of plagioclase microlites as a result of H_2O loss. (4) Decoupling and outgassing of CO_2-rich bubbles. (5) Relatively rapid nucleation of H_2O at moderate supersaturation. (6) Incorporation of small amount of wall rock before fragmentation. (7) Vent wall collapse adds loose coarse lithic fragments after fragmentation and prevents establishment of a stable buoyant plume at many locations.

in our open system assumption the growing bubbles rapidly became decoupled from the melt. Second, the exsolution of some H_2O along with the CO_2 induced some early microlite crystallization that began to increase the effective viscosity of the magma.

As the melt began to rise relatively slowly, crystallization continued, causing a gradual increase in the concentration of H_2O in the melt. Ascent to lower pressure caused the solubility of H_2O to decrease, so that the melt eventually became supersaturated in H_2O. The dominantly plagioclase microlites were not good sites for heterogeneous bubble nucleation, so a high volatile supersaturation developed (Hurwitz and Navon, 1994). At a high enough supersaturation, a population of H_2O bubbles nucleated rapidly and grew quickly. The rapid vesiculation expanded and accelerated the melt; it also increased the melt viscosity and induced more microlite crystallization, both of which increased the effective viscosity of the magma. We suggest that at this point the magma was sufficiently viscous that bubbles were unable to decouple from the melt. This switch from open system behavior at depth to closed system behavior at shallow levels is postulated for eruptions at other basaltic volcanoes, such as Etna (Spilliaert et al., 2006b) and Piton de la Fournaise (Famin et al., 2006).

Based on the limited dispersal of proximal unit 1, the first magma to reach the surface rose less rapidly than the magma that followed, during a period when the conduits were still being established. Due to its slow ascent rate, this early magma was able to interact with groundwater in pores and cracks in the pre-1886 rhyolitic deposits, resulting in phreatomagmatic explosions (proximal unit 1) that helped open the conduits to their full widths. With time, mass flux through the conduit became localized at a few point sources in a manner similar to several well described historical fissure eruptions (e.g.,

Richter et al., 1970; Heliker and Maddox, 2003). At these locations, the magma was able to accelerate extremely rapidly, undergo brittle fragmentation, and erupt with a rapid discharge to produce a high and stable buoyant column. These vents were largely responsible for the widespread Plinian scoria fall and for the more widely dispersed components of the proximal fall deposits, such as the clasts at the widespread proximal section.

Along the rest of the fissure, collapse of weak vent walls caused significant volumes of cold rhyolite to mingle with the gas-pyroclast mixture, resulting in dense, unstable jets that produced beds with very limited dispersals, such as the deposits at the localized proximal section.

4.6 Conclusions

We suggest that rapid ascent and high microlite crystallinity played fundamental roles in driving the 1886 basaltic Plinian eruption of Tarawera. The similarities across all three sections in bubble and groundmass microtextures indicate that all the magma experienced the same conditions for most of ascent. The shared ascent history included relatively rapid nucleation of H_2O-dominated bubbles, nucleation and growth of a very large number and volume of microlites, and development of a high effective viscosity. The magma may also have experienced an early vesiculation of a CO_2-rich volatile phase accompanied by some microlite crystallization, followed by open system loss of the CO_2-rich bubbles. These earliest processes are not well constrained, as they leave no textural signature on the 1886 ejecta.

The likely cause of the divergence in behavior was very shallow and external in nature. Buoyant columns developed at some vents, where vent walls were more stable or high discharge rendered the proportion of engulfed cold vent wall material insignificant. At most vents, wall collapse destabilized the erupting jets and prevented establishment of buoyant plumes.

Acknowledgements

We thank Armin Freundt for contributing unpublished compositional data and calculations for pre-eruptive H_2O content. We are grateful to Helge Gonnermann for numerous insightful discussions of melt rheology and dynamics. Gary Barnes, Julia Hammer, Andy Harris, Don Swanson, and Thor Thordarson contributed helpful comments. Mike Rosenberg and Matthew Patrick provided valuable assistance in the field. This work was funded by NSF grant EAR01-25719.

CHAPTER 5

Conclusions

5.1 Review of the problem

In preparation for presenting the concluding remarks of this dissertation, it is useful to recall what makes an eruption Plinian. If the eruption column can be observed, then an eruption is considered Plinian if it forms a column that is buoyant, sustained, and tall, although a specific minimum height has not been defined. Most Plinian plumes seem to range from 10 to 35 km in height (Walker, 1973), whereas observed subplinian plumes are frequently 4 to 7 km high (e.g., Behncke and Neri, 2003; Andronico et al., 2005; Bonadonna and Houghton, 2005; Neri et al., 2005).

If the eruption is so ancient or remote that no observations or measurements of the plume dimensions are available, then the eruption style is determined by the geometry of its deposit. The deposit must have a sheet-like form to be Plinian. Two quantitative criteria have been proposed. Walker (1973) suggests that the isopach representing 0.01 of the maximum deposit thickness must encompass at least 500 km^2. Pyle (1989) suggests that the ratio of the clast half distance (b_c) to the thickness half distance (b_t) must be no greater than 3. The parameters b_c and b_t are defined as the radial distances over which there is a 50% decrease in the maximum clast diameter and the deposit's thickness, respectively. The maximum clast trend can also be used to estimate column height (Carey and Sparks, 1986).

The critical factor that gives a Plinian eruption its high column and sheet-like dispersal is the intensity. Intensity is synonymous with discharge, the rate of mass

ejected per unit time. Typical Plinian intensities or discharges range from 1.6×10^6 kg/s to 1.1×10^9 kg/s (Carey and Sigurdsson, 1989). The estimated intensities for the Etna 122 BC and Tarawera 1886 eruptions are 8.5×10^7 kg/s and 1.8×10^8 kg/s, respectively (Walker et al., 1984; Coltelli et al., 1998).

Diverse data for Etna 122 BC and Tarawera 1886 have been presented and interpreted in the previous chapters, but so far only limited comparisons have been made between the two deposits. A context for detailed comparison is supplied by revisiting the major questions about basaltic Plinian volcanism. How does basaltic magma erupt with Plinian intensity? Why doesn't it happen more often? How do these eruptions evolve with time? How do these eruptions start and end? Some answers should arise from summarizing and comparing the highlights of the Etna and Tarawera studies.

5.2 Comparisons

Setting

Both Mount Etna and Mount Tarawera are located near active convergent margins with unusual features. Etna is very close to the trench formed by subduction of the African promontory beneath the European plate, but Etna is not an arc volcano; the arc is further northwest (the Aeolian islands). Mantle melting and magma rise beneath Etna are believed to be controlled by transtension along the Malta escarpment (Doglioni et al., 2001). The crust beneath Etna may be unusually thin, ~20 km (Hirn et al., 1997).

Studies based on activity in the 1990s have revealed that Etna has a complex plumbing system with a large magma storage zone 10-15 km deep and one or more smaller reservoirs about 5 km deep (Murru et al., 1999; Caracausi et al. 2003a, 2003b).

Unfortunately, inferences from these data are unlikely to be applicable to storage and ascent conditions in 122 BC, based on the observation that the composition of the 122 BC melt was distinctly more primitive and richer in alkalis than the hawaiite composition typical of historical eruptions prior to 2001. However, in 2001 and 2002, magmas erupted from lower flank vents were compositionally similar to the 122 BC magma. Researchers have proposed that this 2001-2003 flank melt ascended rapidly, bypassing both shallow storage zones and much of the central conduit system, and that this rapid ascent was a major factor in promoting eruption at subplinian intensities (Métrich et al., 2004; Andronico et al., 2005).

Tarawera is part of a volcanic center within an arc associated with subduction of the Pacific plate beneath the Australian plate. This arc is atypical because it has been perturbed by rifting and crustal thinning. The crust in Taupo Volcanic Zone is about 15-18 km thick (Harrison and White, 2004). The basaltic magmas that erupt from Tarawera are believed to rise directly from the lower crust without pausing in magma reservoirs for any significant time (Wilson et al., 1995a).

Etna and Tarawera have contrasting eruptive histories. Etna's eruptive products range from alkali basalt to trachyte (Chester et al., 1985). A major portion of Etna's recent history has been dominated by hawaiite erupting in effusive and weakly explosive styles, but since the 1970's there has been a trend toward more primitive, alkali-rich basalt (Métrich et al., 2004) and more frequent and intense explosive eruptions (Branca and Del Carlo, 2005).

Tarawera is primarily a rhyolitic volcano. The history of Okataina Volcanic Center is dominated by rhyolitic and some limited dacitic volcanism. Many eruptions

had both explosive and effusive (dome growth) phases. Basaltic xenoliths in some deposits show that basalt was present and may have had a role in triggering the silicic eruptions (Nairn et al., 2004), but basalt-dominated explosive eruptions like Tarawera 1886 are rare.

Bulk composition

Key aspects of bulk chemistry for the Plinian phases of the two eruptions are compared in Table 5.1. The Tarawera 1886 magma is more primitive than the Etna 122 BC magma, based on MgO content, and the 122 BC magma is more alkaline than the 1886 magma. The silica and alumina contents are similar for the two magmas. Both also have high initial H_2O contents. The melt inclusion data for Etna 122 BC may underestimate the pre-eruptive CO_2, because recent studies reveal at least 1 wt% initial CO_2 for the very recent eruptions of Etna (Spilliaert et al., 2006a).

Table 5.1. Comparison of selected major element and pre-eruptive volatile contents for the Etna 122 BC and Tarawera 1886 magmas. Data from Coltelli et al. (1998), A. Freundt (pers. comm. 2006), and Chapter 2.

Oxide	Etna 122 BC	Tarawera 1886
SiO_2, wt%	49.6	51.1
Al_2O_3, wt%	18.7	17.2
MgO, wt%	2.9	6.2
K_2O, wt%	1.7	0.5
Na_2O, wt%	4.2	1.8
CaO, wt%	9.2	11.6
H_2O, wt%	1-3	~3
CO_2, ppm	200-900	no data

The higher alkali (Na_2O and K_2O) content of the Etna 122 BC magma may make that melt less viscous. The high alumina contents of both magmas are consistent with the observation that plagioclase is the most abundant and probably the first-nucleating microlite phase for both sets of clasts. Relatively high water contents are important for spurring the main rapid vesiculation that fuels the acceleration necessary to achieve Plinian intensity (Papale et al., 1998).

Bulk densities of clasts

The clasts of Etna 122 BC have lower densities than those of Tarawera 1886. This indicates differences in vesicularities but also in other characteristics. For example, the Tarawera 1886 clasts may have higher microlite contents, and the microlite phases are denser than glass. On the other hand, Etna has more phenocrysts, which are also denser than glass.

Density distributions in most samples of both deposits have tails of dense clasts. In the Etna 122 BC deposit, bimodal density distributions occur at the top of unit C and middle of unit E and indicate that a subpopulation of dense clasts became important toward the end of each Plinian phase. Bimodal density distributions are not observed in the Tarawera 1886 samples; the dense clasts consistently form only a minor portion of the overall clast population.

The Etna clasts became denser with time. The Tarawera clasts maintained the same density with time, or, in the case of the localized proximal section, they show a slight decrease in density with time. These density trends suggest that open system degassing was very important in the late stages of the Etna 122 BC eruption but less important in Tarawera 1886. Microtextural evidence confirms this interpretation.

Vesicles

Overall, the Etna 122 BC clasts show more diversity in their vesicle textures than do the Tarawera 1886 clasts. The modal density clasts of the two eruptions have both similarities and contrasts. The shapes of the bubbles are similar; most bubbles have multiple, irregularly proportioned lobes and fairly smooth, convexly curved outlines. However, the bubbles in the Etna 122 BC modal clasts are smaller, more numerous, and more closely spaced than those of Tarawera 1886 (Fig. 5.1). Etna's bubble number densities range from 2.6×10^{6} to 6.1×10^{7} cm^{-3}, compared to Tarawera's 3.4×10^{6} to 4.0×10^{6} cm^{-3}. The overlap in the bubble number densities suggests that the Tarawera magma had a similar decompression rate to at least part of the Etna magma. The Etna and Tarawera magmas both experienced decompression rates and supersaturation pressures that were higher than those associated with Hawaiian and Strombolian eruptions.

The maximum density clasts of the two deposits share a resemblance. The bubbles are comparable in size (20-200 μm) and have similar complex, somewhat angular shapes. Tiny angular void spaces are present in dense clasts from both deposits; they are interpreted as diktytaxitic voids produced by contraction of the magma during crystallization and cooling (Walker, 1989).

Bubble volume fraction histograms (Fig. 5.2) allow more precise comparison, although the data from the two deposits are not perfectly equivalent. The Etna samples come from different stratigraphic levels at the same location, while the Tarawera samples come from different locations at stratigraphic levels that cannot be correlated. The modal density clasts from samples C1, C2, and E1 of the Etna 122 BC deposit look similar to

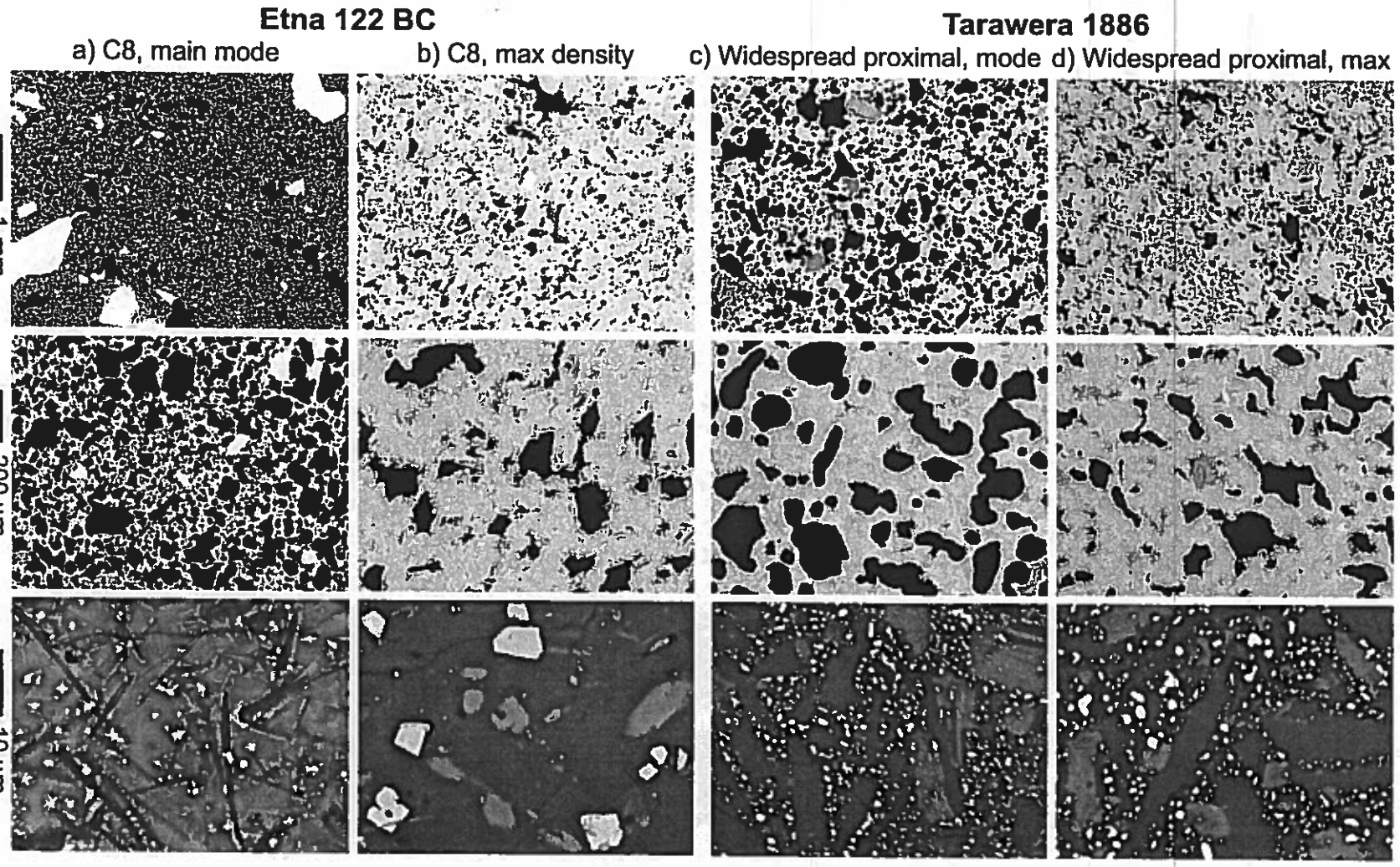

Figure 5.1 Selected backscatter images of one modal density and one maximum density clast from each deposit. The Etna 122 BC mode clast has much smaller bubbles and fewer microlites. The maximum density clasts have similar bubble sizes.

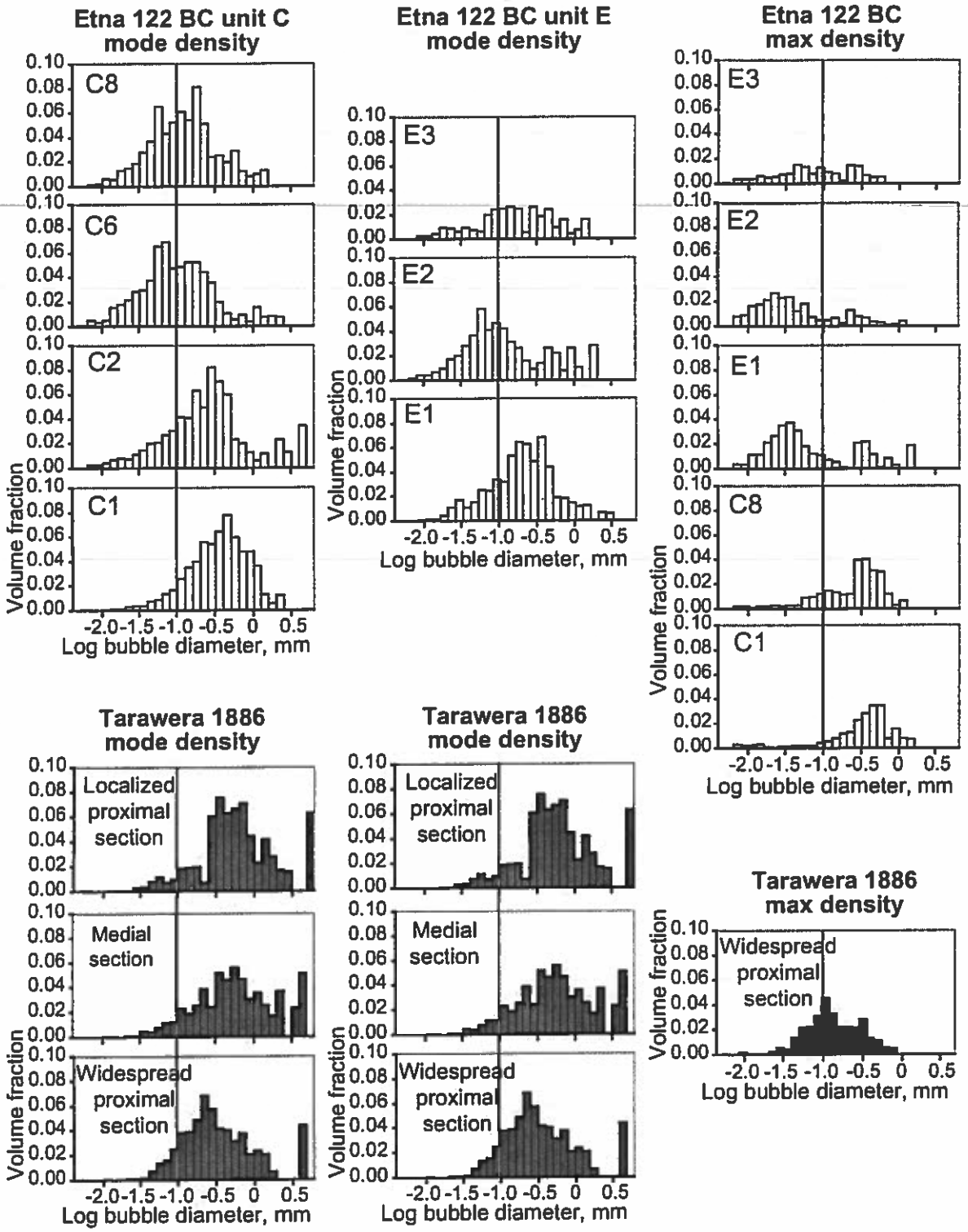

Figure 5.2 Selected histograms of bubble volume fraction with log bubble diameter. Volume fraction values are per volume of bubble-free melt. The set of Tarawera 1886 modal histograms is repeated beneath Etna 122 BC units C and E to facilitate comparison. Vertical lines are drawn through 1 mm bubble diameter for comparison.

the modal clasts from the three sections studied for Tarawera 1886, with the peak volume fraction at 0.2 to 0.5 mm bubble diameter. The histograms also share a negative skew toward small bubbles. The modal Tarawera 1886 clasts all contain a few large (5-6 mm) bubbles that take up a significant volume fraction, but the Etna clasts generally lack bubbles of this size, suggesting that there was less opportunity for bubble coalescence during the 122 BC eruption.

The Etna 122 BC maximum density clasts undergo a strong shift toward smaller bubbles over the transition between the two Plinian phases of that eruption. The shift is attributed to outgassing in some portions of the magma through processes of permeability development and bubble collapse. Only one maximum density clast was measured for Tarawera 1886, and its peak bubble size was found to be directly between the coarser populations of Etna's phase C and the finer populations of Etna's phase E. This suggests that bubble collapse may not have been as pervasive in the Tarawera 1886 magma, but I hesitate to make conclusions based on only one sample.

The clasts from both deposits show power law relationships between bubble number density and bubble diameter. Power laws are also observed on "classical" plots of $\ln(n)$ vs. L, where L is the bubble diameter and n is the number of bubbles in a size bin divided by the size of that bin. Several researchers claim that the $\ln(n)$ vs. L plot should form a straight line, indicating an exponential relationship between n and L, if bubble nucleation and growth processes follow the classical theory developed for crystal nucleation and growth (Mangan et al., 1993; Cashman et al., 1994; Klug and Cashman, 1994; Mangan and Cashman, 1994, Klug et al., 2002). The expectation of an exponential relationship is based on an assumption that degassing is a steady state process. In this

model, bubbles grow out of a given size bin at a constant rate, other bubbles grow into that bin at the same rate, maintaining a steady state (Mangan and Cashman, 1996).

The steady state assumption is contested by some recent findings, including the results of this dissertation. Other researchers have observed curved trends on plots of $\ln(n)$ vs. L (Klug et al., 2002; Gurioli et al., 2005), and some have quantified this curvature and found power law relationships (Gaonac'h et al., 1996; Simakin et al., 1999). Workers who build their interpretations on the steady state assumption explain deviations from an exponential trend as the influence of additional processes such as bubble coalescence and accumulation (Mangan et al., 1993). These additional processes are treated as secondary to the nucleation and growth predicted by classical theory (Mangan and Cashman, 1996). Recent work suggests that the processes that produce power law bubble size distributions are important and widespread, especially for basalts (Blower et al., 2001; Gaonac'h et al., 2005). My work agrees with the newer studies and shows clearly that, in the Etna 122 BC and Tarawera 1886 basalts, coalescence is likely to be the rule, not the exception, from relatively early in the history of ascent of the melt.

Microlites

Microlites form at least 60 vol% of the groundmass in virtually all the clasts from Etna 122 BC and Tarawera 1886 tephras. The high microlite volume fractions and number densities in the Etna 122 BC and Tarawera 1886 clasts contrast with Hawaiian and Strombolian scoria, which are typically microlite-poor (Lautze and Houghton, 2005; Polacci et al., 2006). High number densities of microlites are observed in clasts from both eruptions, suggesting high crystal nucleation rates (Kirkpatrick, 1981; Marsh, 1988) and high rates of decompression in the shallow conduit (Hammer and Rutherford, 2002).

As noted for the bubble textures, the groundmass textures are more diverse in the Etna 122 BC clasts than in the Tarawera clasts. For Tarawera, groundmass textures are fairly uniform regardless of clast density, stratigraphic position, or location along the 1886 fissure. Crystals are generally acicular to prismatic, but many plagioclase laths have swallowtail ends indicative of diffusion-controlled growth. For Etna 122 BC, the groundmass textures are linked to clast density (Fig. 5.1). Low and modal density clasts have microlites with acicular and bladed microlite habits that commonly form radiating clusters in a glassy matrix. High density clasts have higher crystal number densities, more euhedral and prismatic crystal habits, and less glass. A few high density clasts are dominated by relatively coarse interlocking microlites (Fig. 5.1), which may indicate conditions where growth rate greatly exceeded nucleation rate. Alternatively, the coarse microlites may have formed by secondary recrystallization (Means and Park, 1994).

Both the Tarawera and Etna clasts contain domains or zones containing very fine-grained, anhedral crystals that probably nucleated late in ascent. This interpretation suggests that microlite crystallization continued to the point of fragmentation, and possibly afterward, depending on the heat retained by the fragmented clots of magma.

The Tarawera 1886 clasts are more microcrystalline than the Etna 122 BC clasts, but both deposits have enough microlites to affect the bulk viscosities of the magmas. Experiments by Lejeune and Richet (1995) show that crystals begin to interact at about 40 vol% in analog suspensions, causing effective viscosity to increase sharply by several orders of magnitude. Above 60 vol% crystals, effective viscosity continues to increase with crystallinity, but at a much slower rate. The modal clasts contain ≥60 vol% microlites for Etna 122 BC and ≥85 vol% for Tarawera 1886. Therefore, although the

average crystallinities of Etna 122 BC and Tarawera 1886 differ by ~20%, their effects on bulk viscosity may still be similar.

The microlites also affect the fragmentation mechanism. Experiments with Etna magmas erupted in 2001 and 2002 suggest that microlite-poor magmas fragment in ductile fashion but that microlite-rich magmas fragment in brittle fashion (Taddeucci et al., 2006). Brittle fragmentation by the stress or strain rate criteria is consistent with the observation that neither the Etna nor the Tarawera deposits contain achneliths or other fluidal clast textures.

In addition to the Etna 122 BC and Tarawera 1886 eruptions, high microlite crystallinities are associated with relatively high intensity in other basaltic examples (e.g., Keanakako'i layer 6 and Kulanaokuaiki unit 3 tephras; D. Swanson, pers. comm. 2006). Does this mean that a high microlite content is a necessity for basaltic Plinian volcanism? The clasts of another basaltic Plinian eruption, the Fontana Lapilli (Williams, 1983), contain only a few microlites with skeletal habits (Costantini, 2006). I conclude that microlites encourage coupling between gas and melt by increasing effective viscosity, and they also promote brittle fragmentation, but microlites are not a necessary condition for basaltic magma to achieve Plinian intensity.

Other included particles

The Etna clasts contain 1-10 vol% phenocrysts of plagioclase and minor clinopyroxene and olivine. The average phenocryst content of the Tarawera clasts is <1 vol%, and many clasts have no true phenocrysts. Xenoliths in the Etna clasts are rare and made of older basaltic lava. In contrast, small xenoliths are pervasive in the Tarawera scoria; most clasts contain 1-3 vol% rhyolitic xenoliths and xenocrysts.

The phenocrysts in the Etna 122 BC clasts amount to considerably less than the 40 vol% threshold at which crystals start to interact (Lejeune and Richet, 1995), so their effect on the magma's bulk viscosity is negligible compared to that of the microlites. Phenocrysts could affect the eruption by providing nucleation sites for bubbles, and my observations suggest that some phenocrysts were wetted by bubbles. However, most of the phenocrysts are plagioclase, which form inefficient sites for bubble nucleation (Hurwitz and Navon, 1994), and there is no evidence that the phenocrysts triggered widespread heterogeneous bubble nucleation. Also, experiments suggest that it is possible for supersaturation to develop even with nucleation sites present, as long as the number density of sites is less than 1000 cm^{-3} (Mangan et al., 2004).

Like Etna's phenocrysts, Tarawera's xenoliths make up a small volume, but the xenoliths have the additional effect of causing some heat loss by the magma. However, calculations in Chapter 4 show that even with the cooling effect, the xenoliths increase the viscosity very little. Some rhyolite could have melted and mixed with the basalt during the 1886 magma's interaction with the wall rock, but the high ascent rates inferred for both eruptions would not provide much time for melting or chemical interaction between the magma and the incorporated particles. If a rhyolitic component was added to the melt, it was not a large enough quantity to shift the 1886 magma's major element composition away from that of a high-alumina basalt.

Start and end of each eruption

Microtextural results support the idea that fast magma ascent associated with rapid decompression caused the Plinian phases of the Etna 122 BC eruption. The trigger for the fast ascent is not obvious, but it could have been early CO_2 vesiculation and resulting upward acceleration of the magma, or decompression due to deformation of the volcano's flank (Coltelli et al., 1998). The rapid decompression created a large supersaturation pressure and triggered homogeneous bubble nucleation at a high rate. Fast ascent and decompression are likewise proposed for the Plinian phase of the Tarawera 1886 eruption and may likewise have been caused by early CO_2 vesiculation.

The Etna 122 BC eruption declined due to open system degassing that began to develop in the first Plinian phase and became dominant in the second. In my model, the conduit became blocked by stagnant, outgassed magma that was no longer accelerated by coupled bubbles. The eruption ended with passive outgassing and weak phreatomagmatic activity. Outgassing was much more limited during the Plinian phase of the Tarawera 1886 eruption, but the Plinian unit is directly overlain by a phreatomagmatic deposit rich in dense, outgassed juvenile clasts. This suggests a rapid shift toward open system degassing accompanied by a drop in column height and a reversion to weak phreatomagmatic eruptions (Carey et al., 2006). Therefore, both eruptions ended with a switch from closed to open system degassing, but the transition was more gradual for Etna 122 BC.

What caused the basaltic Plinian eruptions?

The two eruptions share a similar sequence of processes (Fig. 5.3). Minor differences arise from factors external to the magma, such as the geometry of the plumbing system and the stability of the conduit and vent walls.

- Magma reservoir: For the Etna 122 BC eruption, some phenocrysts formed during residence in a magma reservoir. For the Tarawera 1886 eruption, no crustal magma reservoir existed, and phenocryst growth was extremely limited.

- Early bubble nucleation: For both eruptions, early nucleation of a CO_2-rich gas phase is a plausible mechanism to increase ascent rate and invoke early microlite nucleation, but, as at Kilauea and in more recent Etna eruptions, no evidence of it is preserved in the clast textures. If an early phase of volatile loss did occur, it may have triggered nucleation of some microlites, which in turn may have increased H_2O concentration in the melt.

- Ascent and decompression rates: For both eruptions, fast decompression led to rapid nucleation of H_2O-dominated bubbles. For the Etna 122 BC eruption, flank deformation has been proposed as a trigger for rapid decompression, but evidence has not yet been found to support or refute this idea. Rapid degassing caused expansion and upward acceleration of the magma and also triggered abundant microlite crystallization.

- Rheological effect of microlites: When microlite crystallinities approached 40 vol%, the magma's effective viscosity increased dramatically.

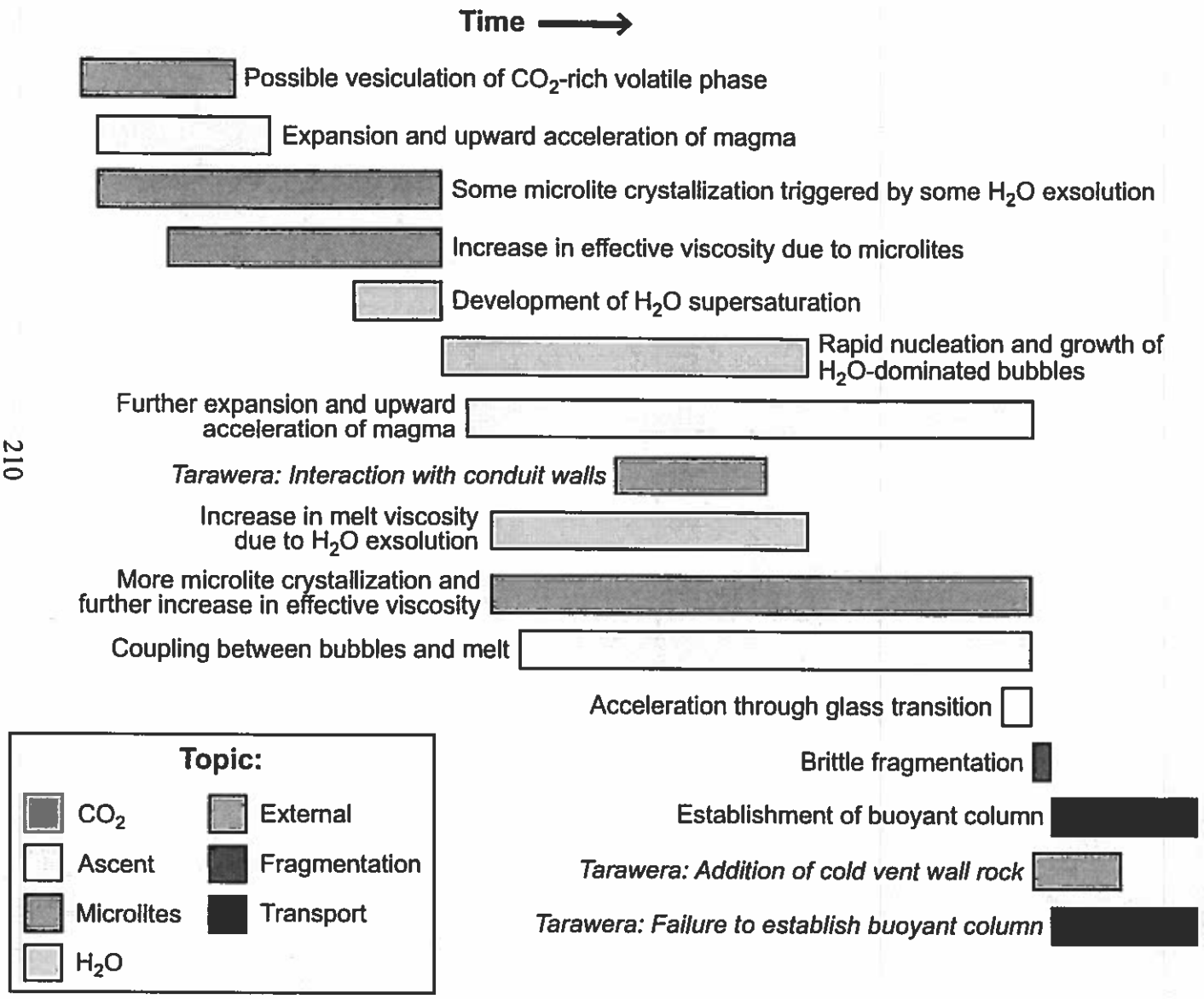

Figure 5.3
Diagram showing sequence of processes in the conduit with time proceeding toward the right (not to scale). Bars are color-coded by topic and show how processes overlap in time. The Etna 122 BC and Tarawera 1886 eruptions follow the same basic pattern, with minor deviations arising from exterior factors.

- Shallow conduit geometry: For the Tarawera 1886 eruption, a long NE-SW trending planar dike split at shallow level into a series of segments with tectonically controlled orientations. For Etna, the form of the shallow conduit is unclear, because there is no proximal exposure.

- Interaction with wall rock: For Tarawera, the magma interacted with the conduit walls to a limited extent, but for Etna, wall rock interaction was not important.

- Fragmentation: For both eruptions, the magma fragmented in a brittle state due to high crystallinity and under conditions of probable high strain rate.

- Vent configuration: For Tarawera, many vents erupted simultaneously, and four Plinian columns fed one large umbrella cloud. For Etna, a single vent generated the Plinian column.

- Vent wall stability: For Tarawera, the stability of the vent walls had a strong effect on the establishment of the buoyant plume. For Etna, vent wall collapses may have contributed some of the ~15 wt% lithic particles, but the plume was not notably affected.

- Transport dynamics: For Tarawera, many erupting jets failed to evolve into fully buoyant plumes. Within the four successful Plinian plumes, many clasts were transported to the umbrella regions, but clasts with a large range of diameters were also released from the margins of the jet portions of the plumes and deposited within ~400 m of vent. For Etna, no exposures close to the vent are preserved.

- Dispersal: For both eruptions, the wind strongly influenced the dispersal of the material that reached the high plume. Dispersal directions were southeast for Etna and north and northeast for Tarawera.

5.3 Summary of conclusions

In the conduit

Bubble and groundmass textures in the Etna 122 BC and Tarawera 1886 scoria contrast strongly with textures observed in typical (i.e., Strombolian and Hawaiian) basaltic eruptions. Even the most locally dispersed Tarawera products have these atypical textures. Thus the processes in the basaltic Plinian eruptions differed from those that govern more typical basaltic styles.

Rapid decompression is inferred for both the Etna and Tarawera eruptions from high number densities of both bubbles and microlites. Rapid ascent is the most likely cause for this decompression. In both eruptions, a high volume fraction of microlites had important effects on effective viscosity and on the state of magma at fragmentation.

The observations lead me to suggest that closed system degassing (coupled degassing) helped accelerate the magma in both eruptions. High effective magma viscosity and rapid ascent helped maintain this coupled behavior.

Open system degassing (outgassing) occurred to a limited extent starting fairly early in each eruption and contributed to the decline and termination of each eruption. In the Etna 122 BC eruption, outgassing affected a gradually increasing proportion of the magma until it completely dominated the conduit at the end of the second Plinian phase.

Outgassing remained limited in the Tarawera eruption until the transition between proximal units 2/3 and 4/5, when it rapidly became dominant.

The principal outgassing process in both eruptions was gas escape through networks of interconnected bubbles and microfractures. Bubble collapse was related to this permeability development. This contrasts with the outgassing mechanism of bubble decoupling that is commonly envisioned for Hawaiian-Strombolian eruptions (e.g., Vergniolle and Jaupart, 1986; Jaupart, 2000; Allard et al., 2005).

The Etna 122 BC eruption featured a curved (parabolic) velocity profile in the conduit, such that magma that ascended along the conduit walls spent more time in the conduit than magma along the axis. The different residence times of different parcels of magma are reflected in the textures of the 122 BC ejecta. It is likely that the Tarawera 1886 conduits were also characterized by curved velocity profiles, but the cross-conduit variation in magma texture was not as pronounced as it was for Etna 122 BC.

In the plume

Studies of the Tarawera 1886 proximal packages suggest that the curved velocity profile in the conduit was inherited by the erupting jet. The slower-moving margins of the jet were less able to support clasts than the faster-moving core of the jet, resulting in near-vent deposition of a large volume of material with a wide grain size range.

In the Tarawera 1886 eruption, closely spaced vents erupted with very different intensities, despite having a uniform bulk composition. Microtextural data show that all the magma shared the same vesiculation history. The differences in eruptive style along the 1886 fissure were primarily caused by collapsed vent wall material entering the vent and perturbing the erupting jet.

5.4. Future directions

Power law relationships between N_V (bubble number density) and L (bubble diameter) are common, especially for basalts, and should not be dismissed as anomalies. Work needs to be done to (a) develop a model that explains power law relationships in thermodynamic and/or kinetic terms, and (b) validate the model with natural systems.

Further experimental work is needed to characterize the effective viscosity trends of suspensions with high particle concentrations. Analog suspensions are useful, but natural magma compositions should also be studied if possible. Studying the detailed nature of the interactions between particles will help improve modeling of such suspensions.

Permeability development followed by bubble collapse is an important but poorly understood outgassing process, especially in basalts. Experiments are needed to study and simulate this type of gas loss. The magma may exhibit a combination of brittle and ductile behavior depending on localized variations in viscosity, stress, or other factors, and this needs to be constrained.

It would be constructive to compile the dispersal and column height data for all relatively intense eruptions of basaltic and similar compositions. Some workers tend to apply the term "Plinian" to any basaltic eruption that seems unusually intense, but many of these eruptions would be more correctly called "subplinian." Examples are the Great Tolbachik eruption of 1975 (Fedotov et al., 1978), the 1986 eruption of Oshima (Sumner, 1998), and the 1783 eruption of Asama (Yasui and Koyaguchi, 2004). More precise use of terminology will allow clearer communication among researchers. A clearer set of criteria that divide Plinian from subplinian may facilitate these efforts. Alternatively, it

may be necessary to recognize that any such criteria would be arbitrary, and there is actually a continuum of basaltic styles.

An experimental study is planned as an extension of the NSF grant that funded this research that will decompress basaltic melt to improve understanding of the changes in bubble and microlite textures with decompression rate. This will also help constrain ascent rate and the relative timing of bubble and microlite formation.

In recent years the previously disparate domains of field-based studies, experiments, and modelling have become increasingly connected. The findings of this research and future studies will contribute to a comprehensive understanding of high-intensity basaltic eruptions that will allow better preparation for the next such event.

REFERENCES

Adams, N.A., Houghton, B.F., Fagents, S.A., Hildreth, W., 2006a. The transition from explosive to effusive eruptive regime: The example of the 1912 Novarupta eruption, Alaska. *Geological Society of America Bulletin 118:* 620-634.

Adams, N.A., Houghton, B.F., Hildreth, W., 2006b. Abrupt transitions during sustained explosive eruptions: examples from the 1912 eruption of Novarupta, Alaska. *Bulletin of Volcanology:* DOI: 10.1007/s00445-006-0067-4.

Allard, P., Burton, M., Mure, F., 2005. Spectroscopic evidence for a lava fountain driven by previously accumulated magmatic gas. *Nature 433:* 407-410.

Allard, P., Carbonnelle, J., Métrich, N., Loyer, H., Zettwoog, P., 1994. Sulfur output and magma degassing budget of Stromboli volcano. Nature *368(6469):* 326-330.

Anderson, A.T., Brown, G.G., 1993. CO_2 contents and formation pressures of some Kilauean melt inclusions. *American Mineralogist 78:* 794–803.

Andronico, D., Branca, S., Calvari, S., Burton, M., Caltabiano, T., Corsaro, R., Del Carlo, P., Garfi, G., Lodato, L., Miraglia, L., Mure, F., Neri, M., Pecora, E., Pompilio, M., Salerno, G., Spampinato, L., 2005. A multi-disciplinary study of the 2002-03 Etna eruption: insights for a complex plumbing system. *Bulletin of Volcanology 67(4):* 314-330.

Armienti, P., Tonarini, S., D'Orazio, M., Innocenti, F., 2002. Genesis and evolution of Mt. Etna alkaline lavas: petrological and St-Nd-B isotope constraints. *Periodico di Mineralogia 73:* 29-52.

Bagdassarov, N.S., Dingwell, D.B., Wilding, M.C., 1996. Rhyolite magma degassing: an experimental study of melt vesiculation. *Bulletin of Volcanology 57:* 587-601.

Barberi, F., Cioni, R., Rosi, M., Santacroce, R., Sbrana, A., Vecci, R., 1989. Magmatic and phreatomagmatic phases in explosive eruptions of Vesuvius as deduced by grain size and component analysis of the pyroclastic deposits. *Journal of Volcanology and Geothermal Research 38:* 287-307.

Barberi, F., Rosi, M., Sodi, A., 1993. Volcanic hazard assessment at Stromboli based on a review of historical data. *Acta Vulcanologica 3:* 173-187.

Barclay, J., Riley, D.S., Sparks, R.S.J., 1995. Analytical models for bubble growth during decompression of high viscosity magmas. *Bulletin of Volcanology 57:* 422-431.

Behncke, B., Neri, M., 2003. The July-August 2001 eruption of Mt. Etna (Sicily). *Bulletin of Volcanology 65*: 461-476.

Belousov, A., Belousova M., 2002. Chikurachki volcano (Kurile islands, Russia): the unique volcano with frequent basaltic plinian eruptions. *Abstracts*, 3rd biennial Workshop on subduction processes emphasizing the Kurile-Kamchatkan-Aleutian Arcs, Fairbanks, Alaska, June 9-15, 2002.

Bibby, H.M., Caldwell, T.G., Davey, F.J., Webb, T.H., 1995. Geophysical evidence on the structure of the Taupo Volcanic Zone and its hydrothermal circulation. *Journal of Volcanology and Geothermal Research 68*: 29-58.

Blackburn, E.A., Wilson, L., Sparks, R.S.J., 1976. Mechanisms and dynamics of strombolian activity. *Journal of the Geological Society of London 132*: 429-440.

Blank, J.G., Brooker, R.A., 1994. Experimental studies of carbon dioxide in silicate melts: solubility, speciation, and stable carbon isotope behavior. In: Carroll, M.R., Holloway, J.R. (Eds.), *Volatiles in Magmas*, Reviews in Mineralogy, Mineralogical Society of America, pp. 157-186.

Blower, J.D., Keating, J.P., Mader, H.M., Phillips, J.C., 2001. Inferring volcanic degassing processes from vesicle size distributions. *Geophysical Research Letters 28:* 347-350.

Blower, J.D., Keating, J.P., Mader, H.M., Phillips, J.C., 2002. The evolution of bubble size distributions in volcanic eruptions. *Journal of Volcanology and Geothermal Research 120:* 1-23.

Bonadonna, C., Ernst, G.G.J., Sparks, R.S.J., 1998. Thickness variations and volume estimates of tephra fall deposits: the importance of particle Reynolds number. *Journal of Volcanology and Geothermal Research 81(3-4):* 173-187.

Bonadonna, C., Phillips, J., 2003. Sedimentation from strong volcanic plumes. *Journal of Geophysical Research 108:* 2340-2368.

Booth, B., Walker, G.P.L., 1973. Ash deposits from the new explosion crater, Etna 1971. *Philosophical Transactions of the Royal Society London A 274:* 147-151.

Bottinga, Y., Weill, D.F., 1972. The viscosity of magmatic silicate liquids: a model for calculation. *American Journal of Science 272:* 438-475.

Branca, S., Del Carlo, P., 2004. Eruptions of Mt Etna during the past 3200 years: a revised compilation integrating the Historical and stratigraphic records. In: Bonaccorso, A., Calvari, S., Coltelli, M., Del Negro, C., Falsaperla, S. (Eds.), *Mt. Etna: Volcano Laboratory*. AGU Geophysical Monograph Series 143, 1-27.

Branca, S., Del Carlo, P., 2005. Types of eruptions of Etna Volcano AD 1670-2003: Implications for short-term eruptive behaviour, *Bulletin of Volcanology:* DOI: 10.1007/s00445-005-0412-z.

Bullard, F.M., 1947. Studies on Paricutin Volcano, Michoacan, Mexico. *Geological Society of America Bulletin 58:* 433-450.

Burgisser, A., Gardner, J.E., 2005. Experimental constraints on degassing and permeability in volcanic conduit flow. *Bulletin of Volcanology 67:* 42-56.

Burnham, C.W., 1994. Development of the Burnham model for prediction of H_2O solubility in magmas. In: Carroll, M.R., Holloway, J.R. (Eds.), *Volatiles in Magmas*, Reviews in Mineralogy, Mineralogical Society of America, pp. 123-129.

Bursik, M.I., Sparks, R.S.J., Gilbert, J.S., Carey, S.N., 1992. Sedimentation of tephra by volcanic plumes 1. Theory and its comparison with a study of the Fogo-A Plinian deposit, Sao Miguel (Azores). *Bulletin of Volcanology 54(4):* 329-344.

Calvari, S., Pinkerton, H., 2004. Birth, growth and morphologic evolution of the 'Laghetto' cinder cone during the 2001 Etna eruption. *Journal of Volcanology and Geothermal Research 132:* 225-239.

Calvari, S., Coltelli, M., Neri, M., Pompilio, M., Scribano, V., 1994. The 1991–1993 Etna eruption: chronology and lava flow field evolution. *Acta Vulcanologica 4:* 1-14.

Caracausi, A., Favara, R., Giammanco, S., Italiano, F., Paonita, A., Pecoraino, G., Rizzo, A., Nuccio, P.M., 2003a. Mount Etna: Geochemical signals of magma ascent and unusually extensive plumbing system. *Geophysical Research Letters 30:* DOI: 10.1029/2002GL015463.

Caracausi, A., Italiano, F., Paonita, A., Rizzo, A., Nuccio, P.M., 2003b. Evidence of deep magma degassing and ascent by geochemistry of peripheral gas emissions at Mount Etna (Italy): Assessment of the magmatic reservoir pressure. *Journal of Geophysical Research 198:* DOI: 10.1029/2002JB002095.

Carey, R.J., 2002. A volcanological study of the proximal deposits from the 1886 Tarawera eruption. Unpublished undergraduate thesis, School of Earth Sciences, University of Tasmania, 103 pp.

Carey, R.J., Houghton, B.F., Sable, J.E., Wilson, C.J.N., 2006. Contrasting grain size and componentry in complex proximal deposits of the 1886 Tarawera basaltic plinian eruption. *Bulletin of Volcanology*, in press.

Carey, S.N., Sigurdsson, H., 1982. Influence of particle aggregation on deposition of distal tephra from the May 18, 1980 eruption of Mount St. Helens volcano. *Journal of Geophysical Research 87(B8):* 7061-7072.

Carey, S.N., Sigurdsson, H., 1989. The intensity of Plinian eruptions. *Bulletin of Volcanology 51:* 28-40.

Carey, S., Sparks, R.S.J., 1986. Quantitative models of fallout and dispersal of tephra from volcanic eruption columns. *Bulletin of Volcanology 48:* 109-125.

Carminati, E., Doglioni, C., 2004. Mediterranean tectonics. In: Selley, R.C., Cocks, L.R.M., Plimer, I.R. (Eds.), *Encyclopedia of Geology*, Elsevier, Amsterdam, The Netherlands, pp. 135-146.

Carrigan, C. R., Schubert, G., Eichelberger, J. C., 1992. Thermal and dynamical regimes of single- and two-phase magmatic flow in dikes. *Journal of Geophysical Research 97(B12)*: 17377-17392.

Cashman, K.V., 1988. Crystallization of Mount St. Helens 1980-1986 dacite: A quantitative textural approach. *Bulletin of Volcanology 50:* 194-209.

Cashman, K.V., 1990. Textural constraints on the kinetics of crystallization of igneous rocks. In: Nicholls, J., Russell, J.K. (Eds.), *Modern Methods of Igneous Petrology*, pp. 259-314.

Cashman, K.V., 1992. Groundmass crystallization of Mount St. Helens dacite, 1980-1986: a tool for interpreting shallow magmatic processes. *Contributions to Mineralogy and Petrology 109:* 431–449.

Cashman, K.V., 1993. Relationship between plagioclase crystallisation and cooling rate in basaltic melts. *Contributions to Mineralogy and Petrology 113:* 126-142.

Cashman, K.V., Blundy, J., 2000. Degassing and crystallization of ascending andesite and dacite. *Philosophical Transactions of the Royal Society of London A 358*: 1487-1513.

Cashman, K.V., Delgado, H., Johnson, E., Pioli, L., Rosi, M., Wallace, P., 2004. A new look at violent Strombolian eruptions - past behavior and future potential. *Abstracts*, IAVCEI General Assembly 2004, Pucon, Chile.

Cashman, K.V., Mangan, M.T., 1994. Physical aspects of magmatic degassing II. Constraints on vesiculation processes from textural studies of eruption products. In: Carroll, M.R., Holloway, J.R. (Eds.), *Volatiles in Magmas*, Reviews in Mineralogy, Mineralogical Society of America, pp. 447-478.

Cashman, K.V., Mangan, M.T., Newman, S., 1994. Surface degassing and modifications to vesicle size distributions in active basalt flows. *Journal of Volcanology and Geothermal Research 61:* 45-68.

Cashman, K.V., Marsh, B.D., 1988. Crystal size distribution (CSD) in rocks and the kinetics and dynamics of crystallization II: Makaopuhi lava lake. *Contributions to Mineralogy and Petrology 99:* 292-305.

Cashman, K.V., Sturtevant, B., Papale, P., Navon, O., 2000. Magmatic fragmentation. In: Houghton, B.F., McNutt, S.R., Rymer, H., Stix, J. (Eds.), *Encyclopedia of Volcanoes*, Academic Press, San Diego, pp. 421-430.

Cashman, K.V., Thornber, C., Kauahikaua, J.P., 1999. Cooling and crystallization of lava in open channels and the transition of Pahoehoe lava to 'A'a. *Bulletin of Volcanology 61*: 306-323.

Cavazza, W., Wezel, F.C., 2003. The Mediterranean region – a geological primer. *Episodes 26:* 160-168.

Chester, D.K., Duncan, A., Guest, J., Kilburn, C., 1985. *Mount Etna, The Anatomy of a Volcano.* Chapman and Hall, London, 406 pp.

Chouet, B., Saccorotti, G., Martini, M., Dawson, P., De Luca, G., Milana, G., Scarpa, R., 1997. Source and path effects in the wave fields of tremor and explosions at Stromboli Volcano, Italy. *Journal of Geophysical Research 102(B7):* 15129-15150.

Cioni, R., Marianelli, P., Santacroce, R., Sbrana, A., 2000. Plinian and subplinian eruptions. In: Houghton, B.F., McNutt, S.R., Rymer, H., Stix, J. (Eds.), *Encyclopedia of Volcanoes*, Academic Press, San Diego, pp. 477-494.

Civetta, L., Galati, R., Santacroce, R., 1991. Magma mixing and convective compositional layering within the Vesuvius magma chamber. *Bulletin of Volcanology 53*: 287-300.

Clocchiatti, R., Condomines, M., Guenot, N., Tanguy, J.C., 2004. Magma changes at Mt Etna: the 2001 and 2002-03 eruptions. *Earth and Planetary Science Letteters 226:* 397-414.

Cole, J.W., 1970. Structure and eruptive history of the Tarawera Volcanic Complex. *New Zealand Journal of Geology and Geophysics 13*: 879-902.

Cole, J.W., 1990. Structural control and origin of volcanism in the Taupo volcanic zone, New Zealand. *Bulletin of Volcanology 52:* 445-449.

Cole, J.W., Darby, D.J., Stern, T.A., 1995. Taupo Volcanic Zone and Central Volcanic Region – back arc structures of North Island, New Zealand. In: Taylor, B. (Ed.), *Back-arc Basins: Tectonism and Magmatism*, Plenum Publishing, New York, pp. 1-28.

Coltelli, M., Del Carlo, P., Vezzoli, L., 1995. Stratigraphy of the Holocene Mt. Etna explosive eruptions. *Periodico di Mineralogia 64:* 141-143.

Coltelli, M., Del Carlo, P., Vezzoli, L., 1998. Discovery of a Plinian basaltic eruption of Roman age at Etna volcano, Italy. *Geology 26:* 1095-1098.

Coltelli, M., Del Carlo, P., Vezzoli, L., 2000. Stratigraphic constrains for explosive activity in the past 100 ka at Etna volcano, Italy. *International Journal of Earth Sciences 89:* 665-677.

Continisio, R., Ferrucci, F., Gaudiosi, G., Lo Bascio, D., Ventura, G., 1997. Malta escarpment and Mt. Etna: early stages of an asymmetric rifting process? Evidences from geophysical and geological data. *Acta Vulcanologica 9:* 45-53.

Costa, A., 2005. Viscosity of high crystal content melts: Dependence on solid fraction. *Geophysical Research Letters 32:* DOI: 10.1029/2005GL024303.

Couch, S., Sparks, R.S.J., Carroll, M.R., 2003. The kinetics of degassing-induced crystallization at Soufrière Hills volcano, Montserrat. *Journal of Petrology 44(8)*: 1477-1502.

Crisp, J., Baloga, S., 1994. Influence of crystallization and entrainment of cooler material on the emplacement of basaltic 'a'a lava flows. *Journal of Geophyiscal Research 99:* 11819-11831.

Criswell, C.W., 1987. Chronology and pyroclastic stratigraphy of the May 18, 1980, eruption of Mount St. Helens, Washington. *Journal of Geophysical Research 92*: 10237-10266.

Darby, D.F., Williams, R.O., 1991. A new geodetic estimate of deformation in the Central Volcanic Region of the North Island, New Zealand. *New Zealand Journal of Geology and Geophysics 34:* 127-136.

Del Carlo, P., Pompilio, M., 2004. The relationship between volatile content and the eruptive style of basaltic magma: the Etna case. *Annals of Geophysics 47*: 1423-1432.

Denlinger, R.P., Hoblitt, R.P., 1999. Cyclic eruptive behavior of silicic volcanoes. *Geology 27(5):* 459-462.

Dingwell, D.B., Romano, C., Hess, K.U., 1996. The effect of water on the viscosity of a haplogranitic melt under P-T-X conditions relevant to silicic volcanism. *Contributions to Mineralogy and Petrology 124:* 19-28.

Dixon, J.E., Clague, D.A., 2001. Volatiles in basaltic glasses from Loihi Seamount, Hawaii: evidence for a relatively dry plume component. *Journal of Petrology 42(3):* 627-654.

Dixon, J.E., Stolper, E.M., 1995. An experimental study of water and carbon dioxide solubilities in mid-ocean ridge basaltic liquids. 2. Applications to degassing, *Journal of Petrology, 36*: 1633-1646.

Dobran, F., 1992. Nonequilibrium flow in volcanic conduits and application to the eruption of Mt St Helens on May 18, 1980, and Vesuvius in AD 79. *Journal of Volcanology and Geothermal Research 49:* 285-311.

Dobran, F., 2001. *Volcanic processes: mechanisms in material transport.* Kluwer Academic/Plenum Publishers, New York, NY, 590 pp.

Doglioni, C., Innocenti, F., Mariotti, G., 2001. Why Mt Etna? *Terra Nova 13(1):* 25-31.

Dvorak, J.J., 1992. Mechanism of explosive eruptions of Kilauea Volcano, Hawaii. *Bulletin of Volcanology 54(8):* 638-645.

Eichelberger, J.C., Carrigan, C.R., Westrich, H.R., Price, R.H., 1986. Non-explosive silicic volcanism. *Nature 323:* 598-602.

Elias, T., Sutton, A.J., Stokes, J.B., Casadevall, T.J., 1998. Sulfur dioxide emission rates of Kilauea Volcano, Hawaii, 1979-1997. *U.S. Geological Survey Open-File Report 98-462:* 40.

Ernst, G.G.J., Sparks, R.S.J., Carey, S.N., Bursik, M.I., 1996. Sedimentation from turbulent jets and plumes. *Journal of Geophysical Research 101:* 5575-5589.

Famin, V., Okumura, S., Peltier, A., Nakashima, S., Bachèlery, P., Delcher, E., 2006. Two degassing paths in magmas from Reunion hotspot: constraints from melt and fluid inclusions. *Geophysical Research Abstracts 8*: 00612, EGU Meeting, Vienna, April 2006.

Fedotov, S.A., Enman, V.B., Magus'kin, M.A., Levin, V.Y., Zharinov, N.A., 1978. Intrusion of basalts and the formation of feeder fissures for the great 1975 Tolbachik eruption, as inferred from geodetic data. *Akademii Nauk Doklady Earth Science Sections 229:* 43-46.

Fierstein, J., Hildreth, W., 1992. The Plinian eruptions of 1912 at Novarupta, Katmai National Park, Alaska. *Bulletin of Volcanology 54:* 646-684.

Fierstein, J., Houghton, B.F., Wilson, C.J.N., Hildreth, W., 1997. Complexities of plinian fall deposition at vent: an example from the 1912 Novarupta eruption (Alaska). *Journal of Volcanology and Geothermal Research 76*: 215-227.

Fink, J.H., Anderson, S.W., Manley, C.R., 1992. Textural constraints on effusive silicic volcanism: beyond the permeable foam model. *Journal of Geophysical Research 97:* 1135-1141.

Fisher, R.V., Schmincke, H.-U., 1984. *Pyroclastic rocks*. Springer-Verlag, Heidelberg, Germany, 472 pp.

Foshag, W., Gonzales, R., 1956. Birth and development of Paricutin volcano. *U.S. Geological Survey Bulletin 965-D:* 355-489.

Froggatt, P.C., 1981. Stratigraphy and nature of Taupo Pumice Formation. *New Zealand Journal of Geology and Geophysics 24*: 231-248.

Froggatt, P.C., Lowe, D.J., 1990. A review of late Quaternary silicic and some other tephra formations in New Zealand: their stratigraphy, nomenclature, distribution, volume, and age. *New Zealand Journal of Geology and Geophysics 33:* 89-109.

Gaonac'h, H., Lovejoy, S., Schertzer, D., 2003. Percolating magmas and explosive volcanism. *Geophysical Research Letters 30(11):* DOI: 10.1029/2002GL016022.

Gaonac'h, H., Lovejoy, S., Schertzer, D., 2005. Scaling vesicle distributions and volcanic eruptions. *Bulletin of Volcanology 67:* 350-357.

Gaonac'h, H., Lovejoy, S., Stix, J., Scherzter, D., 1996a. A scaling growth model for bubbles in basaltic lava flows. *Earth and Planetary Science Letters 139:* 395-409.

Gaonac'h, H., Stix, J., Lovejoy, S., 1996b. Scaling effects on vesicle shape, size and heterogeneity of lavas from Mount Etna. *Journal of Volcanology and Geothermal Research 74:* 131-153.

Garcia, M.O., Rhodes, J.M., Wolfe, E.W., Ulrich, G.E., Ho, R.A., 1992. Petrology of lavas from episodes 2–47 of the Puu Oo eruption of Kilauea Volcano, Hawaii: evaluation of magmatic processes. *Bulletin of Volcanology 55*: 1–16.

Garcia, M.O., Pietruszka, A.J., Rhodes, J.M., 2003. A petrologic perspective of Kilauea Volcano's summit magma reservoir. *Journal of Petrology 44*: 2313-2339.

Gardner, C.A., Cashman, K.V., Neal, C.A., 1998. Tephra-fall deposits from the 1992 eruption of Crater Peak, Alaska: implications of clast textures for eruptive processes. *Bulletin of Volcanology 59:* 537-555.

Gardner, J.E., Hilton, M., Carroll, M.R., 1999. Experimental constraints on degassing of magma: isothermal bubble growth during continuous decompression from high pressure. *Earth and Planetary Science Letters 168:* 201-218.

Gardner, J.E., Thomas, R.M.E., Jaupart, C., Tait, S., 1996. Fragmentation of magma during Plinian volcanic eruptions. *Bulletin of Volcanology 58*: 144–162.

Gerlach, T.M., Taylor, B.E., 1990. Carbon isotope constraints on degassing of carbon dioxide from Kilauea Volcano. *Geochimica et Cosmochimica Acta 54:* 2051-2058.

Geschwind, C.-H., Rutherford, M.J., 1995. Crystallization of microlites during magma ascent: the fluid mechanics of 1980-1986 eruptions at Mount St Helens. *Bulletin of Volcanology 57*: 356-370.

Giordano, D., Dingwell, D.B., 2003a. The kinetic fragility of natural silicate melts. *Journal of Physics of Condensed Matter 15:* S945-S954.

Giordano, D., Dingwell, D.B., 2003b. Viscosity of hydrous Etna basalt: implications for Plinian-style basaltic eruptions. *Bulletin of Volcanology 65:* 8-14.

Gonnermann, H.M., Manga, M., 2003. Explosive volcanism may not be an inevitable consequence of magma fragmentation. *Nature 426*: 432-435.

Graham, I.J., Cole, J.W., Briggs, R.M., Gamble, J.A., Smith, I.E.M., 1995. Petrology and petrogenesis of volcanic rocks from the Taupo Volcanic Zone: a review. *Journal of Volcanology and Geothermal Research 68*: 59-87.

Grove, T.L., Kinzler, R.J., 1986. Petrogenesis of andesites. *Annual Review in Earth and Planetary Science 14:* 417-454.

Gurioli, L., Houghton, B.F., Cashman, K.V., Cioni, R., 2005. Complex changes in eruption dynamics during the 79 AD eruption of Vesuvius. *Bulletin of Volcanology 67:* 144-159.

Hammer, J.E., 2004. Crystal nucleation theory applied to hydrous magma. *American Mineralogist 89:* 1673-1679.

Hammer, J.E., Cashman, K.V., Hoblitt, R.P., Newman, S., 1999. Degassing and microlite crystallization during pre-climactic events of the 1991 eruption of Mt. Pinatubo, Philippines. *Bulletin of Volcanology 60:* 355-380.

Hammer, J.E., Cashman, K.V., Voight, B., 2000. Magmatic processes revealed by textural and compositional trends in Merapi dome lavas. *Journal of Volcanology and Geothermal Research 100:* 165-192.

Hammer, J.E., Manga, M., Cashman, K.V., 1998. Non-equilibrium and unsteady fluid degassing during slow decompression. *Geophysical Research Letters 25(24):* 4565-4568.

Hammer, J.E., Rutherford, M.J., 2002. An experimental study of the kinetics of decompression-induced crystallization in silicic melt. *Journal of Geophysical Research B: Solid Earth 107*: 8-1-8-24.

Harris, A.J.L., Murray, J.B., Aries, S.E., Davies, M.A., Flynn, L.P., Wooster, M.J., Wright, R., Rothery, D.A., 2000. Effusion rate trends at Etna and Krafla and their implications for eruptive mechanisms. *Journal of Volcanology and Geothermal Research 102:* 237-270.

Harris, A.J.L., Neri, M., 2002. Volumetric observations during paroxysmal eruptions at Mount Etna: pressurized drainage of a shallow chamber or pulsed supply? *Journal of Volcanology and Geothermal Research 116:* 79-95.

Harrison, A.J., White, R.S., 2004. Crustal structure of the Taupo Volcanic Zone, New Zealand: Stretching and igneous intrusion. *Geophysical Research Letters 31:* DOI: 10.1029/2004GL019885.

Head, J.W., Wilson, L., 1987. Lava fountain heights at Pu`u 'O`o, Kilauea, Hawaii: Indicators of amount and variations of exsolved magma volatiles. *Journal of Geophysical Research 92:* 13715-13719.

Head, J.W., Wilson, L., 1989. Basaltic pyroclastic eruptions: Influence of gas-release patterns and volume fluxes on fountain structure, and the formation of cinder cones, spatter cones, rootless flows, lava ponds and lava flows. *Journal of Volcanology and Geothermal Research 37:* 261-271.

Heiken, G., 1987. Textural analysis of tephra from a rhyodacitic eruption sequence, Thira (Santorini), Greece. In Marshall J (Ed.), *Clastic Particles*, Van Nostrand-Reinhold Co., New York, pp. 67-78.

Heiken, G., Wohletz, K., 1985. *Volcanic Ash.* University of California Press, Berkley, 246 pp.

Heliker, C.C., Kauahikaua, J., Sherrod, D.R., Lisowski, M., Cervelli, P.F., 2003. The Rise and fall of Pu'u 'O'o Cone, 1983-2002. *U.S. Geological Survey Professional Paper 1676*: 29-51.

Heliker, C.C., Maddox, T.N., 2003. The first two decades of the Pu'u 'O'o-Kupaianaha eruption: chronology and selected bibliography. *U.S Geological Survey Professional Paper 1676*: 1-28.

Herd, R.A., Pinkerton, H., 1997. Bubble coalescence in basaltic lava: its impact on the evolution of bubble populations. *Journal of Volcanology and Geothermal Research 75:* 137-157.

Hess, K., Dingwell, D.B., 1996. Viscosities of hydrous leucogranitic melts: A non-Arrhenian model. *American Mineralogist 81:* 1297-1300.

Hildreth, W., 1983. The compositionally zoned eruption of 1912 in the Valley of Ten Thousand Smokes, Katmai National Park, Alaska. *Journal of Volcanology and Geothermal Research 18:* 1-56.

Hildreth, W., Drake, R.E., 1992. Volcán Quizapu, Chilean Andes. *Bulletin of Volcanology 54:* 93-125.

Hirn, A., Nicolich, R., Gallart, J., Laigle, M., Cernobori, L., ETNASEIS Scientific Group, 1997. Roots of Etna volcano in the faults of great earthquakes. *Earth and Planetary Science Letters 148*: 171-191.

Hirth, J.P., Pound, G.M., St Pierre, G.R., 1970. Bubble nucleation. *Metallurgical Transactions 1:* 939-945.

Hochstein, M.P., Regenauer-Lieb, K., 1989. Heat transfer in the Taupo Volcanic Zone (NZ): role of volcanism and heating by plastic deformation. *Proceedings of the New Zealand Geothermal Workshop 11:* 219-223.

Hochstein, M.P., Smith, I.E.M., Regenauer-Lieb, K., Ehara, S., 1993. Geochemistry and heat transfer processes in Quaternary rhyolitic systems of the Taupo Volcanic Zone, New Zealand. *Tectonophysics 223:* 213-235.

Hogg, A.G., Higham, T.F.G., Lowe, D.J., Palmer, J.G., Reimer, P.J., Newnham, R.M., 2003. A wiggle-rnatch date for Polynesian settlement of New Zealand. *Antiquity 77:* 116-125.

Holloway, J.R., 1976. Fluids in the evolution of granitic magmas: consequences of finite CO_2 solubility. *Geological Society of America Bulletin 87:* 1513-1518.

Holloway, J.R., Blank, J.G., 1994. Application of experimental resutlts to C-O-H species in natural melts. In: Carroll, M.R., Holloway, J.R. (Eds.), *Volatiles in Magmas*. Reviews in Mineralogy, Mineralogical Society of America, pp. 187-230.

Holman, J., 1992. *Heat Transfer*. McGraw-Hill Book Co., London, 713 pp.

Hort, M., Gardner, J.E., 2000. Constraints on cooling and degassing of pumice during Plinian volcanic eruptions based on model calculations. *Journal of Geophysical Research 105*: 25981-26001.

Houghton, B.F., Wilson, C.J.N., 1989. A vesicularity index for pyroclastic deposits. *Bulletin of Volcanology 51:* 451-462.

Houghton, B.F., Wilson, C.J.N., 1998. Fire and water: physical roles of water in large eruptions at Taupo and Okataina calderas. In: Arehart GB, Hulston JR (Eds.), *Water-Rock Interaction*, Proceedings of the 9th International Symposium on Water-Rock Interaction, Taupo, New Zealand, 30 March - 3 April 1998. AA Balkema, Rotterdam, pp 25-30.

Houghton, B.F., Wilson, C.J.N., Del Carlo, P., Coltelli, M., Sable, J.E., Carey, R., 2004a. The influence of conduit processes on changes in style of basaltic plinian eruptions: Tarawera 1886 and Etna 122 BC. *Journal of Volcanology and Geothermal Research 137:* 1-14.

Houghton, B.F., Wilson, C.J.N., Fierstein, J., Hildreth, W., 2004b. Complex proximal deposition during the Plinian eruptions of 1912 at Novarupta, Alaska. *Bulletin of Volcanology 66:* 95-133.

Houghton, B.F., Wilson, C.J.N., McWilliams, M.O., Lanphere, M.A., Weaver, S.D., Briggs, R.M., Pringle, M.S., 1995. Chronology and dynamics of a large silicic magmatic system: Central Taupo Volcanic Zone, New Zealand. *Geology 23(1):* 13-16.

Houghton, B.F., Wilson, C.J.N., Smith, I.E.M., 2000. Shallow-seated controls on styles of explosive basaltic volcanism: a case study from New Zealand. *Journal of Volcanology and Geothermal Research 91*: 97-120.

Hurwitz, S., Navon, O., 1994. Bubble nucleation in rhyolitic melts: Experiments at high pressure, temperature, and water content. *Earth and Planetary Science Letters 122:* 267-280.

Hutton FW (1887) The eruption of Mount Tarawera. *Journal of the Geological Society of London* 43: 178-189.

INGV (Istituto Nazionale di Geofisica e Vulcanologia), 2001. Unita Funzionale Vulcanologia e Geochimica Report. Retrieved October 2005 from http://www.ct.ingv.it/Ufvg/Default.htm.

INGV (Istituto Nazionale di Geofisica e Vulcanologia), 2002. Unita Funzionale Vulcanologia e Geochimica Report. Retrieved October 2005 from http://www.ct.ingv.it/Ufvg/Default.htm.

James, M.R., Bagdassarov, N., Müller, K., Pinkerton, H., 2004. Viscoelastic behaviour of basaltic lavas. *Journal of Volcanology and Geothermal Research 132*: 99-113.

Jaupart, C., 1996. Physical models of volcanic eruptions. *Chemical Geology 128:* 217-227.

Jaupart, C., 1998. Gas loss from magmas through conduit walls during eruption. In: Gilbert, J.S., Sparks, R.S.J. (Eds.), *Physics of Explosive Volcanic Eruptions*, Geological Society Special Publications, pp. 73-90.

Jaupart, C., 2000. Magma ascent at shallow levels. In: Houghton, B.F., McNutt, S.R., Rymer, H., Stix, J. (Eds.), *Encyclopedia of Volcanoes*, Academic Press, San Diego, pp. 237-248.

Jaupart, C., Allegre, C.J., 1991. Gas content, eruption rate and instabilities of eruption regime in silicic volcanoes. *Earth and Planetary Science Letters 102*: 413-429.

Jaupart, C., Vergniolle, S., 1989. The generation and collapse of a foam layer at the roof of a basaltic magma chamber. *Journal of Fluid Mechanics 203:* 347-380.

Johnson, M.C., Anderson, A.T., Rutherford, M.J., 1994. Pre-eruptive volatile contents of magmas. In: Ribbe, P.H., Carroll, M.R., and Holloway, J.R., *Volatiles in Magmas,* Reviews in Mineralogy, Mineralogical Society of America, Washington, D.C., pp. 281–323.

Kamenetsky, V., Clocchiatti, R., 1996. Primitive magmatism of Mt. Etna: insights from mineralogy and melt inclusions. *Earth and Planetary Science Letters 142:* 553-572.

Kaminski, E., Jaupart, C., 1997. Expansion and quenching of vesicular magma fragments in Plinian eruptions. *Journal of Geophysical Research 102:* 12187-12203.

Keam, R.F., 1988. *Tarawera: the volcanic eruption of 10 June 1886.* Published by the author, Auckland, New Zealand, 472 pp.

Kerswell, R.R., 2005. Recent progress in understanding the transition to turbulence in a pipe. *Nonlinearity 18:* R17-R44.

King, P., 2000. Tectonic reconstructions of New Zealand 40 Ma to the present. *New Zealand Journal of Geology and Geophysics 43(4):* 611-638.

Kirkpatrick, R.J., 1981. Kinetics of crystallization of igneous rocks. In: Lasaga AC, Kirkpatrick RJ, editors. *Kinetics of geochemical processes*, Washington, DC: Mineralogical Society of America, pp. 1-81.

Klug, C., Cashman, K.V., 1994. Vesiculation of May 18, 1980, Mount St. Helens magma. *Geology 22:* 468-472.

Klug, C., Cashman, K.V., 1996. Permeability development in vesiculating magmas: implications for fragmentation. *Bulletin of Volcanology 58:* 87-100.

Klug, C., Cashman, K.V., Bacon, C.R., 2002. Structure and physical characteristics of pumice from the climactic eruption of Mount Mazama (Crater Lake), Oregon. *Bulletin of Volcanology 64:* 486-501.

Koyaguchi, T., 1994. Grain-size variation of tephra derived from volcanic umbrella clouds. *Bulletin of Volcanology 56:* 1-9.

Koyaguchi, T., Mitani, N.K., 2005. A theoretical model for fragmentation of viscous bubbly magmas in shock tubes. *Journal of Geophysical Research 110:* DOI: 10.1029/2004JB003513.

Koyaguchi, T., Woods, A., 1996. On the formation of eruption columns following explosive mixing of magma and surface-water. *Journal of Geophysical Research 101(B3)*: 5561-5574.

Koyama, M., Hayakawa, Y., 1996. Syn- and post-caldera eruptive history of Izu Oshima volcano based on tephra and loess stratigraphy. *Journal of Geography 105*: 133-162.

Lanzafame, G., Neri, M., Coltelli, M., Lodato, L., Rust, D., 1997. North-south compression in the Mt Etna region (Sicily): spatial and temporal distribution. *Acta Vulcanologica 9:* 121-133.

Lautze, N.C., Houghton, B.F., 2005. Physical mingling of magma and complex eruption dynamics in the shallow conduit at Stromboli volcano, Italy. *Geology 33:* 425-428.

Lejeune, A., Richet, P., 1995. Rheology of crystal-bearing silicate melts: an experimental study at high viscosities. *Journal of Geophysical Research 100(B3)*: 4215-4229.

Lensky, N.G., Navon, O., Lyakhovsky, V., 2004. Bubble growth during decompression of magma: experimental and theoretical investigation. *Journal of Volcanology and Geothermal Research 129:* 7-22.

Lipman, P.W., Banks, N.G., 1987. Aa flow dynamics, Mauna Loa 1984. *U.S. Geological Survey Professional Paper 1350*: 1527-1568.

Llewellin, E.W., Mader, H.M., Wilson, S.D.R., 2002. The rheology of a bubbly liquid. *Proceedings of the Royal Society of London A 458*: 987-1016.

Lofgren, G., 1974. An experimental study of plagioclase crystal morphology: isothermal crystallization. *American Journal of Science 274:* 243-273.

Lowe, D.J., Newnham, R.M., Ward, C.M., 1999. Stratigraphy and chronology of a 15 ka sequence of multi-sourced silicic tephras in a montane peat bog, eastern North Island, New Zealand. *New Zealand Journal of Geology and Geophysics 42:* 565-579.

Lyakhovsky, V., Hurwitz, S., Navon, O., 1996. Bubble growth in rhyolitic melts: experimental and numerical investigation. *Bulletin of Volcanology 58:* 19-32.

Manga, M., Castro, J., Cashman, K.V., Loewenberg, M., 1998. Rheology of bubble-bearing magmas. *Journal of Volcanology and Geothermal Research 87*: 15-28.

Mangan, M.T., 1990. Crystal size distribution systematics and the determination of magma storage times: The 1959 eruption of Kilauea Volcano, Hawaii. *Journal of Volcanology and Geothermal Research 44:* 295-302.

Mangan, M.T., Cashman, K.V., 1996. The structure of basaltic scoria and reticulite and inferences for vesiculation, foam formation, and fragmentation in lava fountains. *Journal of Volcanology and Geothermal Research 73*: 1-18.

Mangan, M.T., Cashman, K.V., Newman, S., 1993. Vesiculation of basaltic magma during eruption. *Geology 21:* 157-160.

Mangan, M.T., Mastin, L., Sisson, T., 2004. Gas evolution in eruptive conduits: combining insights from high temperature and pressure decompression experiments with steady-state flow modeling. *Journal of Volcanology and Geothermal Research 129:* 23-36.

Mangan, M.T., Sisson, T., 2000. Delayed, disequilibrium degassing in rhyolite magma: decompression experiments and implications for explosive volcanism. *Earth Planetary Science Letters 183:* 441-455.

Marsh, B.D., 1988. Crystal size distribution (CSD) in rocks and the kinetics and dynamics of crystallization I. Theory. *Contributions to Mineralogy and Petrology 99*: 277-291.

Marsh, B.D., 1998. On the interpretation of crystal size distributions in magmatic systems. *Journal of Petrology 39:* 553–599.

Martel, C., Dingwell, D.B., Spieler, O., Pichavant, M., Wilke, M., 2001. Experimental fragmentation of crystal- and vesicle-bearing silicic melts. *Bulletin of Volcanology 63:* 398-405.

Mastin, L.G., Christiansen, R.L., Thornber, C., Lowenstern, J., Beeson, M., 2004. What makes hydromagmatic eruptions violent? Some insights from the Keanakako'i Ash, Kilauea Volcano, Hawai'i. *Journal of Volcanology and Geothermal Research 137:* 15-31.

McBirney, A.R., Murase, T., 1984. Rheological properties of magmas. *Annual Reviews in Earth and Planetary Sciences 12:* 337-357.

McClelland, L., Simkin, T., Sumners, M., Nielsen, E., Stein, T.C., Eds., 1989. *Global volcanism 1975-1985.* Prentice-Hall and American Geophysical Union, 653 pp.

McGuire, W.J., Stewart, I.S., Saunders, S.J., 1997. Intra-volcanic rifting at Mount Etna in the context of regional tectonics. *Acta Vulcanologica 9:* 147-156.

McPhie, J., Walker, G.P.L., Christiansen, R.L., 1990. Phreatomagmatic and phreatic fall and surge deposits from explosions at Kilauea volcano, Hawaii, 1790 A.D.: Keanakakoi ash member. *Bulletin of Volcanology 52:* 334-354.

Means, W.D., Park, Y., 1994. New experimental approach to understanding igneous texture. *Geology 22*: 323-326.

Melnik, O.E., 2000. Dynamics of two-phase conduit flow of high viscosity gas-saturated magma: large variations of sustained explosive eruption intensity. *Bulletin of Volcanology 62:* 153–170

Métrich, N., Allard, P., Spilliaert, N., Andronico, D., Burton, M., 2004. 2001 flank eruption of the alkali- and volatile-rich primitive basalt responsible for Mount Etna's evolution in last three decades. *Earth and Planetary Science Letters 228*: 1-17.

Métrich, N., Clocchiatti, R., Mosbah, M., Chaussidon, M., 1993. The 1989-1990 activity of Etna magma mingling and ascent of H2O-Cl-S-rich basaltic magma - evidence from melt inclusions. *Journal of Volcanology and Geothermal Research 59:* 131-144.

Métrich, N., Rutherford, M.J., 1998. Low pressure crystallization paths of H_2O-saturated basaltic-hawaiitic melts from Mt Etna: Implications for open-system degassing of basaltic volcanoes. *Geochimica et Cosmochimica Acta 62:* 1195–1205.

Moore, G., Vennemann, T., Carmichael, I.S.E., 1995. Solubility of water in magmas to 2 kbar. *Geology 23:* 1099-1102.

Moores, E.M., Fairbridge, R.W., Eds., 1998. *Encyclopedia of European and Asian Regional Geology.* Encyclopedia of Earth Sciences Series, Chapman and Hall.

Mourtada-Bonnefoi, C.C., Mader, H.M., 2003. Experimental observations of the effect of crystals and pre-existing bubbles on the dynamics and fragmentation of vesiculating flows. *Journal of Volcanology and Geothermal Research 129:* 83-97.

Munson, B.R., Young, D.F., Okiishi, T.H., 1990. *Fundamentals of Fluid Dynamics.* John Wiley & Sons, New York, 843 pp.

Murase, T., McBirney, A.R., 1973. Properties of some common igneous rocks and their melts at high temperatures. *Geological Society of America Bulletin 84(11)*: 3563–3592.

Murru, M., Montuori, C., Wyss, M., Privitera, E., 1999. The locations of magma chambers at Mt. Etna, Italy, mapped by b-values. *Geophysical Research Letters 26*: 2553-2556.

Mysen, B.O., 1977. The solubility of H_2O and CO_2 under predicted magma genesis conditions and some petrological and geophysical implications. *Reviews of Geophysics and Space Physics 15:* 351-361.

Nairn, I.A., 1979. Rotomahana-Waimangu eruption, 1886: Base surge and basalt magma. *Journal of Geology and Geophysics 22(3):* 363-378.

Nairn, I.A., 1989. Sheet V16 AC *Mount Tarawera.* Geological map of New Zealand 1:50000. Department of Scientific and Industrial Research, Wellington, New Zealand.

Nairn, I.A., Cole, J.W., 1981. Basalt dikes in the 1886 Tarawera Rift. *New Zealand Journal of Geology and Geophysics 24(5-6)*: 585-592.

Nairn, I.A., Shane, P.R., Cole, J.W., Leonard, G.J., Self, S., Pearson, N., 2004. Rhyolite magma processes of the ~ AD 1315 Kaharoa eruption episode, Tarawera volcano, New Zealand. *Journal of Volcanology and Geothermal Research 2732:* 1-30.

Namiki, A., Manga, M., 2005. Response of a bubble bearing viscoelastic fluid to rapid decompression: Implications for explosive volcanic eruptions. *Earth and Planetary Science Letters 236*: 269-284.

Navon, O., Chekhmir, A., Lyakhovsky, V., 1998. Bubble growth in highly viscous melts: theory, experiments, and autoexplosivity of dome lavas. *Earth and Planetary Science Letters 160:* 763-776.

Navon, O., Lyakhovsky, V., 1998. Vesiculation processes in silicic magmas. In: Gilbert, J.S., Sparks, R.S.J. (Eds.), *Physics of Explosive Volcanic Eruptions*, Geological Society, London, Special Publications, London, pp. 27-50.

Neri, M., Acocella, V., Behncke, B., Maiolino, V., Ursino, A., Velardita, R., 2005. Contrasting triggering mechanisms of the 2001 and 2002-2003 eruptions of Mount Etna (Italy). *Journal of Volcanology and Geothermal Research 144*: 235-255.

Neuville, D..R., Courtial, P., Dingwell, D.B., Richet, P., 1992. Thermodynamic and rheological properties of rhyolite and andesite melts. *Contributions to Mineralogy and Petrology 113(4):* 572-581.

Newman, S., Epstein, S., Stolper, E., 1988. Water, carbon dioxide and hydrogen isotopes in glasses from the ca. 1340 A.D. eruption of the Mono Craters, California: Constraints on degassing phenomena and initial volatile content. *Journal of Volcanology and Geothermal Research 35:* 75-96.

Nielsen, R.L., Drake, M.J., 1979. Pyroxene-melt equilibria. *Geochimica Cosmochimica Acta 43:* 1259-1272.

Nimis, P., 1999. Clinopyroxene geobarometry of magmatic rocks – Part 2. Structural geobarometers for basic to acid, tholeiitic and mildly alkaline magmatic systems. *Contributions to Mineralogy and Petrology 135:* 62-74.

Orsi, G., Gallo, G., Heiken, G., Wohletz, K., Yu, E., Bonani, G., 1992. A comprehensive study of pumice formation and dispersal: the Cretaio tephra of Ischia (Italy). *Journal of Volcanology and Geothermal Research 53:* 329-354.

Papale, P., 1998. Volcanic conduit dynamics. In: Freundt, A., Rosi, M. (Eds.), *From Magma to Tephra: Modelling physical Processes of Explosive Volcanic Eruptions*, Elsevier, Amsterdam, pp. 55-89.

Papale, P., 1999a. Modeling of the solubility of a two-component H_2O+CO_2 fluid in silicate liquids. *American Mineralogist 84(4):* 477-492.

Papale, P., 1999b. Strain-induced magma fragmentation in explosive eruptions. *Nature 397:* 425-428.

Papale, P., Barsanti, M., Barbato, D.,Moretti, R., 2006. A statistical method to determine total H2O and CO2 budgets in magmas. *Geophysical Research Abstracts 8*: 00612, EGU Meeting, Vienna, April 2006.

Papale, P., Neri, A., Macedonio, G., 1998. The role of magma composition and water content in explosive eruptions – 1. Conduit ascent dynamics. *Journal of Volcanology and Geothermal Research 87:* 75-93.

Papale, P., Rossi, M., 1993. A case of no-wind plinian fallout at Pululagua caldera (Ecuador): implications for models of clast dispersal. *Bulletin of Volcanology 55:* 523–535.

Parfitt, E.A., 2004. A discussion of the mechanisms of explosive basaltic eruptions. *Journal of Volcanology and Geothermal Research 134:* 77-107.

Parfitt, E.A., Wilson L., 1994. The 1983-86 Pu'u 'O'o eruption of Kilauea volcano, Hawaii: a study of dike geometry and eruption mechanisms for a long-lived eruption. *Journal of Volcanology and Geothermal Research 59:* 179-205.

Parfitt, E.A., Wilson, L., 1995. Explosive volcanic eruptions - IX. The transition between Hawaiian-style lava fountaining and Strombolian explosive activity. *Geophysical Journal International 121:* 226-232.

Parfitt, E.A., Wilson, L., 1999. A Plinian treatment of fallout from Hawaiian lava fountains. *Journal of Volcanology and Geothermal Research 88:* 67-75.

Pettijohn, F.J., 1957. *Sedimentary Rocks*, 2nd ed. New York: Harper and Row, 718 pp.

Pinkerton, H., Stevenson, R.J., 1992. Methods of determining the rheological properties of magmas at sub-liquidus temperatures. *Journal of Volcanology and Geothermal Research 53:* 47-66.

Polacci, M., Corsaro, R.A., Andronico, D. 2006. Coupled textural and compositional characterization of basaltic scoria: insights into the transition from Strombolian to fire fountain activity at Mount Etna, Italy. Geology 34 (3), 201-204.

Polacci, M., Pioli, L., Rosi, M., 2003. The Plinian phase of the Campanian Ignimbrite eruption (Phlegrean Fields, Italy): evidence from density measurements and textural characterization of pumice. *Bulletin of Volcanology 65:* 418-432.

Proussevitch, A.A., Sahagian, D.L., 1996. Dynaimcs of coupled diffusive and decompressive bubble growth in magmatic systems. *Journal of Geophysical Research 101(B8):* 17447-17455.

Proussevitch, A.A., Sahagian, D.L., Anderson, A.T., 1993. Dynamics of diffusive bubble growth in magmas: isothermal case. *Journal of Geophysical Research 98(B12):* 22283-22307.

Pyle, D.M., 1989. The thickness, volume and grainsize of tephra fall deposits. *Bulletin of Volcanology 51:* 1-15.

Richter, D.H., Eaton, J.P., Murata, K.J., Ault, W.U., Krivoy, H.L., 1970. Chronological narrative of the 1959-60 eruption of Kilauea Volcano, Hawaii. *U.S. Geological Survey Professional Paper 537-E:* 73 pp.

Riedel, C., Ernst, G.G.J., Riley, M., 2003. Controls on the growth and geometry of pyroclastic constructs. *Journal of Volcanology and Geothermal Research 127:* 121-152.

Ripepe, M., 1996. Evidence for gas influence on volcanic seismic signals recorded at Stromboli. *Journal of Volcanology and Geothermal Research 70:* 221-233.

Ripepe, M., Gordeev, E.I., 1999. Gas bubble dynamics model for shallow volcanic tremor at Stromboli. *Journal of Geophysical Research 104(B5):* 10639-10654.

Roscoe, R., 1952. The viscosity of suspensions of rigid spheres. *British Journal of Applied Physics 3*: 267-269.

Rutherford, M.J., Hill, P.M., 1993. Magma ascent rates from amphibole breakdown: an experimental study applied to the 1980-1986 Mount St. Helens eruptions. *Journal of Geophysical Research 98:* 19667-19685.

Saar, M.O., 1998. *The relationship between permeability, porosity, and microstructure in vesicular basalts.* M.S. Thesis, University of Oregon, 91 pp.

Saar, M.O., Manga, M., 1999. Permeability-porosity relationship in vesicular basalts, *Geophysical Research Letters 26:* 111-114.

Saar, M.O., Manga, M., Cashman, K.V., Fremouw, S., 2001. Numerical simulations of the onset of yield strength in crystal-melt suspensions. *Earth and Planetary Science Letters 187:* 367-379.

Sable, J.E., Houghton, B.F., Del Carlo, P., Coltelli, M., 2006a. Cross-conduit heterogeneity and shifting degassing behavior during the Etna 122 BC basaltic plinian eruption. *Journal of Volcanology and Geothermal Research*, in review.

Sable, J.E., Houghton, B.F., Wilson, C.J.N., Carey, R.J., 2006b. Complex proximal sedimentation from Plinian plumes: the example of Tarawera 1886. *Bulletin of Volcanology* DOI: 10.1007/s00445-006-0057-6.

Sahagian, D.L., 1985. Bubble migration and coalescence during the solidification of basaltic lava flows. *Journal of Geology 93:* 205–211.

Sahagian, D.L., Anderson, A.T., Ward, B., 1989. Bubble coalescence in basalt flows: Comparison of a numerical model with natural examples. *Bulletin of Volcanology 52:* 49-56.

Sahagian, D.L., Proussevitch, A.A., 1998. 3D particle size distributions from 2D observations: stereology for natural applications. *Journal of Volcanology and Geothermal Research 84:* 173- 196.

Sarda, P., Graham, D., 1990. Mid-ocean ridge popping rocks: Implications for degassing at ridge crests. *Earth and Planetary Science Letters 97:* 268-289.

Sarna-Wojcicki AM, Shipley S, Waitt Jr. RB, Dzurisin D, Wood SH (1981) Areal distribution, thickness, mass, volume, and grain size of air-fall ash from six major eruptions of 1980. In: Lipman PW, Mullineaux DR (eds) The 1980 eruptions of Mount St Helens, Washington. *U.S. Geological Survey Professional Paper 1250*, Washington DC, pp 577-600.

Scasso, R., Corbella, H., Tiberi, P., 1994. Sedimentological analysis of the tephra from the 12-15 August 1991 eruption of Hudson volcano. *Bulletin of Volcanology 56:* 121-133.

Scriven, L.E., 1959. On the dynamics of phase growth. *Chemical Engineering Science 10:* 1-13.

SEAN (Scientific Event Alert Network), 1988. Lonquimay (Chile) volcanic activity report. *SEAN Volcanic Activity Reports 1988.*

Self, S., 1976. The Recent volcanology of Terceira, Azores. *Journal of the Geological Society 132:* 645-666.

Self, S., Sparks, R.S.J., 1978. Characteristics of widespread pyroclastic deposits formed by the interaction of silicic magma and water. *Bulletin Volcanologique 41*: 196-212.

Seyfried, R., Freundt, A., 2000. Experiments on conduit and eruption behavior of basaltic volcanic eruptions. *Journal of Geophysical Research 105(B10):* 23727-23740.

Shaw, H.R., 1972. Viscosities of magmatic silicate liquids: an empirical model of prediction. *American Journal of Science 272:* 870-893.

Sherman, P., 1968. General properties of emulsions and their constituents. In: Sherman, P. (Ed.), *Emulsion Science*, Academic Press, London, pp. 131-212.

Signorelli, S., Vaggelli, G., Francalanci, L., Rosi, M., 1999. Origin of magmas feeding the Plinian phase of the Campanian Ignimbrite eruption, Phlegrean Fields, Italy: constraints based on matrix-glass and glass-inclusion compositions. *Journal of Volcanology and Geothermal Research 91*: 199-220.

Simakin, A.G., Armienti, P., Epelbaum, M.B., 1999. Coupled degassing and crystallization: experimental study at continuous pressure drop, with application to volcanic bombs. *Bulletin of Volcanology 61:* 275-287.

Simkin, T., Siebert, L., 1994. *Volcanoes of the World.* Geoscience Press, Tucson, AZ.

Smith, J.V., 1997. Shear thickening dilatancy in crystal-rich flows. *Journal of Volcanology and Geothermal Research 79*: 1-8.

Smith, S.P., 1886a. *The eruption of Tarawera: A report to the Surveyor General.* N Z Government Printer, Wellington, New Zealand, 84 pp.

Smith, S.P., 1886b. Preliminary report on the volcanic eruption at Tarawera. *Journal of the House of Representatives 26:* 1-4.

Sonder, I., Zimanowski, B., Büttner, R., 2006. Non-Newtonian viscosity of basaltic magma. *Geophysical Research Letters 33:* DOI: 10.1029/2005GL024240.

Sparks, R.S.J., 1978. The dynamics of bubble formation and growth in magmas: a review and analysis. *Journal of Volcanology and Geothermal Research 3:* 1-37.

Sparks, R.S.J., 1986. The dimensions and dynamics of volcanic eruption columns. *Bulletin of Volcanology 48:* 3-15.

Sparks, R.S.J., Barclay, J., Jaupart, C., Mader, H.M., Phillips, J.C., 1994. Physical aspects of magma degassing I. Experimental and theoretical constraints on vesiculation, *Volatiles in Magmas*, Reviews in Mineralogy, Mineralogical Society of America, pp. 413-445.

Sparks, R.S.J., Brazier, S., 1982. New evidence for degassing processes during explosive eruptions. *Nature 295:* 218-220.

Sparks, R.S.J., Bursik, M.I., Ablay, G.J., Thomas, R.M.E., Carey, S.N., 1992. Sedimentation of tephra by volcanic plumes - 2. Controls on thickness and grain-size variations of tephra fall deposits. *Bulletin of Volcanology 54:* 685-695.

Sparks, R.S.J., Bursik, M.I., Carey, S.N., Gilbert, J.S., Glaze, L.S., Sigurdsson, H., Woods, A.W., 1997. *Volcanic Plumes*, John Wiley & Sons, Chichester, 574 pp.

Sparks, R.S.J., Wilson, L., Sigurdsson, H., 1981. The pyroclastic deposits of the 1875 eruption of Askja, Iceland. *Philosophical Transactions of the Royal Society A 299:* 242-273.

Sparks, R.S.J., Wright, J.V., 1979. Welded air-fall tuffs. *Geological Society of America Special Paper 180*: 155-166.

Spera, F.J., 2000. Physical properties of magmas. In: Houghton, B.F., McNutt, S.R., Rymer, H., Stix, J. (Eds.), *Encyclopedia of Volcanoes.* Academic Press, San Diego, pp. 171-190.

Spieler, O., Kennedy, B., Kueppers, U., Dingwell, D.B., Scheu, B., Taddeucci, J., 2004. The fragmentation threshold of pyroclastic rocks. *Earth and Planetary Science Letters 226*: 139-148.

Spilliaert, N., Allard, P., Métrich, N., Sobolev, A.V., 2006a. Melt inclusion record of the conditions of ascent, degassing and extrusion of volatile-rich alkali basalt during the powerful 2002 flank eruption of Mount Etna (Italy). *Geophysical Research Abstracts 8*: 00612, EGU Meeting, Vienna, April 2006.

Spilliaert, N., Métrich, N., Allard, P., 2006b. S-Cl-F degassing during ascent and eruption of water-CO_2-rich alkali basalt: modelling and relationship with eruptive styles on Mount Etna. *Geophysical Research Abstracts 8*: 00612, EGU Meeting, Vienna, April 2006.

Stern, T.A., 1985. A back-arc basin formed within continental lithosphere: the Central Volcanic Region of New Zealand. *Tectonophysics 112:* 385-409.

Stix, J., Arlez, J., Calvache, M.L., Cortés, G.P., Fischer, T.P., Gomez, D., Ordonez, M., Torres, R., Williams, S.N., 1993. A model of degassing at Galeras volcano, Colombia, 1988-1993. *Geology 21:* 963-967.

Sumner, J.M., 1998. Formation of clastogenic lava flows during fissure eruption and scoria cone collapse: the 1986 eruption of Izu-Oshima volcano, Eastern Japan. *Bulletin of Volcanology 60:* 195-212.

Sutton, A.N., 1995. Evolution of a large magmatic system: Taupo volcanic centre, New Zealand. Ph.D. Thesis, The Open University, Milton Keynes, UK, 416 pp.

Sutton, A.N., Blake, S., Wilson, C.J.N., Charlier, B.L.A., 2000. Late Quaternary evolution of a hyperactive rhyolite magmatic system: Taupo volcanic centre, New Zealand. *Journal of the Geological Society 157:* 537-552.

Swanson, D.A., Duffield, W.A., Jackson, D.B., Peterson, D.W., 1979. Chronological narrative of the 1969-71 Mauna Ulu eruption of Kilauea Volcano, Hawaii. *U.S. Geological Survey Professional Paper 1056*: 1-55.

Taddeucci, J., Andronico, D., Büttner, R., Zimanowski, B., Scarlato, P., 2006. The effect of crystal content on the fragmentation of explosively erupting basaltic magma. *Geophysical Research Abstracts 8*: 00612, EGU Meeting, Vienna, April 2006.

Taddeucci, J., Spieler, O., Ichihara, M., Dingwell, B., 2004. Vesiculation, flow, and fragmentation of viscoelastic magma: inferences from an American toy. *Eos Transactions AGU 85(17)*, Joint Assembly Supplement, Abstract V24A-01.

Tait, S., Jaupart, C., Thomas, R., Gardner, J., 1998. Constraints on cooling rates and permeabilities of pumice in an explosive eruption jet from color and magnetic mineralogy. *Journal of Volcanology and Geothermal Research 86*: 79-91.

Tanguy, J., Condomines, M., Kieffer, G., 1997. Evolution of Mount Etna magma: Constraints on the present feeding system and eruptive mechanism. *Journal of Volcanology and Geothermal Research 75:* 221-250.

Thomas, A.P.W., 1888. *Report on the eruption of Tarawera and Rotomahana*, New Zealand Government Printer, Wellington, New Zealand, 74 pp.

Thomas, R.M.E., Sparks, R.S.J., 1992. Cooling of tephra during fallout from eruption columns. *Bulletin of Volcanology 54:* 542-553.

Tokarev, P., 1983. Calculation of the magma discharge, growth in the height of the cone and dimensions of the feeder channel of crater 1 in the Great Tolbachik fissure eruption, July 1975. In: Fedotov S, Markhinin Y (Eds.), *The Great Tolbachik Fissure Eruption*, Cambridge University Press, Cambridge, pp. 27-35.

Toramaru, A., 1989. Vesiculation process and bubble size distributions in ascending magmas with constant velocities. *Journal of Geophysical Research 94:* 17523-17542.

Toramaru, A., 1990. Measurement of bubble size distributions in vesiculated rocks with implications for quantitative estimation of eruption processes. *Journal of Volcanology and Geothermal Research 43:* 71-90.

Toramaru, A., 1995. Numerical study of nucleation and growth of bubbles in viscous magmas. *Journal of Geophysical Research 100:* 1913-1931.

Toramaru, A., 2006. BND (bubble number density) decompression rate meter for explosive volcanic eruptions. *Journal of Volcanology and Geothermal Research 154(3-4):* 303-316.

Tuffen, H., Dingwell, D.B., Pinkerton, H., 2003. Repeated fracture and healing of silicic magma generates flow banding and earthquakes? *Geology 31*: 1089-1092.

Turnbull, D., 1964. Thermodynamics and kinetics of formation of the glass state and initial devitrification. In: Prins, J.A. (Ed.), *Physics of non-crystalline solids: Proceedings of the 1964 International Conference, Delft*, North Holland, Amsterdam, pp. 41-56.

Valentine, G.A., Groves, K.R., 1996. Entrainment of country rock during basaltic eruptions of the Lucero volcanic field, New Mexico. *Journal of Geology 104:* 71-90.

Van der Molen, I., Paterson, M., 1979. Experimental deformation of partially melted granite. *Contributions to Mineralogy and Petrology 70*: 299-318.

Vergniolle, S., 1996. Bubble size distribution in magma chambers and dynamics of basaltic eruptions. *Earth and Planetary Science Letters 140*: 269– 279.

Vergniolle, S., Brandeis, G., 1996. Strombolian explosions - 1. A large bubble breaking at the surface of a lava column as a source of sound. *Journal of Geophysical Research 101(B9):* 20433-20448.

Vergniolle, S., G. Brandeis, Mareschal, J.-C., 1996. Strombolian explosions - 2. Eruption dynamics determined from acoustic measurements. *Journal of Geophysical Research 101(B9):* 2044-20466.

Vergniolle, S., Jaupart, C., 1986. Separated two-phase flow and basaltic eruptions. *Journal of Geophysical Research 91:* 12842-12860.

Vergniolle, S., Mangan, M., 2000. Hawaiian and Strombolian eruptions. In: Houghton, B.F., McNutt, S.R., Rymer, H., Stix, J. (Eds.), *Encyclopedia of Volcanoes*, Academic Press, San Diego, pp. 447-461.

Walker, G.P.L., 1973. Explosive volcanic eruptions: a new classification scheme. *Geologische Rundschau 62:* 431-446.

Walker, G.P.L., 1980. The Taupo Pumice: product of the most powerful known (ultraplinian) eruption? *Journal of Volcanology and Geothermal Research 8*: 69-94.

Walker, G.P.L., 1981. Plinian eruptions and their products. *Bulletin Volcanologique 44*: 223-240.

Walker, G.P.L., 1989. Spongy pahoehoe in Hawaii: a study of vesicle-distribution patterns in basalt and their significance. *Bulletin of Volcanology 51*: 199-209.

Walker, G.P.L., Croasdale, R., 1972. Characteristics of some basaltic pyroclastics. *Bulletin Volcanologique 35(2)*: 303-317.

Walker, G.P.L., Self, S., Wilson, L., 1984. Tarawera 1886, New Zealand - a basaltic plinian fissure eruption. *Journal of Volcanology and Geothermal Research 21:* 61-78.

Walker, G.P.L., Wilson, L., Bowell, E.L.G., 1971. Explosive volcanic eruptions - I. The rate of fall of pyroclasts. *Geophysical Journal of the Royal Astronomical Society 22:* 377-383.

Wallace, P., Anderson, A.T., 2000. Volatiles in magmas. In: Houghton, B.F., McNutt, S.R., Rymer, H., Stix, J. (Eds.), *Encyclopedia of Volcanoes*, Academic Press, San Diego, pp. 149-170.

Westrich, H.R., Eichelberger, J.C., 1994. Gas transport and bubble collapse in rhyolitic magma: an experimental approach. *Bulletin of Volcanology 56:* 447-458.

Westrich, H.R., Gerlach, T.M., 1992. Magmatic gas source for the stratospheric SO_2 cloud from the June 15, 1991 eruption of Mount Pinatubo. *Geology 20:* 867-870.

Whitham, A.G., Sparks, R.S.J., 1986. Pumice. *Bulletin of Volcanology 48:* 209-223.

Williams, S.N., 1983. Plinian airfall deposits of basaltic composition. *Geology 11:* 211-214.

Williams, W.L., 1887. Phenomena connected with the Tarawera eruption of 10th of June as observed at Gisborne. *Transactions of the New Zealand Institute 19:* 380-382.

Wilson, C.J.N., Houghton, B.F., McWilliams, M.O., Lanphere, M.A., Weaver, S.D., Briggs, R.M., 1995a. Volcanic and structural evolution of Taupo Volcanic Zone, New Zealand: a review. *Journal of Volcanology and Geothermal Research 68:* 1-28.

Wilson, C.J.N., Rogan, A.M., Smith, I.E.M., Northey, D.J., Nairn, I.A., Houghton, B.F., 1984. Caldera volcanoes of the Taupo Volcanic Zone, New Zealand. *Journal of Geophysical Research 89:* 8463-8484.

Wilson, L., 1972. Explosive volcanic eruptions - II. The atmospheric trajectories of pyroclasts. *Geophysical Journal of the Royal Astronomical Society 30*: 381-392.

Wilson, L., 1976. Explosive volcanic eruptions - III. Plinian eruption columns. *Geophysical Journal of the Royal Astronomical Society 45:* 543-556.

Wilson, L., Head, J.W., 1981. Ascent and emplacement of basaltic magma on the Earth and Moon. *Journal of Geophysical Research 86:* 2971-3001.

Wilson, L., Parfitt, E.A., Head, J.W., 1995b. Explosive volcanic eruptions - VIII. The role of magma recycling in controlling the behaviour of Hawaiian-style lava fountains. *Geophysical Journal International 121:* 215-225.

Wilson, L., Sparks, R.S.J., Huang, T.C., Watkins, N.D., 1978. The control of volcanic column eruption heights by eruption energetics and dynamics. *Journal of Geophysical Research 83*: 1829-1836.

Wilson, L., Sparks, R.S.J., Walker, G.P.L. 1980. Explosive volcanic eruptions - IV. The control of magma properties and conduit geometry on eruption column behaviour. *Geophysical Journal of the Royal Astronomical Society 63*: 117-148.

Wilson, L., Walker, G.P.L., 1987. Explosive volcanic eruptions - VI. Ejecta dispersal in plinian eruptions: the control of eruption conditions and atmospheric properties. *Geophysical Journal of the Royal Astronomical Society 89*: 657-679.

Wohletz, K., 1986. Explosive magma-water interactions: thermodynamics, explosions mechanisms, and field studies. *Bulletin of Volcanology 48*: 245-264.

Wolfe, E.W., Neal, C.A., Banks, N.G., Duggan, T.J., 1988. Geologic observations and chronology of eruptive events in the Puu Oo eruption of Kilauea Volcano, Hawaii: Episodes 1 through 20, January 3, 1983, through June 8, 1984. In: Wolfe, E.W. (Ed.), *U.S. Geological Survey Professional Paper 1463*, 1–97.

Woods, A.W., 1988. The fluid dynamics and thermodynamics of eruption columns. *Bulletin of Volcanology 50*: 169-193.

Woods, A.W., Bower, S.M., 1995. The decompression of volcanic jets in a crater during explosive volcanic eruptions. *Earth and Planetary Science Letters 131:* 189-205.

Woods, A.W., Cardoso, S.S.S., 1997. Triggering basaltic volcanic eruptions by bubble-melt separation. *Nature 385:* 518-520.

Yasui, M., Koyaguchi, T., 2004. Sequence and eruptive style of the 1783 eruption of Asama Volcano, central Japan: a case study of an andesitic explosive eruption generating fountain-fed lava flow, pumice fall, scoria flow and forming a cone. *Bulletin of Volcanology 66:* 243-262.

Zhang, Y., 1999. A criterion for the fragmentation of bubbly magma based on brittle failure theory. *Nature 402*, 9: 648-650.

Zhang, Y., Behrens, H., 2000. H_2O diffusion in rhyolitic melts and glasses. *Chemical Geology 169*: 243-262.

Zhang, Y., Stolper, E.M., 1991. Water diffusion in basaltic melts. *Nature 351*: 306-309.